

LITHUANIAN ENERGY INSTITUTE

JUSTINA JASELIŪNAITĖ

THE INFLUENCE OF COHERENT FLOW  
STRUCTURES ON THE THERMOHYDRAULIC  
EFFICIENCY OF MICROCHANNELS

Doctoral dissertation  
Technological Sciences, Energetics and Power Engineering (T 006)

2026, Kaunas

The doctoral dissertation has been prepared at the Laboratory of Nuclear Installation Safety of the Lithuanian Energy Institute in 2021-2025. The research has been sponsored by the Research Council of Lithuania.

The doctoral right has been granted to Kaunas University of Technology together with Lithuanian Energy Institute.

**Research supervisor:**

Senior Researcher Dr. Marijus ŠEPORAITIS (Lithuanian Energy Institute, Technological Sciences, Energetics and Power Engineering, T 006).

**Edited by:** English language editor Lina Abraitienė (UAB “BELLA VERBA”), Lithuanian language editor Irma Urbonavičienė (No. 670485).

**Dissertation Defence Board of Energetics and Power Engineering Science Field:**

Chief Researcher Dr. Viktorija GRIGAITIENĖ (Lithuanian Energy Institute, Technological Sciences, Energetics and Power Engineering, T 006) – **chairperson**;

Prof. Dr. Hab. Ali Cemal BENIM (Düsseldorf University of Applied Sciences, Germany, Technological Sciences, Energetics and Power Engineering, T 006);

Chief Researcher Dr. Algis DŽIUGYS (Lithuanian Energy Institute, Technological Sciences, Energetics and Power Engineering, T 006);

Chief Researcher Dr. Gediminas RAČIUKAITIS (State Research Institute Center for Physical Sciences and Technology, Technological Sciences, Materials Engineering, T 008);

Assoc. Prof. Dr. Giedrė STRECKIENĖ (Vilnius Gediminas Technical University, Technological Sciences, Energetics and Power Engineering, T 006).

The dissertation defence will be held on 13 February 2026, at 1 p.m. at the meeting hall of the Lithuanian Energy Institute in the meeting of the Dissertation Defence Board of the Energetics and Power Engineering Science Field.

Address: Breslaujos 3-202, LT-44403 Kaunas, Lithuania.

Tel. +370 37 401 805; email: studijos@lei.lt

The dissertation was sent out on 13 January 2026.

The dissertation is available on the website <http://ktu.edu>, at the library of Kaunas University of Technology (Gedimino 50, Kaunas) and at the library of Lithuanian Energy Institute (Breslaujos 3, Kaunas).

LIETUVOS ENERGETIKOS INSTITUTAS

JUSTINA JASELIŪNAITĖ

KOHERENTINIŲ TEKĖJIMO STRUKTŪRŲ  
ĮTAKA MIKROKANALŲ  
TERMOHIDRAULINIAM EFEKTYVUMUI

Daktaro disertacija  
Technologijos mokslai, energetika ir termoinžinerija (T 006)

Kaunas, 2026

Disertacija rengta 2021–2025 metais Lietuvos energetikos instituto Branduolinių įrenginių saugos laboratorijoje. Mokslinius tyrimus rėmė Lietuvos mokslo taryba.

Doktorantūros teisė Kauno technologijos universitetui suteikta kartu su Lietuvos energetikos institutu.

**Mokslinis vadovas:**

vyresn. m. d. dr. Marijus ŠEPORAITIS (Lietuvos energetikos institutas, technologijos mokslai, energetika ir termoinžinerija, T 006).

**Redagavo:** anglų kalbos redaktorė Lina Abraitienė (UAB “BELLA VERBA”), lietuvių kalbos redaktorė Irma Urbonavičienė (IDV veiklos pažyma Nr. 670485).

**Energetikos ir termoinžinerijos mokslo krypties disertacijos gynimo taryba:**

vyr. m. d. dr. Viktorija GRIGAITIENĖ (Lietuvos energetikos institutas, technologijos mokslai, energetika ir termoinžinerija, T 006) – **pirmininkė**;

prof. habil. dr. Ali Cemal BENIM (Diuseldorfo taikomųjų mokslų universitetas, Vokietija, technologijos mokslai, energetika ir termoinžinerija, T 006);

vyr. m. d. dr. Algis DŽIUGYS (Lietuvos energetikos institutas, technologijos mokslai, energetika ir termoinžinerija, T 006);

vyr. m. d. dr. Gediminas RAČIUKAITIS (Valstybinis mokslinių tyrimų institutas Fizinių ir technologijos mokslų centras, technologijos mokslai, medžiagų inžinerija, T 008);

doc. dr. Giedrė STRECKIENĖ (Vilniaus Gedimino technikos universitetas, technologijos mokslai, energetika ir termoinžinerija, T 006).

Disertacija bus ginama viešame Energetikos ir termoinžinerijos mokslo krypties disertacijos gynimo tarybos posėdyje 2026 m. vasario 13 d. 13 val. Lietuvos energetikos instituto posėdžių salėje.

Adresas: Breslaujos g. 3-202, LT-44403 Kaunas, Lietuva.

Tel. +370 37 401 805; el. paštas [studijos@lei.lt](mailto:studijos@lei.lt)

Disertacija išsiųsta 2026 m. sausio 13 d.

Su disertacija galima susipažinti interneto svetainėje <http://ktu.edu>, Kauno technologijos universiteto bibliotekoje (Gedimino g. 50, Kaunas) ir Lietuvos energetikos instituto skaitykloje (Breslaujos g. 3, Kaunas,).

# CONTENTS

<b>LIST OF TABLES</b> .....	7
<b>LIST OF FIGURES</b> .....	8
<b>ABBREVIATIONS</b> .....	12
<b>NOMENCLATURE</b> .....	13
<b>INTRODUCTION</b> .....	19
<b>1. LITERATURE REVIEW</b> .....	23
1.1. Microchannel thermohydraulic efficiency.....	24
1.2. Impact of geometric parameters .....	24
1.3. Coherent structures .....	29
1.4. Analytical methods and modelling.....	33
1.5. Pin fin thermohydraulic efficiency.....	36
1.6. Flow regimes and scaling effects in microscale pin fin arrays .....	38
1.7. The overview of literature analysis and the author's contribution to the research field .....	41
<b>2. METHODOLOGY</b> .....	43
2.1. Governing equations.....	43
2.1.1. General form of the Navier-Stokes equations .....	43
2.1.2. URANS.....	44
2.1.3. Dimensionless quantities .....	46
2.2. Boundary conditions.....	48
2.2.1. Zero gradient .....	51
2.2.2. Fixed value .....	51
2.2.3. No-slip .....	52
2.2.4. Cyclic.....	52
2.2.5. Mapped.....	53
2.2.6. $\omega$ wall function .....	53
2.2.7. $k$ wall function .....	54
2.2.8. Calculated.....	54
2.2.9. Wall heat flux .....	54
2.3. Experiments used for validation .....	55
2.3.1. Experiment uncertainties .....	55
2.4. Geometry .....	57
2.5. Geometry of investigated cases .....	58
<b>3. MODEL VALIDATION</b> .....	62
3.1. Uncertainty analysis .....	62
3.1.1. Geometrical simplification .....	63
3.1.2. Input uncertainties .....	65
3.1.3. Conjugate heat transfer simplification.....	66
3.2. Mesh quality assessment .....	67
3.3. Hydraulics validation.....	70
3.4. Heat transfer validation .....	72
3.5. Pearson correlation coefficients.....	72

<b>4. RESULTS</b> .....	<b>75</b>
4.1. Friction factor and flow topology .....	75
4.1.1. Cylinders vs double-cylinders .....	75
4.1.2. Cylinders vs ellipses .....	77
4.1.3. Cylinders vs cones vs hourglasses based on K-type pin fin arrays .....	78
4.1.4. Cylinders vs cones vs hourglasses based on R-type pin fin arrays.....	88
4.2. $\Omega$ criteria investigation .....	90
4.3. $TKE$ , $KE$ and $\Omega$ relationship .....	96
4.4. Heat transfer .....	99
4.5. Overall performance .....	102
4.6. Performance evaluation using flow dynamics.....	103
4.6.1. Performance evaluation using kinetic energy.....	104
4.6.2. Performance evaluation using $\Omega$ .....	108
<b>5. CONCLUSIONS</b> .....	<b>117</b>
<b>6. SANTRAUKA</b> .....	<b>119</b>
6.1. Įvadas .....	119
6.2. Literatūros apžvalga .....	122
6.3. Modeliavimo metodika.....	124
6.4. Patikra .....	131
6.4.1. Neapibrėžčių analizė.....	131
6.4.2. Modelio patikra.....	135
6.5. Rezultatai .....	138
6.5.1. Hidraulinės charakteristikos .....	138
6.5.2. $\Omega$ kriterijaus analizė.....	145
6.5.3. Šilumos perdavimo charakteristikos.....	148
6.5.4. Termohidraulinis efektyvumas .....	151
6.5.5. Termohidraulinis efektyvumas taikant $\Omega$ .....	152
6.6. Išvados .....	156
<b>LIST OF REFERENCES</b> .....	<b>158</b>
<b>CURRICULUM VITAE AND DESCRIPTION OF CREATIVE ACTIVITIES (CV)</b> .....	<b>169</b>
<b>LIST OF SCIENTIFIC PAPERS AND SCIENTIFIC CONFERENCES</b> .....	<b>170</b>
<b>APPENDICES</b> .....	<b>172</b>
Appendix 1. Hydraulic diameter, heating area, pin area, pin volume and flow volume of investigated cases .....	172

## LIST OF TABLES

<b>Table 1.</b> Coherent structure features in laminar and turbulent flows.....	30
<b>Table 2.</b> Classification of critical points in fluid fields with associated streamline patterns and description.....	34
<b>Table 3.</b> Coefficients of eq. 8 and eq. 9 .....	38
<b>Table 4.</b> Flow regimes by Zdravkovich and Bearman (1997) .....	38
<b>Table 5.</b> Channel classification by Kandlikar and Grande (2003).....	40
<b>Table 6.</b> Knudsen number ranges for various types of flow .....	41
<b>Table 7.</b> Boundary conditions for simulations under non thermal and thermal scenarios across various computational domains .....	49
<b>Table 8.</b> Uncertainties of measurements .....	56
<b>Table 9.</b> Summary of pin fin array geometries, arrangements, and simulation conditions .....	59
<b>Table 10.</b> Maximum $y^+$ value and cell first thickness for different meshes.....	68
<b>Table 11.</b> GCI analysis for $\Delta p$ , $Nu$ , and $A_\Omega$ using three successive meshes.....	69
<b>Table 12.</b> Experimental and numerical pressure drop and inlet velocity data for the entire channel.....	73
<b>Table 13.</b> Experimental and numerical pressure drop and inlet velocity data for cyclic domain.....	73
<b>Table 14.</b> Flow regimes – orange represents steady flow, while magenta indicates unsteady flow.....	90
<b>Table 15.</b> Interpretation of vortical structures based on $A_\Omega$ , $V_\Omega$ , and $\Omega$ magnitudes	95
<b>Table 16.</b> Deviation of $Nu$ from the R-C-S case for R-type geometries.....	101
<b>Table 17.</b> Correlation between Nusselt number and transverse velocity metric for different channel height fractions .....	110

## LENTELIŲ SĄRAŠAS

<b>18 lentelė.</b> Skirtingų skaičiavimo sričių šiluminių ir adiabatinių modelių kraštinių sąlygų parinkimas.....	125
<b>19 lentelė.</b> Mikrokanalo kliūčių formos, išdėstymų ir modeliavimo sąlygų santrauka .....	128
<b>20 lentelė.</b> GCI analizė slėgio nuostoliams, Nuselto skaičiui ir koherentinių struktūrų plotui.....	135
<b>21 lentelė.</b> Sūkurių interpretacija pagal $A_\Omega$ , $V_\Omega$ ir $\Omega$ dydžius.....	148
<b>22 lentelė.</b> Nuselto skaičiaus nuokrypis skirtingiems R-T ir R-H mikrokanalams, lyginant su R-C-S .....	149

## LIST OF FIGURES

<b>Fig. 1.</b> Classification of microchannel design features.....	25
<b>Fig. 2.</b> Area and perimeter of cross sectional flow between pins in a staggered arrangement.....	47
<b>Fig. 3.</b> Geometric model of microchannel pin fin array featuring R- and K-type configurations.....	58
<b>Fig. 4.</b> Mesh domain decomposition for CFD simulations: from entire channel to cyclic domain.....	63
<b>Fig. 5</b> Numerical results of $\Delta p$ versus $u_{in}$ for entire channel, periodic part and cyclic domain.....	65
<b>Fig. 6</b> Model compressibility and the influence of initial temperature on the results.....	66
<b>Fig. 7.</b> a) Pressure drop b) area of vortical structures c) Nusselt number d) temperatures at various $Re$ , comparing simulations with and w/o the solid part.....	67
<b>Fig. 8.</b> Mesh comparison across identical domain.....	68
<b>Fig. 9.</b> Effect of mesh fineness on a) $\Delta p$ , b) $Nu$ and c) $A_Q$ for Reynolds numbers of 178 and 735.....	69
<b>Fig. 10.</b> $\Delta p$ Versus $u_{in}$ against experimental data of Renfer et al. (2013).....	71
<b>Fig. 11.</b> Comparison of $\Delta p$ results from the entire channel and cyclic domain with experimental data reported by Kosar et al. (2011).....	71
<b>Fig. 12.</b> Comparison of modelling results of $Nu$ from the cyclic domain with experimental data reported by Renfer et al. (2013).....	72
<b>Fig. 13.</b> Comparison of $f$ between R-C-I and R-DC-I configurations.....	76
<b>Fig. 14.</b> Velocity fields and flow streamlines for R-C-I and R-DC-I at varying $Re$ .....	77
<b>Fig. 15.</b> a) $\Delta p$ vs $u_{in}$ and b) $f$ vs $Re$ .....	77
<b>Fig. 16.</b> a) $\Delta p$ and $D_h$ dependence on $P_r$ b) rate of $\Delta p$ change versus the rate of $\Delta A_s$ change.....	78
<b>Fig. 17.</b> a) $\Delta p$ and b) $f$ dependence on $Re$ .....	79
<b>Fig. 18</b> $f$ of conical fin fins for different pitches at various $Re$ .....	81
<b>Fig. 19.</b> Velocity streamlines with critical points on a) middle plane, b) in between middle and endwall, c) near endwall for K-C.....	83
<b>Fig. 20.</b> Velocity streamlines with critical points on a) middle plane, b) in between middle and endwall, and c) near endwall for K-H19.....	84
<b>Fig. 21.</b> Velocity streamlines with critical points on a) near the upper endwall, b) middle, c) near the lower endwall for K-T14-A-P250.....	85
<b>Fig. 22.</b> Velocity streamlines with critical points on a) near the upper endwall, b) middle, c) near the lower endwall for K-T14-B-P250.....	86

<b>Fig. 23.</b> Mean velocity streamlines with critical points on vertical midplane for K-C, K-H19, K-T14-A-P250 and K-T14-B-P250.....	87
<b>Fig. 24.</b> Topological flow structure based on the $\Omega$ criterion a) K-C b) K-H19 c) K-T14-A-P250 d) K-T14-B-P250 .....	88
<b>Fig. 25.</b> $f$ dependence on $Re$ of different R-type geometries .....	89
<b>Fig. 26.</b> $A_{\Omega}/V_{\Omega}$ dependence on $Re$ with different $P$ of K-type geometries.....	91
<b>Fig. 27.</b> $A_{\Omega}/A_{\Omega,min}$ dependence on the $V_{\Omega}/V$ of K-type geometries .....	92
<b>Fig. 28.</b> a) Fraction of total volume occupied by vortical structures ( $V_{\Omega}/V$ ), b) variation of occupied area ( $dV_{\Omega}$ ) with $Re$ of R-type geometries.....	94
<b>Fig. 29.</b> Relative area of coherent structures for R-type geometries .....	94
<b>Fig. 30.</b> $\Omega$ values for the coherent structures and for the entire flow for R-type geometries.....	95
<b>Fig. 31.</b> Normalised $KE$ and $KE_{fluc}$ dependency on $\Omega$ of K-type geometries .....	99
<b>Fig. 32.</b> Variation of a) $T_{ave}$ , b) $T_w$ , and c) $Nu$ for different configurations across the investigated $Re$ of R-type geometries.....	100
<b>Fig. 33.</b> $T_{min}$ and $T_{max}$ wall temperatures for different configurations.....	101
<b>Fig. 34.</b> $\delta_T$ for different configurations across the investigated $Re$ range of R-type geometries.....	102
<b>Fig. 35.</b> Time-averaged impact of pin fin shape on the $TPI$ as a function of $Re$ ....	103
<b>Fig. 36.</b> Comparison of $Tef$ of different K-type geometries .....	105
<b>Fig. 37.</b> $\ln(KE/KE_{fluc})$ versus $f$ .....	106
<b>Fig. 38.</b> $\ln(KE/KE_{fluc})$ dependence on $Re$ and $P$ .....	107
<b>Fig. 39.</b> Dependence of $Tef$ on $f$ and $\ln(KE/KE_{fluc})$ for each $Re$ and $P$ set a) all modelled cases, b) selected cases with similar $f$ .....	108
<b>Fig. 40.</b> Velocity components metrics for different averaging height.....	111
<b>Fig. 41.</b> Modelled and predicted $Nu$ based on transverse velocity components.....	112
<b>Fig. 42</b> a) $AA\Omega \cdot VV\Omega$ b) $1 - \Omega v - \Omega v \cdot \Omega v^2$ c) $L \cdot uz^2 + ux^2v0.8$ vs $Re$ .....	113
<b>Fig. 43.</b> Multivariable analysis of thermohydraulic efficiency based on vortex geometry, energy distribution and flow directionality .....	114
<b>Fig. 44</b> $\eta_{\Omega}$ dependence on $Re$ .....	115
<b>Fig. 45.</b> Errors in numerical values of $\eta_{\Omega}$ compared to $TPI$ .....	116
<b>Fig. 46</b> Comparison of original $TPI$ (black line) with calculated $\eta_{\Omega}(TPI)$ values ..	116

## PAVEIKSLŲ SĄRAŠAS

<b>47 pav.</b> $\Delta p$ priklausomybė nuo $u_{in}$ visam kanalui, periodinei daliai ir ciklinei sričiai .....	132
<b>48 pav.</b> Modelio spūdumo ir pradinės temperatūros įtaka rezultatams.....	132

<b>49 pav.</b> a) slėgio nuostoliai b) koherentinių struktūrų plotas c) Nuselto skaičius d) temperatūrų priklausomybė nuo $Re$ .....	133
<b>50 pav.</b> Tinklelio tankumo įtaka a) slėnio nuostoliams, b) Nuselto skaičiui ir c) koherentinių struktūrų plotui, kai $Re = 178$ ir $735$ .....	134
<b>51 pav.</b> Modeliuojamo slėgio kritimo visame kanale ir ciklinėje srityje palyginimas su Renfer ir kt. (Renfer et al., 2013) eksperimentiniais rezultatais .....	136
<b>52 pav.</b> Viso kanalo ir ciklinės srities slėgio kritimo modeliavimo rezultatų palyginimas su eksperimentiniais duomenimis Kosar ir kt. (Koşar et al., 2011) ...	136
<b>53 pav.</b> Ciklinės srities $Nu$ modeliavimo rezultatų palyginimas su eksperimentiniais duomenimis (Renfer et al., 2013) .....	137
<b>54 pav.</b> R-C-I ir R-DC konfigūracijų $f$ palyginimas.....	138
<b>55 pav.</b> a) $\Delta p$ priklausomybė nuo įtekėjimo greičio ir b) $f$ priklausomybė nuo $Re$	139
<b>56 pav.</b> a) $\Delta p$ ir b) $f$ priklausomybė nuo $Re$ K tipo konfigūracijoms.....	139
<b>57 pav.</b> Pasipriešinimo koeficientas skirtingo kampo kūginėms kliūtims esant skirtingam atstumui tarp jų ir $Re$ .....	141
<b>58 pav.</b> Greičio srauto linijos ir kritiniai taškai įvairiuose K-C ir K-H19 mikrokanalų skerspjūviuose .....	142
<b>59 pav.</b> Greičio srauto linijos ir kritiniai taškai įvairiuose K-T14-A-P250 ir K-T14-B-P250 mikrokanalų skerspjūviuose .....	143
<b>60 pav.</b> Greičio srautų linijos ir kritiniai taškai vertikaliuose K-C, K-H19, K-T14-A-P250 ir K-T14-B-P250 mikrokanalų skerspjūviuose .....	143
<b>61 pav.</b> $f$ priklausomybė nuo $Re$ R tipo mikrokanalų konfigūracijose .....	144
<b>62 pav.</b> $A_{\Omega}/V_{\Omega}$ priklausomybė nuo $Re$ .....	145
<b>63 pav.</b> Normalizuota sūkurių ploto priklausomybė nuo tūrio.....	146
<b>64 pav.</b> a) Sūkurių užimama bendro tūrio dalis ( $V_{\Omega}/V$ ) priklausomybė nuo $Re$ , b) užimto ploto kitimo ( $dV_{\Omega}$ ) priklausomybė nuo $dRe$ .....	147
<b>65 pav.</b> a) Vidutinės temperatūros, b) sienelės temperatūros ir c) Nuselto skaičiaus kitimas skirtingoms konfigūracijoms tiriamame $Re$ .....	149
<b>66 pav.</b> Minimalios ir maksimalios sienelės temperatūros vertės skirtingoms mikrokanalų konfigūracijoms.....	150
<b>67 pav.</b> Temperatūros netolygumas kintant $Re$ skirtingoms mikrokanalų konfigūracijoms.....	151
<b>68 pav.</b> Kliūčių konfigūracijų įtaka šiluminio našumo indeksui.....	152
<b>69 pav.</b> a) $AA\Omega \cdot VV\Omega b) 1 - \Omega v - \Omega v \cdot \Omega v^2$ c) $L \cdot uz^2 + ux^2 v^0.8$ priklausomybės nuo $Re$ .....	153
<b>70 pav.</b> Daugianarė termohidraulinio efektyvumo analizė, pagrįsta sūkurių charakteristikomis, energijos pasiskirstymu ir srauto kryptingumu .....	154
<b>71 pav.</b> $\eta_{\Omega}$ priklausomybė nuo $Re$ .....	155
<b>72 pav.</b> $\eta_{\Omega}$ reikšmių paklaidos, lyginant su $TPI$ .....	155

**73 pav.** *TPI* (juoda linija) palyginimas su apskaičiuotomis  $\eta_{\Omega}(TPI)$  vertėmis ..... 156

## ABBREVIATIONS

A	–	Unidirectional pin fins
B	–	Bidirectional pin fins
C	–	Cylindrical pin fins
CFD	–	Computational fluid dynamics
DC	–	Double-cylinder pin fins
DMD	–	Dynamic mode decomposition
E	–	Elliptical pin fins
GCI	–	Grid convergence index
H	–	Hourglass-shaped pin fins
MAE	–	Mean absolute error
MRE	–	Mean relative error
PIV	–	Particle image velocimetry
POD	–	Proper orthogonal decomposition
RANS	–	Reynolds-averaged Navier Stokes
RMSE	–	Root mean square error
SST	–	Shear stress transport
T	–	Conical pin fins

## NOMENCLATURE

Notation	Units	Definition
$A$	$[\text{m}^2]$	Area
$\mathbf{A}$	$[-]$	Symmetric velocity tensor
$A_{int}$	$[\text{m}^2]$	Internal area of microchannel (pins, upper/lower wall)
$a$	$[-]$	Frobenius term of the symmetric velocity tensor
$\mathbf{B}$	$[-]$	Anti-symmetric velocity tensor
$b$	$[-]$	Frobenius term of the anti-symmetric velocity tensor
$C_{11}, C_{12}, C_{13}, C_{14}, C_{15}$	$[-]$	Constant for eq. 6 [91]
$C_{21}, C_{22}, C_{23}, C_{24}, C_{25}$	$[-]$	Constant for eq. 7 [92]
$CD_{k\omega}$	$[\text{kg}/(\text{m}^3\text{s}^2)]$	Turbulence cross-diffusion term
$c_p$	$[\text{J}/(\text{kg K})]$	Specific heat at constant pressure
$C_\mu$	$[-]$	Constant (0.09)
$D$	$[\text{m}]$	Diameter
$E$	$[\text{J}/\text{kg}]$	Total energy
$e$	$[\text{J}/\text{kg}]$	Internal energy
$\mathbf{F}$	$\text{N}/\text{kg}$	Body force per unit mass
$F_1, F_2$	$[-]$	$k$ - $\omega$ SST model blending functions
$f$	$[-]$	Friction factor
$g$	$[\text{m}/\text{s}^2]$	Gravitational acceleration
$GCI^{21}, GCI^{32}$	$[\%]$	Grid Convergence Index (fine-medium) (medium-coarse)
$H$	$[\text{m}]$	Height
$h$	$[\text{W}/(\text{m}^2 \text{K})]$	Convective heat transfer coefficient
$\mathbf{I}$	$[-]$	Identity matrix
$i$	$[-]$	Time index (from 1 to $N$ )
$j$	$[-]$	Cell index (from 1 to $M$ )
$KE$	$[\text{J}]$	Total kinetic energy
$KE_{fluc}$	$[\text{J}]$	Fluctuating kinetic energy
$Kn$	$[-]$	Knudsen number
$k$	$[\text{m}^2/\text{s}^2]$	Turbulent kinetic energy
$L$	$[\text{m}]$	Characteristic length or pipe length

Notation	Units	Definition
$N$	[-]	Number of time steps
$Nu$	[-]	Nusselt number
$\mathbf{n}$	[-]	Unit normal vector
$M$	[-]	Number of cells
$P$	[m]	Pin pitch
$p$	[Pa]	Pressure
$Pr$	[-]	Prandtl number
$P_k$	[m <sup>2</sup> /s <sup>3</sup> ]	Production term of turbulent kinetic energy
$\Delta p$	[Pa]	Pressure drop
$q$	[W/m <sup>2</sup> ]	Heat flux
$Q$	[m <sup>3</sup> /s]	Volumetric flow rate
$\mathbf{R}$	[N/m <sup>2</sup> ]	Reynolds stress tensor
$R^2$	[-]	Coefficient of determination
$Re$	[-]	Reynolds number
$r$	[-]	Grid refinement ratio
$r_p$	[-]	Pearson correlation coefficient
$r^{21}$	[-]	Grid refinement ratio (fine to medium)
$r^{32}$	[-]	Grid refinement ratio (medium to coarse)
$T$	[K]	Temperature
$t$	[s]	Time
$TPI$	[-]	Thermal performance index
$Tef$	[-]	Thermohydraulic efficiency index
$\mathbf{u}$	[m/s]	Velocity
$\nabla \mathbf{u}$	[s <sup>-1</sup> ]	Velocity tensor
$V$	[m <sup>3</sup> ]	Volume
$y$	[m]	Distance to wall
$y^+$	[-]	Nondimensional distance to wall
$\alpha$	[m <sup>2</sup> /s]	Thermal diffusivity
$\alpha_V$	[-]	Void fraction
$\alpha, \beta, \beta^*, \sigma_k, \sigma_\omega, \sigma_{\omega 2}$	[-]	Model coefficients (Section 2.1.2)
$\gamma$	[-]	Specific heat
$\delta_T$	[K]	Temperature non-uniformity

Notation	Units	Definition
$\varepsilon$	[-]	Pin fin effectiveness (1.5)
$\epsilon$	[m]	Pipe roughness height
$\varepsilon_a^{21}, \varepsilon_a^{32}$	[%]	Approximate relative error (fine-medium) (medium-coarse)
$\varepsilon_{ext}^{21}, \varepsilon_{ext}^{32}$	[%]	Extrapolated relative error (fine-medium) (medium-coarse)
$\eta$	[-]	Thermal-hydraulic performance index
$\Theta$	[°]	Angle of conicity
$\kappa$	[W/(m K)]	Thermal conductivity
$\lambda$	[Pa s]	Second viscosity coefficient
$\lambda_2$	[s <sup>-1</sup> ]	Vortex identification method
$\Lambda$	[m]	Mean free path for gases
$\mu$	[kg/(m s)]	Dynamic viscosity
$\nu$	[m <sup>2</sup> /s]	Kinematic viscosity
$\xi$	[-]	Apparent order of accuracy (Section 3.3)
$\xi$	[-]	Small positive number
$\Pi$	[m]	Perimeter
$\Gamma$	[-]	Boundary
$\rho$	[kg/m <sup>3</sup> ]	Density
$\rho_S$	[-]	Spearman coefficient
$\sigma$	[-]	Uncertainty
$\tau$	[N/m <sup>2</sup> ]	Viscous stress tensor
$\Phi$	[Kg/(m s <sup>3</sup> )]	Viscous dissipation function
$\phi$	[-]	variable
$\phi_1, \phi_2, \phi_3$	[depends]	Solution variable at each mesh (fine, medium, coarse)
$\phi_{ext}^{21}, \phi_{ext}^{32}$	[-]	Extrapolated solution to zero grid size (fine- medium) (medium-coarse)
$\Omega$	[-]	Omega criterion (Scalar function measuring the balance between rotation and strain)
$\omega$	[1/s]	Specific dissipation rate

Subscripts

Notation	Definition
0	Flat channel
<i>ave</i>	average
<i>atm</i>	atmospheric
<i>cell</i>	cell
<i>d</i>	Based on the pin fin thickness
<i>dm</i>	Domain
<i>eff</i>	effective
<i>exp</i>	experiment
<i>inr</i>	inner
<i>i</i>	i-th measurement in time
<i>in</i>	inlet
<i>int</i>	internal
<i>f</i>	bulk
<i>fluc</i>	fluctuating
<i>fluid</i>	fluid
<i>fixed</i>	fixed
<i>h</i>	hydraulic
<i>ht</i>	Heat transfer
<i>j</i>	Component index
<i>jet</i>	jet
<i>jtj</i>	Jet to jet
<i>lon</i>	longitudinal
<i>lam</i>	laminar
<i>left</i>	left
<i>log</i>	log-layer
<i>lon</i>	longitudinal
<i>map</i>	mapped
<i>max</i>	maximum
<i>mean</i>	mean
<i>mid</i>	middle height
<i>min</i>	minimum
<i>mod</i>	modelling
<i>n</i>	n-th time sample

Notation	Definition
<i>o</i>	outer
<i>out</i>	outlet
<i>ov</i>	Overall
<i>Q</i>	Volumetric flow rate
<i>Re</i>	Reynolds
<i>right</i>	right
<i>t</i>	turbulent
<i>trg</i>	target
<i>tr</i>	transverse
<i>src</i>	source
<i>S</i>	Surface area
<i>vis</i>	viscous
<i>w</i>	Near wall
<i>v</i>	vortex
<i>x</i>	x-direction component
<i>z</i>	z-direction component
$\Omega$	Vortical
$\nu$	Kinematic viscosity
$\Delta p$	Pressure drop
$\tau$	Shear stress

### Superscripts

Notation	Definition
<i>T</i>	Transposed

### Pin fin array geometry notation

Notation	Definition
R	Renfer et al. (Renfer et al., 2011, 2013) based staggered pin fin channel, with height of 200 $\mu\text{m}$ , $P = 200 \mu\text{m}$ and $D = 100 \mu\text{m}$ , unless otherwise stated.

Notation	Definition
K	Kosar et al. (Kosar et al., 2011) based a staggered pin fin channel, with height of 243 $\mu\text{m}$ , $P = 250 \mu\text{m}$ , and $D = 100 \mu\text{m}$ , unless otherwise stated.
C	Cylindrical pin fins
DC	Double-cylinder pin fins
E	Elliptical pin fins
T	Tapered conical pin fins
H	Hourglass-shaped pin fins
A	Unidirectional conicity of conical pins
B	Bidirectional conicity of conical pins
P	The pitch between pins, when differing from that of R-based or K-based configurations
S	Staggered arrangement
I	Inline arrangement

## INTRODUCTION

Heat dissipation has become an increasingly important and complex engineering challenge as electronic components continue to shrink rapidly in size. The growing functionality of electronic systems and accelerating technological advancement lead to greater heat generation – even in compact devices. Although advanced integrated circuits offer improved energy efficiency, the heat density generated by energy losses increases with each new generation. This creates a critical need to efficiently remove more heat from increasingly smaller volumes to ensure system reliability, longevity, and stable operation.

Traditional heat-removal methods, such as natural convection and conventional heat exchangers, are no longer sufficient to meet the demands of modern electronic systems. As a result, there is a growing interest in advanced, alternative solutions that can deliver higher thermal management efficiency. One of the most promising approaches is microchannel cooling, where cooling structures are integrated directly into the chip. This technology enables effective heat removal from minimal volumes by leveraging a high surface-area-to-volume ratio and unique flow characteristics.

The flow structure within microchannels is one of key factors in determining the heat transfer intensity and the heat exchanger's overall performance. In such systems, liquids or gases flow through densely packed arrays of cylinder-shaped or other obstacles. Due to this geometry, the flow is forced to continuously change direction as it meanders around the obstacles, forming complex vortices. In laminar flow conditions, recirculating zones with stationary vortices form behind each obstacle – these are thermal stagnation regions that can cause localised overheating and reduce overall cooling efficiency. When the flow becomes unstable, vortices begin to detach from the obstacles, interact with one another, and merge, creating a more complex flow pattern. While this enhances heat transfer, it also increases pressure losses.

An optimally designed obstacle array configuration should generate unsteady flow to ensure effective heat transfer while minimising hydraulic losses. Flow instabilities enhance fluid mixing, thereby increasing convective heat exchange and improving overall cooling efficiency. The thermohydraulic performance index (*TPI*) combines both the friction factor and the Nusselt number, providing a balanced assessment of thermal efficiency relative to flow resistance. However, the *TPI* formula does not directly incorporate any unsteadiness parameter, even though it is a key mechanism for both friction losses and enhanced heat transfer.

Computations can be highly resource-intensive when simulating flow and heat transfer processes using numerical methods (CFD), especially with high-resolution models, demanding substantial time and computational power. As a result, heat transfer modelling may be omitted to enable faster design iterations and optimisation,

particularly when analysing a wide range of microchannel or other cooling-structure configurations.

When analysing heat transfer systems, flow parameters can be used as an alternative to  $Nu$  for performance evaluation. Parameters such as turbulent kinetic energy and dissipation rate – or, even better, the  $\Omega$  criterion – can be used to develop an alternative formula for estimating ‘virtual’ or approximate thermohydraulic performance.

### **The object of the research**

Fluid flow in a microchannel array featuring pin fins of different geometries.

### **The aim of the doctoral dissertation**

This doctoral research, based on the investigation of flow structures in microchannels, aimed to develop a coherent structure-based method for assessing thermo-hydraulic efficiency.

### **Tasks of the doctoral dissertation**

To achieve the aim of the work, the following tasks were raised:

1. Research the influence of the shape of pin fins on pressure losses and thermal performance.
2. Research the characteristics of coherent structures depending on the flow stability.
3. Research the characterising pattern of coherent structures depending on the shape of pin fins and flow stability.
4. Create a method based on a quantitative coherent structures analysis for predicting thermohydraulic efficiency.

### **Statements for the defence**

1. A small variation in the pins’ cross-sectional profile along their axis enhances thermohydraulic performance. While greater variations may shift the onset of unsteady flow to lower Reynolds numbers or leave the flow regime unchanged, they simultaneously increase or decrease both pressure drop and heat transfer.
2. Within the steady regime, an increase in the  $Re$  is accompanied by a consistent enlargement of the coherent structures’ area while their volume decreases. However, at the onset of unsteady flow, the structures’ volume increases significantly, after which it gradually declines.

3. A pin's cross-sectional profile that changes along its axis reduces the magnitude of dimensional variation of coherent structures during the transition between flow regimes.
4. The developed thermohydraulic efficiency assessment method quantifies the interaction surface of coherent vortices. It evaluates the coupling between their intensity and transverse flow motion to predict the flow's potential for heat transport and dissipation without solving the energy equation.

### **Scientific novelty**

For the first time, the analysis of coherent  $\Omega$  structures is applied to microchannel studies, which allowed us to determine a direct quantitative relationship between the flow topology and thermohydraulic efficiency. This approach enables us to predict heat-removal characteristics solely from hydrodynamic data (without solving the energy equation). Based on the research, a method based on flow structural analysis is proposed for the design and optimisation of cooling systems operating under high-heat-flux conditions.

### **Practical value**

Based on the analysed flow characteristics and the geometric parameters of the obstacles, the proposed thermohydraulic efficiency assessment methodology enables the preliminary evaluation, comparison, and optimisation of microchannels. This will facilitate the design and application of various obstacle shapes and configurations, allowing microchannel optimisation using computational fluid dynamics (CFD).

### **Scientific approval**

The results presented in this dissertation were published in three scientific journal articles and one book chapter with an impact factor referenced in the "Clarivate Analytics" "Web of Science database. The results were also presented at six international conferences.

### **Structure and contents**

This dissertation is structured to guide the reader through the research in a logical way. It begins with an Introduction defining the research problem and objectives. The Literature Review then situates the study within current scientific understanding and introduces the principles of the advanced  $\Omega$  coherent structure analysis method relevant to this work. The Methodology chapter subsequently details the specific numerical simulation approach employed for the microchannel analysis.

Subsequent chapters systematically present the core research: beginning with an analysis of hydraulic characteristics (friction factor) and flow topology for various pin

fin geometries; this is followed by the application of the  $\Omega$  method to identify coherent flow structures and explore their relationship with flow unsteadiness metrics ( $TKE$ ,  $KE$ ). The investigation then covers thermal properties and overall thermohydraulic performance, culminating in a performance evaluation approach that leverages insights from the  $\Omega$ -identified structures, alongside a discussion of optimisation strategies derived from these findings.

The dissertation concludes with a Summary of Findings, Conclusions, and a list of Referenced Literature.

## 1. LITERATURE REVIEW

Electronic devices are rapidly progressing, providing enhanced computing power in increasingly smaller sizes. However, this miniaturisation has led to a greater concentration of heat generation. The amount of heat produced per unit area can approach  $1000 \text{ W/cm}^2$  (Joshi et al., 2023). While humidity, vibration and dust may cause electronics to fail, as power and heat levels rise, the issue of overheating electronic components is becoming a growing concern, causing more than half of failures (Khattak & Ali, 2019). The higher heat densities can negatively impact performance, reliability, and longevity. Excessive heat can cause electronic circuits to malfunction, degrade materials, and, in extreme cases, cause complete failure. Traditional cooling methods often struggle to keep up with the increasing thermal demands of modern microelectronics, requiring advanced cooling solutions. New micro cooling systems include, but are not limited to, spray cooling, microchannel heat sinks, heat pipes, and jet impingement (Sadique et al., 2022).

Moore's Law states that transistor density doubles every eighteen months, increasing the need for greater heat dissipation. Early microprocessors had  $\sim 2.3\text{k}$  transistors, while modern CPUs (e.g. Intel Core i9-13900K, AMD Ryzen 7950X) have  $\sim 20\text{-}30$  billion transistors, high-end GPUs (e.g., NVIDIA RTX 4090) have  $\sim 76$  billion transistors, Apple M3 Max  $\sim 92$  billion transistors, AI chips (e.g., NVIDIA H100, Google TPU v5)  $\sim 80\text{-}100$  billion transistors, and memory chips (e.g. Samsung 1Tb V-NAND SSD storage chip) over 1 trillion transistors. While Moore's law predicted that the number of transistors would double every  $\sim 2$  years, advances in chip design, 3D stacking, and new architectures continue to push the limits (Kim et al., 2024).

Passive flow perturbation is a method to alter fluid flow without requiring additional energy. This approach has been explored using pin fins, ribs, and dimples, which help disturb boundary layers and enhance turbulence (irregular fluid motion) in microchannels (Coşkun & Çetkin, 2020; Deshmukh et al., 2023; Z. Wang et al., 2022). Due to their high heat transfer capabilities and compact design, microchannels have attracted significant attention in thermal management applications (Bhandari et al., 2024; Joshi et al., 2023; Khattak & Ali, 2019; Rahman et al., 2024; Sadique et al., 2022; Yu et al., 2024). Microchannels are tiny, narrow channels that allow coolant to flow through them, efficiently removing heat from electronic components. Due to their small size, microchannels provide a large heat exchange surface area, enabling faster and more effective cooling than conventional methods. The rapid movement of liquid through these channels absorbs heat and carries it away, preventing hot spots from forming on delicate electronic parts. Additionally, advancements in microfluidic technology have enabled the development of optimised microchannel designs,

including variations in channel geometry, flow patterns, and coolants, further improving thermal regulation, which will be discussed below.

The microchannel cooling method is not only valuable for electronics cooling but also can be used in the cooling of fusion energy (Zhou et al., 2025), automobile radiator enhancement (Amol Dhumal et al., 2024), micro heat sinks for hydrogen storage (Keshari & Maiya, 2018), gas turbine blade cooling (Ahn, 2025), and for thermoelectric generators (Lin & Kiflemariam, 2019) and more (He et al., 2021).

### **1.1. Microchannel thermohydraulic efficiency**

Microchannel-based cooling systems have gained significant attention among cooling techniques due to their ability to dissipate high heat loads while maintaining a compact design. The thermohydraulic efficiency of microchannels, defined by their ability to transfer heat while effectively reducing pressure drop ( $\Delta p$ ) and energy consumption, plays a key role in optimising cooling performance.

### **1.2. Impact of geometric parameters**

The performance of microchannel cooling systems is greatly influenced by their geometric design. Parameters such as channel width, height, aspect ratio, shape, and spacing directly affect heat transfer efficiency, fluid flow characteristics, and  $\Delta p$ . Furthermore, microchannels have different configurations: some are rectangular, others have wavy or corrugated paths, and some contain pin fin arrays, ribs, cavities, bifurcations, and other features. Design matters, especially in optimising thermal performance and minimising  $\Delta p$ . Geometry selection plays a crucial role in balancing heat dissipation and fluid flow resistance. For instance, wavy or corrugated channels enhance mixing and turbulence, improving heat transfer (Ghorbani et al., 2022), while pin fin arrays and ribs disrupt boundary layers to increase cooling efficiency (Yu et al., 2024). Similarly, bifurcations and cavities can influence flow distribution and thermal uniformity (Sadique et al., 2022). A well-designed microchannel system ensures efficient heat removal while maintaining manageable pressure losses, making it essential in electronics cooling, biomedical devices, and high-performance thermal management systems.

The main design parameters are shown in Fig. 1. Regarding pin fin arrays, the key parameters for them are pin fin density, arrangement, pitch, and shape. They may have some other variables, such as tip clearance. All those parameters will be discussed further.

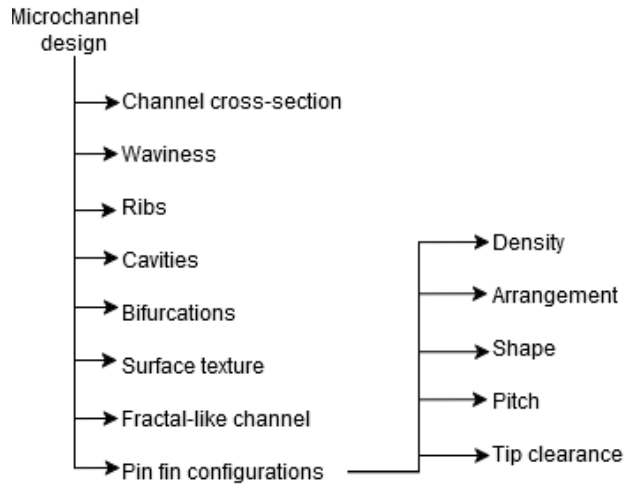


**Fig. 1.** Classification of microchannel design features

The pin fin density is affected by the pin pitch and the spatial arrangement. Over four decades of research on cylindrical pin fin arrays have shown that the configuration significantly impacts thermal properties. Early studies have revealed that a staggered pin fin arrangement enhances heat transfer efficiency compared to an inline arrangement, although it increases  $\Delta p$  (Sparrow et al., 1980). This suggests that a smaller surface area is needed when the heat flux and flow rate are fixed.

Jeng et al. (2007) investigated square and cylinder pin fin arrays in inline and staggered arrangements having different pitches ( $697 \leq Re_d \leq 10960$ , Reynolds based on pin fin thickness, coolant – air). They found that inline cylinder pins with high pitch have a higher  $\Delta p$  than square pins, but with low pitch, the opposite holds, or at least  $\Delta p$  is equivalent. In addition, the heat transfer of inline square pin fin arrays is usually lower than that of inline cylinder pin fin arrays. Furthermore, when the Reynolds number ( $Re$ ) is high, the Nusselt number ( $Nu$ ) of the staggered square pin fin array may be up to 20% larger than that of the inline cylinder pin fin array.

Bhandari et al. (2023) comprehensively explored the influence of prism pin fin sides on thermohydraulic performance ( $56 \leq Re \leq 280$ , coolant – water). The sides of the prism varied from 3 (triangle) to 9. They concluded that the triangular pin fin has the lowest thermal performance, while the square has the highest. Thus, the 4-sided prism is considered the most effective. The further change on the prism side is negligible.

Polat et al. (2022) evaluated circular, square and diamond-shaped pin fin arrays ( $100 \leq Re \leq 350$ , coolant – water). They pointed out that the best heat transfer performance and least favourable  $\Delta p$  are achieved by diamond-shaped pin fins, followed by square and circular-shaped pin fins.

The numerical work by Aguirre et al. (2022) dealt with cylindrical and hexagonal pin fin arrays. Unlike others, they stated that hexagonal pin fins increase  $\Delta p$  without increasing heat transfer; therefore, they are ineffective.

Al-Abboodi et al. (2022) explored circular, elliptical, square and drop-shaped pin fin arrays in inline and staggered arrangements. They discovered that elliptical pin fins had the highest  $Nu$ , while square pin fins had the highest  $\Delta p$ .

Various pin fin shapes, including circular, rectangular, square, triangular, rhombic, hexagonal, trapezoidal, and semicircular ( $100 \leq Re \leq 900$ , coolant–air), were thoroughly studied by Khoshvaght-Aliabadi et al. (2018). The highest heat transfer and  $\Delta p$  values were found for half-circular pin fins. However, the circular and hexagonal pin fins are the best overall. Another important finding is that the pin fin shape gradually loses its advantages because the effect of  $Re$  on  $\Delta p$  is more pronounced than the effect on heat transfer as  $Re$  increases.

Parlak et al. (2024) researched the thermohydraulic efficiency of inline and staggered arrangements of cylindrical, square, triangular and elliptical pin fin arrays ( $6000 \leq Re \leq 44000$ , coolant – air). All configurations had the same surface area. Despite the pin fin shape, the staggered arrangement yielded a higher friction factor ( $f$ ) and a lower temperature difference between the coolant and the ambient, leading to a higher  $Nu$ . When comparing shapes, triangular and square pin fins outperform others in  $Nu$ .

Lv et al. (2022) conducted research on longitudinal spacings in staggered pin fin arrays, where spacings were 2-4 pin fin diameters ( $100 \leq Re \leq 800$ , coolant – water). They found that small spacing delays vortex shedding, but the fluid mixing is more intense. However, a large spacing has flow characteristics similar to a single pin fin.

Sakanova et al. (2018) studied various streamlined pin fin designs, including cone and hydrofoil shapes, and compared their performance with cylindrical fins under both laminar and turbulent flow conditions using air and water as coolants ( $31250 \leq Re \leq 156250$ , coolant – air, fuel). The numerical analysis revealed that the cone-shaped pin fins achieved the highest heat transfer coefficient due to the flow separation effect. In contrast, the hydrofoil heat sink exhibited the lowest heat transfer coefficient and  $\Delta p$  out of all streamlined shapes, attributed to the absence of flow separation.

The study by Gijoy et al. (2025) examined an asymmetric elliptical-cylindrical pin fin array ( $2500 \leq Re \leq 6250$ , turbulent flow, coolant – air). The updated geometry features a halved, elliptical front section designed to enhance interaction with the incoming airflow. The results showed reduced  $\Delta p$  and improved heat transfer, and the efficiency of the pin fin array was optimised by 2.25 times compared to cylinders. Other researchers have also concluded that streamlined shapes yield the best heat

transfer performance (İzci et al., 2015; Saravanan & Umesh, 2018; Serkan Şahin et al., 2023; P. Wang & Chen, 2019).

A study done by Ates et al. (2022) investigated elliptical pins and their distribution and the effect of tip clearance on performance (125-325 kg/(m<sup>2</sup>s), coolant – water). They concluded that tip clearance does not improve heat transfer, and elliptical pin fins can enhance heat transfer by 35% compared to a plain channel. Several studies have concluded that a large tip clearance does not contribute to a notable improvement in thermohydraulic performance, but a relatively small tip clearance may be beneficial (Bhandari & Prajapati, 2022; Mei et al., 2014; Moores et al., 2009). However, the improvement is observed only in the laminar regime at low  $Re$ , and no effect is observed at high  $Re$ .

Most studies consider changing the pin fin's shape, but few consider changing its vertical cross-section. However, some studies use perforations to enhance fluid mixing and heat transfer. Zohora et al. (2023) proposed a hyperbolic, wavy and crinkled pin with and without perforations ( $8500 \leq Re \leq 44502$ , coolant–air). The hyperbolic pin with elliptical perforation had the highest hydrothermal performance; even without perforation, it increased  $Nu$  by 16.8% compared to the cylindrical pin.

Pati et al. (2018) investigated the thermal behaviour of pin fins with different arrangements, including cylindrical and conical pin shapes ( $3400 \leq Re \leq 34000$ , coolant – air). A lower  $\Delta p$  and  $Nu$  were observed in staggered arrangements. This is primarily because staggered arrangements have half as many pins as inline arrangements. More space between the staggered pins creates more space for vortex formation, making this arrangement better. Besides, when comparing cylindrical pins with conical ones, the latter enhances thermal performance and reduces  $\Delta p$ .

Yang et al. (2025) modified cylindrical pin fins by incorporating a central sphere, forming a lantern-shaped design, and conducted numerical simulations at high  $Re$  ( $5000 \leq Re \leq 30,000$ ). Their findings indicated that the lantern-shaped pin fins increased the thermal performance index by approximately 4%.

Another experimental investigation examined twisted-tape pin fins with a  $Re$  range of 5000-15,000 (Chang et al., 2021). The results demonstrated that the twisting effect induced the formation of vortices, significantly enhancing heat transfer. Consequently, the  $Nu$  increased almost five times. However, this improvement was due to a significant increase in the Fanning friction factor, which rose by approximately 39. As a result, the overall thermal performance factor increased on average from 1.39 to 1.55 times.

Mesgarpour et al. (2019) conducted numerical simulations of rigid and porous tapered pin fins, revealing that porous pin fins improve heat transfer under laminar flow conditions. In another study, tapered pin fins were compared with cylindrical ones, analysing the impact of the taper ratio (the ratio of tip diameter to base diameter)

(Ahmadian-Elmi et al., 2021). While the tapered pin fins exhibited a slight reduction in convective heat transfer, they also significantly reduced  $\Delta p$ , improving overall performance.

Similarly, Abuşka and Çorumlu (2023) conducted experimental research on conical pin fin heat sinks, focusing on pin arrangement ( $2000 \leq Re \leq 16\,000$ ). They found that a modified staggered arrangement of conical pin fins provided the highest thermohydraulic performance compared to a conventional staggered layout.

Further extending this research, Çorumlu (2024) explored the effects of input power and ambient temperature on the thermal performance of conical pin fins. A comparative study of conical, cross-cut, and flat heat sinks demonstrated that conical pin fin arrays achieved superior thermal efficiency, reducing thermal resistance by up to 27.78% compared to cross-cut pin fins. Another investigation assessed various pin fin geometries (Huang & Wu, 2021) and concluded that tapered pin fins had the lowest thermal resistance, 18.7% lower than cylindrical pin fins. Lv et al. (2023) also conducted numerical simulations on cylindrical, conical, truncated, and bullet-shaped pin fins, finding that truncated cones were the most effective design due to the combination of minimal  $\Delta p$  and low thermal resistance.

Another important finding from Souida et al. (2022) is that thermal resistance can be reduced by 83.52-192.3% compared to cylindrical pin fins, and significantly reduce  $\Delta p$  by 100.38-343.32%. The same trends of better thermal and hydraulic performance of the cone pin fins were reported by Tahsin et al. (2024), Al-Karooshi et al. (2024). Moreover, the data reported by Naphon et al. (2007) showed that tapered pin fins' heat transfer performance increases when arranged staggered.

On the other hand, another experimental study showed that truncated cones' performance evaluation criterion values were lower than those of cylinders, squares, or hexagons (Zhang et al., 2021). Compared to squares, the truncated cones' performance evaluation criterion value may be lower by 38.5%.

There are more exotic pin fin array designs, such as double-cross pin fins (Ismail, 2024), rectangular fork shape (Hossain et al., 2025), piranha pin fins (Kishore et al., 2024), Kagome and body-centred cubic lattice arrays (Liang et al., 2021) which leads to improved heat transfer and fluid-flow dynamics. Even though these intricate designs significantly improve thermal management and are highly effective in many engineering applications, their main limitation is their manufacturing complexity. Their complex geometry and unconventional designs make them challenging to fabricate using standard production techniques, making them less practical for widespread industrial use.

The reviewed studies consistently indicate that pin fin geometry significantly impacts heat transfer and fluid flow characteristics. The comparison between streamlined and sharp-edged pin fins reveals that cylindrical and elliptical pins

experience lower heat transfer due to smoother flow patterns, resulting in reduced  $\Delta p$ . In contrast, sharp-edged designs such as triangular and square pin fins enhance heat transfer by increasing turbulence, but at the cost of higher pressure losses. Tapered cone pin fins enhance heat dissipation by disrupting the thermal boundary layer and reducing stagnant zones, thereby lowering surface temperatures. These designs exhibit superior thermohydraulic performance by promoting more favourable flow dynamics and turbulence structures than cylindrical pin fins. Additionally, the staggered pin fin arrangement further improves heat transfer by forcing the fluid flow to meander, accelerating the transition to turbulence, and enhancing thermal performance. These findings highlight the importance of geometric optimisation in designing efficient pin fin cooling systems.

### 1.3. Coherent structures

Coherent flow structures play a vital role in pin fin arrays' thermal and hydrodynamic performances, which are widely used in heat exchangers (Qin et al., 2023), gas turbine blade cooling (Ahn, 2025), and electronics thermal management. These structures, formed by the interaction between the flow and the pin fin geometries, significantly influence heat transfer and  $\Delta p$  characteristics.

Coherent fluid flow structures refer to spatially and temporally organised patterns of vorticity, velocity, or turbulence that persist for significant durations and influence the overall flow dynamics (Hussain, 1983). A coherent structure can be defined as a region of turbulent or laminar flow in which the motion of fluid elements is correlated over a particular spatial and temporal scale (Fiedler, 1988). These structures are responsible for energy and momentum transport in turbulent flows and often exhibit periodic or quasi-periodic behaviour.

The spatial scale of a coherent structure refers to the physical size over which the flow shows correlated behaviour. These can range from small vortices to large, organised vortex structures. For example, the alternating vortices in the wake of a cylinder remain spatially organised at certain intervals downstream (Lewis & Radko, 2020).

The temporal scale of a coherent structure indicates how long it remains correlated before breaking down or evolving. For instance, vortex shedding occurs at a characteristic Strouhal number that remains consistent over time (Spedding, 2002). Large vortices tend to persist longer and decay more slowly, whereas small vortices break down quickly due to energy cascading towards smaller scales. Nonetheless, these features can still be considered coherent structures, with their coherence depending on their lifetime, spatial extent (i.e., the width, length, or volume over which the flow pattern maintains some form of organised behaviour), and level of organisation. Although turbulence is often associated with randomness, it still exhibits

recurring patterns in which energy, momentum, and vorticity are transported in an organised manner. When coherent structures are correlated in both space and time, they extend over a characteristic distance and persist for a particular time before evolving or dissipating.

Examples of coherent structures in pin fin arrays include, but are not limited to, shear layers and vortices (Jiang et al., 2022), Föppl vortices (Protas, 2004), horseshoe vortices (Jiang et al., 2022), wake structures (Pereira et al., 2018), recirculation zones (Bauri, 2022), hairpin vortices (Dennis, 2015), rolls and streaks (Dennis, 2015), jets and plumes (Amor et al., 2024). As the flow encounters the leading edges of the pin fins, shear layers are formed that later shed into vortices. These vortices enhance turbulence, thereby increasing local heat transfer. Furthermore, coherent structures form around pin fins as the boundary layer wraps around the leading edge, creating a vortex system that affects both local and downstream heat transfer. Moreover, periodic vortex shedding (similar to von Kármán vortex streets) influences turbulence and mixing downstream behind the pin fins.

Coherent structures emerge due to various fluid dynamic instabilities, such as Kelvin-Helmholtz instability, Rayleigh-Taylor instability, Taylor-Görtler vortices, the Orr mechanism, and nonlinear interactions (Fiedler, 1988; Jiao et al., 2021; Mercier et al., 2020).

Coherent structures play a significant role in energy transfer, transporting energy from larger to smaller scales. They also affect boundary-layer flow resistance and enhance scalar transport in combustion processes, atmospheric flows, and ocean currents. Moreover, coherent structures contribute to the initiation and maintenance of boundary-layer turbulence and free-shear flows.

Although coherent structures are often associated with turbulent flows, they are not exclusive to turbulence. They also appear in laminar flows, including cases with steady vortices, for example, Föppl vortices, where the flow remains organised and does not undergo chaotic mixing (Cao et al., 2021). In laminar flow, coherent structures arise due to shear layer instability (before transitioning to turbulence), boundary layer separation, and vortex formation in closed and open flows.

**Table 1.** Coherent structure features in laminar and turbulent flows

<b>Feature</b>	<b>Laminar flow structures</b>	<b>Turbulent flow structures</b>
Stability	Stable, persistent	Highly dynamic, evolving
Predictability	Deterministic patterns	Stochastic behavior
Shape	Smooth vortex formations	Irregular, multi-scale vortices
Scale	Large, well-defined regions	Wide range of scales
Energy transport	Low energy transport	High energy/momentum transport

Coherent structures do not have to be exactly the same over space and time, but they must have some degree of correlation at some spatial and temporal scale (Adrian, 2007; Tong et al., 2025). The key idea behind coherence in fluid dynamics is that these structures maintain a recognisable pattern even as they evolve, deform, or interact with other structures. The level of similarity can vary depending on the following factors:

- Self-similarity (scaling behaviour), where structures can grow or shrink while maintaining a self-similar shape (Tsuruhashi et al., 2022). For instance, vortex rings in a jet expand as they move downstream but retain their characteristic form.
- Evolution without loss of identity occurs when structures stretch, tilt, or deform but remain correlated over time. For instance, hairpin vortices in boundary layers can merge or elongate while maintaining their basic structure (Adrian, 2007).
- Intermittency and partial coherence occur when some structures are partially coherent, meaning they appear intermittently rather than continuously present (Pan & Banerjee, 1995). For instance, turbulent bursts in the boundary layer occur sporadically but show repeated patterns.
- Large-scale and small-scale coherence: while large-scale structures persist for more extended periods and have stronger coherence, small-scale vortices break down quickly and lose coherence due to turbulent energy cascades (H. Wang et al., 2021).

Coherent structures are identified using experimental and numerical methods:

- Flow Visualisation (e.g., dye injection, schlieren imaging).
- Particle Image Velocimetry (PIV) – measures velocity fields.
- Proper Orthogonal Decomposition (POD) – decomposes flow into dominant modes.
- Dynamic Mode Decomposition (DMD) – identifies coherent structures from time-resolved data.
- Wavelet Transform Analysis – detects localised flow structures.
- Vorticity and Q-Criterion – mathematical indicators for vortex detection.

Experimental methods for identifying coherent structures rely on physical measurements and observations of fluid flow. Techniques such as flow visualisation (e.g., dye injection, schlieren imaging) provide qualitative insights into flow behaviour, whereas PIV offers quantitative velocity-field measurements. These methods are crucial for validating numerical simulations, understanding turbulence,

and studying real-world fluid dynamics. However, resolution, optical access, and measurement noise often limit experimental methods.

Numerical methods for identifying coherent structures are based on computational analysis of flow data obtained from simulations or experiments. Techniques such as proper orthogonal decomposition (POD) and dynamic mode decomposition (DMD) extract dominant flow patterns and time-dependent structures, while wavelet transform analysis helps detect localised turbulent features. Additionally, mathematical criteria such as vorticity and Q-Criterion are widely used to identify vortices and coherent structures directly from computational fluid dynamics (CFD) simulations. These methods enable a high-resolution, cost-effective analysis of complex flows and are essential for turbulence modelling, aerodynamic optimisation, and flow control strategies.

The  $\Omega$  method was chosen for use in combination with critical points theory for vortex detection because it provides an accurate, objective, and theoretically grounded approach to identifying vortical structures in fluid flows. These methods complement each other by combining a robust quantitative vortex criterion with a topological classification framework for analysing flow structures.

The  $\Omega$  method is particularly well-suited for vortex detection as it provides a normalised measure of the rotational dominance in a flow field. Unlike other vortex identification criteria, such as Q-Criterion and  $\lambda_2$ , this method effectively highlights vortex structures in laminar and turbulent flows. It captures weak and strong vortices, making it useful for various fluid dynamics applications (Belkacem, 2021; Y. Zhang et al., 2019). It is also less sensitive to noise and computational grid resolution, making it a more stable and reliable choice for CFD-based vortex detection.

By integrating critical points theory, the  $\Omega$  method gains further theoretical strength. Critical points theory analyses singularities in the velocity field, such as stagnation points, saddle points, and vortex cores, which define the topological behaviour of flow structures. This theory systematically classifies flow regions based on their local velocity gradient tensors, enabling precise identification and differentiation of vortex structures from other coherent flow features. The methods used will be described in Section 1.4.

The investigation of vortical structures is gaining increased significance, as Sreenivasa (Sreenivasan, 2019) emphasises their critical role in understanding heat transfer mechanisms. Consequently, to understand the flow dynamics and thermal transport processes, it is necessary to study their formation during flow through pin arrays. The study of low  $Re$  flows is facilitated by the universality of small-scale turbulence (Schumacher et al., 2014), which suggests that specific turbulent characteristics remain consistent across various flow configurations. This concept is particularly relevant to analysing the behaviour of vortical structures in pin fin arrays.

Some researchers have already investigated the flow behaviour in different pin fin configurations. For instance, Raza et al. (2024) performed a numerical analysis to evaluate the influence of various pin fin shapes, including cylindrical, pentagonal, hexagonal, square, and triangular configurations and their twisted counterparts. Their findings of streamlines demonstrated that twisted pin fins create three-dimensional secondary flows and vortex structures, leading to improved thermal performance. Similarly, Chang et al. (2021) examined the impact of twisted pin fins on thermal and hydraulic characteristics, specifically analysing the vortical flows induced by these structures. The study revealed that complex vortex formations contributed to significant velocity nonuniformities and high-gradient variations. Yan et al. (2021) evaluated the heat transfer performance by comparing the streamline distribution between different pin fin geometries. Their investigation focused on curved and inclined pin fins, revealing that the interaction and balance between jet-like flow and longitudinal secondary flow are key factors influencing heat transfer efficiency. In pin fin arrays, secondary flow refers to the organised cross-stream motion and vortex structures that arise perpendicular to the primary flow direction as a result of geometric modifications such as twisting, curving, or inclining the fins. Unlike turbulence, which is chaotic and broadband, secondary flows are deterministic and strongly governed by the pin fin shape and arrangement. Studies have shown that these flows manifest as vortices and jet-like motions that redistribute momentum and enhance mixing, thereby playing a critical role in improving heat transfer performance in complex pin fin configurations.

#### **1.4. Analytical methods and modelling**

Critical points theory in fluid mechanics refers to analysing points in a flow field where key flow properties, such as velocity, pressure, or vorticity, exhibit significant changes or singular behaviour (Perry & Fairlie, 1975). In fluid mechanics, saddle points, nodes, and foci are critical points in a flow field where the velocity gradients exhibit distinct behaviours, influencing fluid motion patterns (see Table 2).

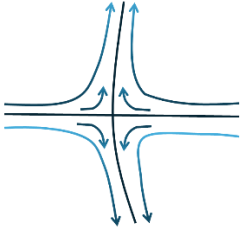
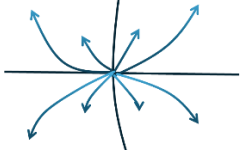
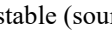
A saddle point is a location in the flow where streamlines diverge in one direction and converge in another, resembling a saddle shape in a vector field. These points indicate unstable equilibrium, often occurring in flow separation and recirculation regions. Saddle points are crucial in turbulence studies and boundary-layer flow analysis because they help determine flow instability and vortex formation. Saddle points appear where streamlines diverge in one direction and converge along another, forming an X-shaped pattern. These are regions of unstable equilibrium, often occurring in flow separations or recirculation zones.

Nodes are critical points where streamlines converge (attractive/stable node) or diverge (repulsive/unstable node). Stable nodes occur when both eigenvalues are

negative, meaning that the fluid elements move towards the point, often representing sinks in the flow. Unstable nodes occur when both eigenvalues are positive, indicating that the fluid moves outward from the point, often representing sources in the flow. Nodes are fundamental in studying stagnation flows, where fluid accumulates or disperses, as seen near impinging jets or flow stagnation regions on airfoils.

Foci are points in a flow field where streamlines exhibit a spiralling motion around the point rather than moving directly toward or away from it. This occurs when the eigenvalues of the velocity gradient tensor are complex conjugates, resulting in rotational and swirling effects. Stable foci appear when the real parts of the eigenvalues are negative, meaning that streamlines spiral inward, indicating energy dissipation in viscous flows. Unstable foci occur when the real parts of the eigenvalues are positive, leading to outward spiralling streamlines, which are common in vortex shedding and turbulence generation.

**Table 2.** Classification of critical points in fluid fields with associated streamline patterns and description

Critical point	Visual pattern	Description
Saddle point		Saddle points appear where streamlines diverge in one direction and converge along another, forming an X-shaped pattern. These are regions of unstable equilibrium, often occurring in flow separations or recirculation zones.
Nodes	<p>Stable (sink)</p>  <p>Unstable (source)</p> 	Stable nodes (sink): all streamlines converge to a single point, indicating a flow accumulation or stagnation. Unstable nodes (source): streamlines diverge outward, indicating a flow expansion or source region. Nodes commonly appear in stagnation flows or near boundary layers where the flow decelerates or accelerates.
Foci	<p>Stable (sink)</p>  <p>Unstable (source)</p> 	Stable foci (spiral sink): streamlines spiral inward towards the centre, often indicating energy dissipation in a vortex or turbulent region. Unstable foci (spiral source): streamlines spiral outward, suggesting rotational-

		motion amplification, often observed in vortex shedding and turbulence formation.
--	---	---

There are several methods for studying flow structures, which can be divided into different generations. The first-generation methods include streamlines (Lotfi & Sundén, 2020; Raza et al., 2024) and vorticity (Bai et al., 2019; Chang et al., 2021; Liu et al., 2019) and are based on vorticity, while second-generation methods include, but are not limited to, the Q criterion (Bai et al., 2019; Kadiyala & Chattopadhyay, 2018; Liu et al., 2019; Y. Zhang et al., 2019) and the  $\lambda_2$  criterion (Liu et al., 2019), which is based on the velocity gradient tensor. They decompose the gradient into symmetric (strain rate) and antisymmetric (rotation rate) parts. Third-generation methods include newer approaches such as  $\Omega$  (Bai et al., 2019; Liu et al., 2019; Y. Zhang et al., 2019), Liutex (Liu et al., 2016, 2019), and Rortex (Bai et al., 2019). They are designed to provide more unambiguous identification of vortical structures by isolating the ‘true’ swirling motion even in flows with high shear or complex deformations. It is important to highlight that these methods are objective and do not rely on subjective assessment. A comparison of these methods reveals that while the Q criterion struggles to detect weaker structures, third-generation methods can identify them (Belkacem, 2021; Y. Zhang et al., 2019). Furthermore, the  $\Omega$  is unaffected by the threshold values and can identify strong, medium and weak vortices equally.

Using a delayed detached-eddy simulation, Chen et al. (1993) conducted a numerical study of the flow around a cylinder at  $Re = 27000$ . They identified vortical structures using the Omega-Liutex method, which revealed complex vortex interactions with significant three-dimensional characteristics. Recent studies have also applied the  $\Omega$  to study vortical structures in a scroll pump (Song et al., 2023), a multi-stage double-suction centrifugal pump (Zhao et al., 2024), and the flow around a hydrofoil (‘Application of Omega Identification Method in the Ventilated Cavities Around a Surface-Piercing Hydrofoil’, 2023). All these studies confirm that the  $\Omega$  method is a highly reliable and effective tool for analysing vortical structures.

The  $\Omega$  method is used to identify vortical structures in a fluid flow by analysing the flow’s rotational characteristics. It is based on the vorticity tensor and is particularly effective in detecting complex vortex dynamics in three-dimensional flows. The  $\Omega$  is defined using the second invariant of the velocity gradient tensor, which helps identify regions of the flow where rotation dominates. The  $\Omega$  basically tells where rotation dominates over strain. In many turbulent and complex flows, relying solely on the vorticity magnitude can be misleading because high shear can produce large vorticity even in the absence of a true vortex (Jeong & Hussain, 1995).

The  $\Omega$  addresses this by comparing the rotational (or antisymmetric) and strain (or symmetric) components of the local velocity gradient.

The  $\Omega$  formula is defined as the ratio of the norm of the rotation rate tensor to the sum of the norms of the rotation and strain rate tensors (Liu et al., 2016, 2019):

$$\Omega = \frac{b}{a+b+\xi} \quad (1)$$

here  $\Omega$  – Omega criterion (Scalar function measuring the balance between rotation and strain);

$b$  – Frobenius term of anti-symmetric velocity tensor;

$a$  – Frobenius term of symmetric velocity tensor;

$\xi$  – represents a small positive value added to prevent division by zero.

Where the strain rate tensor (symmetric part):

$$a = \text{trace}(\mathbf{A}^T \mathbf{A}) = \sum_{i=1}^3 \sum_{j=1}^3 (\mathbf{A}_{ij})^2 \quad (2)$$

$$\mathbf{A} = \frac{1}{2} (\nabla \mathbf{u} + \nabla \mathbf{u}^T) \quad (3)$$

here  $\mathbf{A}$  – symmetric velocity tensor;

$\nabla \mathbf{u}$  – velocity tensor.

The rotation rate tensor (antisymmetric part):

$$b = \text{trace}(\mathbf{B}^T \mathbf{B}) = \sum_{i=1}^3 \sum_{j=1}^3 (\mathbf{B}_{ij})^2 \quad (4)$$

$$\mathbf{B} = \frac{1}{2} (\nabla \mathbf{u} - \nabla \mathbf{u}^T) \quad (5)$$

$$\nabla \mathbf{u} = \frac{1}{2} (\nabla \mathbf{u} + \nabla \mathbf{u}^T) + \frac{1}{2} (\nabla \mathbf{u} - \nabla \mathbf{u}^T) = \mathbf{A} + \mathbf{B} \quad (6)$$

here  $\mathbf{B}$  – Anti-symmetric velocity tensor.

The value of  $\Omega$  lies between 0 and 1. A value of 0 indicates a purely strain-dominant region, while a value of 1 corresponds to a purely rotational region. In practical applications, a threshold of 0.52 is often selected (Liu et al., 2016). Regions with  $\Omega \geq 0.52$  are typically identified as vortical regions. This threshold effectively distinguishes areas where the rotation is sufficiently strong relative to the strain, thereby indicating the presence of a vortex.

### 1.5. Pin fin thermohydraulic efficiency

Pin fin effectiveness is a critical parameter in evaluating the thermal performance of pin fin arrays in heat exchangers. It quantifies the ability of a pin fin array to enhance heat transfer relative to a reference surface without fins. The effectiveness of a pin fin array depends on multiple factors, including pin geometry, material properties, flow conditions, and thermal conductivity.

The most commonly known parameter is the thermohydraulic performance index, often referred to as *TPI* (Webb, 1981; Y. Xu et al., 2023). It is defined as the ratio between the actual heat transfer,  $\Delta p$ , or  $f$ :

$$TPI = \frac{Nu}{\left(\frac{f}{f_0}\right)^{\frac{1}{3}}} \text{ or } \frac{Nu}{\left(\frac{\Delta p}{\Delta p_0}\right)^{\frac{1}{3}}} \text{ or } \frac{Nu}{f^{\frac{1}{3}}} \quad (7)$$

Here *TPI*– thermal performance index;

*Nu* – Nusselt number;

*Nu*<sub>0</sub> – flat channel Nusselt number

*f* – friction factor;

*f*<sub>0</sub> – flat channel friction factor;

$\Delta p$  – pressure drop.

*Nu* is representing the ratio of convective to conductive heat transfer, is defined as:

$$Nu = \frac{hL}{\kappa} \quad (8)$$

Where the convective heat transfer coefficient (*h*) is defined as:

$$h = \frac{q}{T_w - T_f} \quad (9)$$

Sundaram et al. (Sundaram et al., 2021) had estimated pin fin efficiency as a function of pin fin height and heat transfer coefficient, after getting results, developed a pin fin effectiveness correlation. It has a form of (the variables here do not have the same meaning as those listed in the nomenclature):

$$\varepsilon = C_{11} \alpha_V^{C_{12}} \left(\frac{P}{A}\right)^{C_{13}} \left(\frac{H}{D_2}\right)^{C_{14}} \left(1 - \frac{D_{inr}}{D_0}\right)^{C_{15}} \quad (10)$$

here *C*<sub>11</sub>, *C*<sub>12</sub>, *C*<sub>13</sub>, *C*<sub>14</sub>, *C*<sub>15</sub> – constants;

$\alpha_V$  – void fraction;

*P* – pin pitch;

*A* – area;

*H* – height;

*D* – diameter.

Another author also wrote a correlation for fin effectiveness (Singh et al., 2019) when jet is present, it has the shape of:

$$\varepsilon = C_{21} Re^{C_{22}} \left(\frac{P_{jet}}{D_{jet}}\right)^{C_{23}} \left(\frac{P_{jtj}}{D_{jet}}\right)^{C_{24}} Pr^{C_{25}} \quad (11)$$

here *C*<sub>21</sub>, *C*<sub>22</sub>, *C*<sub>23</sub>, *C*<sub>24</sub>, *C*<sub>25</sub> – constants;

$Pr$  – Prandtl number.

**Table 3.** Coefficients of eq. 8 and eq. 9

Coefficient of eq. 7		$C_{11}$	$C_{12}$	$C_{13}$	$C_{14}$	$C_{15}$
Values		3.1249	0.0030	0.0625	0.4011	0.0326
Coefficient of eq. 8		$C_{21}$	$C_{22}$	$C_{23}$	$C_{24}$	$C_{25}$
Values	Target Surface	Concentric	0.405676	0.146864	0.07462	0.049543
		Cubic	0.504119	0.114745	0.08452	0.032524
		Cylindrical	0.56636	0.087997	0.02921	0.000719

Nonetheless, there are no flow-unsteadiness-based or coherent-structure-based performance criteria that would indirectly correlate with thermal performance. his approach could serve as a surrogate for traditional metrics, reducing the need to explicitly model heat transfer while enabling faster and more physically grounded assessments of pin fin array designs.

### 1.6. Flow regimes and scaling effects in microscale pin fin arrays

Before exploring the complex flow regimes around pin fin arrays, it is essential to understand the flow behaviour around a single circular cylinder, which serves as a fundamental building block in fluid dynamics. The single-cylinder case provides critical insights into flow separation, vortex formation, and transition mechanisms that also influence the behaviour of flow through pin fin arrays.

Zdravkovich and Bearman (1997) studied the flow around a single cylinder and identified distinct regimes based on the  $Re$  (see Table 4). Between  $Re \approx 4$ -5 and 30-48, steady separation occurs, forming Föppl vortices. In the range  $Re \approx 30$ -48 to 180-200, the flow becomes unsteady, characterised by a Karman-Bénard vortex street.

Further transitions occur in the wake: from laminar eddy transition ( $Re \approx 180$ -250) to irregular eddy transition ( $Re \approx 220$ -400). Following this, shear-layer transitions begin in subcritical zones ( $Re \approx 350$  to 200,000), eventually progressing into complex boundary-layer transitions, including pre-critical, single-bubble, and supercritical states, extending beyond  $Re \approx 3.5$  million and leading toward the ultimate turbulent regime.

**Table 4.** Flow regimes by Zdravkovich and Bearman (1997)

Stability	Zone	Laminar	Transitional	Turbulent	$Re$ ranges
Steady		Creeping flow (no-separation)			0 – 4-5
		Föppl vortices			4-5 – 30-48

	(Steady separation)		
	Karman-Benard eddy street	30-48 – 180-200	
<b>Unsteady</b>	Wake	Lower transition	180-200 – 220-250
		Upper transition	220-250 – 350-400
	Shear layer	Lower subcritical	350-400 – $10^3$ - $2 \cdot 10^3$
		Intermediate subcritical	$10^3$ - $2 \cdot 10^3$ – $2 \cdot 10^4$ - $4 \cdot 10^4$
		Upper subcritical	$2 \cdot 10^4$ - $4 \cdot 10^4$ – $1 \cdot 10^5$ - $2 \cdot 10^5$
	Boundary layer	Pre-critical	$1 \cdot 10^5$ - $2 \cdot 10^5$ – $3 \cdot 10^5$ - $3.4 \cdot 10^5$
		Single bubble	$3 \cdot 10^5$ - $3.4 \cdot 10^5$ – $3.8 \cdot 10^5$ - $4 \cdot 10^5$
		Two-bubble	$3.8 \cdot 10^5$ - $4 \cdot 10^5$ – $5 \cdot 10^5$ - $10^6$
		Supercritical	$5 \cdot 10^5$ - $10^6$ – $3.5 \cdot 10^6$ - $6 \cdot 10^6$
		Post-critical	$3.5 \cdot 10^6$ – $6 \cdot 10^6$ – (?)
	Invariable	(?) – $\infty$	
	Ultimate		

Flow regimes in pin fin arrays are primarily determined by  $Re$ , pin geometry, spacing, and fluid properties. At low  $Re$ , the flow tends to remain laminar, exhibiting orderly streamlines with limited mixing and lower heat transfer coefficients. As the  $Re$  increases, the flow transitions to turbulence, accompanied by vortex shedding, flow separation, and wake interactions that significantly enhance convective heat transfer but also increase pressure loss.

Unlike simple channel flows, where flow regime classification is relatively well-defined (e.g., laminar for  $Re < 2000$ , turbulent for  $Re > 4000$ , and transitional in between), the categorisation of flow regimes in pin fin arrays is more complex and application-specific. This complexity arises from the repeated interruption of flow by the pin structures, which induces local acceleration, separation, wake formation, and vortex shedding – even at relatively low  $Re$ .

According to Žukauskas (1972) investigation flow in pin fin arrays is predominantly laminar when  $Re < 1000$ , mixed or subcritical  $500 < Re < 200000$ , and predominantly turbulent at  $Re > 200000$ . But he also noted that staggered arrays with small longitudinal pitch at  $Re > 1000$  flow become turbulent instantly. Furthermore, a  $6D$  distance is needed so that the wake zone is not influenced by the nearby pin.

While other authors suggest that wake transition (vortex shedding) happens when  $Re = 500-700$  (F. Xu et al., 2018), and irregular vortex wake at  $Re = 850-1000$ . Unsteady Von Karman vortex street happens when  $Re > 550$  (Qiu et al., 2020).

A flow is considered not steady (i.e., unsteady or time-dependent) when its properties (such as velocity, pressure, or temperature) change with time at a given location:

$$\frac{\partial \phi}{\partial t} \neq 0 \quad (12)$$

here  $\phi$  – variable;

$t$  – time.

In contrast, steady flow means these properties remain constant over time at every fixed point in space. Therefore, if vortex shedding occurs behind pins and the resulting wake fluctuates over time, the flow is unsteady. If residuals oscillate over time after initial convergence or the solution never stabilises into a fixed pattern, the flow is unsteady. In this paper, the flow will be categorised into steady and unsteady.

Another important point is the size-based classification of heat exchangers into channels. Equally important is the selection of an appropriate modelling strategy, either classical or molecular.. Kandlikar and Grande (2003) classified channels by their size (see Table 5).

**Table 5.** Channel classification by Kandlikar and Grande (2003)

Conventional channels	$D_h > 3 \text{ mm}$
Minichannels	$3 \text{ mm} \geq D_h > 200 \text{ }\mu\text{m}$
Microchannels	$200 \text{ }\mu\text{m} \geq D_h > 10 \text{ }\mu\text{m}$
Transitional channels	$10 \text{ }\mu\text{m} \geq D_h > 0.1 \text{ }\mu\text{m}$
Transitional microchannels	$10 \text{ }\mu\text{m} \geq D_h > 1 \text{ }\mu\text{m}$
Transitional nanochannels	$1 \text{ }\mu\text{m} \geq D_h > 0.1 \text{ }\mu\text{m}$
Molecular microchannels	$0.1 \text{ }\mu\text{m} \geq D_h$

Single-phase flow is expected to be unaffected for liquids, as the hydraulic diameter is in the range  $200 \text{ }\mu\text{m} \geq D_h > 10 \text{ }\mu\text{m}$ . These dimensions are a few orders of magnitude higher than the molecular mean free flow path. For liquids such as water, the molecular free path is minimal, so the continuum assumption is well justified in microchannels. Another review study supports that the fluid (for example, water) can be treated as a continuum medium even when the hydraulic diameter is down to a few  $\mu\text{m}$  (Rosa et al., 2009). Therefore, no fundamental change in flow physics (for single-phase liquids) is expected, assuming the continuum hypothesis holds.

On the other hand, it was indicated that for single-phase gas flow in microchannels, the type of flow depends on Knudsen number ( $Kn$ ) (see Table 6) (Kandlikar & Grande, 2003).

$$Kn = \frac{\lambda}{D_h}$$

here  $Kn$  – Knudsen number;

$\Lambda$  – free mean path for gases.

For air, helium, or hydrogen flow, the slip-flow condition for microchannels applies when  $200 \mu\text{m} \geq D_h > 10 \mu\text{m}$ . When  $Kn$  is less than 0.1, rarefaction effects become important. In the slip region, typical of microchannels, the continuum theory can be modified by applying a slip ratio at the wall.

**Table 6.** Knudsen number ranges for various types of flow

Range of $Kn$	Type of flow
$0.001 > Kn$	Continuum flow, no rarefaction effects
$0.1 > Kn > 0.001$	Slip flow, rarefaction effects that can be modelled with a modified continuum theory accounting for wall slip
$10 > Kn > 0.1$	Transitional flow, a type of flow between slip flow and free molecular flow that is analysed statistically, i.e., with the Boltzmann equation
$Kn > 10$	Free molecular flow: motion of individual molecules must be modelled and then treated statistically

### 1.7. The overview of literature analysis and the author’s contribution to the research field

The body of existing research clearly shows a strong emphasis on enhancing the thermal and hydraulic performance of microchannel heat sinks, particularly through variations in pin fin geometry and arrangement. Numerous studies have examined how different shapes, such as cylindrical, square, elliptical, conical, and others, affect flow behaviour and heat transfer. These investigations primarily focus on optimising geometric parameters to increase efficiency, usually by evaluating empirical correlations or derived indices such as  $TPI$  or pin fin effectiveness. While such metrics are useful, they are often based on results obtained through detailed CFD simulations or experimental setups that may not fully capture the underlying flow physics.

One of the main limitations identified in the literature is the lack of attention given to the flow structures that determine the thermal performance. Although widely acknowledged in broader fluid dynamics contexts, the role of coherent vortical structures has not been systematically explored in pin fin arrays. Most existing studies rely on streamlined visualisation or average flow quantities, which offer limited insight into the spatial and temporal organisation of the flow. The connection between

flow structures, such as vortex shedding, shear layers, and recirculation zones, and the resulting heat transfer and pressure loss characteristics remains largely qualitative.

This thesis aims to fill this gap by investigating the formation, evolution, and impact of coherent flow structures in microchannels with various pin fin configurations. Using high-fidelity numerical simulations and advanced vortex identification methods, specifically, the  $\Omega$  criterion coupled with critical points theory, the study examines how geometric parameters and flow regimes influence vortical behaviour. Rather than relying solely on heat transfer and pressure drop values, the study considers the flow physics more directly, aiming to understand the mechanisms that govern performance.

The key outcome of this work is the development of a new evaluation approach based on the analysis of coherent structures. This framework enables prediction of thermohydraulic efficiency without explicitly solving energy equations, providing a more efficient and physically meaningful alternative to traditional modelling techniques. The method offers the potential to improve the preliminary design process and to better understand the mechanisms of flow-induced enhancement in microscale cooling applications.

In this way, the thesis contributes a new layer of depth to the field. Shifting the focus to the dynamics of coherent structures and their relationship to thermal performance introduces a novel evaluation strategy that complements existing metrics and may reduce computational costs. The results have implications for designing and optimising microchannel heat sinks in electronics cooling and beyond.

## 2. METHODOLOGY

The study employs CFD to model the thermal and fluid-dynamic behaviour of flow in pin fin arrays, utilising the unsteady Reynolds-Averaged Navier-Stokes (URANS) technique. The URANS approach is adopted for its computational efficiency in capturing time-averaged flow properties and heat transfer characteristics across the pin fin array. For turbulence modelling, the  $k-\omega$  SST model was used exclusively due to its superior accuracy in predicting boundary-layer behaviour under complex flow conditions. The simulations were carried out using OpenFOAM v10, an open-source CFD toolbox that enables flexible implementation of various turbulence models and solver configurations. Most simulations assumed a compressible fluid, except for those conducted during the initial full-channel validation stage and some in the results section. Information on fluid compressibility will be provided in each section.

### 2.1. Governing equations

This study's fluid flow and heat transfer equations are based on the laws of conservation of mass, momentum, and energy. They are expressed as the Navier-Stokes equations, modified and solved numerically depending on the turbulence modelling method used.

#### 2.1.1. General form of the Navier-Stokes equations

The compressible Navier-Stokes equations are given as follows (Batchelor, 2010):

Continuity equation:

$$\nabla \cdot \mathbf{u} = 0 \quad (13)$$

here  $\mathbf{u}$  – velocity.

Momentum equation:

$$\frac{\partial \mathbf{u}}{\partial t} + (\mathbf{u} \cdot \nabla) \mathbf{u} = -\frac{1}{\rho} \nabla p + \nu \nabla^2 \mathbf{u} + \frac{1}{\rho} \mathbf{F} \quad (14)$$

here  $\rho$  – density;

$\nu$  – kinematic viscosity;

$\mathbf{F}$  – body force per unit mass.

Energy equation:

$$\frac{\partial T}{\partial t} + (\mathbf{u} \cdot \nabla) T = \alpha \nabla^2 T + \frac{\Phi}{\rho c_p} \quad (15)$$

here  $T$  – temperature;

$\alpha$  – thermal diffusivity;

$\Phi$  – viscous dissipation function;

$c_p$  – specific heat at constant pressure.

The compressible Navier-Stokes equations are given as follows:

Continuity equation:

$$\frac{\partial \rho}{\partial t} + \nabla \cdot (\rho \mathbf{u}) = 0 \quad (16)$$

Momentum equation:

$$\frac{\partial(\rho \mathbf{u})}{\partial t} + \nabla \cdot (\rho \mathbf{u} \otimes \mathbf{u}) = -\nabla p + \nabla \cdot \boldsymbol{\tau} + \rho \mathbf{F} \quad (17)$$

$$\boldsymbol{\tau} = \mu[\nabla \mathbf{u} + (\nabla \mathbf{u})^T] + \lambda(\nabla \cdot \mathbf{u})\mathbf{I} \quad (18)$$

here  $\boldsymbol{\tau}$  - viscous stress tensor;

$\mu$  – dynamic viscosity;

$\lambda$  – second viscosity coefficient;

$\mathbf{I}$  – identity matrix.

Energy equation:

$$\frac{\partial(\rho E)}{\partial t} + \nabla \cdot [\mathbf{u}(\rho E + p)] = \nabla \cdot (\boldsymbol{\tau} \cdot \mathbf{u} - \mathbf{q}) + \rho \mathbf{F} \cdot \mathbf{u} \quad (19)$$

$$E = e + \frac{1}{2}|\mathbf{u}|^2 \quad (20)$$

$$\mathbf{q} = -\kappa \nabla T \quad (21)$$

here  $E$  – total energy;

$\mathbf{q}$  – heat flux;

$e$  – internal energy;

$\kappa$  – thermal conductivity.

These equations form the foundation for the RANS approach.

### 2.1.2. URANS

The URANS formulation involves decomposing the instantaneous velocity, pressure and density fields into mean and fluctuating components (Wilcox, 2010):

$$u(x, t) = \bar{u}(x, t) + u'(x, t) \quad (22)$$

Substituting them into the Navier-Stokes equations and averaging yields:

Continuity equation:

$$\frac{\partial \bar{\rho}}{\partial t} + \nabla \cdot (\bar{\rho} \bar{\mathbf{u}}) = 0 \quad (23)$$

Momentum equation:

$$\frac{\partial(\bar{\rho} \bar{\mathbf{u}})}{\partial t} + \nabla \cdot (\bar{\rho} \bar{\mathbf{u}} \otimes \bar{\mathbf{u}}) = -\nabla \bar{p} + \nabla \cdot \bar{\boldsymbol{\tau}} - \nabla \cdot \mathbf{R} + \bar{\rho} \mathbf{g} \quad (24)$$

here  $\mathbf{R}$  – Reynolds stress tensor;

$\mathbf{g}$  – gravitational acceleration.

$$\bar{\boldsymbol{\tau}} = \mu[\nabla\bar{\mathbf{u}} + (\nabla\bar{\mathbf{u}})^T] + \lambda(\nabla \cdot \bar{\mathbf{u}})\mathbf{I} \quad (25)$$

$$\mathbf{R} = \overline{\rho\mathbf{u}' \otimes \mathbf{u}'} \quad (26)$$

Energy equation:

$$\frac{\partial(\bar{\rho E})}{\partial t} + \nabla \cdot [\bar{\mathbf{u}}(\bar{\rho E} + \bar{p})] = \nabla \cdot (\bar{\mathbf{u}} \cdot \bar{\boldsymbol{\tau}} - \bar{q} - q_t - \mathbf{R} \cdot \bar{\mathbf{u}}) + \bar{\rho} \mathbf{g} \cdot \bar{\mathbf{u}} \quad (27)$$

$$\bar{q} = -\kappa \nabla \bar{T} \quad (28)$$

$$q_t = \overline{\rho \mathbf{u}' e'} \quad (29)$$

In turbulent flow modelling, the averaging of the Navier–Stokes equations introduces additional unknowns, namely the Reynolds stresses, which require closure to solve the system. This is achieved using turbulence models such as the k- $\omega$  SST (shear stress transport) model (Menter, 1994). This two-equation turbulence model combines the k- $\omega$  model in the near-wall region and the k- $\epsilon$  model in the outer region using a blending function. The equations for turbulent kinetic energy ( $k$ ) and specific dissipation rate ( $\omega$ ) are as follows:

$$\frac{\partial(\rho k)}{\partial t} + \nabla \cdot (\rho u k) = P_k - \beta^* \rho \omega k + \nabla \cdot [(\mu + \sigma_k \mu_k) \nabla k] \quad (30)$$

$$\frac{\partial(\rho \omega)}{\partial t} + \nabla \cdot (\rho u \omega) = \alpha \frac{\omega}{k} P_k - \beta \rho \omega^2 + \nabla \cdot [(\mu + \sigma_\omega \mu_t) \nabla \omega] + 2(1 - F_1) \rho \sigma_{\omega 2} \frac{1}{\omega} \nabla k \cdot \nabla \omega \quad (31)$$

here  $k$  – turbulent kinetic energy;

$P_k$  – production term of turbulent kinetic energy

$\alpha, \beta, \beta^*, \sigma_k, \sigma_\omega, \sigma_{\omega 2}$  – model coefficients;

$\omega$  – specific dissipation rate;

$F_1, F_2$  – k- $\omega$  SST model blending functions.

Turbulent viscosity is computed as:

$$\mu_t = \frac{\rho k}{\max(\omega, F_2 \cdot \omega)} \quad (32)$$

The blending functions  $F_1$  and  $F_2$  control the transition between the k- $\omega$  and k- $\epsilon$  models:

$$F_1 = \tanh \left( \left[ \min \left( \max \left( \frac{\sqrt{k}}{\beta^* \omega y}, \frac{500\nu}{y^2 \omega} \right), \frac{4\rho\sigma_{\omega 2} k}{CD_{k\omega} y^2} \right) \right]^4 \right) \quad (33)$$

$$CD_{k\omega} = \max \left( 2\rho\sigma_{\omega 2} \frac{1}{\omega} \nabla k \cdot \nabla \omega, 10^{-10} \right) \quad (34)$$

$$F_2 = \tanh \left( \left[ \max \left( \frac{2\sqrt{k}}{\beta^* \omega y}, \frac{500\nu}{y^2 \omega} \right) \right]^2 \right) \quad (35)$$

In this research, the flow reaches a  $Re$  of up to 800, at which point unsteady flow has a notable impact. The  $k-\omega$  SST turbulence model was chosen for its demonstrated effectiveness in capturing transitional flow regimes (Bovati et al., 2021; Li et al., 2016; D. Zhang, 2017), making it particularly suitable for accurately representing the flow behaviour.

The time step was automatically controlled to maintain the Courant-Friedrichs-Lewy (CFL) number at a nearly constant value of unity, ensuring numerical stability and temporal accuracy.

### 2.1.3. Dimensionless quantities

Dimensionless quantities are numerical values that characterise physical phenomena without specific units. These quantities are crucial in engineering, physics, and fluid dynamics because they allow the comparison of different systems and the derivation of generalised laws.

The hydraulic diameter is a concept used to analyse fluid flow in non-circular ducts and channels. It is defined to provide an equivalent diameter for irregular cross-sections, allowing the use of standard dimensionless numbers (e.g.  $Re$ ) in flow analysis. The hydraulic diameter is given by (White, 2011):

$$D_h = \frac{4A}{\Pi} \quad (36)$$

here  $D_h$  - hydraulic diameter;

$\Pi$  – perimeter.

In the analysis of pin fin arrays, the choice of characteristic length, particularly the  $D_h$ , plays a critical role in accurately capturing the flow and heat transfer characteristics. Several studies have adopted the pin diameter as the characteristic dimension (İzci et al., 2015; Koşar et al., 2011; M. Lv et al., 2022; Mei et al., 2014; Moores et al., 2009; Qiu et al., 2020; Sparrow et al., 1980). However, this approach is limited in scope and becomes inappropriate for non-cylindrical pins, such as cones, hourglass, or tapered geometries, where the diameter varies along the pin height. In such cases, using a single diameter value fails to reflect the changing cross-sectional flow conditions.

Alternatively, other authors define  $D_h$  based on the overall channel cross-sectional area and wetted perimeter (Abuşka & Çorumlu, 2023; Aguirre et al., 2022; Al-Karooshi et al., 2024; Bhandari & Prajapati, 2021, 2022; Khoshvaght-Aliabadi et al., 2018; Liang et al., 2021; Mesgarpour et al., 2019; Polat et al., 2022; Serkan Şahin et al., 2023; Souida et al., 2022; F. Xu et al., 2018). While this channel-based approach is more general, it still yields a uniform  $D_h$  across cases, regardless of variations in pin shape (İzci, pitch, or arrangement (F. Xu et al., 2018). Consequently, it

oversimplifies fluid dynamics, often underestimating flow resistance and failing to accurately capture local heat transfer behaviour.

To overcome these limitations, this study adopts a geometry-dependent hydraulic diameter calculated based on the actual crossflow passage between adjacent pins. This  $D_h$  is derived from the local pin spacing, incorporating transverse and longitudinal pitch as well as pin diameter (as illustrated in Fig. 2). Unlike conventional methods, this approach dynamically accounts for variations in pin shape and array configuration, thus providing a more realistic representation of the effective flow area and wetted perimeter throughout the array.

This distinction is particularly critical in staggered pin fin arrays, where the flow does not proceed straight between rows but instead follows a zigzag or angled path due to the offset geometry. Therefore, the  $D_h$  is calculated based on a cross-section aligned with the actual flow path rather than one perpendicular to the overall flow direction. This allows for better capture of the actual constricted passages and surface interactions that influence pressure drop and heat transfer.

Notably, Renfer et al. (Renfer et al., 2013) also employed the same  $D_h$  approach in his work, which further supports the validity of this method. In the present study, experimental data from Renfer’s work were used for validation.

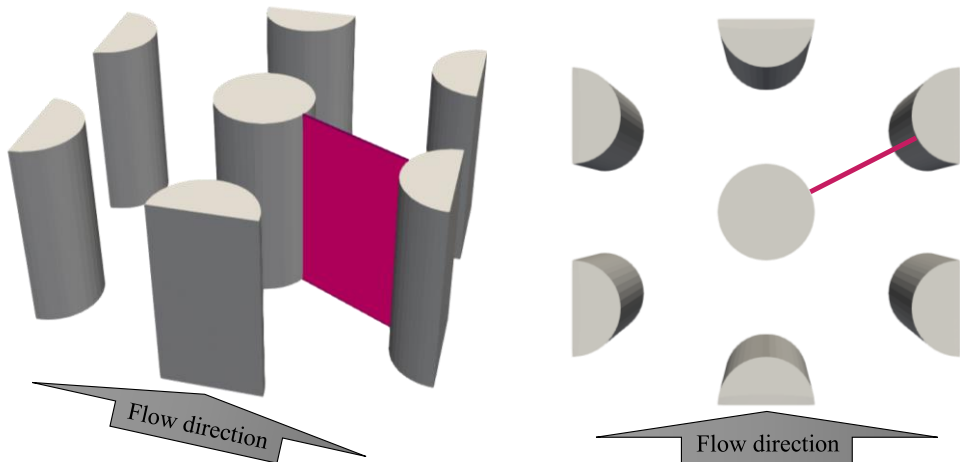


**Fig. 2.** Area and perimeter of cross sectional flow between pins in a staggered arrangement

The  $Re$  is used to predict the flow regime of a fluid (laminar, transitional, or turbulent). It is defined as (Reynolds, 1895):

$$Re = \frac{\rho u D_h}{\mu} = \frac{u D_h}{\nu} \quad (37)$$

here  $Re$  – Reynolds number.

The  $f$  measures the resistance to fluid flow due to surface roughness and viscosity. The Moody chart illustrates how  $f$  varies with  $Re$ : in the laminar regime,  $f$  decreases linearly with  $1/Re$ ; in the transitional regime,  $f$ , the trend becomes irregular and strongly dependent on inlet disturbances and geometry. However, due to the flow instabilities, mixing and momentum transfer are enhanced so that the measured  $f$  rises above the laminar line. In a turbulent regime,  $f$  generally decreases with increasing  $Re$ .

Typical forms of the  $f$  for laminar flow in a circular pipe (White, 2011):

$$f = \frac{64}{Re} \quad (38)$$

For turbulent flow (when  $Re > 4000$ ) (Colebrook, 1939):

$$\frac{1}{\sqrt{f}} = -2 \log_{10} \left( \frac{\epsilon}{3.7D} + \frac{2.51}{Re\sqrt{f}} \right) \quad (39)$$

here  $\epsilon$  - pipe roughness height

The formula used for CFD calculations when  $\Delta p$  is known (White, 2011):

$$f = \frac{2\Delta p D_h}{\rho u^2 L} \quad (40)$$

here  $L$  – characteristic length or pipe length.

In this study, the measured pressure drop is recast into  $f$ , which accounts for both viscous shear along the channel walls and, predominantly, the form drag generated by the pin fin array. Rather than treating each pin as an individual local-loss element, the periodic obstacles are homogenised into a distributed resistance; thus,  $f$  should be interpreted as an effective loss coefficient rather than a pure wall-friction factor. This provides a compact way to characterise the combined influence of wall shear and obstacle-induced resistance on the microchannel's overall hydraulic performance.

The  $Nu$  represents the ratio of convective to conductive heat transfer across a boundary. A high  $Nu$  indicates strong convection, while a low number suggests that heat transfer is primarily due to conduction.

The  $TPI$  is used to evaluate the efficiency of thermal systems, often in heat exchangers or cooling applications. It indicates the system's efficiency in providing high heat transfer while minimising frictional losses. A higher  $TPI$  suggests that heat transfer is significantly improved without a significant increase in  $\Delta p$ . A lower  $TPI$  implies the system experiences excessive friction losses relative to the heat transfer.

## 2.2. Boundary conditions

CFD boundary conditions (BC) are crucial for defining the physical domain and governing the fluid flow behaviour in a microchannel simulation. They specify how the fluid interacts with the boundaries of the computational domain and influence the accuracy and stability of the numerical solution. This section outlines the boundary

conditions applied in the CFD simulations for this dissertation, detailing their selection and implementation.

The CFD simulations in this study utilised a combination of boundary conditions tailored to the specific problem being modelled. This includes inlet, outlet, pin fins, upper/lower walls, right wall, left wall, and fluid-to-solid wall BC. Each modelled case of the problem (entire channel, domain, etc.) has a different combination of BC, considering suitability for the problem (see Table 7). Some BCs are explained in the validation section, for example, why the mapped BC was used instead of cyclic (see Section 3.1.2).

Microchannels fabricated using different techniques exhibit varying degrees of absolute surface roughness ( $\epsilon$ ). For instance, Shima et al. (2016) reported an average surface roughness of 8.4-9.6 nm for silicon microchannels produced via DRIE, while Park et al. (2020) observed DRIE scallop depths of approximately 130-230 nm, which could be reduced to below 20 nm through optimised post-etch smoothing processes. Based on the reported surface roughness, the corresponding relative roughness for Renfer et al. (2013) DRIE microchannel lies in the range of approximately 0.00004-0.001. According to standard hydraulic-smooth criteria,  $\epsilon^+ < 5$  ( $\epsilon^+ = \epsilon u^*/\nu$ ) (White, 2011), this magnitude of surface roughness is far below the level required to disturb the viscous layer. Such small roughness values indicate that the walls are hydraulically smooth, and the effect of roughness on pressure drop and flow structure is negligible.

Similarly, the impact on the thermal boundary layer can be evaluated using the ratio  $\epsilon/\delta_t$ . For typical microchannel flows with water ( $Pr \approx 7$ ), the thermal boundary layer thickness is of the order of a few micrometres, much lower than the hydraulic boundary layer (Schlichting & Gersten, 2017). Meaning the surface irregularities are fully embedded within the thermal boundary layer. Consequently, the channel can also be considered thermally smooth, and roughness-induced heat transfer enhancement is expected to be negligible.

The obstacles used in the study were considered hydrodynamically smooth. As a result, surface roughness effects were not explicitly accounted for in the analysis. This assumption is supported by the literature, where such obstacles are typically treated as hydrodynamically smooth due to their manufacturing precision and material properties (Qiu et al., 2020).

**Table 7.** Boundary conditions for simulations under non thermal and thermal scenarios across various computational domains

	Without heat transfer		
	Entire channel	Periodic part	Cyclic domain
Inlet	$p = p_{in}$ $\nabla \mathbf{u} \cdot \mathbf{n} = 0$ $k = k_{in}$	$p = p_{in}$ $\nabla \mathbf{u} \cdot \mathbf{n} = 0$ $k = k_{in}$	$\phi_{in} = \phi_{out}$

	$\omega = \omega_{in}$	$\omega = \omega_{in}$	
Outlet	$p = p_{atm}(0)$ $\nabla \mathbf{u} \cdot \mathbf{n} = 0$ $\nabla k \cdot \mathbf{n} = 0$ $\nabla \omega \cdot \mathbf{n} = 0$	$p = p_{atm}(0)$ $\nabla \mathbf{u} \cdot \mathbf{n} = 0$ $\nabla k \cdot \mathbf{n} = 0$ $\nabla \omega \cdot \mathbf{n} = 0$	
Pin fins	$\mathbf{u} = 0$ $\nabla p \cdot \mathbf{n} = 0$ $\nabla k \cdot \mathbf{n} = 0$ $\omega$ wall function	$\mathbf{u} = 0$ $\nabla p \cdot \mathbf{n} = 0$ $\nabla k \cdot \mathbf{n} = 0$ $\omega$ wall function	$\mathbf{u} = 0$ $\nabla p \cdot \mathbf{n} = 0$ $\nabla k \cdot \mathbf{n} = 0$ $\omega$ wall function
Upper/ lower walls	$\mathbf{u} = 0$ $\nabla p \cdot \mathbf{n} = 0$ $\nabla k \cdot \mathbf{n} = 0$ $\omega$ wall function	$\mathbf{u} = 0$ $\nabla p \cdot \mathbf{n} = 0$ $\nabla k \cdot \mathbf{n} = 0$ $\omega$ wall function	$\mathbf{u} = 0$ $\nabla p \cdot \mathbf{n} = 0$ $\nabla k \cdot \mathbf{n} = 0$ $\omega$ wall function
Right wall	$\mathbf{u} = 0$ $\nabla p \cdot \mathbf{n} = 0$ $\nabla k \cdot \mathbf{n} = 0$ $\omega$ wall function	$\phi_{right} = \phi_{left}$	$\phi_{right} = \phi_{left}$
Left wall	$\mathbf{u} = 0$ $\nabla p \cdot \mathbf{n} = 0$ $\nabla k \cdot \mathbf{n} = 0$ $\omega$ wall function		
With heat transfer			
	Cyclic domain w/o solid part	Cyclic domain with solid part	
Inlet	$\mathbf{u}_{in} = \mathbf{u}_{out}$ $p = f(eq)$ $k_{in} = k_{out}$ $\omega_{in} = \omega_{out}$ $T_{in} = T_{fixed}$	<i>Fluid</i> $\mathbf{u}_{in} = \mathbf{u}_{out}$ $p = f(eq)$ $k_{in} = k_{out}$ $\omega_{in} = \omega_{out}$ $T_{in} = T_{fixed}$ <i>Solid</i> $\phi_{in} = \phi_{out}$	
Outlet	$\nabla \mathbf{u} \cdot \mathbf{n} = 0$ (if outflow) $\mathbf{u} = 0$ (if outflow) $p = f(eq)$ $\nabla k \cdot \mathbf{n} = 0$ (if outflow) $k = k_{fixed}$ (if outflow) $p = f(eq)$ $\nabla \omega \cdot \mathbf{n} = 0$ (if outflow) $\omega = \omega_{fixed}$ (if outflow) $\nabla T \cdot \mathbf{n} = 0$ (if outflow) $T = T_{fixed}$ (if outflow)	<i>Fluid</i> $\nabla \mathbf{u} \cdot \mathbf{n} = 0$ (if outflow) $\mathbf{u} = 0$ (if outflow) $p = f(eq)$ $\nabla k \cdot \mathbf{n} = 0$ $\nabla \omega \cdot \mathbf{n} = 0$ <i>Solid</i> $\phi_{in} = \phi_{out}$	

Pin fins	$\mathbf{u} = 0$ $p = f(eq)$ $\nabla k \cdot \mathbf{n} = 0$ $\omega \text{ wall function}$ $\nabla T \cdot \mathbf{n} = 0$	-
Upper/ lower walls	$\mathbf{u} = 0$ $p = f(eq)$ $\nabla k \cdot \mathbf{n} = 0$ $\omega \text{ wall function}$ $\frac{\partial T}{\partial \mathbf{n}} = \frac{q_{fixed}}{k}$	<i>Solid</i> $\frac{\partial T}{\partial \mathbf{n}} = \frac{q_{fixed}}{k}$
Left/Right wall	$\phi_{right} = \phi_{left}$	<i>Fluid</i> $\phi_{right} = \phi_{left}$ <i>Solid</i> $\phi_{right} = \phi_{left}$
Fluid to solid	-	<i>Fluid</i> $\mathbf{u} = 0$ $p = f(eq)$ $k \text{ wall function}$ $\omega \text{ wall function}$ $q_{fluid} = q_{solid}$ <i>Solid</i> $q_{solid} = q_{fluid}$

### 2.2.1. Zero gradient

Zero gradient is a form of Neumann or second-type boundary condition where the gradient of a variable normal to the boundary is set to zero:

$$\nabla \phi \cdot \mathbf{n} = 0 \quad (41)$$

$\phi$  – is the variable of interest (e.g., temperature or velocity),  $\mathbf{n}$  – defines direction normal to the boundary surface.

In simple terms, it means the variable (such as temperature, velocity, pressure, or turbulence quantities) is extrapolated directly from the interior towards the boundary. When implemented in a discretised numerical model, this condition ensures that the boundary value is effectively equal to the value in the nearest cell centre adjacent to the boundary face, implying no change or variation normal to the boundary.

### 2.2.2. Fixed value

The fixed value boundary condition assigns a specified constant value to a variable at the domain boundary, making it one of the fundamental boundary

conditions. It is also known as a Dirichlet or first-type boundary condition, expressed mathematically as:

$$\phi|_{\Gamma} = \phi_{fixed} \quad (42)$$

$\phi_{fixed}$  – is the prescribed value at the boundary.

This condition can be used for both scalar and vector fields, including pressure, temperature, velocity, and other relevant quantities in a simulation.

### 2.2.3. No-slip

The no-slip boundary condition is a fundamental assumption in fluid mechanics, stating that the fluid velocity at a solid boundary equals the velocity of the boundary itself. For a stationary wall, this means the fluid has zero velocity relative to the wall:

$$\mathbf{u} = 0 \quad (43)$$

This condition creates a velocity gradient near the wall, leading to shear stresses and frictional effects in the flow. In CFD simulations, such as OpenFOAM, the no-slip condition is applied by setting the wall velocity to zero for stationary surfaces, ensuring accurate representation of boundary-layer development and wall-friction effects in the simulation.

### 2.2.4. Cyclic

In periodic flow simulations with cyclic boundary conditions, such as fully developed channel or pipe flows, the flow domain is treated as infinitely repeating, and the boundary condition enforces:

$$\phi_{in} = \phi_{out} \quad (44)$$

This implies no net pressure difference across the domain via the BCs, which, in turn, results in no driving force unless an external mechanism is introduced.

Mathematically, it introduces a force per unit volume that is adjusted at each timestep to drive the flow towards a target mean velocity ( $\mathbf{u}_{trg}$ ). The approach acts like a proportional controller, calculating the difference between the current domain-averaged velocity and the desired target velocity, and then determining the required body force to bridge this gap over the timestep. This method is particularly effective in simulations with cyclic boundary conditions where no natural pressure drop exists, as it mimics the effect of a pressure gradient while preserving periodicity. Consequently, the mean velocity force ensures a physically realistic, fully developed flow, facilitating accurate calculation of turbulent statistics and friction factors.

$$\bar{\mathbf{u}} = \mathbf{u}_{trg} \quad (45)$$

$\bar{\mathbf{u}}$  – domain-averaged velocity,  $\mathbf{u}_{target}$  – given value.

At each time step:

$$\mathbf{f} = \rho \frac{\mathbf{u}_{trg} - \bar{\mathbf{u}}}{\Delta t} \quad (46)$$

Pressure difference is not imposed directly; effective pressure drop is calculated from the force. The effective pressure drop corresponding to this force over the domain length is:

$$\Delta p_{eff} = |\mathbf{f}| \cdot L \quad (47)$$

This represents the effective or virtual pressure drop required to drive the same flow rate in a real, non-periodic physical system.

The cyclic BC enforces strict periodicity by ensuring that the temperature exiting one boundary re-enters at the opposite boundary, effectively creating an infinite repeating domain. However, in simulations with net heat addition, using a cyclic BC will cause the temperature to continually increase, as there is no mechanism for heat removal. In contrast, applying a mapped BC allows the inlet temperature to be set based on values from another patch, such as a fixed-temperature region, thereby preventing unbounded temperature rise. Although this breaks the simulation's periodicity, it enables boundary temperature control, ensuring thermal stability when periodic heat accumulation is not physically meaningful.

### 2.2.5. Mapped

The mapped boundary condition is used to transfer field values from a source patch to a target patch, ensuring continuity across interfaces in multi-region or conjugate heat transfer simulations. Mathematically, it imposes that the value of a field at the mapped boundary equals the value at the corresponding location on the source boundary:

$$\phi_{map} = \phi_{src} \quad (48)$$

$\phi_{map}$  – is the value at the target patch (where the BC is applied),  $\phi_{src}$  – is the value at the source patch (from which the field is mapped).

This means that quantities such as temperature, velocity, or pressure are directly mapped from the source to the target patch, maintaining physical consistency across regions.

### 2.2.6. $\omega$ wall function

The *OmegaWallFunction* is a wall boundary condition for the specific dissipation rate  $\omega$  used in  $k$ - $\omega$  turbulence models, such as  $k$ - $\omega$  SST, in OpenFOAM. It calculates an appropriate near-wall value of  $\omega$  based on the local  $y^+$ , applying an analytical formula in the viscous sublayer and a log-law-based formula in the logarithmic region:

$$\omega_{vis} = \frac{6\nu_w}{\beta_1 y^2} \quad (49)$$

$$\omega_{log} = \frac{\sqrt{k}}{c_\mu \kappa y} \quad (50)$$

$$\omega = \omega_{vis} \text{ when } y^+ \leq y_{lam}^+$$

$$\omega = \omega_{log} \text{ when } y^+ > y_{lam}^+$$

This ensures accurate and stable turbulence predictions near walls by preventing unphysical values of  $\omega$ , whether the mesh fully resolves the boundary layer or uses wall functions to model it.

If the mesh is fine near the wall, *OmegaWallFunction* calculates  $\omega$  based on viscosity and distance. If the mesh is coarse, it uses a formula based on turbulence quantities and log-law theory to set  $\omega$  appropriately to ensure stable, accurate results.

### 2.2.7. *k* wall function

The *kqRWallFunction* is a wall boundary condition used to specify the turbulent kinetic energy

*k* at walls in high  $y^+$  mesh regions when using RANS turbulence models. It calculates *k* based on the friction velocity, assuming an equilibrium turbulent boundary layer governed by the log-law. Mathematically, it is defined as:

$$k = \frac{u_\tau^2}{\sqrt{C_\mu}} \quad (51)$$

where  $C_\mu$  is a model constant (typically 0.09), and  $u_\tau$  – is the friction velocity.

### 2.2.8. Calculated

The calculated boundary condition is generally intended for derived fields rather than primary solved variables like pressure; it can work in specific cases, such as mapped or coupled boundaries in OpenFOAM. In these situations, pressure does not require a direct boundary condition because its value is determined internally through the mapping or coupling process.

$$\phi = f(\text{solver equations or other fields}) \quad (52)$$

The pressure at a calculated BC boundary is not imposed; it is directly obtained from the solution of the pressure equation in the solver.

### 2.2.9. Wall heat flux

The *externalWallHeatFluxTemperature* is a wall boundary condition for temperature in OpenFOAM that imposes an external heat flux or heat transfer coefficient and external temperature, computing the wall temperature accordingly.

When given a fixed heat flux  $q$  (W/m<sup>2</sup>), the BC enforces:

$$-q = -k \frac{\partial T}{\partial n} \quad (53)$$

The BC imposes:

$$\frac{\partial T}{\partial n} = \frac{q_{fixed}}{k} \quad (54)$$

The BC sets the temperature gradient based on your input heat flux, and the solver then calculates the resulting wall temperature.

### 2.3. Experiments used for validation

Several experimental data were selected to validate the model. One of them is the experiments of Renfer et al. (2011, 2013), which investigated both heated and unheated microchannels.

The microchannel configuration has both an inline and a staggered pin fin arrangement. The microchannels were made from silicon using deep reactive ion etching (DRIE). The chip heat transfer area was a square  $10 \times 10 \text{ mm}^2$  with a channel height of  $200 \text{ }\mu\text{m}$ . To achieve uniform heat flux, rectangular  $300 \text{ nm}$ -thick NiCr 80/20 metal layers were deposited on the back side to form a resistive thin-film heater. Both sides were heated unless  $\mu\text{LIF}$  measurements were taken, in which case one side was heated. A heat flux of  $720 \text{ kW/m}^2$  was used for the experiments.

The flow was driven by a rotary pump in order to reduce pulsations that can cause flow disruption and premature transients. When the flow exceeded  $50 \text{ ml/min}$ , the variation in velocity and flow rate was less than 2%. The flow rate was measured using a laminar pressure-gradient flow sensor with a scale accuracy of 2%. A differential pressure gauge with a range of 0-2.0 bar and an accuracy of 0.2% was used to measure the pressure difference between the measurement points. A  $\mu\text{PIV}$  system, consisting of an epi-fluorescence microscope, was used for flow visualisation. All measurements were performed at room temperature using deionised water as the working fluid, with a small amount of sodium hydroxide added to adjust the pH and reduce the accumulation of anionic particles (seeded fluorescent particles) on the barriers and walls.

The second experiment was done by Kosar et al. (2011). The microchannel was made using the DRIE process. The microchannel is  $1.5 \text{ mm}$  wide,  $10 \text{ mm}$  long, and  $243 \text{ }\mu\text{m}$  high. There are 40 rows of cylindrical pins in the longitudinal direction and alternating 5 or 6 columns in the transverse direction. The cylindrical pin diameter is  $100 \text{ }\mu\text{m}$ , and the longitudinal and transverse pitches are  $250 \text{ }\mu\text{m}$ . The experiments are conducted at room temperature ( $22 \text{ }^\circ\text{C}$ ) with deionised water and have no heat supply, thus maintaining adiabatic conditions.

The selected  $Re$  ranges were based on experimental data, and it would be inappropriate to extrapolate them significantly beyond the measured values. This explains why some results start at  $Re = 200$ , while others begin at  $Re = 30$ ; each range corresponds to the conditions under which reliable experimental measurements were obtained.

#### 2.3.1. Experiment uncertainties

Reliable interpretation of experimental data relies on a comprehensive analysis of measurement uncertainties. Differential pressure measurements across the test section were obtained using a sensor with  $\pm 2 \text{ mbar}$  accuracy, resulting in a maximum

uncertainty of 1.7% at low  $Re$ ; at high  $Re$ , the uncertainty was lower. The volumetric flow rate was controlled and measured using a high-precision laminar flow element with an uncertainty of  $\pm 10$  mL/min. Therefore, it resulted in up to 13% uncertainty.

Temperature data were acquired using multiple techniques, each contributing a specific measurement uncertainty given in Table 8.

**Table 8.** Uncertainties of measurements

Measurement Method	Uncertainty
RTDs (wall surface)	$\pm 0.2$ K
T-type Thermocouples (inlet/outlet)	$\pm 0.1$ K
Infrared Thermography	$\pm 0.2$ K
Microscale LIF ( $\mu$ LIF)	$\pm 2.3$ K (RMS error)

The uncertainty in the  $h$ , and consequently the  $Nu$ , was estimated using the standard method of uncertainty propagation:

$$\sigma_{ht} = \sqrt{\left(\frac{\partial ht}{\partial Q_{eff}}\right)^2 \sigma_{Q_{eff}}^2 + \left(\frac{\partial ht}{\partial T_{RTD}}\right)^2 \sigma_{T_{RTD}}^2 + \left(\frac{\partial ht}{\partial T_{in}}\right)^2 \sigma_{in}^2 + \left(\frac{\partial ht}{\partial T_{out}}\right)^2 \sigma_{out}^2} \quad (55)$$

The partial derivatives were computed based on a rearranged form of the energy balance equation, and the implicit function theorem was applied to obtain the sensitivities with respect to each variable.

At the lowest  $Re$  tested, the maximum relative uncertainty in the Nusselt number was 6.9%, whereas at the highest  $Re$ , it decreased to 2.3%, due to improved signal-to-noise ratio and stabilised flow behaviour.

During the experiments, the fluid temperature was maintained between 20°C and 25°C, but the exact temperature at each test point was not recorded. As a result, the kinematic viscosity  $\nu$ , which is temperature-dependent, could not be determined with complete precision. This temperature variation introduced an additional source of uncertainty in estimating  $\nu$ , since viscosity can vary significantly over this temperature range. Consequently, a conservative relative uncertainty of  $\pm 11\%$  was assigned to the kinematic viscosity in the uncertainty analysis to account for this variability.

To ensure a reliable interpretation of the experimental data, a combined uncertainty analysis was conducted for key fluid dynamic and thermal parameters. The following relative uncertainties were identified for the relevant input quantities:

- Volumetric flow rate:  $\pm 13\%$
- Kinematic viscosity:  $\pm 11\%$
- Pressure drop:  $\pm 1.7\%$

These values were used to compute the propagated uncertainty for parameters such as the Reynolds number. Assuming the uncertainties in  $Q$  (arise from measurement equipment) and  $v$  (from not giving details in the article) are independent, the combined relative uncertainty in the  $Re$  is given by:

$$\left(\frac{r_{Re}}{Re}\right) = \sqrt{\left(\frac{r_Q}{Q}\right)^2 + \left(\frac{r_v}{v}\right)^2} = \sqrt{(13\%)^2 + (11\%)^2} = 17\% \quad (56)$$

This propagated  $\pm 17\%$  uncertainty in  $Re$  significantly influences the interpretation of flow regime classification, particularly in transitional flow conditions, where slight variations in  $Re$  can result in different flow behaviour.

Also, Renfer et al. (Renfer et al., 2011) reported geometric tolerances in pin diameter of  $\pm 5 \mu\text{m}$  and in pin pitch of  $\pm 10 \mu\text{m}$  for pins nominally  $100 \mu\text{m}$  in diameter and  $200 \mu\text{m}$  in pitch, corresponding to a potential  $\pm 5\text{--}10\%$  variation in key flow-defining dimensions.

## 2.4. Geometry

The microchannel geometric configuration is based on the experiments performed by Renfer et al. (2011, 2013) and Kosar et al. (2011). The first one has a height of  $200 \mu\text{m}$ , a width of  $10 \text{ mm}$ , and a length of  $10 \text{ mm}$ . The diameter of the cylindrical pin is  $100 \mu\text{m}$ , while the pitch is  $200 \mu\text{m}$ . They are arranged in both an inline and staggered manner. There were 50 pin fins in the longitudinal and transverse directions, for a total of 2500 pin fins. The  $Re$  ranged from 178 to 735.

On the other hand, Kosar et al. (2011) used an array of  $10 \text{ mm}$  in length,  $0.243 \text{ mm}$  in height, and  $1.5 \text{ mm}$  in width. There were 40 cylindrical pin fins in the longitudinal direction and alternating 5 or 6 in the transverse direction. The pin diameter is  $100 \mu\text{m}$ , and the transverse and longitudinal pitch is  $250 \mu\text{m}$ . The  $Re$  ranged from 49 to 149.

The domains of both microchannel configurations are shown in Fig. 3. The microchannel geometric configurations studied by Renfer et al. (2011, 2013) (R-type) and Kosar et al. (2011) (K-type) share similarities in using cylindrical pin fins with a pin diameter of  $100 \mu\text{m}$  to enhance fluid mixing and heat transfer. However, they differ significantly in their  $Re$ . This contrast in flow regimes was a key factor in selecting these two configurations for analysis, allowing to investigate how changes in flow behaviour impact hydrothermal performance. Examining both designs can provide valuable insights into optimising microchannel configurations for specific applications, whether they require enhanced laminar flow characteristics or turbulent mixing for improved heat management.

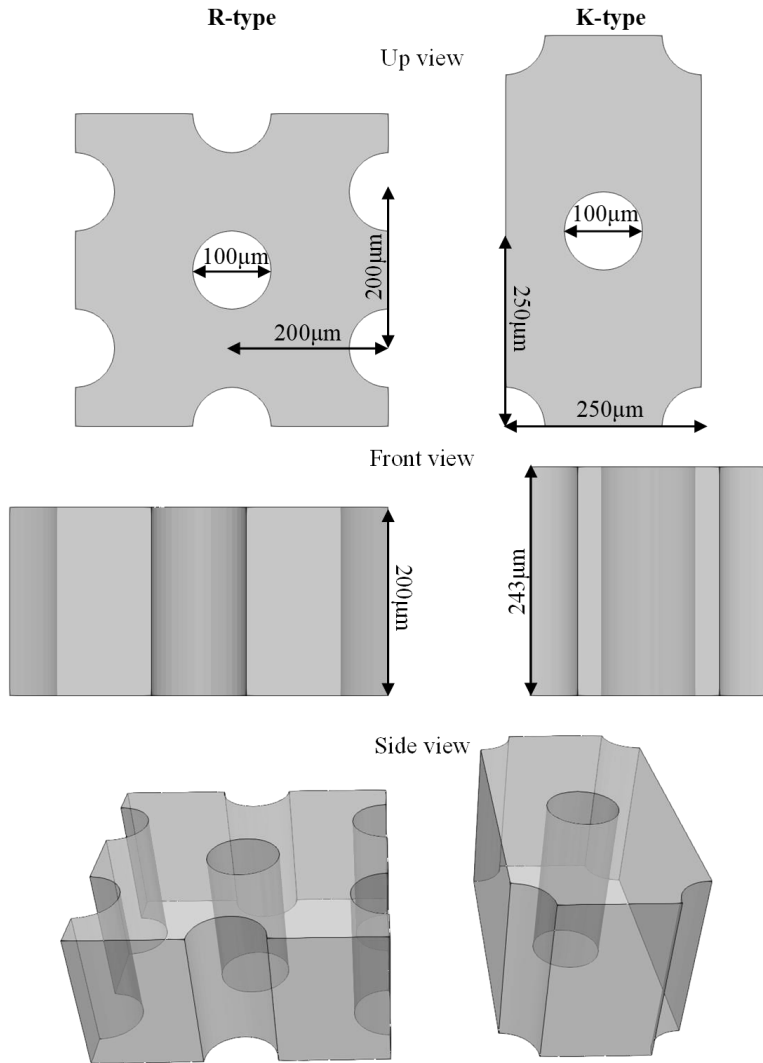


**Fig. 3.** Geometric model of microchannel pin fin array featuring R- and K-type configurations

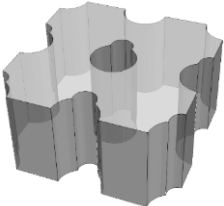
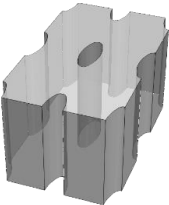
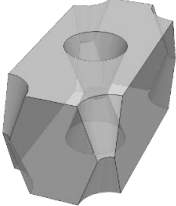
## 2.5. Geometry of investigated cases

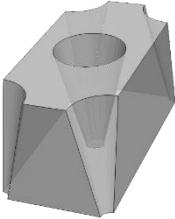
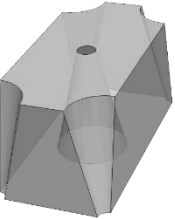
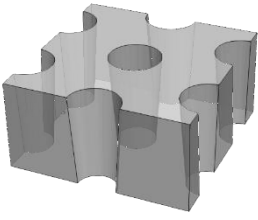
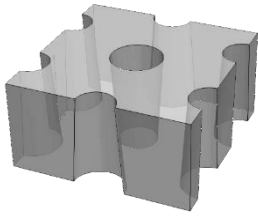
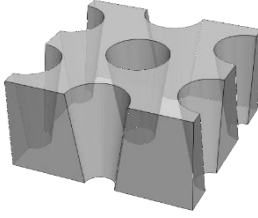
Various geometries were used in this research, with the primary ones illustrated in Fig. 3. Additional geometries are detailed in Table 9, which provides the simulation conditions. More information on  $D_h$ , heating area, pin fin area, and volume is available in Appendix 1.

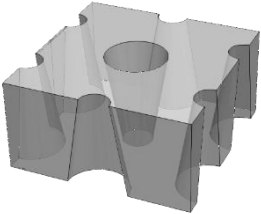
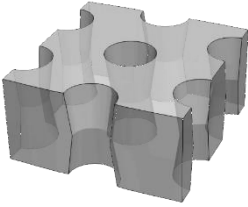
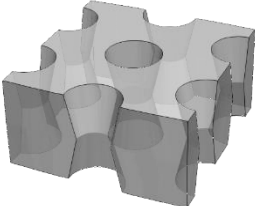
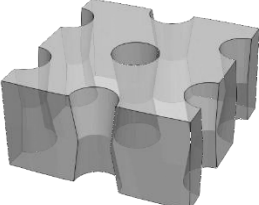
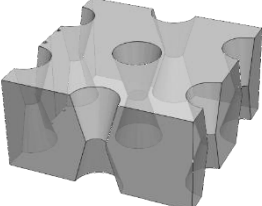
The case naming follows a structured format: the first mandatory letter denotes the source of the experimental data – Renfer et al. (R) or Kosar et al. (K). The second mandatory letter represents the pin fin shape, including cylinder (C), double-cylinder

(DC), ellipse (E), conical (T), or hourglass (H). A numerical value indicating the inclination angle in conical or hourglass configurations follows if applicable. This may be followed by “A” or “B”, indicating unidirectional (A) or bidirectional (B) conicity. Finally, the letter “P” signifies a pitch modification and a numerical value indicating the pitch variation. A total of 90 pin fin array variants were investigated, excluding the original configurations.

**Table 9.** Summary of pin fin array geometries, arrangements, and simulation conditions

Picture & name	Geometry		Conditions
	Arrangement	Pin fins	
 <p>R-DC</p>	<p>Inline  <math>P = 200 \mu\text{m}</math>  <math>H = 200 \mu\text{m}</math></p>	<p>Double-cylinder  <math>D_1 = 100 \mu\text{m}</math>  <math>D_2 = 50 \mu\text{m}</math></p>	<p><math>u_{in} = 1.25 - 2.25 \text{ m/s}</math>            Fluid – water            (16°C)            k-<math>\omega</math> SST            Adiabatic</p>
 <p>R-E-P60</p>  <p>R-E-P120</p> <p>R-E(Pitch)</p>	<p>Inline  <math>P_{lon} = 200 \mu\text{m}</math>  <math>P_{tr} = 50 - 140 \mu\text{m}</math></p>	<p>Ellipses  <math>D_x = 100 \mu\text{m}</math>  <math>D_y = 40 \mu\text{m}</math></p>	<p><math>u_{in} = 0.165 - 1.584 \text{ m/s}</math>            Fluid – water            (16°C)            k-<math>\omega</math> SST            Adiabatic</p>
	<p>Staggered  <math>P = 250 \mu\text{m}</math>  <math>H = 243 \mu\text{m}</math></p>	<p><math>D_w = 140 \mu\text{m}</math>  <math>D_{mid} = 53.6 \mu\text{m}</math>  <math>\Theta = 19.573^\circ</math></p>	<p><math>Re = 85 - 117</math>            Fluid – water            (22°C)            k-<math>\omega</math> SST            Adiabatic</p>

K-H19			
 <p data-bbox="235 433 409 460">K-T14-A-P250</p> <p data-bbox="194 493 437 520">K-T(angle)-A-P(pitch)</p>	<p data-bbox="538 462 714 551">Staggered  <math>P = 200\text{-}300\ \mu\text{m}</math>  <math>H = 243\ \mu\text{m}</math></p>	<p data-bbox="776 371 953 433"><math>D_1 = 41.8 - 91.6\ \mu\text{m}</math></p> <p data-bbox="795 462 933 524"><math>D_2 = 108.4 - 158.2\ \mu\text{m}</math></p> <p data-bbox="802 553 927 642">Depends on angle <math>2^\circ - 13.48^\circ</math></p>	<p data-bbox="989 433 1139 578"><math>Re = 40 - 117</math>  Fluid – water  (22°C)  k-<math>\omega</math> SST  Adiabatic</p>
 <p data-bbox="235 755 409 782">K-T14-B-P250</p> <p data-bbox="194 815 437 842">K-T(angle)-B-P(pitch)</p>			
 <p data-bbox="274 1079 351 1106">R-T4-A</p>	<p data-bbox="564 1190 689 1279">Staggered  <math>P = 200\ \mu\text{m}</math>  <math>H = 200\ \mu\text{m}</math></p>	<p data-bbox="795 1062 933 1152"><math>D_1 = 86\ \mu\text{m}</math>  <math>D_2 = 114\ \mu\text{m}</math>  <math>\Theta = 4.004^\circ</math></p>	<p data-bbox="989 1146 1139 1292"><math>Re = 200 - 800</math>  Fluid – water  (<math>T_{in} = 20^\circ\text{C}</math>)  k-<math>\omega</math> SST</p>
 <p data-bbox="274 1341 351 1368">R-T4-B</p>			
 <p data-bbox="274 1601 351 1628">R-T8-A</p>		<p data-bbox="795 1452 933 1541"><math>D_1 = 66\ \mu\text{m}</math>  <math>D_2 = 134\ \mu\text{m}</math>  <math>\Theta = 9.648^\circ</math></p>	

 <p>R-T8-B</p>			
 <p>R-H8</p>		$D_1 = 86 \mu\text{m}$ $D_2 = 114 \mu\text{m}$ $\Theta = 7.97^\circ$	
 <p>R-H13</p>		$D_1 = 76 \mu\text{m}$ $D_2 = 122 \mu\text{m}$ $\Theta = 12.953^\circ$	
 <p>R-H9</p>		$D_1 = 70 \mu\text{m}$ $D_2 = 100 \mu\text{m}$ $\Theta = 8.531^\circ$	
 <p>R-H16</p>		$D_1 = 42 \mu\text{m}$ $D_2 = 100 \mu\text{m}$ $\Theta = 16.172^\circ$	

### 3. MODEL VALIDATION

To begin the CFD validation process, an entire channel simulation using the RANS and URANS approaches with the *simpleFoam* and *pimpleFoam* solvers was conducted. This setup is designed to replicate the experimental geometry and flow conditions as closely as possible, serving as a baseline case. By modelling the entire pin fin array, including inlet and outlet regions, this simulation can capture all relevant flow phenomena such as developing flow. The resulting data will be used to establish a reference solution that accounts for the effects of real geometric and boundary-condition features observed in the experiment.

Following the entire channel simulation, a reduced-domain model will be developed using a periodic part and a cyclic domain of a pin fin array. The objective here is to reduce the computational cost while retaining significant accuracy. This smaller domain will also use the URANS approach with *pimpleFoam*, and results such as pressure drop and/or velocity will be directly compared with the results from the entire channel. A good match between the two would justify using the smaller domain in subsequent thermal and parametric studies.

Next, thermal effects will be introduced into the validated reduced domain by switching to the *buoyantFoam* solver. This solver will allow the modelling of heat transfer through a pin fin array. It is critical to ensure that boundary conditions, such as heat flux, wall temperatures, and mass flow rates, are consistent with the previous simulations and experimental setup. The results will then be compared with experimental data to assess the accuracy of the thermal modelling.

If the cyclic domain model shows strong agreement with both the entire channel simulation and experimental data, a mesh convergence study will be performed using the simplified domain. This study involves running simulations with successively refined meshes and examining the stability of key results such as Nusselt number and pressure loss. The goal is to identify a mesh that offers a good balance between accuracy and computational efficiency.

Finally, quantitative metrics such as RME and percentage deviation will be used to assess the differences between CFD results and experimental data. These statistical tools will help quantify the level of agreement and provide objective evidence of the simulation's reliability for both flow and thermal parameters.

#### 3.1. Uncertainty analysis

In this study, an uncertainty analysis is conducted to systematically assess the influence of modelling assumptions and simplifications on the accuracy of CFD simulations. First, geometrical simplification is achieved by reducing the computational domain from the entire channel to a periodic segment and then to a cyclic domain to validate the applicability of cyclic boundary conditions. Also, the

impact of turbulence and flow modelling choices is examined through a comparison of RANS and URANS approaches, as well as compressible and incompressible formulations. Subsequently, input uncertainties are examined, focusing on variations in initial temperature and viscosity to evaluate their influence on the pressure drop. Finally, a simplification of conjugate heat transfer is applied by neglecting solid regions and modelling only the fluid domain, thereby reducing computational cost while maintaining physical relevance.

### 3.1.1. Geometrical simplification

The physical model of the microchannel was first simplified to a periodic segment and then to a cyclic domain to reduce computational costs. This reduction in domain size allows the use of more advanced turbulence models, such as URANS instead of RANS.

For both the entire channel and periodic part cases, the pressure drop was prescribed as a boundary condition. In the cyclic domain, however, cyclic (for incompressible) or mapped (for compressible) boundary conditions were applied, where the velocity  $u$  was specified as the initial condition (boundary conditions for each geometry are prescribed in Table 7). The applied geometries are presented in Fig. 4.

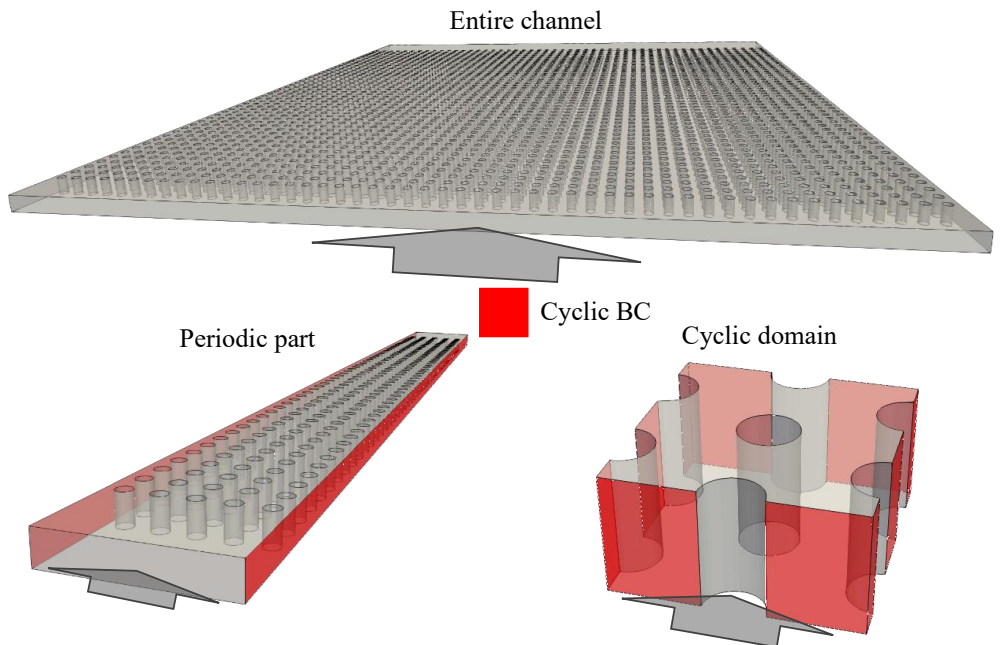


**Fig. 4.** Mesh domain decomposition for CFD simulations: from entire channel to cyclic domain

The pressure–velocity coupling is primarily managed using the SIMPLE and PIMPLE algorithms, depending on the simulation type. For transient simulations, the PIMPLE scheme is employed with multiple correctors and non-orthogonal corrections to improve stability. Pressure correction relies on the GAMG solver, complemented by different smoothers, such as Gauss-Seidel or DIC, to ensure robust convergence. Velocity, turbulence, and other scalar transport equations are solved using smoothSolver with symmetric Gauss-Seidel smoothing. In contrast, for compressible cases, additional solvers, such as PBiCGStab with DILU, are used to enhance robustness.

The numerical setup uses Euler or steady-state time discretisation, with Gauss linear for gradients and Gauss linear corrected for Laplacians. Divergence terms apply to second-order upwind-biased schemes. Interpolation is linear with corrected surface-normal gradients.

The relationship between the inlet velocity and the pressure drop is shown in Fig. 5. The graph also includes an error margin of 10% based on experimental measurements. In addition to the choice of computational domain, different modelling strategies were compared: RANS versus URANS and compressible versus incompressible formulations. The results indicate that fluid compressibility has a negligible effect on the predictions. Because the emphasis here is on geometry comparison rather than validation, the complete modelling validation is provided in Sections 3.3 and 3.4.

A comparison of the  $u_{in}$  across the entire channel with the periodic segment shows deviations of 12.8% for the incompressible case and 11.6% for the compressible case. In comparison, the difference in  $u_{in}$  between the entire channel and cyclic domain models is relatively small – 4.67%. The most significant deviation occurs when the flow transitions from steady to unsteady behaviour. Interestingly, flow regime transitions occur earlier in the cyclic domain, as the flow there quickly reaches a developed state. This highlights the advantage of cyclic boundary conditions in promoting faster establishment of flow characteristics compared to conventional boundary setups.

The study confirms that cyclic boundary conditions effectively reproduce the microchannel’s pressure distribution and flow characteristics while reducing computational costs and maintaining high accuracy. The only notable difference between the models is the variation in the flow when it becomes unstable. Cyclic boundary conditions do not account for inlet and outlet effects, which can cause the transition to unsteady flow to occur earlier compared to the entire channel simulations.

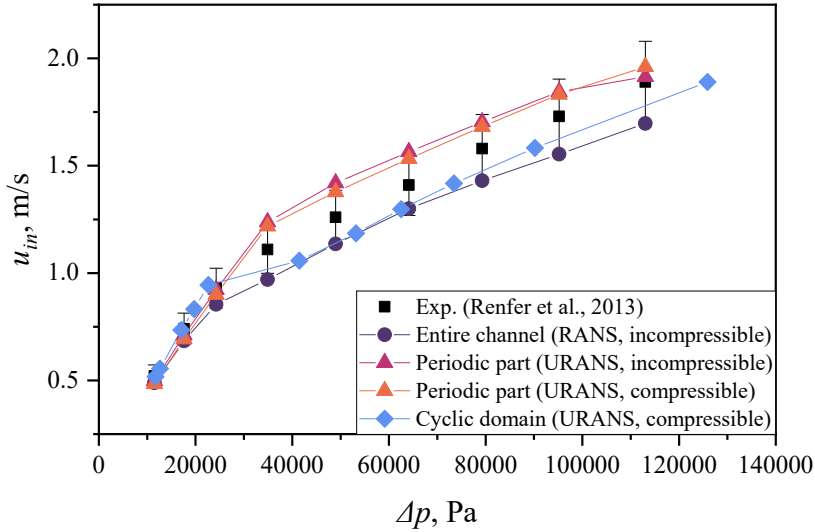


**Fig. 5** Numerical results of  $\Delta p$  versus  $u_{in}$  for entire channel, periodic part and cyclic domain

### 3.1.2. Input uncertainties

As previously mentioned, the kinematic viscosity may vary by up to 11% and the temperature by up to 20% due to experimental uncertainty, since the exact temperature was not recorded during the experiments.

Therefore, the uncertainty in operating conditions (initial temperature and viscosity) was investigated. To address this, the impact of uncertainty in operating conditions, specifically the initial temperature and viscosity, on pressure drop was investigated. The analysis was performed using the cyclic domain for both compressible and incompressible cases, under steady and unsteady flow regimes. The results, presented in Fig. 6. The difference between higher and lower initial temperatures (20 °C and 25 °C) results in a variation of 19.7–26.1% in the  $\Delta p$  values.

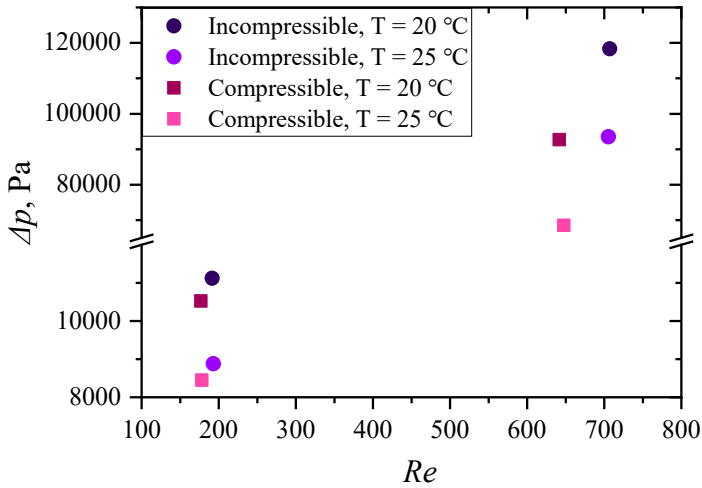


**Fig. 6** Model compressibility and the influence of initial temperature on the results

### 3.1.3. Conjugate heat transfer simplification

In computational heat transfer studies, particularly those involving microchannels and finned structures, the representation of the solid region often increases computational demand. While the inclusion of conjugate heat transfer ensures a complete description of both conduction in the solid and convection in the fluid, this approach may not always be necessary. For highly conductive materials, internal temperature gradients within the solid remain small relative to those in the working fluid, suggesting that the solid can sometimes be excluded from the computational domain without compromising predictive accuracy in the quantities of primary interest.

The present work investigates the implications of omitting the solid domain in the numerical modelling of a silicon-based microchannel pin fin array. A comparative analysis was performed between simulations incorporating the solid region and those limited to the fluid domain. The comparison focuses on parameters central to thermal–hydraulic performance, including  $\Delta p$ ,  $Nu$ ,  $T_w$ ,  $T_{mid}$ ,  $A_\Omega$ , which were compared between cases with and without a solid region. The *MRE* is 5.3% for  $\Delta p$ , 3.6% for  $A_\Omega$ , 14.1% for  $Nu$ , and less than 0.5% for  $T_w$  and  $T_{mid}$ . The most significant deviation was observed in the transition region, where the absence of the solid region caused a delay in the transition and sharper variations in the flow properties. This resulted in a higher *MRE* when the transition-induced changes in the  $Re$  range were taken into account. For example, excluding  $Re = 346$  and  $422$  from the comparison would reduce the *MRE* of  $Nu$  to approximately 7%.

In unsteady flow, the deviations are relatively minimal, indicating that the impact of excluding the solid region becomes negligible in the area of primary interest. Therefore, this simplification provides a practical trade-off: it allows significant savings in computational resources while maintaining accuracy where it matters most – in the unsteady regime, where the study’s main insights are focused. The comparison of pressure and heat transfer characteristics confirms that the reduced-area calculations are consistent and reasonable.

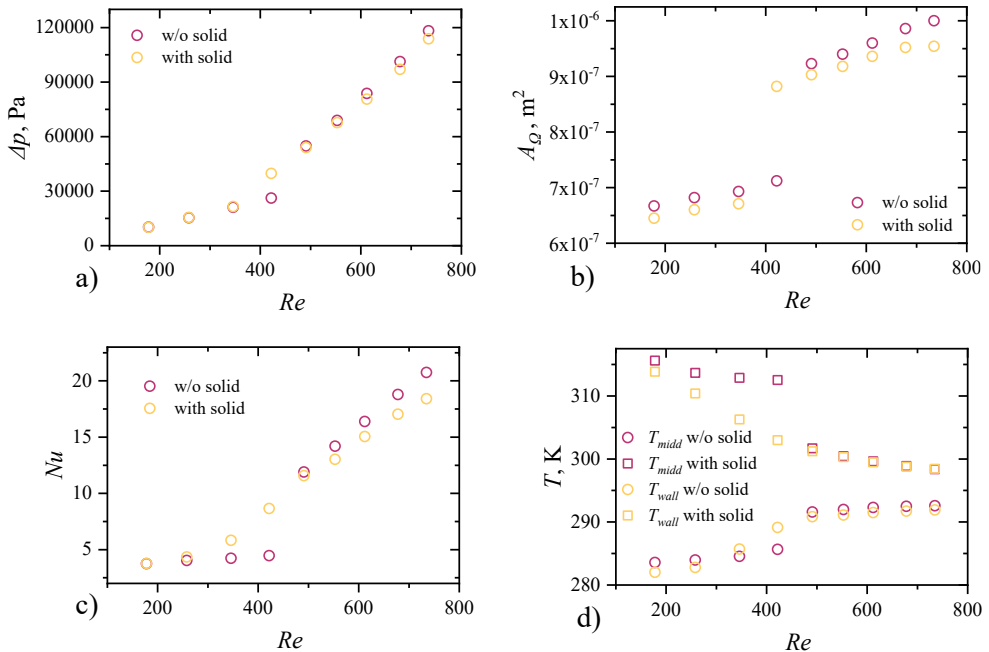


**Fig. 7.** a) Pressure drop b) area of vortical structures c) Nusselt number d) temperatures at various  $Re$ , comparing simulations with and w/o the solid part

### 3.2. Mesh quality assessment

The mesh quality was evaluated using a combination of mesh convergence and grid convergence index (GCI). The mesh convergence technique involved systematic mesh refinement and observation of changes in the simulation results to ensure that the solution stabilised as the mesh density increased. This process helped identify the minimum mesh resolution required to achieve reliable results without unnecessary computational expense.

At the same time, the GCI was employed to quantify the uncertainty associated with the numerical solution. GCI provides a systematic method for assessing how variations in mesh density affect the results, enabling a more accurate evaluation of mesh quality (Roache, 1997). By calculating GCI values for different mesh

configurations, we could determine the level of confidence in the simulation results and ensure that they were within acceptable limits. Together, these methods provided a robust framework for assessing mesh quality, leading to more accurate and reliable simulation results.

A cyclic domain without a solid part was selected to analyse mesh convergence and GCI calculation. Five mesh configurations were compared: Mesh 1 with 44,032 elements, Mesh 2 with 72,160 elements, Mesh 3 with 118,272 elements, Mesh 4 with 198,016 elements, and Mesh 5 with 396,032 elements (see Fig. 8), evaluated at both the lowest and highest  $Re$  investigated.

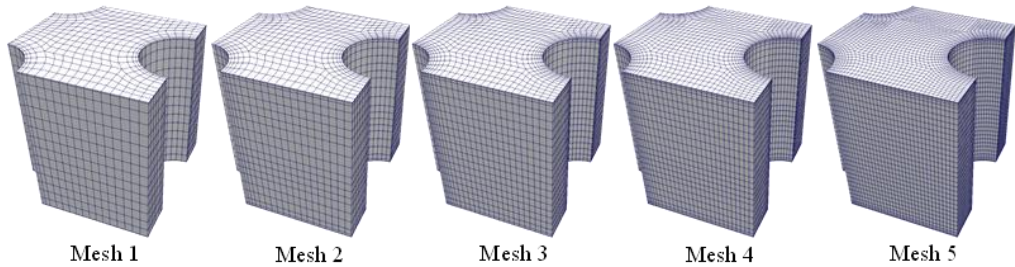


**Fig. 8.** Mesh comparison across identical domain

It is preferred that  $r$  be greater than 1.3 (Roache, 1997). In all cases, the wall distance parameter  $y^+$  was maintained below 1 to ensure proper boundary layer resolution. Table 10 presents results of both the maximum  $y^+$  (ensuring it does not exceed 1) along with the first cell thickness.

**Table 10.** Maximum  $y^+$  value and cell first thickness for different meshes

	Maximum $y^+$		Thickness of the first cell	
	Pin fin	Upper/lower wall	From pin fin	From upper/lower wall
Mesh 1	8.19E-03	1.58E-03	1.72E-06	7.79E-07
Mesh 2	2.20E-03	1.79E-03	1.26E-06	9.40E-07
Mesh 3	3.71E-03	2.51E-03	1.42E-06	1.23E-06
Mesh 4	1.34E-02	2.04E-03	2.69E-06	1.23E-06
Mesh 5	9.02E-03	4.22E-03	2.48E-06	1.62E-06

The results for  $\Delta p$ ,  $Nu$  and  $A_Q$  are presented in Fig. 9. At low  $Re$ , the pressure differences among the meshes were approximately 1%. At high  $Re$ , no significant difference was observed between Meshes 4 and 5; however, there were 7% differences between Meshes 3 and 4, 4% between Meshes 3 and 2, and 7% between Meshes 2 and 1.

At low  $Re$ ,  $Nu$  showed differences of about 2% between Meshes 2-5 and an 8% difference between Meshes 1 and 2. At high  $Re$ ,  $Nu$  variations can reach up to 22%,

with the smallest difference of 8% between Meshes 4 and 5. Similarly, the differences in  $A_Q$  were uniform across  $Re$ , with the least variation of approximately 3% between Meshes 4 and 5.

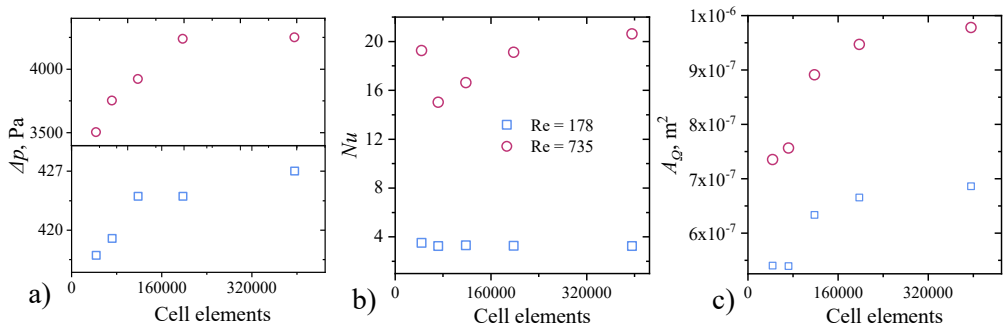


**Fig. 9.** Effect of mesh fineness on a)  $\Delta p$ , b)  $Nu$  and c)  $A_Q$  for Reynolds numbers of 178 and 735

The GCI method was applied to Meshes 3, 4, and 5 at  $Re$  of 735 to assess the validity of the mesh for calculations (see Table 11). The approximate errors between Meshes 5 and 4 were 0.26% for  $\Delta p$ , 7.3% for  $Nu$ , and 3.17% for  $A_Q$ . In comparison, Meshes 4 and 3 errors were 7.5% for  $\Delta p$ , 13% for  $Nu$ , and 6% for the  $A_Q$ . The external errors for Meshes 4 and 5 were recorded as 0.62%, 3.68%, and 1.92% for  $\Delta p$ ,  $Nu$ , and  $A_Q$ , respectively, while the errors between Meshes 3 and 4 were significantly higher at 20.31%, 9.68%, and 5.36%.

The GCI results indicate that the grid convergence between Meshes 5 and 4 is quite satisfactory, with minimal errors (GCI values of 0.78% for  $\Delta p$ , 4.77% for  $Nu$ , and 2.45% for  $A_Q$ ). However, the transition from Mesh 4 to Mesh 3 shows at least a three times greater error (GCI values of 31.85% for  $\Delta p$ , 13.4% for  $Nu$ , and 7.08% for  $A_Q$ ), suggesting that the resolution of Mesh 3 may be inadequate or that numerical errors related to the grid resolution may be affecting the results.

**Table 11.** GCI analysis for  $\Delta p$ ,  $Nu$ , and  $A_Q$  using three successive meshes

	$\Delta p$	$Nu$	$A_Q$
<i>Mesh 5-3</i>	396032, 198016, 118272		
$r_{21}$	2		
$r_{32}$	1.674		
$\varphi_1, \varphi_2, \varphi_3$	4 250, 4 239, 3 922	20.6, 19.11, 16.63	21.53, 21.32, 19.64
$\xi$	0.499	1.543	1.387
$\varphi_{ext}^{21}$	4276.60	21.41	$10^{-6}$
$\varepsilon_a^{21}$	0.26%	7.31%	3.17%
$\varepsilon_{ext}^{21}$	0.62%	3.68%	1.92%
$GCI^{21}$	0.78%	4.77%	2.45%
$\varphi_{ext}^{32}$	5319.07	21.16	$10^{-6}$
$\varepsilon_a^{32}$	7.48%	13.02%	5.91%

$\varepsilon_{ext}^{32}$	20.31%	9.68%	5.36%
$GCI^{\beta 2}$	31.85%	13.40%	7.08%

The results from Mesh 4 demonstrate good convergence with low GCI and error values, indicating that further refinement is unlikely to improve simulation accuracy significantly. Therefore, it is concluded that the medium mesh with approximately 198016 elements is sufficient for an accurate analysis of the problem under consideration. Consequently, this mesh will serve as a basis for further analyses involving other configurations, such as cyclic domains with solid components or various pin fin shapes.

### 3.3. Hydraulics validation

To maintain consistency with the experimental conditions, a specified  $\Delta p$  was applied between the inlet and outlet boundaries in the CFD simulations, rather than prescribing a  $u_{in}$  directly. However, in the cyclic domain, the initial boundary condition was prescribed in terms of  $u_{in}$ . Because the inlet area in the cyclic domain is different from that in the entire channel,  $u_{in}$  was recalculated to the original channel  $u_{in}$ .

The  $u_{in}$  of the entire channel was extracted from the simulations and compared directly to the corresponding values reported in the experimental data. This comparison ensured that the simulated flow rate matched the experimental flow behaviour at the same pressure drop, thereby providing a solid basis for validating both the entire channel and reduced-domain models. Otherwise, for the cyclic domain,  $\Delta p$  was compared to experimental data, since  $u_{in}$  was given.

The results of the modelling and experiment are given in Fig. 10. A  $\pm 10\%$  error range around the experimental data is shown. The simulations using the entire channel align well with the experimental trend ( $MRE_{u_{inlet}} = 10\%$ ). While the cyclic domain has  $MRE_{\Delta p}$  of 12%. Both numerical data overestimate either  $u_{in}$  or  $\Delta p$ . Nevertheless, the overall agreement with the experiment confirms the validity of the results.

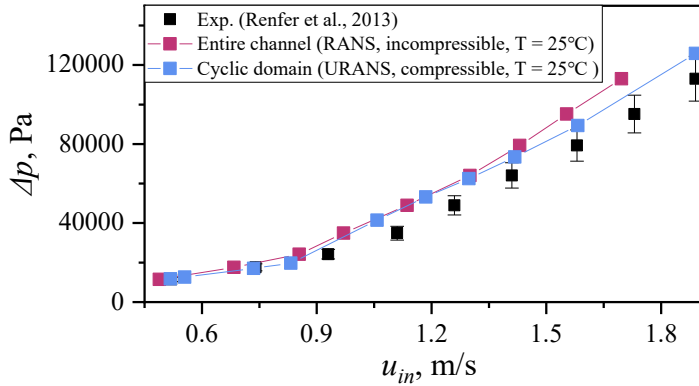


**Fig. 10.**  $\Delta p$  Versus  $u_{in}$  against experimental data of Renfer et al. (2013)

Further validation of  $\Delta p$  was conducted using the experimental results from Kosar et al. (2011). A comparison of the entire channel and cyclic domain with the experimental data is shown in Fig. 11. In this case, a predominantly steady regime was observed, consistent with the experiment. The  $MRE_{\Delta p}$  between the numerical results of the entire channel and the experiment is 7 %, while for the cyclic domain it is 12 %. The cyclic domain shows an underestimation. This underestimation is likely due to the use of a periodicity in the simulation, which does not consider the inlet’s effects. Since the inlet region plays an important role in the overall  $\Delta p$ , excluding it from the cyclic domain leads to lower predicted values than the experimental results. Nevertheless, the overall agreement with the experiment confirms the validity of the results.

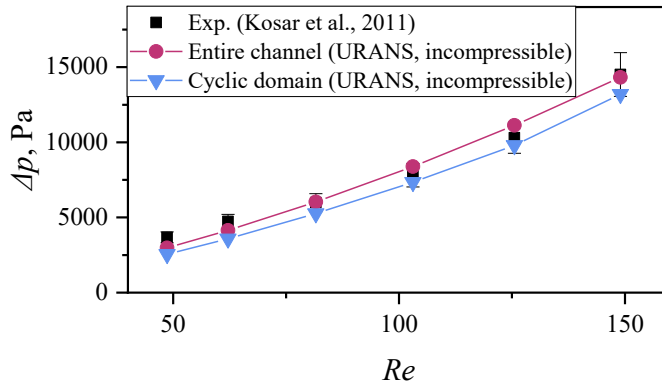


**Fig. 11.** Comparison of  $\Delta p$  results from the entire channel and cyclic domain with experimental data reported by Kosar et al. (2011)

### 3.4. Heat transfer validation

Another important aspect of model validation is heat transfer, specifically  $Nu$ . The results for the cyclic domain w/o solid were compared with the experimental results of Renfer et al. (2011, 2013) in Fig. 12. In the steady flow regime,  $Nu$  remains relatively constant, with no significant increase. However, a sharp jump in  $Nu$  occurs after reaching  $Re$  of approximately 491, indicating the onset of flow transition.

The overall MRE for the  $Nu$  is 10%, with a significantly lower MRE of 3% after the transition point (after  $Re = 491$ ). The delay can be attributed to the use of cyclic boundary conditions in the model. Since the cyclic conditions do not account for inlet and outlet effects, the transition is delayed compared to the experimental results when these boundary conditions are naturally present. Despite this delay, the results show good agreement with the experimental data, especially after the transition, confirming the model's validity for heat transfer predictions.

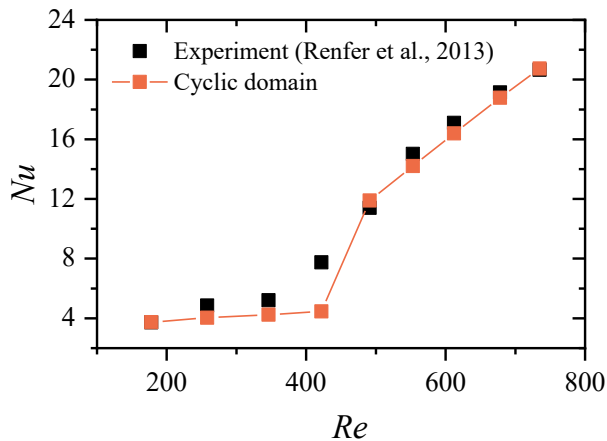


**Fig. 12.** Comparison of modelling results of  $Nu$  from the cyclic domain with experimental data reported by Renfer et al. (2013)

### 3.5. Pearson correlation coefficients

Additionally, to assess how well the model reproduces the experimental results, the Pearson correlation coefficient ( $r_p$ ) was calculated. The Pearson correlation coefficient is a statistical measure of the strength and direction of the linear relationship between two variables. In the context of CFD validation, it quantifies how closely the numerical predictions follow the experimental data. While error metrics such as MAE or RMSE provide information about the magnitude of deviations, the Pearson coefficient directly addresses whether the CFD model reproduces the trend of the experimental measurements. A value of  $r$  close to +1 indicates that as the

experimental variable increases (e.g., inlet velocity with pressure), the model output increases in nearly the same proportion, which is crucial in confirming that the model captures the correct physics of the problem. The initial/calculation data is presented in Table 12 and Table 13.

**Table 12.** Experimental and numerical pressure drop and inlet velocity data for the entire channel

$\Delta p$ , Pa	$u_{exp}$ , m/s	$u_{mod}$ , m/s
11495	0.52	0.488939
17608	0.74	0.683444
24252.5	0.93	0.854296
34883.7	1.11	0.970066
48970.1	1.26	1.13604
64119.6	1.41	1.30024
79269.1	1.58	1.43032
95215.9	1.73	1.55339
113023	1.89	1.69641

**Table 13.** Experimental and numerical pressure drop and inlet velocity data for cyclic domain

$u_{in}$ , m/s	$\Delta p_{exp}$ , Pa	$\Delta p_{mod}$ , Pa
0.52	11495	11786.67
0.74	17608	17288.44
0.93	24252.5	29135.83
1.11	34883.7	46292.65
1.26	48970.1	59408.33
1.41	64119.6	72767.19
1.58	79269.1	89109.09
1.73	95215.9	106870.1
1.89	113023	125875

Formula for  $r_p$ :

$$r_p = \frac{\sum_{i=1}^n (u_{exp(i)} - \bar{u}_{exp})(u_{mod(i)} - \bar{u}_{mod})}{\sqrt{\sum_{i=1}^n (u_{exp(i)} - \bar{u}_{exp})^2} \sqrt{\sum_{i=1}^n (u_{mod(i)} - \bar{u}_{mod})^2}} \quad (57)$$

For the present case, the correlation between experimental  $u_{in}$  and the CFD-predicted values for the entire channel was calculated using nine paired data points across a wide pressure range. The result was  $r_p = 0.999$ . Similarly, the correlation between experimental  $\Delta p$  and modelling for the cyclic domain yielded the same value,

0.999. These values are extremely close to unity, indicating near-perfect linear agreement between CFD predictions and experimental measurements. This suggests that the governing flow physics are well captured.

## 4. RESULTS

The results section is structured into two primary categories: hydraulic performance, covering analyses of the 4.1. Friction factor and 4.2.  $\Omega$  criteria investigation and 4.3.  $TKE$ ,  $KE$  and  $\Omega$  relationship, while 4.4. Heat transfer focuses on heat transfer characteristics. These two aspects are integrated into a comprehensive 4.5. Overall performance and 4.6. Performance evaluation using sections.

It is important to note that not all geometries were subjected to heat transfer simulations. Some configurations were analysed solely to assess their feasibility and potential for further investigation.

Furthermore, the detailed examination was limited to specific pin fin shapes with uniform cross-sections along their height, namely the double-cylinder and elliptical types, while other shapes were not considered. This decision was based on the extensive prior research available on such geometries and the predictable, monotonic nature of the vortex structures they generate. Therefore, the main research object is pin fins with non-uniform cross-sectional profiles along their height, specifically conical and hourglass geometries. These designs were selected due to their promising ability to improve heat transfer efficiency and flow dynamics.

The results are grouped based on two geometries and their respective  $Re$  ranges. The first group follows the K-type pin fin arrays, with  $Re$  values up to 115, which are classified as low- $Re$  despite some configurations experiencing vortex shedding. The second group is based on R-type pin fin arrays, with  $Re$  ranging from 200 to 800, and is considered to fall within the high  $Re$  regime.

In all further simulations,  $Re$  was calculated considering the velocity as the inlet velocity in the cyclic domain, not in the channel:

$$Re = \frac{2u_{in_{dm}} \cdot Dh}{\nu} \quad (58)$$

Therefore,  $u_{in_{dm}}$  is scaled by a factor of two to recover the inlet velocity of the entire pin fin channel.

### 4.1. Friction factor and flow topology

#### 4.1.1. Cylinders vs double-cylinders

The results and analysis are presented in Section 4.1.1. are also presented in the publication <sup>1</sup>. In this section, the flow is treated as incompressible.

A comparative analysis of the  $f$  between the cylindrical pin fin array (R-C-I) and the double-cylinder pin fin array (R-DC-I) is presented in Fig. 13. Under steady flow conditions ( $Re = 300$ ), the  $f$  in the R-DC-I fin array was 8 % lower than that of the R-

---

<sup>1</sup> Jaseliūnaitė, J., Šeporaitis, M. Numerical Modelling of Flow Behavior in a Micro Cylinder and Double-Cylinder Pin-Fin Arrays. In: Proceedings of the 13th Asian Computational Fluids Dynamics Conference. ACFD22. DOI: 10.11159/ffhmt23.172

C-I. This reduction was attributed to the more stable flow characteristics in the R-DC-I configuration. In contrast, the higher  $Re$  in the R-C-I induced flow instabilities leads to an increased  $f$ . Even in the vortex shedding regime, the R-DC-I exhibited lower hydraulic resistance, although the  $f$  was reduced to 21% at  $Re = 541$ . On average, the R-DC-I configuration exhibits a 37% lower  $f$  compared to the R-C-I within the investigated  $Re$  range ( $300 < Re < 541$ ).

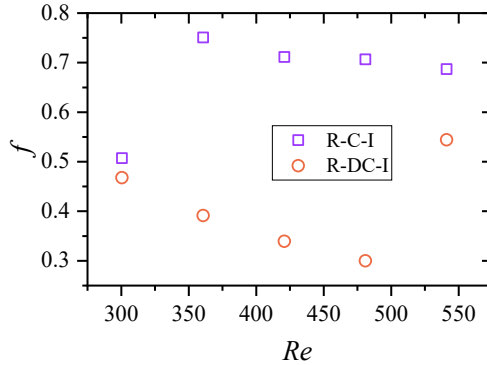


**Fig. 13.** Comparison of  $f$  between R-C-I and R-DC-I configurations.

The transition from steady to unsteady flow occurs at  $Re = 300$  for the R-C-I array, while the transition is delayed until  $Re > 500$  for the R-DC-I array. This indicates that the flow transition occurs more rapidly in the R-C-I configuration than in the R-DC-I configuration. Furthermore, while the flow remains steady, the size of stagnant vortices forming behind the obstacles is significantly smaller in the R-DC-I array (see Fig. 14). This reduction in vortex size is attributed to the decreased spacing between the pins, which limits the free space available for vortex development. Additionally, these vortices are more compressed in the R-DC-I, as they are constrained by the narrower obstacles, with the rear end of the R-DC-I fin being smaller than that of the R-C-I fin.

As the flow becomes unstable and transitions into the vortex-shedding regime, the vortices behind the fins are disrupted and integrated into the main flow. It has been observed that the vortex formed behind the R-C-I fin (see Fig. 14 Top right box) is more fully developed and takes the shape of a single, coherent vortex, as noted by Renfer et al. [73] in their experimental studies. In contrast, the R-DC-I (see Fig. 14 Bottom right box) does not allow the vortex to develop fully, causing it to collapse and dissipate rapidly.

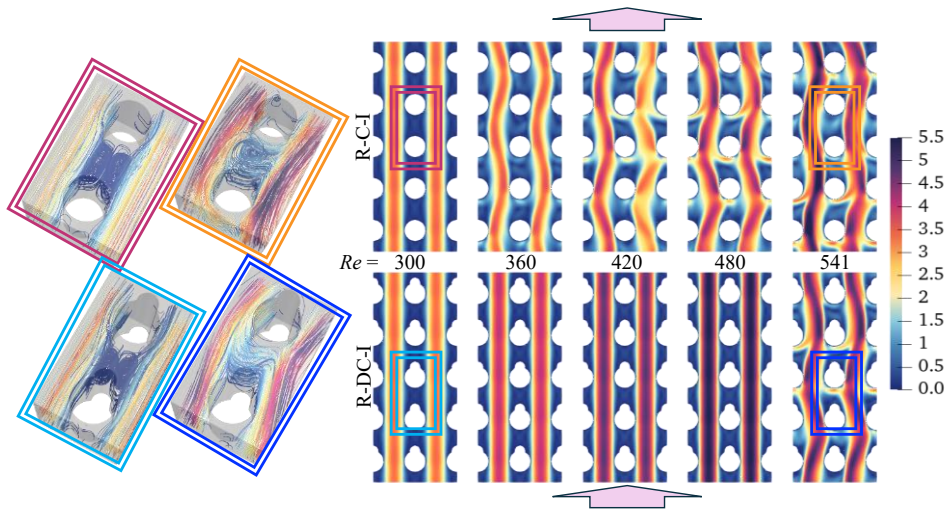


**Fig. 14.** Velocity fields and flow streamlines for R-C-I and R-DC-I at varying  $Re$

#### 4.1.2. Cylinders vs ellipses

The results and analysis are presented in Section 4.1.2. are also presented in the publication <sup>2</sup>. In this section, the flow is treated as incompressible.

Elliptical pin fin arrays with variable transverse pitch (R-E-P(X)) were compared with each other and with R-C-I in Fig. 15.  $\Delta p$  may be the lowest in the R-C-I case in the steady regime when the  $u_{in}$  is the same in all cases. However, the  $f$  plots reveal that elliptical pin fins have the advantage of lower  $f$  and tend to keep the flow steady for longer.

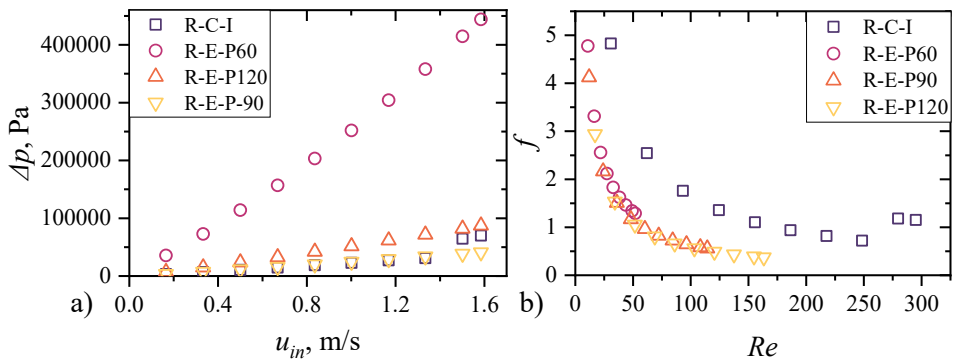


**Fig. 15.** a)  $\Delta p$  vs  $u_{in}$  and b)  $f$  vs  $Re$

<sup>2</sup> Jaseliūnaitė, J., Šeporaitis, M. Numerical Study Of Transverse Pitch Effect On Pressure Loss In An Inline Array Of Elliptical Pins. In: Proceedings of the 10 th International Conference on Fluid Flow, Heat and Mass Transfer . FFHMT'23. DOI: 10.11159/ffhmt23.172

The influence of  $P_{tr}$  on the  $\Delta p$  is presented in Fig. 16. It is evident that  $\Delta p$  values increase with decreasing  $P_{tr}$  and  $D_h$ . However, this increase in  $\Delta p$  follows a different trend than the parabolic trend. This behaviour can be attributed to flow separation: as the velocity between the pin fins increases, the boundary layer becomes thinner, causing the separation points to shift upstream.

Beyond a  $P_{tr} \approx 100 \mu\text{m}$ , further increase has little effect on reducing the  $\Delta p$ , primarily because the boundary layer separation points and the vortices behind the pin fins remain nearly unchanged, even as the velocity between adjacent pins decreases.

Consequently, evaluating the rate of change of  $\Delta p$  to the surface area ( $A_S$ ), as shown in Fig. 16 b), provides a valuable metric for assessing the thermohydraulic performance of the array. The results indicate that the most efficient configuration among those studied corresponds to  $P_{tr} = D_x (100 \mu\text{m})$ . However, a ratio of  $P_{tr} = 0.8D_x$  also offers a viable option for achieving enhanced thermal performance.

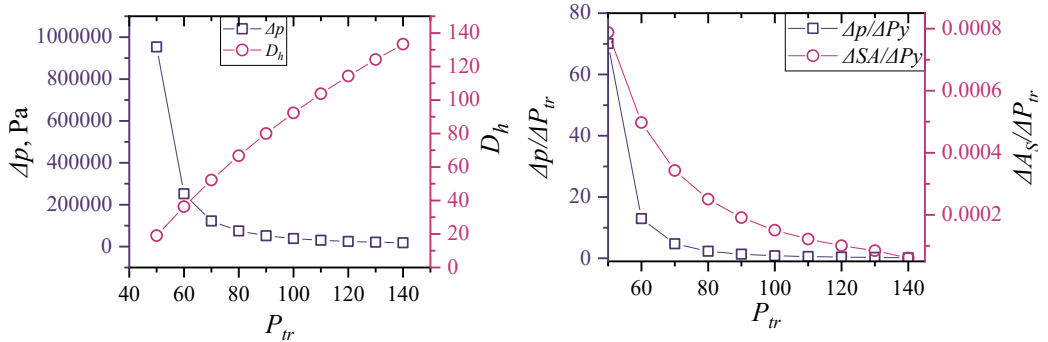


**Fig. 16.** a)  $\Delta p$  and  $D_h$  dependence on  $P_{tr}$  b) rate of  $\Delta p$  change versus the rate of  $\Delta A_S$  change

#### 4.1.3. Cylinders vs cones vs hourglasses based on K-type pin fin arrays

The results and analysis are presented in Section 4.1.3. are also presented in the publication<sup>3,4</sup>. In this section, the flow is treated as incompressible.

Elliptical and double-cylinder pin fin geometries maintain a constant cross-section throughout their height, resulting in more predictable aerodynamic

<sup>3</sup> Jaseliūnaitė, J., Šeporaitis, M. (2024). Comparative Assessment of Flow Patterns and Hydrodynamics in Cylindrical and Hourglass-Shaped Pin-Fin Configurations. In: Benim, A.C., Bennacer, R., Mohamad, A.A., Ocoń, P., Suh, SH., Taler, J. (eds) *Advances in Computational Heat and Mass Transfer. ICCHMT 2023. Lecture Notes in Mechanical Engineering*. Springer, Cham. [https://doi.org/10.1007/978-3-031-67241-5\\_62](https://doi.org/10.1007/978-3-031-67241-5_62)

<sup>4</sup> Jaseliūnaitė J., Šeporaitis, M. Extensive computational fluid dynamics analysis of microchannel flow topology and friction factor in arrays of conical pin-fins. *Physics of Fluids*. 2024, Vol 36, 094118. <https://doi.org/10.1063/5.0220609>

characteristics and relatively uniform flow distribution between the fins. In contrast, hourglass and conical configurations feature a variable cross-section: in hourglass fins, the narrowest section is at the midpoint, while in conical fins, the cross-section gradually decreases or increases depending on the direction of conicity.

The  $\Delta p$  and  $f$  graph is presented in Fig. 17. Before the analysis, it should be noted that the flow within the K-H19 array remains unsteady across all investigated  $Re$  (from 80 to 117). In contrast, in the K-C array, flow unsteadiness occurs only when  $Re$  exceeds 117, as in K-T14-A-P250. At the same time, K-T14-B-P250 does not experience vortex shedding in any investigated  $Re$ .

The data in Fig. 17 indicate that K-H19 enhances hydraulic performance by reducing the  $\Delta p$  by 6–14% compared to K-C. Despite K-C and K-H19 pin geometries having the same volume, the K-C possesses a 23% greater surface area, which may account for its higher  $\Delta p$ . Moreover, K-H19 exhibits a more complex flow structure than K-C.

Although no significant reduction of  $\Delta p$  of conical pin fins compared to K-C has been indicated, they reduce  $f$  by 6 % in the steady regime and up to 11 % in the unsteady regime, while K-H19 reduces it by 4%.

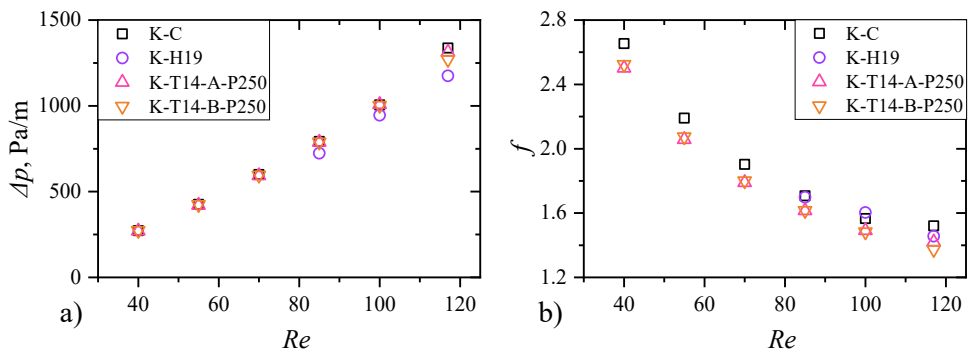


**Fig. 17.** a)  $\Delta p$  and b)  $f$  dependence on  $Re$

Fig. 18 details the relationship between the  $f$  and the conicity angle for conical pin fin arrays, considering various pitches ( $P$ ) and  $Re$ . Within this figure, both the  $f$  and its percentage deviation are plotted. Blue lines are used to denote pin fin arrays with a unidirectional (A) conicity orientation, while black lines indicate arrays with a bidirectional (B) conicity orientation. Additionally, coloured regions highlight different flow regimes, with the upper and lower portions corresponding to the unidirectional (A) and bidirectional (B) orientations, respectively.

Conicity is the angle representing the variation in the diameter of pin fins relative to their height. The horizontal cross-section of the pin fins stays uniform in the midplane of the array but changes at the upper and lower end walls. The pin fin

with a conicity of  $13.48^\circ$  shows an 11.3% increase in volume and a 2.83% increase in surface area compared to the cylindrical pin fin (K-C).

A larger pitch requires a lower  $Re$  to start vortex shedding. The increased  $D_h$  resulting from the larger  $P$  allows for a higher  $Re$  number while achieving a lower  $f$ . For example, increasing the pitch from 200 to 300  $\mu\text{m}$  increases the flow volume by 61 % and decreases  $f$  by approximately 1.6 times at  $Re = 117$ .

The  $P$  does not affect the relationship between  $f$  and  $Re$ . Regardless of the  $P$ , increasing  $Re$  from 40 to 55 results in a 17–19% increase in  $f$ ; from 55 to 70, a 12–14% increase; from 70 to 85, a 10–11% increase; from 85 to 100, an 8–9% increase; and from 100 to 117, a 2–7% increase. Also, the rate at which  $f$  increases with respect to  $Re$  is not significantly affected by the  $P$ . For example, the  $f$  between  $Re = 40$  and  $Re = 117$  increases by an average of 43 % for unidirectional and 46 % for bidirectional pin fin at any  $P$ .

When the  $P$  exceeds the channel height (250  $\mu\text{m}$ ), and the flow is steady, the arrangement of the pin fins has a negligible effect on the flow characteristics. Nevertheless, the arrangement becomes significant once the flow transitions to the vortex-shedding regime. Specifically, unidirectional (A) pin fins exhibit lower  $f$  in steady flow with the  $P$  of 200–225  $\mu\text{m}$  and in unsteady flow with  $P = 200 \mu\text{m}$ . Conversely, bidirectional (B) pin fins stabilise the flow, resulting in a lower  $f$ .

The relationship between the  $f$  and the conicity angle appears unclear at different  $Re$ ; no definitive trend can be established. Models with unidirectional (A) pin fins produce consistent and intuitively predictable results. In contrast, models with bidirectional (B) pin fins may exhibit varying trends. Specifically, increasing the cone angle may lead to an increase, a decrease, or no change in  $f$ .

The cone angle and pattern type have a greater impact at lower  $P$  values. For instance, with a  $P = 200 \mu\text{m}$  and a low  $Re$  (steady flow), these factors can change  $f$  by up to 9%. A slight increase in  $P$  to 225  $\mu\text{m}$  reduces this variation to 7%. However, for steady flow ( $Re = 40$ –85), when  $P$  is larger than channel height, the effect of different pin orientation patterns on  $f$  is minimal. In all cases, increasing the cone angle decreases  $f$ .

Fig. 18 indicates that for all  $P$  greater than 225  $\mu\text{m}$ ,  $f$  decreases with increasing cone angle, regardless of whether the pin fins are unidirectional or bidirectional. However, at  $P$  of 200  $\mu\text{m}$ , the bidirectional pattern shows no change in  $f$  with varying angles, while the unidirectional pattern significantly reduces  $f$  as the angle increases.

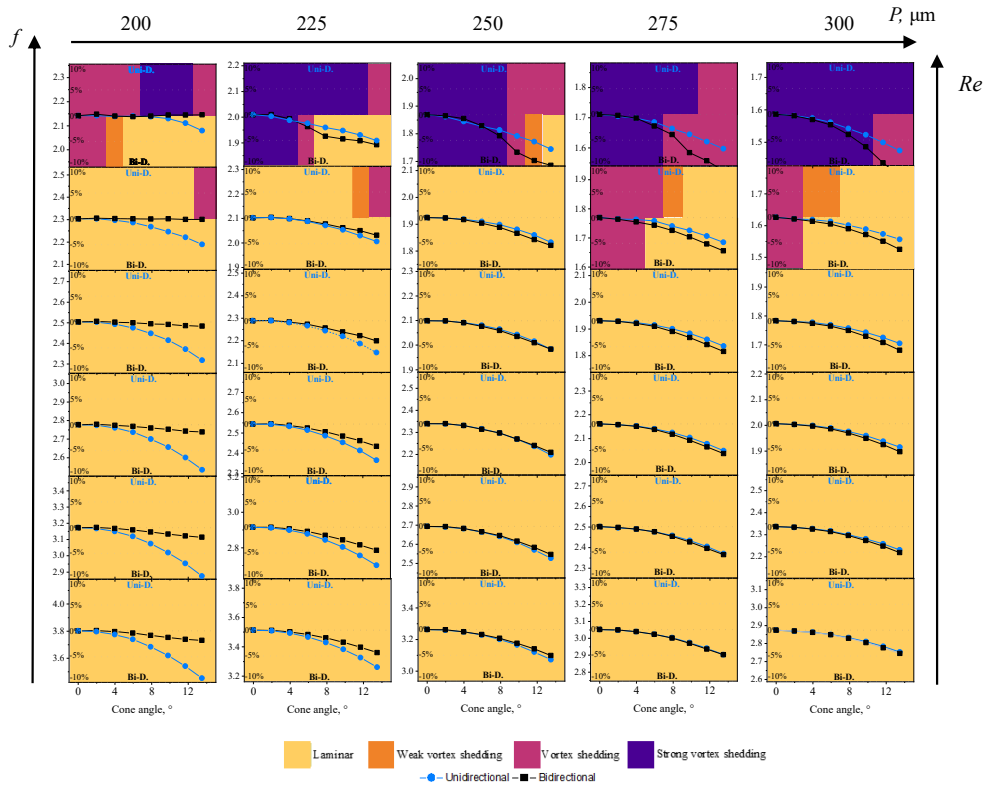


**Fig. 18**  $f$  of conical fin fins for different pitches at various  $Re$

The distributions of streamline in the midplane, near the endwalls, and in the intermediate region for the K-C and K-H19 configurations are shown in Fig. 19 and Fig. 20. Additionally, the midplane and the planes near the upper and lower endwalls for the K-T14-A-P250 and K-T14-B-P250 configurations are presented in Fig. 21 and Fig. 22. The vertical midplane of all aforementioned arrays is shown in Fig. 23. Furthermore, critical points, including nodes, foci, and saddles, are identified and marked on these planes. Fig. 24 presents the iso-surfaces at  $\Omega = 0.52$ , providing further insight into the flow topology.

The K-C exhibits a typical flow pattern observed around a cylindrical body (see Fig. 19) (Lekkala et al., 2022). No significant differences in flow structure are observed between the midplane and the region between the midplane and the endwall plane, indicating that the vortex structures maintain integrity throughout the channel.

The key topology characteristics of all arrays are similar. The freestream flow separates as it passes around the pins (see Fig. 19 and Fig. 20 a), b) and Fig. 21 and Fig. 22 b) and Fig. 24). The detached flow bypasses obstacles in a distinct manner for each configuration, leading to variations in the wake pattern, which will be further explored later. Despite these differences in wake formation, the flow near the endwalls

has a consistent pattern. Initially, the freestream flow detaches from the endwall surface, originating from the saddle point before the obstacle (see Fig. 19 and Fig. 20 c Fig. 21 a) Fig. 22 b)). A stable saddle point and a half-node point indicate flow roll-up due to an adverse pressure gradient, which generates a horseshoe vortex (see Fig. 24). This vortex extends downstream.

Horseshoe vortices in front of conical pin fins develop solely at one endwall, where the thicker end of the pin fin is located. This is supported by the lack of a saddle point, which is essential for the creation of a horseshoe vortex (Tobak & Peake, 1982; Younis et al., 2014). Consequently, the boundary layer remains attached to the endwall, preventing the formation of a horseshoe vortex around the obstacle.

As discussed previously, differences in wake patterns arise from the different ways the flow bypasses obstacles (Derakhshandeh & Alam, 2019). The detachment of the flow from the trailing edge of the obstacles arises from both the freestream and the half-node point. The detached flow in the K-C array rolls towards the vortex foci behind the pin, initiating vortex shedding. Regarding the mean flow, the K-C array features two distinct foci and a saddle point, which is a typical configuration for the time-averaged wake of a bluff body (Forouzi Feshalami et al., 2022). This results in a stable pattern of counter-rotating vortex shedding without external disruptive forces destabilising the vortices.

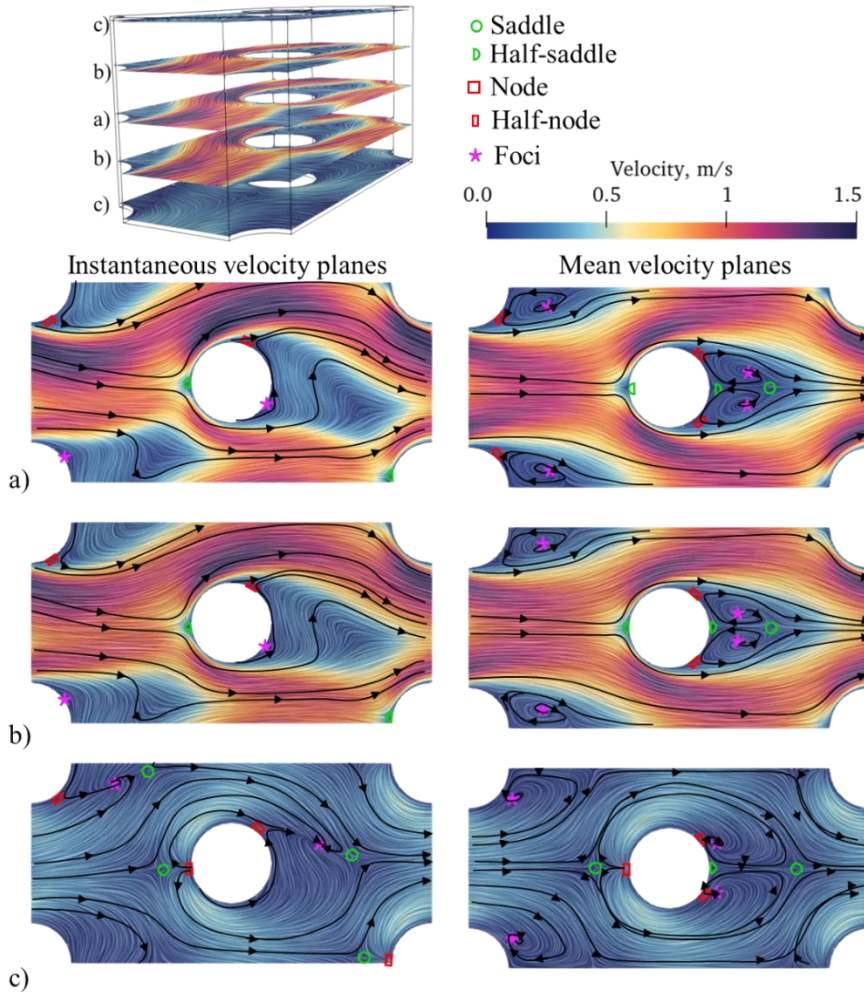


**Fig. 19.** Velocity streamlines with critical points on a) middle plane, b) in between middle and endwall, c) near endwall for K-C

In contrast, the mean flow around the K-H19 array does not exhibit symmetrical foci points along the midplane. Instead, a node point is formed (see Fig. 20 a). As the fluid passes through a constricted section of the hourglass shape, flow accelerates due to the narrowing geometry. This constriction increases velocity, which can improve heat transfer and mixing. Additionally, the two jet-like flows formed behind the pins merge towards the centre after flow impingement (see Fig. 24). This collision prevents the formation of stagnant vortices, creating a node point.

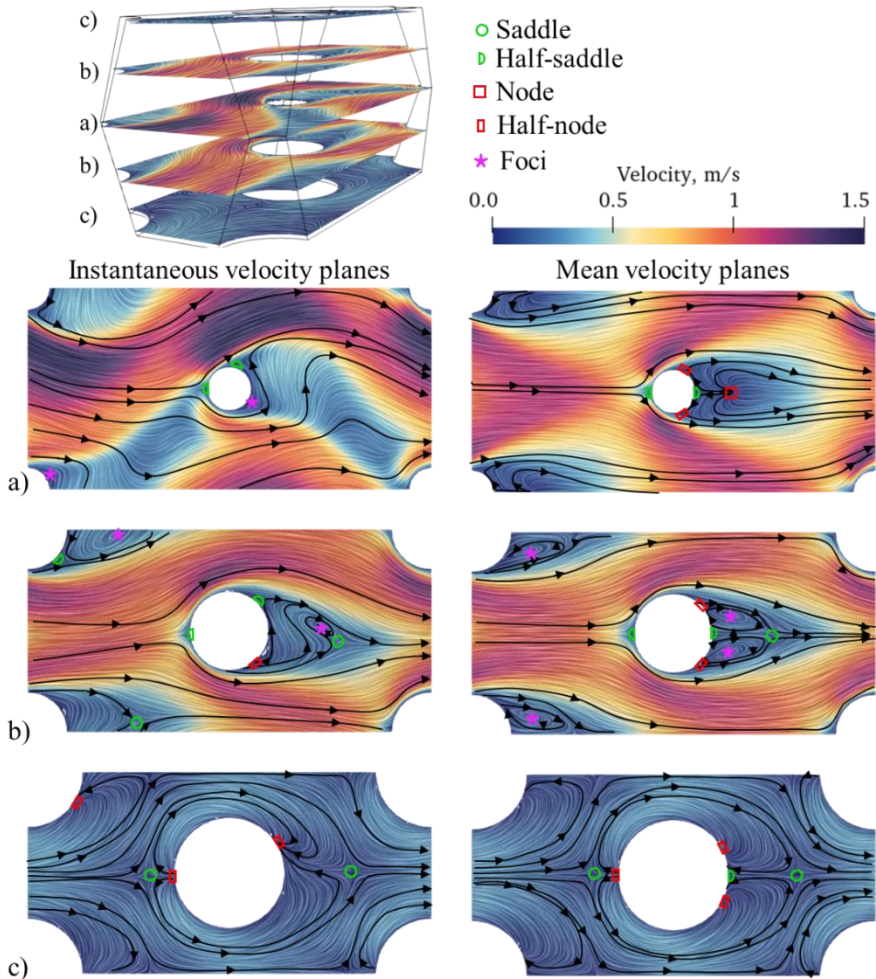


**Fig. 20.** Velocity streamlines with critical points on a) middle plane, b) in between middle and endwall, and c) near endwall for K-H19

The unique hourglass shape, characterised by a conical and a narrow neck, improves hydraulic characteristics. However, research is being conducted on conical pin fin arrays with varying taper angles to further enhance heat transfer efficiency and overall performance.

The symmetrical flow around the conical pin fin generates a wake with two counter-rotating vortices behind the pins. Nonetheless, the bidirectional (K-T14-B-P250) pin fins have no foci points in the horizontal midplane, meaning no steady vortices are present. Similar to unidirectional (A) conicity, secondary flow influences the flow structure in the horizontal midplane behind the bidirectional (B) pin fins. However, the effect varies depending on the conicity direction of each pin. Moreover,

in an array of bidirectional (B) pin fins, the vortices generated behind the pin fins are spread throughout the entire height of the channel due to the interaction of nearly balanced secondary counterflows.

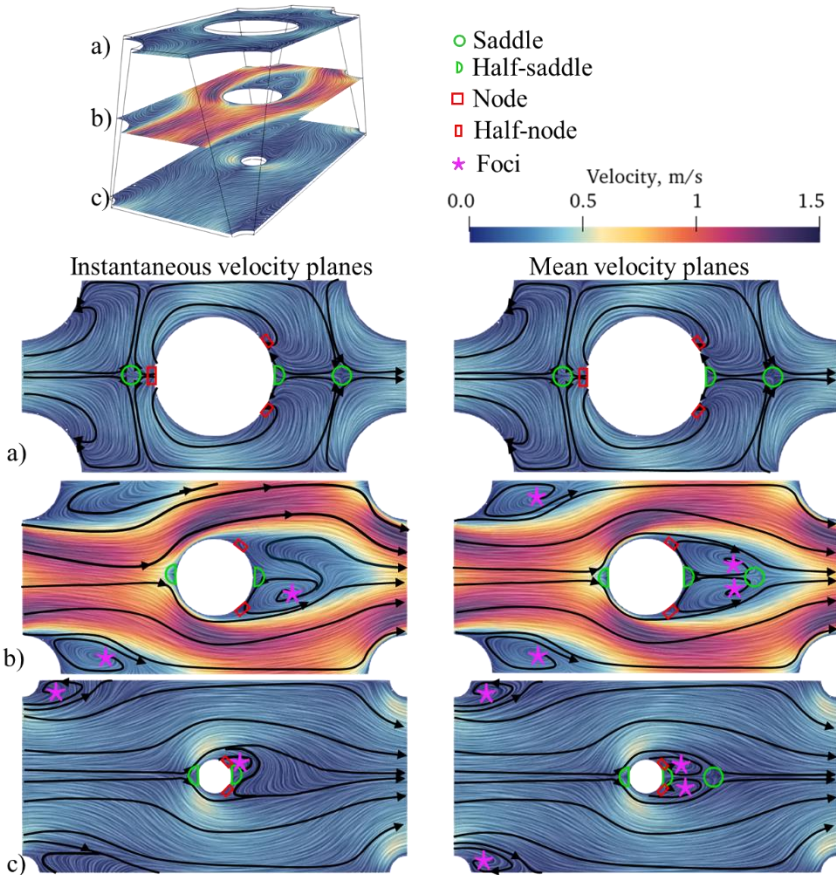


**Fig. 21.** Velocity streamlines with critical points on a) near the upper endwall, b) middle, c) near the lower endwall for K-T14-A-P250

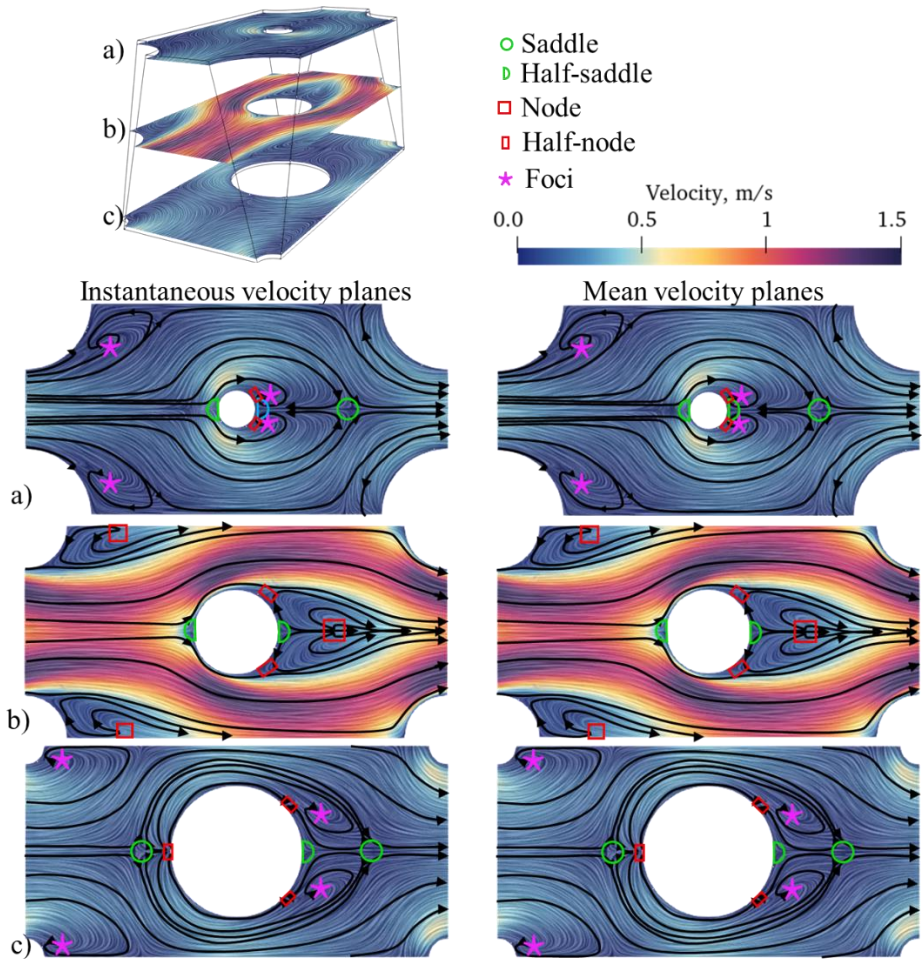


**Fig. 22.** Velocity streamlines with critical points on a) near the upper endwall, b) middle, c) near the lower endwall for K-T14-B-P250

The critical point in the vertical plane (see Fig. 23 ) in the K-C and K-H19 cases exhibits symmetry. However, the conicity of the pin fins causes these points to displace due to secondary counterflows. Notably, the flow stability in the bidirectional conical pin fin array is greater than that observed in unidirectional conical arrays despite the more complex flow topology of the former. This increased stability can be attributed to the more balanced opposing secondary flows behind the pin fins, which align the position of the half-node point and create an additional stagnation point at the narrower end of the conical pin fin.

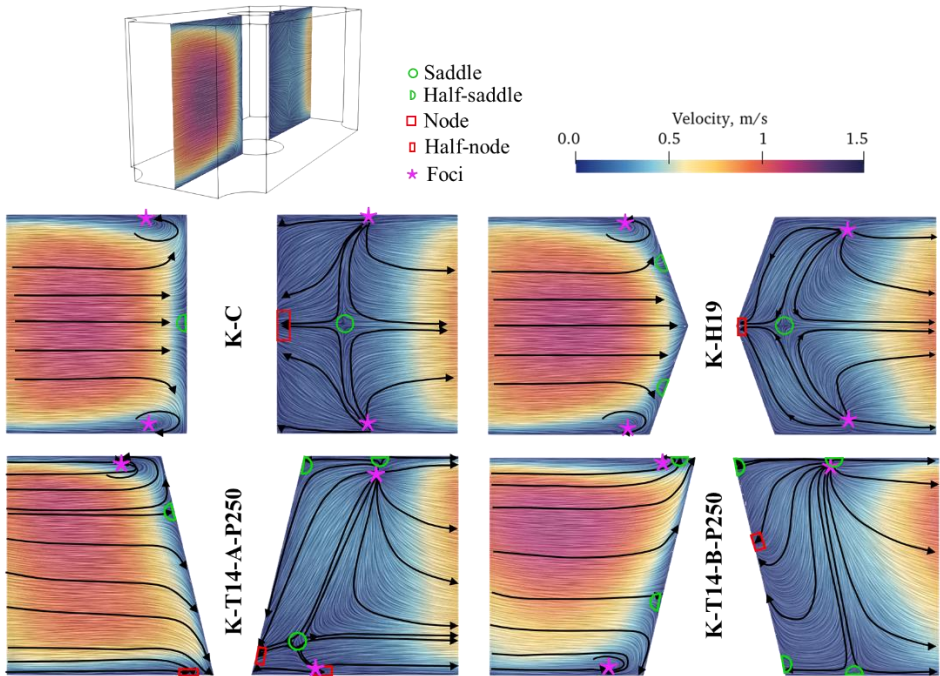


**Fig. 23.** Mean velocity streamlines with critical points on vertical midplane for K-C, K-H19, K-T14-A-P250 and K-T14-B-P250

The primary distinction between the flow patterns in the K-C and K-H19 arrays lies in their geometries. The K-H19 has a constriction that accelerates the flow through the centre of the pins, potentially enhancing heat transfer compared to K-C. Furthermore, the vortices in the K-C remain more consistent throughout the channel height. In contrast, the vortices in the K-H19 array are disrupted at the midplane, where the two flow streams collide. This results in the K-H19 generating more small vortices characterised by more complex structures and dynamics of vortex motion.

Upstream of a conical pin fin, the flow, driven by the pressure gradient, is directed toward the endwall, where the pin fin's narrower end is located. Unlike the K-C array, which exhibits a symmetrical flow in its wake (see Fig. 24 a), the conical pin fins generate an asymmetrical secondary flow on their rear surface. Specifically, the stronger flow emanates from the thicker end of the pin fin. It collides with the weaker flow originating from the thinner end, with the intersection point closer to the thinner end. This interaction enhances mass transfer between the end walls. Furthermore, in a bidirectional pin fin array, the secondary flows alternate their intersection points with each change in the orientation of the pin fin conicity, thereby further intensifying the mixing process.

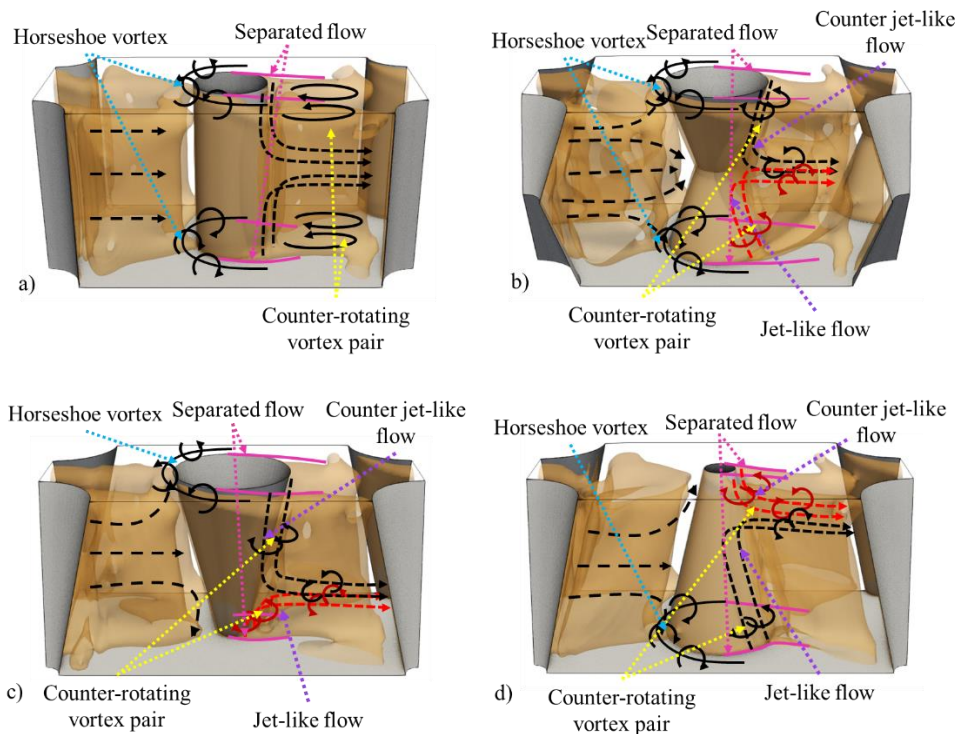


**Fig. 24.** Topological flow structure based on the  $\Omega$  criterion a) K-C b) K-H19  
c) K-T14-A-P250 d) K-T14-B-P250

#### 4.1.4. Cylinders vs cones vs hourglasses based on R-type pin fin arrays

The results and analysis are presented in Section 4.1.4. are also presented in the publication<sup>5</sup>. In this section, the flow is treated as compressible (water properties taken from the OpenFOAM database), and all computations are performed in a cyclic domain.

Next, focusing on R-type geometries, the study evaluates nine pin fin shapes, including the standard cylindrical type. The pressure loss characteristics of these configurations are presented in Fig. 25. The study evaluates how variations in pin fin geometry affect  $f$ , considering factors such as shape-induced flow separation, wake formation, and vortex shedding.

It is evident that the R-T8-B configuration has the lowest  $f$  even beyond  $Re > 500$ , attributed to its exceptional flow stabilisation effect (see Fig. 25). In contrast, other conical pins demonstrate lower  $f$  than cylindrical or conical pin fins, despite

<sup>5</sup> Jaseliūnaitė, J., Šeporaitis, M. The Potential of Hourglass-Shaped Pin-Fins on Enhancing Thermohydraulic Performance in Microchannel Arrays // Heat Transfer Engineering

vortex shedding. The difference between the unidirectional and bidirectional cases remains negligible when the taper angle is small. However, a significant difference emerges between the A and B configurations as the angle increases. As previously noted, the bidirectional arrangement improves flow stabilisation. Meanwhile, the unidirectional arrangement induces stronger flow interactions and unsteadiness, which may favour enhanced mixing, resulting in the lowest  $f$  at the highest  $Re$ , suggesting a tendency for reduced friction while maintaining flow instability.

The hourglass-shaped pin also facilitates an earlier transition to unstable flow. Meanwhile, the  $f$  exhibits an approximately linear trend within the investigated  $Re$  range. Cases with a higher hydraulic diameter ( $D_h$ ) underwent a more rapid transition. Although hourglass-shaped pin fins generally exhibit a higher  $f$  than their conical or cylindrical counterparts, the R-H16 configuration demonstrates a distinct decreasing trend. This observation suggests that the hourglass shape possesses potential advantages in optimising flow characteristics.

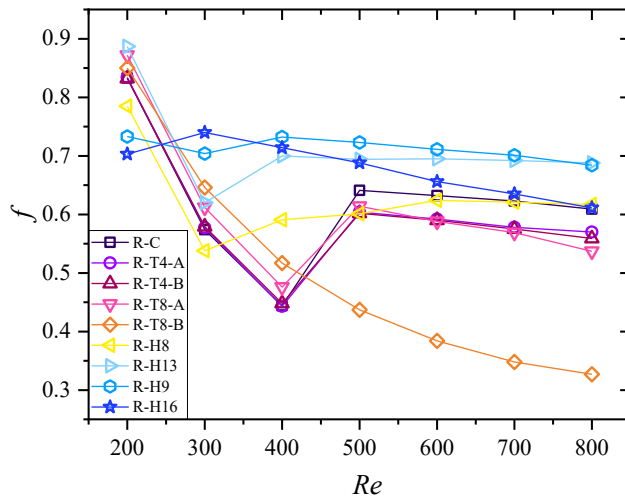


**Fig. 25.**  $f$  dependence on  $Re$  of different R-type geometries

The transition to unsteady flow is summarised in Table 14. The flow through an array of cylindrical pin fins maintains a relatively constant cross-sectional area, delaying the transition to unsteady flow. In contrast, the varying constrictions of the hourglass-shaped pin fins cause alternating acceleration and deceleration of the fluid across successive rows. These rapid velocity fluctuations destabilise the flow, leading to an earlier transition to unsteady flow compared to other cases. Although conical pin fins also introduce variations in cross-sectional area, their transition to unsteady flow occurs at approximately the same  $Re$  as cylindrical pin fins, suggesting that their

geometric influence on flow stability is less pronounced than that of hourglass-shaped fins.

**Table 14.** Flow regimes – orange represents steady flow, while magenta indicates unsteady flow

Flow regime	R-C	R-T4-A	R-T4-B	R-T8-A	R-T8-B	R-H8	R-H13	R-H9	R-H16
200	Orange	Orange	Orange	Orange	Orange	Orange	Orange	Orange	Orange
300	Orange	Orange	Orange	Orange	Orange	Orange	Orange	Magenta	Magenta
400	Orange	Orange	Orange	Orange	Orange	Magenta	Magenta	Magenta	Magenta
500	Magenta	Magenta	Magenta	Magenta	Orange	Magenta	Magenta	Magenta	Magenta
600	Magenta	Magenta	Magenta	Magenta	Orange	Magenta	Magenta	Magenta	Magenta
700	Magenta	Magenta	Magenta	Magenta	Orange	Magenta	Magenta	Magenta	Magenta
800	Magenta	Magenta	Magenta	Magenta	Orange	Magenta	Magenta	Magenta	Magenta

Compared to previously studied cases similar to those of Koşar et al. (2011) It is important to note that the  $Re$  interval in those studies was approximately 15, whereas in the present analysis, it is 100. As a result, the transition to unsteady flow in conical pin fins cannot be accurately determined. However, based on the observed trends, the transition behaviour of conical pin fins is more similar to that of cylindrical pin fins than to that of hourglass-shaped ones.

#### 4.2. $\Omega$ criteria investigation

The results and analysis presented in Section 4.2 are also presented in the publication <sup>4,5,6,7</sup>. In this section, the flow is assumed incompressible for K-type cases and compressible for R-type cases (using water properties from the OpenFOAM database), with all calculations carried out in a cyclic domain.

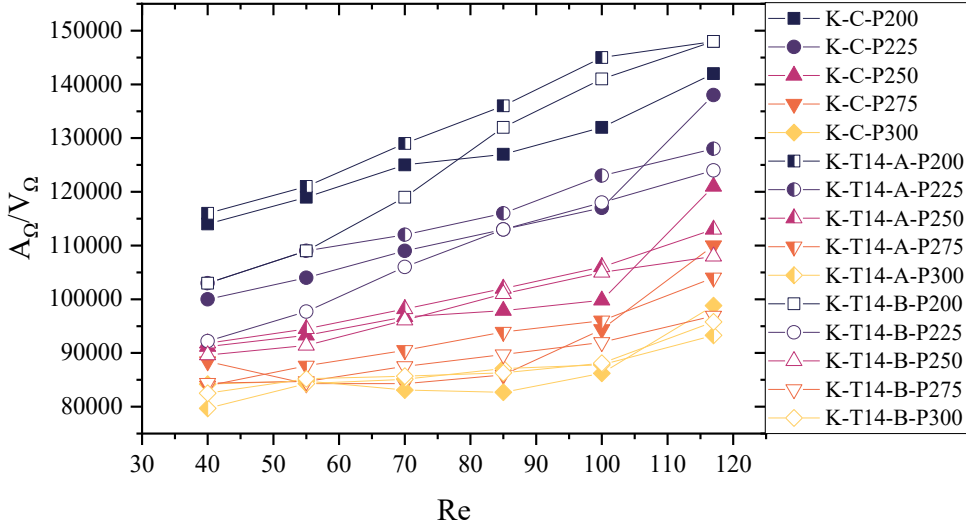
The  $\Omega$  criterion analysis is not limited to evaluating the mean value; it can also be applied to identify vortical structures by determining their occupied area and volume.

Fig. 26 illustrates the relationship between the vortical structures' area-to-volume ratio ( $A_\Omega/V_\Omega$ ) and the  $Re$  and  $P$  of the K-type. As expected, the lowest  $P$  corresponds to the highest  $A_\Omega/V_\Omega$ , as the reduced domain size restricts the formation of vortices. When unsteady flow disrupts vortical structures, their  $A_\Omega/V_\Omega$  increases

<sup>6</sup> Jaseliūnaitė J., Šeporaitis M. Analysis of Vortical Structures in Flow Through Pin-fin Arrays Using  $\Omega$  Criterion In: Proceedings of the 19th OpenFOAM workshop. Beijing, China, 2024, 25-28 June.

<sup>7</sup> Jaseliūnaitė J., Šeporaitis M. Advances in Vortical Structure Analysis for Superior Heat Transfer in Pin-Fin Microchannels. 23rd IACM Computational Fluids Conference – CFC 2025. March 17-20, Santiago, Chile, 2025

significantly, especially for cylindrical pin fins. Bidirectional pin fin arrays generally have the lowest  $A_\Omega/V_\Omega$  values due to greater flow stability. However, due to their lower blockage ratio, their  $A_\Omega/V_\Omega$  falls between those of unidirectional and cylindrical pin fin arrays at the highest  $P$ .



**Fig. 26.**  $A_\Omega/V_\Omega$  dependence on  $Re$  with different  $P$  of K-type geometries

Fig. 26 represents only the area and volume of vortical structures, excluding the volume and surface area of the inner walls of the modelled domain. Meanwhile, Fig. 27 illustrates the relationship between vortical structures' area and volume ratio. The area of the vortical structures ( $A_\Omega$ ) is defined as the volumetric surface area occupied by vortical structures. To eliminate the influence of geometric scaling, this value is normalised by the smallest area within a given  $P$  ( $A_{\Omega,min}$ ). This normalisation ensures consistent comparability across different pin fin configurations and flow regimes, allowing the analysis to focus on relative variations in vortex evolution rather than on absolute magnitudes dictated by geometry. The vortical structure volume ( $V_\Omega$ ) is defined as the total volume occupied by all identified vortical structures within the considered domain. The  $V_\Omega$  is normalised to the total modelled volume ( $V$ ). Both  $A_\Omega$  and  $V_\Omega$  represent the sum of all vortices, providing global measures of their spatial extent.

At larger pitches, vortical structures occupy a larger fraction of the domain. For example, at  $P = 200 \mu\text{m}$ , the vortical volume fraction ( $V_\Omega/V$ ) is approximately 4–5% greater than at  $P = 300 \mu\text{m}$ . A smaller  $P$  constricts the flow path, improving fluid interaction by reducing the available space for flow. This restriction suppresses large-scale coherent structures and promotes greater interaction with surfaces, leading to

increased local instability and energy dissipation. Despite this, the flow remains steady or transitional at lower  $P$ .

Conversely, a larger  $P$  provides more space for developing coherent flow structures, including larger vortices. This increased spacing facilitates stronger interactions between flow layers, accelerating the transition to unsteady flow even at lower  $Re$ . Additionally, a larger  $P$  allows the formation of a smoother and more stable boundary layer along the sidewalls between pin fins, reducing unsteady flow separation and reattachment and decreasing fluctuations in kinetic energy. A smaller  $P$  generally reduces vortical surface area and volume regardless of the pin shape.

Overall,  $V_{\Omega}/V$  decreases with increasing  $Re$ , while the  $A_{\Omega}$  increases. Notably, under unstable flow conditions (marked in violet), the  $A_{\Omega}/A_{\Omega,min}$  increases significantly – by 8% to 17% – with increasing  $P$ , indicating that vortices break down into smaller structures. In contrast, cases of moderate instability (marked in red) show only a slight increase in  $A_{\Omega}/A_{\Omega,min}$  and often a decrease in volume, suggesting that although vortex shedding occurs, vortices do not completely break up into smaller structures but tend to remain connected.

Interestingly, bidirectional pin fins, at the lowest  $P$ , exhibit remarkably high  $V_{\Omega}/V$  and  $A_{\Omega}/A_{\Omega,min}$  at high  $Re$ , even though the flow remains steady. At low  $Re$ ,  $A_{\Omega}/A_{\Omega,min}$  is comparable to other configurations. However, it increases significantly with  $Re$ , indicating that as  $Re$  increases, the vortical structures persist and continue to expand in volume rather than dissipate.

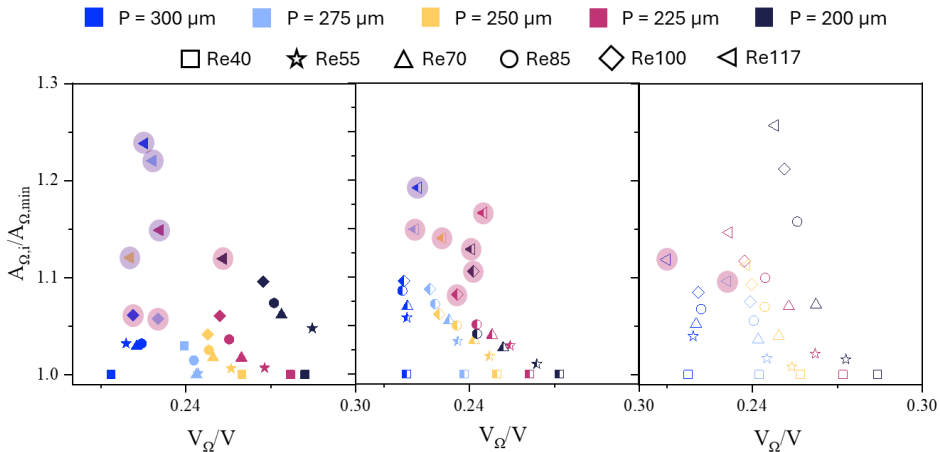


**Fig. 27.**  $A_{\Omega}/A_{\Omega,min}$  dependence on the  $V_{\Omega}/V$  of K-type geometries

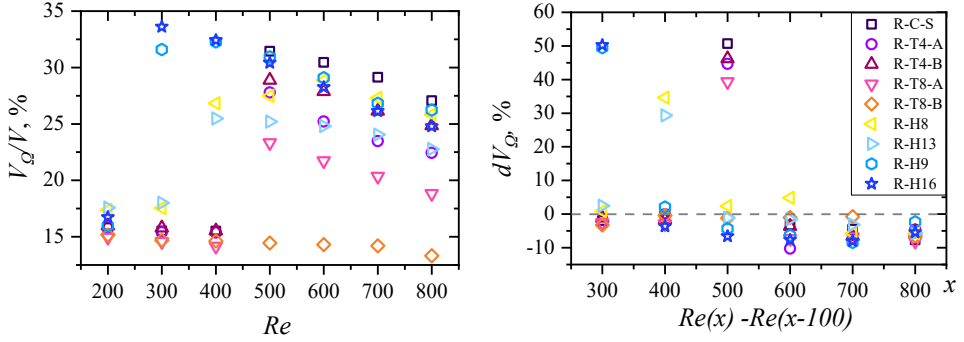
Fig. 28 a) illustrates the area occupied by the coherent structures identified using the  $\Omega$  criterion, and Fig. 28 b) presents its variation with  $Re$  for the R-type.

The results indicate that vortices occupy approximately 15–17% of the total array volume in the steady flow regime. This relatively small and consistent volume fraction reflects the minimal vortex activity characteristic of stable steady flow. There are slight variations among the different configurations, but no significant deviations are observed.

However, after the transition to the unsteady flow, this percentage can increase to 32%, effectively doubling compared to the steady flow state. This nearly twofold increase represents the expansion of coherent vortical regions and the onset of more complex flow dynamics. Configurations like R-H16 and R-T4-B exhibit more pronounced increases, indicating a greater sensitivity to unsteady vortex formation, while others, such as R-H13 and R-H8, display more restrained behaviour, potentially due to structural features that inhibit the formation or expansion of vortices.

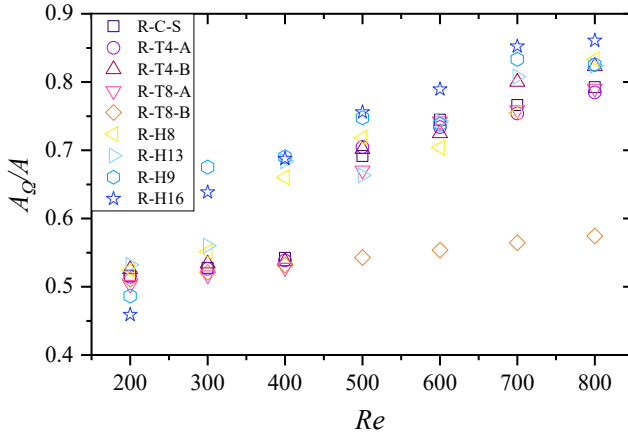
Fig. 28 b) complements  $\Omega$  analysis by showing the variation in the occupied volume ( $dV_\Omega$ ) with  $Re$ . In the steady regime, most configurations exhibit a negative or near-zero  $dV_\Omega$ , indicating a contraction or stagnation of the vortex-occupied volume, possibly due to increased flow alignment and reduced instability. However, when the flow becomes unsteady, most configurations exhibit positive  $dV_\Omega$ , reflecting an expansion of the vortex regions. In contrast, others revert to negative values, suggesting fragmentation or contraction of coherent structures into smaller unsteady vortices. Both trends in the post-transition regime indicate that the relationship between  $Re$  and vortical structure behaviour is non-linear. While the initial transition to unsteady flow promotes the growth of vortical regions, further increases in  $Re$  may lead to structural breakdown and more chaotic mixing.

Overall, the figures highlight the sensitivity of R-type configurations to changes in the flow regime. The sharp increase in  $V_\Omega/V$  highlights the critical role of the coherent structures in the flow transition. Meanwhile, the variation in  $dV_\Omega$  reveals the dynamic nature of vortex behaviour, characterised by growth and contraction, depending on the configuration and flow conditions. These insights are essential for understanding energy dissipation, flow resistance, and the underlying mechanics of flow transition.



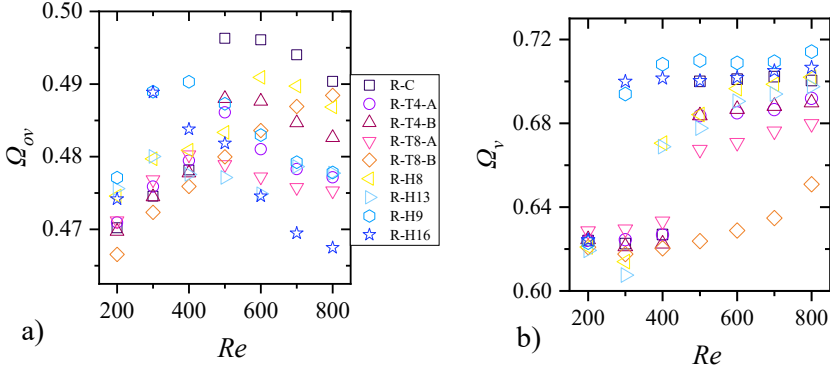
**Fig. 28.** a) Fraction of total volume occupied by vortical structures ( $V_Q/V$ ), b) variation of occupied area ( $dV_Q$ ) with  $Re$  of R-type geometries

Fig. 29 shows the ratio of coherent structure area to the total flow surface area ( $A_Q/A$ ). The data indicate that hourglass-shaped microchannels consistently exhibit the highest  $A_Q/A$  values, averaging 68–72%. In comparison, conical obstacles reach 54–66%, while cylindrical ones reach about 65%. Under steady flow,  $A_Q/A$  averages 46–55%, but in unsteady flow, it increases to 74–81%. Transitioning between regimes can raise  $A_Q/A$  by up to 28%.



**Fig. 29.** Relative area of coherent structures for R-type geometries

Fig. 30 presents the  $\Omega$  values for the entire flow field ( $\Omega_{ov}$ ) and within coherent structures ( $\Omega_v$ ).  $\Omega_v$  reflects vortex strength, which is highest in hourglass-shaped configurations and lowest in conical ones. The highest  $\Omega_{ov}$  occurs in the R-C configuration after the transition to unsteady flow. However,  $\Omega_{ov}$  tends to decrease after the transition, while  $\Omega_v$  increases with rising  $Re$ .



**Fig. 30.**  $\Omega$  values for the coherent structures and for the entire flow for R-type geometries

Table 15 can be considered a systematic tool for summarising and interpreting previously obtained and analysed results related to the characteristics of coherent flow structures. It is based on three key parameters: the surface area of coherent structures ( $A_\Omega$ ), the volume they occupy ( $V_\Omega$ ), and an intensity metric that reflects the strength of the vortex or the rotational intensity of the flow ( $\Omega$ ).

By combining these parameters, it becomes possible to gain a more comprehensive understanding of the flow behaviour and its potential impact on heat transfer and hydraulic resistance. For example, when all three values are high, this indicates strong, spatially extensive, and actively interacting vortices that effectively enhance fluid mixing and improve heat transfer. Conversely, low values for all parameters suggest weak, small-scale vortices with minimal influence on the overall flow dynamics.

Intermediate or mixed values help identify whether the structures are stable, fragmented, or indicative of transitional flow regimes. This type of classification not only deepens understanding of numerical analysis results but also enables more accurate comparison of different geometric configurations and their behaviour under various flow conditions.

Overall, the table serves as a valuable interpretive tool that links quantitative indicators to qualitative flow characteristics, thereby facilitating both analysis and evaluation of results.

**Table 15.** Interpretation of vortical structures based on  $A_\Omega$ ,  $V_\Omega$ , and  $\Omega$  magnitudes

$A_\Omega$	$V_\Omega$	$\Omega$	Interpretation
High	High	High	Strong, spatially extensive, highly interactive vortices, likely to enhance mixing and heat transfer
Low	Low	Low	Weak and small vortices, minimal flow disturbance

High	Low	High	Many small, energetic vortices with large surface interaction.
Low	High	Low	Large but weak or stagnant vortices, possibly recirculation zones
High	Low	Low	Many small but weak vortices, possibly early shear layer instabilities not yet rolling up fully. Potentially transitional regime
Low	High	High	Large, strong vortices with relatively small surface interaction. It could be stable vortex cores
Low	Low	High	Small, very intense vortices — might represent isolated vortex cores or transitional bursts.
High	High	Low	Large coherent regions, but not much stronger than the background – could indicate turbulent but disorganised flow or vortex breakdown

### 4.3. TKE, KE and $\Omega$ relationship

The results and analysis presented in Section 4.3 are also presented in the publication<sup>4</sup>.

The total kinetic energy ( $KE$ ) of a fluid flow consists of two components: the mean kinetic energy ( $KE_{mean}$ ), associated with the bulk motion of the fluid, and the fluctuating kinetic energy ( $KE_{fluc}$ ) due to unsteady flow. Mathematically, this is expressed as follows:

$$KE = KE_{mean} + KE_{fluc} \quad (59)$$

In CFD, the equations are discretised due to the subdivision of the flow domain into finite cells. Time-averaging was applied to account for temporal variations, and kinetic energy was evaluated based on the internal surface area of the microchannel (including pin surfaces and upper/lower walls) rather than the total fluid volume; therefore, the units are  $J/m^2$ . Since the flow is considered incompressible, the density is assumed to be constant (heat transfer is not taken into account in the cases studied in this chapter). The  $KE$  and  $KE_{fluc}$  are calculated using the following equations:

$$KE = \frac{\rho}{2A_{int}} \frac{\sum_{i=1}^N (\sum_{j=1}^M u_j^2 V_{cell,j})_i \Delta t_n}{\sum_{i=1}^N \Delta t_n} \quad (60)$$

$$KE_{fluc} = \frac{\rho}{2A_{int}} \sum_{j=1}^M (\overline{u_{x,j}^2} + \overline{u_{y,j}^2} + \overline{u_{z,j}^2}) V_{cell,j} \quad (61)$$

In each calculation cell, the velocity fluctuations of the x, y and z components are calculated separately:

$$\overline{u_j^2} = \frac{\sum_{i=1}^N (u_j - \bar{u}_j)_i^2 \Delta t_n}{\sum_{i=1}^N \Delta t_n} \quad (62)$$

In these formulas, the flow field is resolved both in space and time, so two counters are used:  $M$  is the total number of computational cells (control volumes) in the microchannel region being integrated, and  $j=1, \dots, M$  indexes those cells. While  $N$

is the number of stored time samples used for averaging, and  $i=1, \dots, N$  indexes those time instants.

In fluid dynamics,  $KE_{fluc}$  is a key parameter for quantifying turbulence intensity, representing the kinetic energy per unit mass associated with velocity fluctuations. Turbulence is caused by factors such as vortices, flow instabilities, velocity variations, boundary-layer interactions, and flow separation, all of which contribute to chaotic and unpredictable fluctuations in the velocity field. The extent to which these factors influence  $KE_{fluc}$  depends on the flow conditions and the scale of observation.

When performing convective heat transfer analysis, using  $KE_{fluc}$  as the kinetic energy per unit mass of unsteady vortices can lead to an overestimation of the results. Another important step in analysing mass, momentum, and energy transport in unsteady flows is identifying coherent structures. The  $\Omega$  criterion is an effective tool for examining these structures, providing insight into the rotational dynamics of unsteady flow. Visualisation and analysis of coherent structures make it possible to assess the distribution of  $KE_{fluc}$  at various motion scales.

As the rotational motion in the flow increases,  $KE_{fluc}$  also increases due to fluctuations in rotational and translational motion. However, while  $KE_{fluc}$  quantifies the total unsteady motion, the  $\Omega$  criterion specifically captures the rotational component. Their relationship depends on the flow conditions and the presence of coherent vortical structures.

In unsteady flows, energy transfer mechanisms influence the redistribution of kinetic energy among different scales of motion. Most of the turbulent kinetic energy is eventually dissipated at the smallest scales, where it is converted into heat. In systems with strong external influences such as rotation (large  $\Omega$ ), the structure and efficiency of this energy transfer can be significantly altered, sometimes reducing the rate at which unsteady motions extract energy from the mean flow.

Fig. 31 presents the variation of  $\Omega$  with normalised  $KE$  and  $KE_{fluc}$  over the entire range of  $P$  and  $Re$ .

- Effect of  $P$ : lower  $P$  values correspond to lower  $KE$ , and the difference between  $P = 200 \mu\text{m}$  and  $P = 300 \mu\text{m}$  is approximately 27–33%, as increased confinement limits flow acceleration and instabilities generation.
- Effect of  $Re$ : as  $Re$  increases,  $KE$  naturally increases. However, at  $Re = 40$ ,  $KE$  is low, and  $\Omega$  is relatively high for all  $P$  values, indicating that even under low energy flux conditions, stronger rotational structures are formed.
- Effect of instability: unstable flow cases generally exhibit the highest  $\Omega$  values because they contain more vortical structures than steady flow ones. However, bidirectional pin fins with the lowest  $P$  values exhibit particularly high  $\Omega$  in unstable cases, likely due to the flow confinement and stabilisation effects of directing the flow to walls.

It is important to note that  $KE$  exhibits a parabolic dependence on  $\Omega$  for varying  $Re$  at constant  $P$  and for varying  $P$  at constant  $Re$ . An exception occurs in the unstable cases of cylindrical pin fins where  $Re = 117$ . This parabolic trend arises from the interaction between flow blockage, acceleration around the pin, and unsteady flow generation:

- At higher  $P$ , flow unsteadiness increases, leading to increased  $KE$  and  $\Omega$ .
- At lower  $P$  and low  $Re$ ,  $\Omega$  increases due to strong, stagnant vortices in the steady flow.

For different pin fin configurations, the vertex of the parabola – indicating the optimal balance between flow instability and flow stability – occurs at:

- Cylindrical pin fins:  $P \approx 250 \mu\text{m}$ ,  $Re \approx 70\text{--}85$
- Unidirectional pin fins:  $P \approx 250\text{--}275 \mu\text{m}$ ,  $Re \approx 55\text{--}70$
- Bidirectional pin fins:  $P \approx 250 \mu\text{m}$ ,  $Re \approx 70$

These vertices may represent critical points where the optimal spacing enhances convective cooling while maintaining steady flow. In cooling applications, transitioning to a steady regime is beneficial in low-power or idle states when efficient cooling with minimal noise and energy consumption is required.

At moderate  $P$  ( $\sim 250 \mu\text{m}$ ), flow unsteadiness is maximised without excessive blockage, resulting in peak efficiency. On the other hand, at high  $P$ , the distance between pins becomes too large to effectively disrupt the flow; thus,  $KE_{fluc}$  reduces and  $\Omega$  increases.

The relationship between  $KE_{fluc}$  and  $\Omega$  provides insight into the onset of flow instabilities. A sharp increase in  $KE_{fluc}$  indicates the development of unsteady flow.

For cylindrical and unidirectional pin fins,  $KE_{fluc}$  increases by a factor of up to 100 from  $Re = 40$  to  $Re = 117$ , representing a significant unsteady flow enhancement. These instabilities may improve heat transfer efficiency by increasing mixing and convective transport. However, they also contribute to higher hydraulic losses, which must be considered in practical applications.

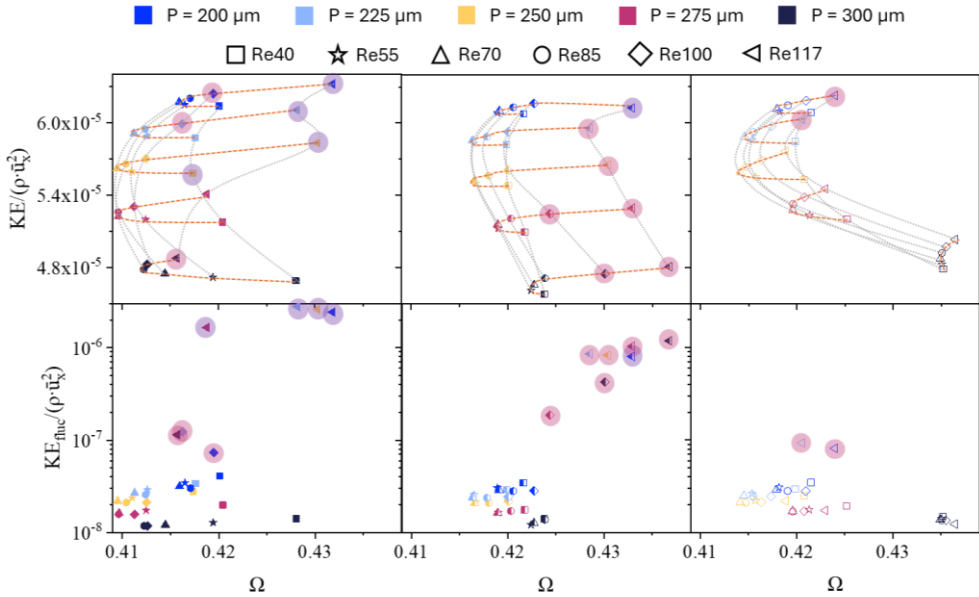


**Fig. 31.** Normalised  $KE$  and  $KE_{fluc}$  dependency on  $\Omega$  of K-type geometries

#### 4.4. Heat transfer

The results and analysis presented in Section 4.4. are also presented in the publication <sup>5,7</sup>.

Heat transfer analysis of R-C, R-T, and R-H configurations was conducted using  $Nu$  and temperature non-uniformity ( $\delta_T$ ) as performance evaluation metrics. Additional graphs are provided, showing the wall temperature ( $T_w$ ) and the average temperature ( $T_{ave}$ ). In this section, the flow is treated as compressible (water properties taken from the OpenFOAM database), and all computations are performed in a cyclic domain.

Similar to the previously analysed  $f$  trends, the R-T8-B configuration exhibits distinct heat transfer behaviour. Despite having the lowest  $T_{ave}$ , it maintains the highest  $T_w$  due to its steady flow characteristics and the presence of stagnant vortices. As a result, it also has the lowest  $Nu$ , up to twice that of R-C-S.

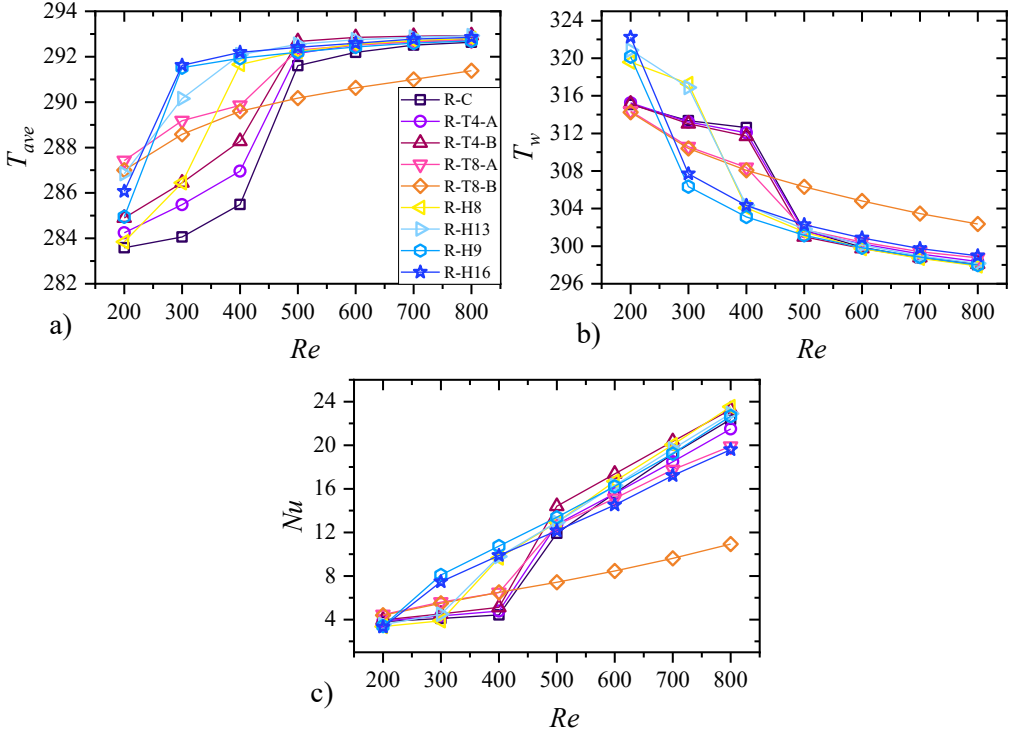


**Fig. 32.** Variation of a)  $T_{ave}$ , b)  $T_w$ , and c)  $Nu$  for different configurations across the investigated  $Re$  of R-type geometries

Comparing the  $Nu$  deviation of each configuration to R-C-S across different  $Re$  yields mixed results (see Table 16). It was calculated as follows:

$$Nu \text{ Deviation} = \frac{1}{n} \sum_{i=1}^n \frac{Nu_{Re=i}^{any \ case} - Nu_{Re=i}^{R-C}}{Nu_{Re=i}^{any \ case}} \quad (63)$$

For instance, R-T8-A demonstrates superior hydraulic performance across the entire  $Re$  studied (see Section 4.1. Friction factor and flow topology). However, its thermal performance deteriorates in the specific range of  $500 \leq Re \leq 800$  (this range was chosen because all cases (except R-T8-B) have transitioned to unstable flow). The same applies to R-T4-A and R-H16 cases. In most cases studied, when  $Re \geq 500$ , the  $Nu$  values decrease compared to the overall trend (see Table 15). This does not indicate a drop in performance but instead reflects an uneven transition to unsteady flow, leading to these results. Once the transition stabilises, the trend is expected to continue (after  $Re = 500$ , except for the R-T8-B case). Consequently, R-T4-B and R-H8 stand out as the most significant cases due to the highest deviation in  $Nu$  compared to the base cylindrical pin fin array.

**Table 16.** Deviation of  $Nu$  from the R-C-S case for R-type geometries

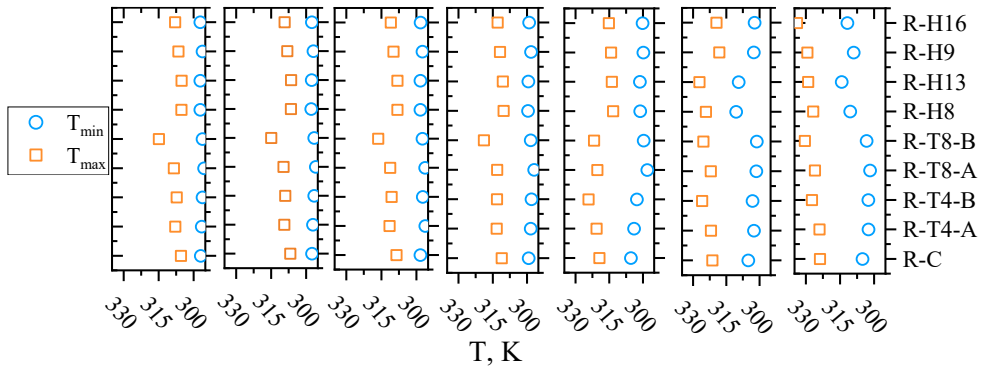
$Nu$ Deviation (%)	R-T4-A	R-T4-B	R-T8-A	R-T8-B	R-H8	R-H13	R-H9	R-H16
$200 \leq Re \leq 800$	1.80%	9.13%	7.92%	-39.67%	8.40%	10.33%	16.09%	7.77%
$500 \leq Re \leq 800$	-2.71%	6.60%	-7.87%	-96.04%	5.23%	3.01%	1.78%	-11.01%

Fig. 33 represents the minimum and maximum wall temperatures, while Fig. 34 shows the difference between them, defined as  $\delta_T$ :

$$\delta_T = T_{max} - T_{min} \quad (64)$$

The parameter  $\delta_T$  provides insight into the uniformity of heat distribution within the system. The lowest  $\delta_T$  values are observed for the R-H13, R-H8 and R-C-S cases, indicating a more uniform heat distribution, which is generally favourable for thermal management. Despite this, hourglass-shaped pin fins exhibit the highest  $T_{min}$  at low  $Re$  numbers and some of the lowest  $T_{max}$  at high  $Re$ , suggesting a potential benefit in stabilising temperature fluctuations across different flow regimes.

As previously mentioned, the R-T4-B demonstrates a higher  $Nu$  compared to R-C-S. However, its  $\delta_T$  remains among the highest, indicating a less uniform heat distribution. Additionally, its  $T_{max}$  in the low  $Re$  range is one of the highest, suggesting the formation of localised hot spots with greater temperature differences than the other configurations.



**Fig. 33.**  $T_{min}$  and  $T_{max}$  wall temperatures for different configurations

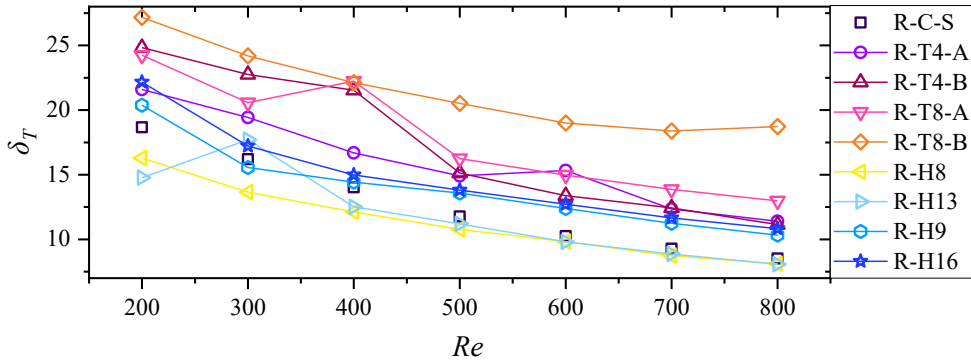


**Fig. 34.**  $\delta_T$  for different configurations across the investigated  $Re$  range of R-type geometries

#### 4.5. Overall performance

The results and analysis presented in Section 4.5. are also presented in the publication<sup>5,7</sup>. In this section, the flow is treated as compressible (water properties taken from the OpenFOAM database), and all computations are performed in a cyclic domain.

The findings indicate that even minor changes in obstacle geometry, such as the conicity angle, can significantly impact fluid patterns and heat transfer efficiency. Variations in the obstacle’s cross-sectional profile introduce secondary flows, which enhance convection and heat transfer. However, secondary or jet-like flows in pin fin arrays come with a significant drawback: unsteady flow significantly increases  $\Delta p$ . As a result, it is important to carefully design the flow field to minimise unnecessary hydraulic losses from vortex generation, flow instability, and secondary flow formation.

To assess the balance between heat transfer and pressure loss, the  $TPI = Nu/f^{1/3}$  is used to measure overall efficiency in various pin fin arrangements (see Fig. 35). In the low  $Re$  region ( $Re = 200-300$ ), the  $TPI$  values of R-T8-A and R-T8-B are the highest, 13–25% higher than R-C-S. However, at high  $Re$  ( $Re = 500-800$ ), R-T8-B has not experienced a regime change and has the lowest  $TPI$  values, 41–66% lower than R-C-S. Meanwhile, the  $TPI$  of the R-T8-A is also a few per cent lower than that of R-C-S.

Among the pin fin designs studied, R-T4-B, followed by R-H8, performed best across the full range of  $Re$  values. R-T4-B improved  $TPI$  by an average of 10% across the entire investigated  $Re$  range, while R-H8 improved  $TPI$  only after the transition by an average of 6%. In the steady flow regime, this case is 7% lower than R-C-S.

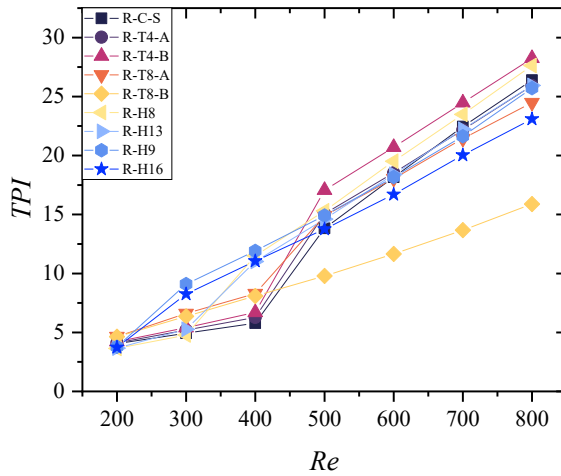


**Fig. 35.** Time-averaged impact of pin fin shape on the  $TPI$  as a function of  $Re$

#### 4.6. Performance evaluation using flow dynamics

The results and analysis presented in Section 4.6., as well as in all its subsections, are also presented in the publication<sup>4,7</sup>.

An optimally designed pin fin configuration should generate sufficient unsteadiness to facilitate efficient thermal transport while minimising hydraulic losses. Unsteadiness enhances mixing in the flow, thereby increasing convective heat transfer and improving overall cooling performance. The Thermohydraulic Performance Index ( $TPI$ ) formula accounts for both  $f$  and  $Nu$ , yielding a balanced measure of thermal efficiency versus flow resistance. However, it does not explicitly include an unsteady-flow parameter, even though unsteadiness is a critical mechanism for friction losses and for enhancing heat transfer. In essence, while  $TPI$  indirectly captures the effects of unsteadiness through its influence on friction and heat transfer, it does not directly quantify the intensity or magnitude of unsteady flow.

In CFD, modelling heat transfer processes, especially at fine resolutions, can be resource-intensive, requiring substantial computing time and power. For this reason, excluding direct heat transfer modelling could lead to significantly faster evaluations, allowing faster design iterations and optimisations, especially when exploring a wide range of pin fin or other cooling configurations. To achieve this, unsteadiness-related parameters could replace  $Nu$  in performance evaluation. By using unsteadiness indicators such as turbulent kinetic energy, dissipation rate, or even  $\Omega$  criteria, an alternative formula can be derived to estimate an apparent or "virtual" thermohydraulic efficiency.

An attempt to develop such an unsteadiness-based performance metric will be presented in this section.

#### 4.6.1. Performance evaluation using kinetic energy

The quantities  $KE_{fluc}$  and  $KE$  can be used as indicators of the efficiency of pin fin arrays in evaluating flow disturbances and heat transfer. An optimally designed pin fin configuration should generate sufficient instabilities to facilitate efficient thermal transport while minimising hydraulic losses.

Areas with higher  $KE_{fluc}$  generally correlate with increased heat transfer coefficients (Saito & De Lemos, 2006), indicating enhanced convective performance. The ratio  $KE/KE_{fluc}$  is a dimensionless parameter that quantifies the proportion of total kinetic energy associated with turbulent fluctuations. This ratio allows comparison of different pin fin designs in terms of their unsteadiness-inducing capabilities.

Moreover, the  $f$ , another dimensionless quantity, represents the resistance to flow due to friction and is influenced by both the flow regime and the geometric configuration. By simultaneously analysing the  $KE/KE_{fluc}$  ratio and the  $f$ , it is possible to predict the thermal characteristics of a pin fin array without directly simulating the heat transfer. As the flow transitions from steady to unsteady,  $KE_{fluc}$  increases exponentially. Applying the natural logarithm to this relationship linearises the data, making it easier to interpret.

$Tef$  is introduced as an efficiency indicator, linking  $f$  to the ratio of total and fluctuating kinetic energy. It is intended to capture the balance between flow stability, vortex-induced instabilities, and their contribution to convective heat transfer:

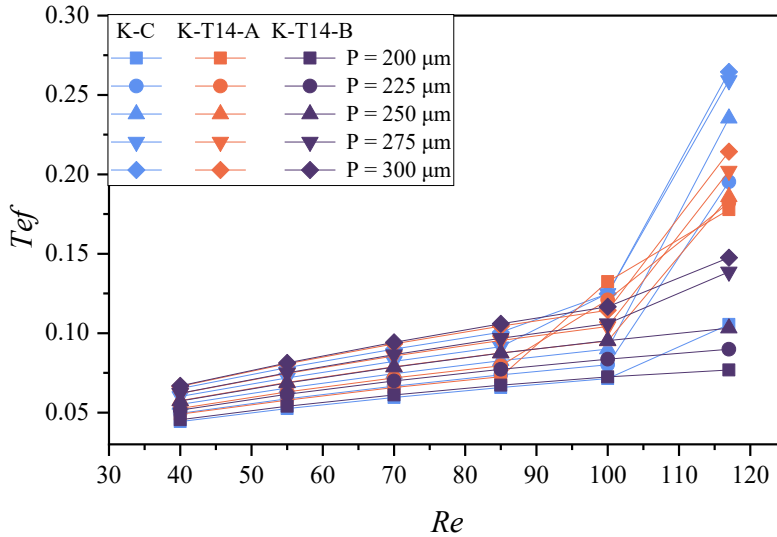
$$Tef = \frac{1}{f \cdot \ln\left(\frac{KE}{KE_{fluc}}\right)} \quad (65)$$

Fig. 36 presents the results of eq. 35 with varying  $P$  and  $Re$ . The data reveal a trend:  $Tef$  increases with increasing  $Re$ . Furthermore, when the  $P$  is constant, and the flow remains stable, the cylindrical pin fin arrays exhibit the lowest  $Tef$ , suggesting lower flow instabilities and thermal efficiency in this regime. At low  $P$  under steady-flow conditions, unidirectional (A) pin fin arrays exhibit the highest  $Tef$  values. However, this trend changes at higher  $P$ , where bidirectional pin fin arrays become the most efficient.

With the onset of flow instabilities, typically around  $Re \approx 100$ ,  $Tef$  increases sharply, indicating that the increased flow unsteadiness has significantly improved thermal performance. For instance, comparing  $Re = 100$  and  $Re = 117$ , the increase in  $Tef$  can be substantial: from 21% in bidirectional arrays to 62% in cylindrical pin fin arrays with  $P = 300$  and 250, respectively.

However, this increase in efficiency is primarily driven by the magnitude of  $KE_{fluc}$ . At  $Re = 117$ , the cylindrical pin fin array is the most efficient because its  $KE_{fluc}$

and  $KE$  values are high under unstable flow conditions. Furthermore, in highly unstable regimes, the vortical structures within cylindrical pin fin arrays have one of the highest surface areas.

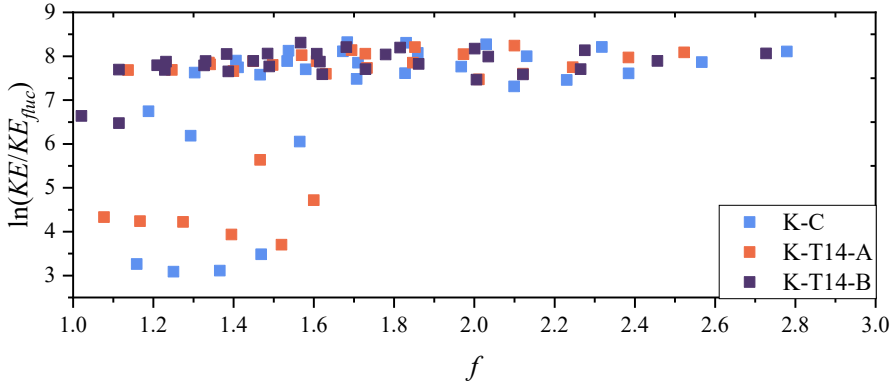


**Fig. 36.** Comparison of  $Tef$  of different K-type geometries

Fig. 37 graphically depicts the correlation between the  $f$  and the kinetic energy component defined in eq. 46 to clarify the relationship between flow resistance and unsteady flow characteristics. Most of the data points cluster at high values of  $\ln(KE/KE_{fluc})$ , with a broad distribution of  $f$  values. This suggests that the  $f$  can vary significantly depending on other influencing parameters.

Conversely, at lower values of  $\ln(KE/KE_{fluc})$ , the  $f$  exhibits a less pronounced increase, indicating a weaker dependence on instabilities in these regimes. As discussed earlier, the  $f$  is highly sensitive to both the  $Re$  and the  $P$ , which accounts for the variability in  $f$  observed at unsteady flows.

The trend observed when  $\ln(KE/KE_{fluc}) < 7$  can be attributed to the onset of flow instabilities. These instabilities lead to a significant reduction in  $\ln(KE/KE_{fluc})$  and are accompanied by a corresponding decrease in the  $f$ , highlighting the transitional behaviour in the flow dynamics.



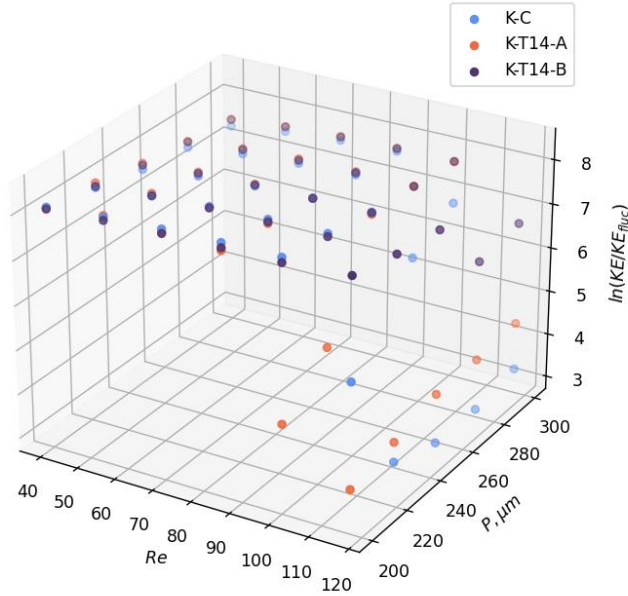
**Fig. 37.**  $\ln(KE/KE_{fluc})$  versus  $f$ .

Fig. 38 highlights that the dependence of  $\ln(KE/KE_{fluc})$  on both  $Re$  and  $P$  remains relatively weak before the onset of a flow regime transition happens. This observation aligns with trends previously noted in Fig. 37. While the geometry of pin fins influences local flow features, such as vortex shedding, wake formation, and frictional effects, the kinetic energy is a more reliable indicator of overall flow behaviour.

The  $Re$  remains a key parameter in predicting the transition from steady to unsteady flow. Despite that, once the flow stabilises in the steady regime, the kinetic energy characteristics tend to remain consistent and largely independent of specific geometric variations. As a result, the differences among steady cases (characterised by  $\ln(KE/KE_{fluc}) > 7$ ) are minimal. In contrast, more substantial variation emerges in the unsteady regime, where geometric effects become more pronounced.

The interaction between  $Re$  and pin fin geometry dictates the onset, structure, and persistence of flow unsteadiness. In the range where  $\ln(KE/KE_{fluc}) < 7$ , flow characteristics become increasingly sensitive to geometric configuration, underscoring the role of geometry in triggering and shaping unsteady flow behaviour.

In summary, following the transition to unsteady flow, both  $Re$  and  $P$  significantly influence the system's kinetic energy dynamics.  $Re$  governs flow instabilities, while geometric features regulate flow patterns and promote unsteadiness through localised disturbances. Together, these factors control the distribution and dissipation of energy within the flow field, making them critical design considerations in microchannel heat transfer applications.



**Fig. 38.**  $\ln(KE/KE_{fluc})$  dependence on  $Re$  and  $P$

To integrate the initial parameters,  $Re$  and  $P$ , with the components of the thermal efficiency factor  $Tef$  and  $Tef$  itself, an additional visualisation was constructed (see Fig. 39). The colour scale in this figure represents the magnitude of  $Tef$ . The graph clearly distinguishes between stable and unstable flow regimes: in unstable flows,  $\ln(KE/KE_{fluc})$  tends to be lower, whereas in stable flows with higher  $Re$ ,  $f$  is reduced.

Among the tested geometries, the bidirectional conical pin fin configuration yields the lowest values  $\ln(KE/KE_{fluc})$ . Interestingly, the  $f$  remains relatively insensitive to pin fin shape, although specific geometries affect other flow parameters. In cylindrical pin fin arrays, the  $P$  strongly influences  $\ln(KE/KE_{fluc})$ , whereas in bidirectional configurations, the  $f$  is more sensitive to  $P$  variations. These results suggest that the  $f$  is a dominant factor in determining microchannel performance. For example, at  $Re = 100$ , two cylindrical pin fin arrays with  $P = 300 \mu\text{m}$  and  $275 \mu\text{m}$  show a 9% difference in  $f$  and an 8% difference in  $\ln(KE/KE_{fluc})$ . Yet,  $Tef$  remains nearly unchanged – highlighting the leading role of friction in certain conditions.

However, this is not universally true. As shown in Fig. 39 b), for cases with similar friction coefficients ( $1.45 < f < 1.58$ ), the ordering of friction values does not align with trends in  $Tef$ . This indicates that, within the range of parameters studied, the kinetic energy component in eq. 46 can exert an influence on  $Tef$ , which competes with the  $f$ . Therefore, both terms should be considered when evaluating and optimising the thermal-hydraulic performance of pin fin microchannel systems.

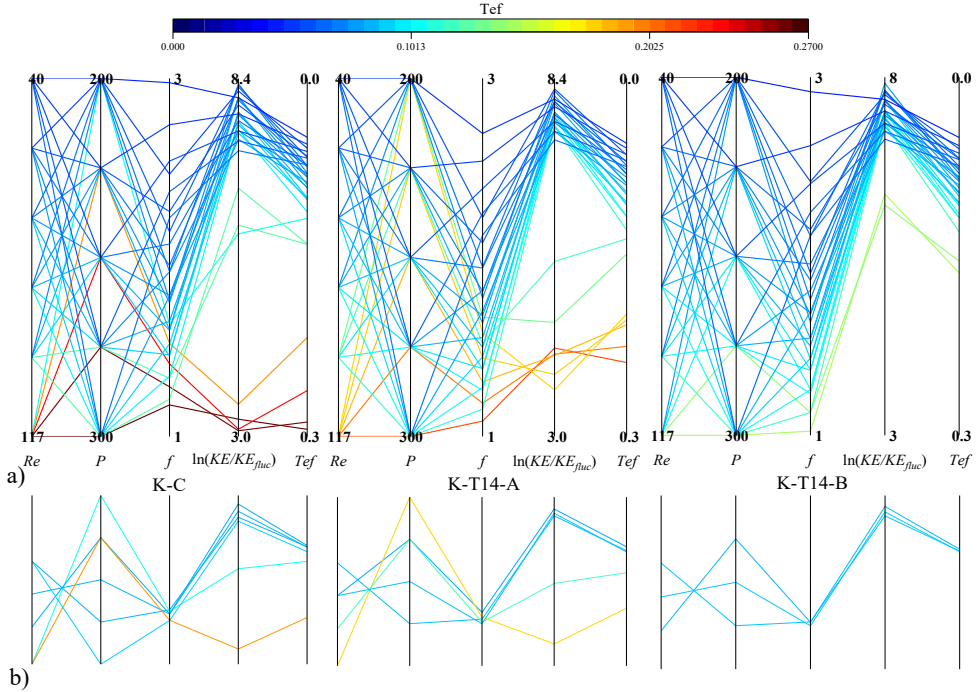


**Fig. 39.** Dependence of  $T_{ef}$  on  $f$  and  $\ln(Ke/KE_{fluc})$  for each  $Re$  and  $P$  set a) all modelled cases, b) selected cases with similar  $f$ .

In summary, evaluating the magnitudes of  $KE_{fluc}$ ,  $KE$ , and the  $f$  enables the preliminary optimisation of thermal and hydraulic performance before conducting detailed heat transfer simulations. A higher  $KE/KE_{fluc}$  ratio indicates more intense flow redistribution, which can enhance convective heat transfer, while the  $f$  reflects the energy loss due to flow resistance. These energy-based analyses provide valuable insights that help develop more accurate predictive models and efficient simulation frameworks for pin fin array systems. The proposed methodology establishes a basis for integrating coherent vortex analysis into the design of microchannel cooling systems, thereby facilitating future optimisation efforts.

#### 4.6.2. Performance evaluation using $\Omega$

The performance evaluation using coherent structures may be very beneficial when heat transfer is not simulated and thermohydraulic efficiency is to be predicted. The vortical structure area, including its volume, may indicate the potential for vortex shedding. High  $V_{\Omega}$  shows the volume occupied by vortices, while  $A_{\Omega}$  shows the surface interaction level. A high  $A_{\Omega}$  indicates interface-rich flow, which enhances convective heat transfer. Moreover,  $\Omega_v/\Omega_{ov}$  shows the strength of vortices related to the whole

flow. In comparison, transverse velocity components can show the strength of side circulation.

Therefore, the formula for efficiency evaluation was selected to consist of:

$$\begin{aligned} & \text{Vortical volume and area} \cdot \text{vortex strength} \\ & \cdot \text{transverse velocity components} \end{aligned}$$

And has a form of:

$$\eta_{\Omega} = 1.25 \cdot \sqrt{\left(\frac{A}{A_{\Omega}} \cdot \frac{V}{V_{\Omega}}\right)} \cdot \left(\left(1 - (\Omega_v - \Omega_{ov})\right) \cdot \Omega_v\right)^2 \cdot \left(\frac{L \cdot \sqrt{u_z^2 + u_x^2}}{\nu}\right)^{0.8} \quad (66)$$

In many convective systems, circulation does not occur strictly along the primary direction (in this case, the y-direction); instead, weaker transverse motions arise due to buoyancy forces, wall effects, or vortices. These cross-stream velocities, even if not dominant, play an important role in transporting fluid from near the heated walls into the bulk flow and bringing cooler fluid back toward the surface. This continual exchange reduces the thickness of the thermal boundary layer, steepens the temperature gradient at the wall, and thereby increases the Nusselt number. In this way, the formula captures how the intensity of side circulation governs the effectiveness of convective heat transfer, linking transverse momentum transport directly to thermal performance. The term  $\sqrt{u_z^2 + u_x^2}$  capture the strength of side circulation. This expression is Nusselt/Reynolds-based for side circulation:

$$\frac{L \cdot \sqrt{u_z^2 + u_x^2}}{\nu} \quad (67)$$

It predicts the amount of extra mixing within the thermal boundary layer.  $L$  is the same as used for calculating the Nusselt number.

The velocity components,  $u_y$ ,  $u_z$  and  $u_x$ , were evaluated over different fractions of the channel height to assess their representativeness for predicting heat transfer efficiency (see Fig. 40). Their magnitude provides a direct indication of how effectively heat can be transported away from the heated surface, and consequently, of the expected Nusselt number.

Initially, the average values of  $\sqrt{u_z^2 + u_x^2}$  were calculated across the full channel height. However, concerns were raised that stagnation zones and vortical recirculation far from the heated walls may artificially inflate the apparent transverse velocity without contributing meaningfully to wall-bulk exchange. To address this, reduced sampling regions were considered, limited to 10% and 20% of the channel height adjacent to the heated walls (see Fig. 40). The results confirmed that the 10% region underestimates the effective circulation, producing poor correlation with the modelled Nusselt numbers, whereas the 20% region yielded the highest predictive accuracy

(lowest RMSE, MAE, and MAPE; highest  $R^2$ ) (see Table 17). Nevertheless, the full-height definition was ultimately adopted as the preferred metric. While its statistical performance is slightly below the 20% case, it still provides reliable prediction accuracy. It is far more practical, since it avoids the need for localised sampling and can be applied consistently across cases (Fig. 41). In this way, the use of full-height averaged transverse velocity components balances physical representativeness with methodological simplicity and remains an effective proxy for quantifying the intensity of side circulation responsible for heat transfer enhancement.

**Table 17.** Correlation between Nusselt number and transverse velocity metric for different channel height fractions

<b>Metric</b>	<b>10 % of</b>	<b>20 %</b>	<b>Full height channel</b>
<b>Pearson <math>r_p</math></b>	0.975799	0.988723	0.988210
<b><math>R^2</math></b>	0.952183	0.977573	0.9766
<b>Spearman <math>\rho_s</math></b>	0.975950	0.988383	0.9882
<b>Linear fit</b>	$Nu = 1.019527 + \frac{0.795944 \cdot L \cdot \sqrt{u_z^2 + u_x^2}}{\nu}$	$Nu = 1.318226 + \frac{0.630245 \cdot L \cdot \sqrt{u_z^2 + u_x^2}}{\nu}$	$Nu = 3.3155 + \frac{0.25675 \cdot L \cdot \sqrt{u_z^2 + u_x^2}}{\nu}$
<b>RMSE</b>	1.4404	0.986	1.01
<b>MAE</b>	1.1140	0.776	0.80
<b>MAPE</b>	12.70 %	8.59 %	8.8 %

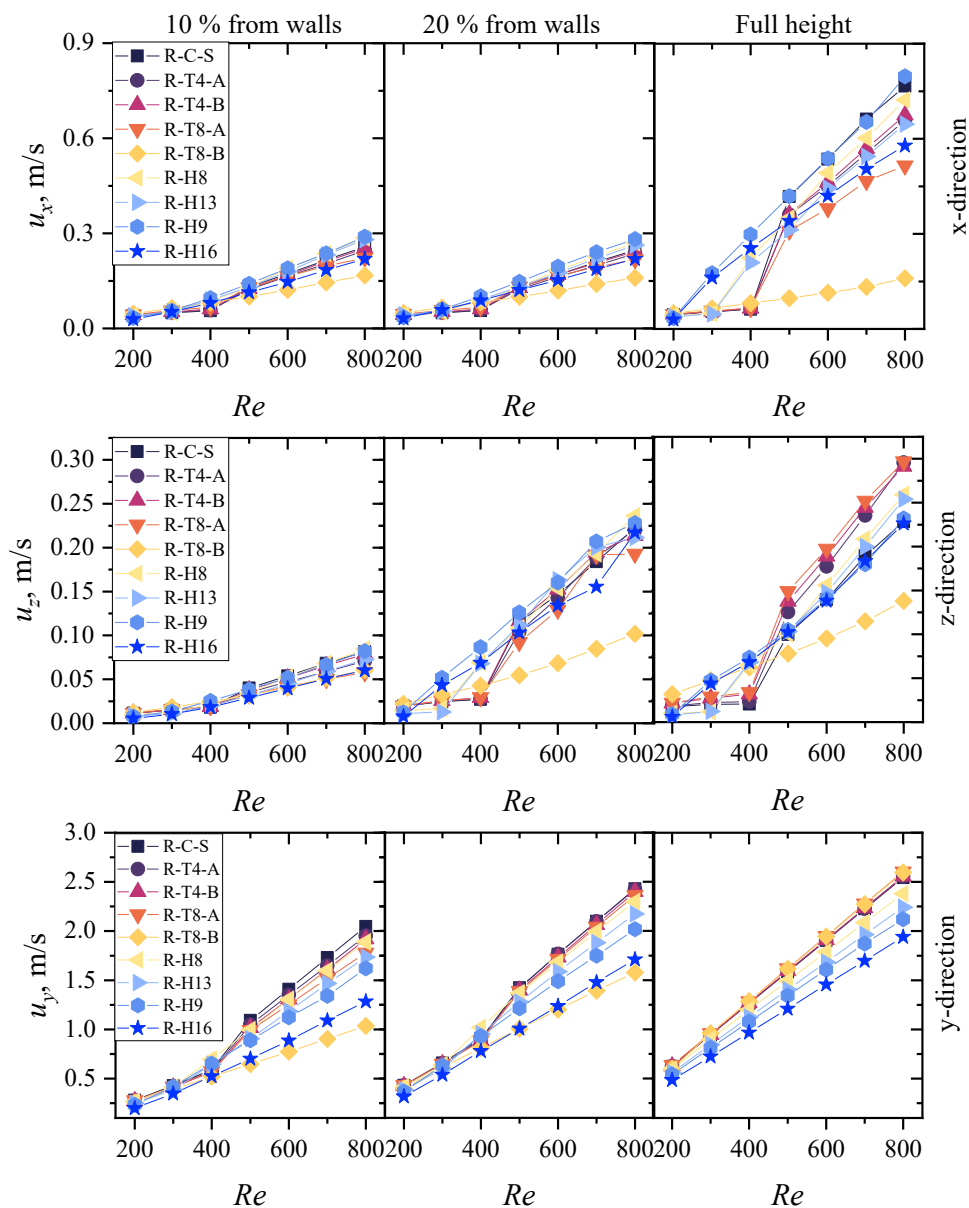


**Fig. 40.** Velocity components metrics for different averaging height

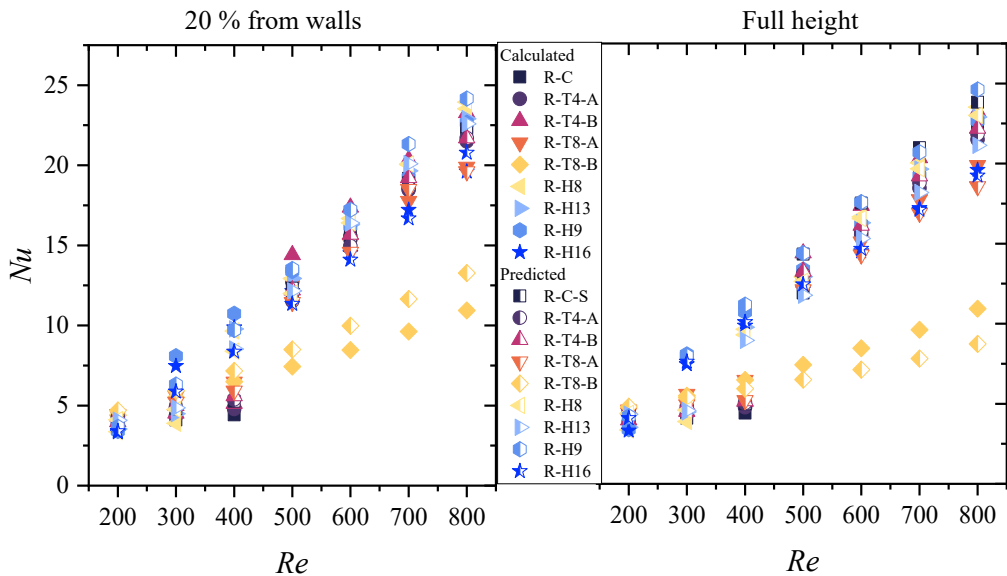


**Fig. 41.** Modelled and predicted  $Nu$  based on transverse velocity components

Fig. 42 shows values of every component of eq. 69. The first component shows the relative vortical volume and area and represents the interface area and occupied volume of vortical structures. Low values reflect intense interaction between vortices and the surrounding fluid – potentially enhancing convective heat transfer. The second component represents the relative strength of coherent structures. It is effectively a self-limiting mechanism: high  $\Omega_v$  is beneficial until it becomes excessive relative to the background flow. Therefore, the term penalises excessively strong vortices relative to the overall flow, promoting a balance between coherent mixing and energy efficiency. The final component contrasts the beneficial vertical flow, which helps transfer heat from the wall to the core.

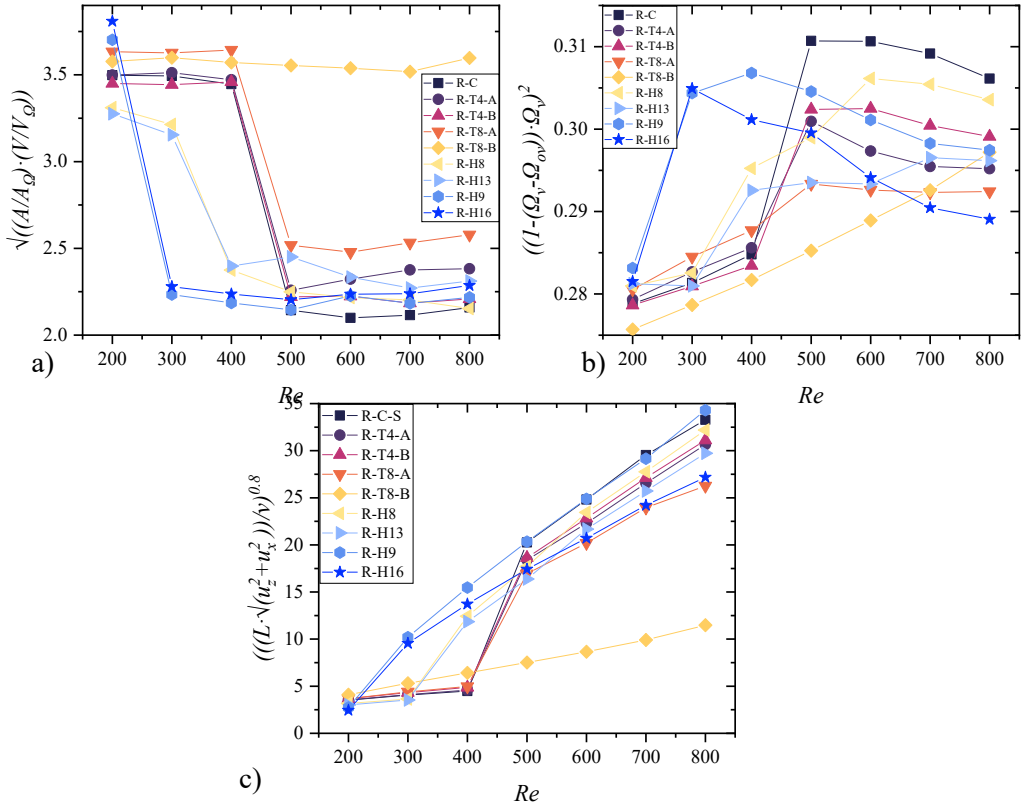


**Fig. 42** a)  $\sqrt{\left(\frac{A}{A_\Omega} \cdot \frac{V}{V_\Omega}\right)}$  b)  $\left((1 - (\Omega_v - \Omega_{ov})) \cdot \Omega_v\right)^2$  c)  $\left(\frac{L \cdot \sqrt{u_z^2 + u_x^2}}{v}\right)^{0.8}$  vs  $Re$

Parallel coordinates plot (see Fig. 43) provides a comprehensive multivariable visualisation of thermohydraulic efficiency  $\eta_\Omega$  across different flow configurations and  $Re$ . Each polyline represents a specific case (e.g., R-H16, R-T8-B, etc.), with colour indicating the resulting efficiency, ranging from low (purple) to high (red), as shown by the colour bar on the right.

The first and second axes identify the geometric cases tested, followed by  $Re$ , which provides insight into the flow regime. The third axis combines two geometric descriptors of vortical structures: the normalised surface area and volume of vortices

$\sqrt{\left(\frac{A}{A_\Omega} \cdot \frac{V}{V_\Omega}\right)}$ , representing how effectively vortices interact with the flow. Lower values in this dimension indicate enhanced mixing and convective heat transfer

potential. The next axis,  $((1-(\Omega_v-\Omega_{ov}))\cdot\Omega_v)^2$ , penalises excessively strong vortices, favouring cases where vortex strength is significant but not overwhelmingly dominant relative to the overall flow.

Subsequent axes assess the transverse motion of the flow. The normalised vertical velocity component reflects beneficial wall-to-core heat transport. The final axis shows the computed thermohydraulic efficiency  $\eta_\Omega$ , which integrates these flow-structure metrics into a single performance measure.

From the plot, high-efficiency designs (represented by red-orange lines) favours design with  $A_\Omega$  and  $V_\Omega$ , especially when accompanied by a strong transverse velocity component that supports convective transport from the heated walls to the main flow. It is clear from the multivariable analysis (Fig. 43) that first component divides cases to two parts lower and higher than 3, higher shows that vortices are small, under development, and in most cases, they do not result in high  $\eta_\Omega$ . While low values show high vortex interaction. Configurations such as R-H8, R-H9, and R-H13 clearly fall into this category. In contrast, lower-efficiency designs like R-T4-A show weak vortex development and low transverse transport. Additionally, increasing the  $Re$  generally improves performance, especially for geometries that enhance coherent vortex formation and flow alignment.

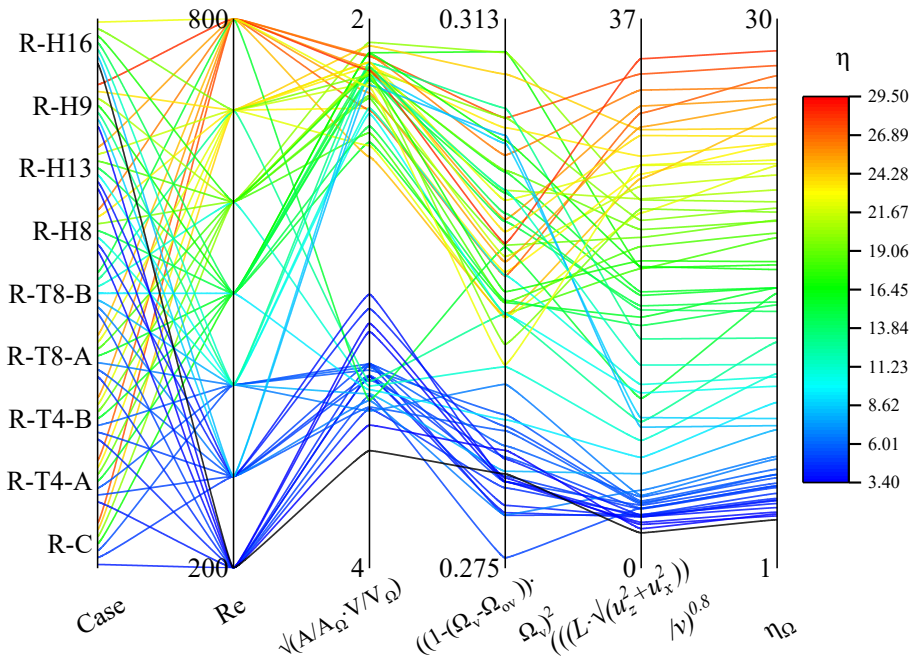


**Fig. 43.** Multivariable analysis of thermohydraulic efficiency based on vortex geometry, energy distribution and flow directionality

Fig. 44 presents the thermohydraulic efficiencies  $TPI$  and  $\eta_\Omega$  across various design configurations under a range of flow conditions. Also, the error for each  $Re$  for all geometries is shown in Fig. 45 and comparison of original  $TPI$  and calculated  $\eta_\Omega(TPI)$  values is given in Fig. 46. The proposed formula  $\eta_\Omega$  provides an excellent approximation of the target  $TPI$  values. By combining the three datasets through a power-law relationship, it captures both the scaling behaviour with transverse velocity component and the moderating influence of vortices interaction and strength. The fit reproduces the original  $TPI$  table with very high accuracy – the overall error across all data points ( $Re = 200–800$ ) remains small, and the numerical trends align closely with the given values. Across nine configurations and  $Re = 200–800$ , the per cent errors between  $\eta_\Omega$  and  $TPI$  are small overall (MAPE  $\approx 6.1\%$ , median  $4.8\%$ ). By configuration, the lowest average deviations occur for R-H16 ( $\sim 4.0\%$ ) and R-H8 ( $\sim 4.3\%$ ), followed by R-T8-B ( $\sim 4.5\%$ ), while R-H9 shows the highest mean error ( $\sim 9.2\%$ ). The main outlier is 25% at  $Re = 300$  for R-H13; otherwise, variability is modest, especially for R-H16, R-T4-A, R-H8, and R-H9. The formula preserves the expected rankings between columns, keeping R-T4-B among the highest, R-T8-B as the lowest, and R-H16 near the bottom. The Spearman correlation is 0.99, indicating a monotonic relationship. Taken together, the data indicate that the proposed  $\eta_\Omega$  formula closely tracks  $TPI$  across flow conditions and largely preserves the expected ranking across designs.

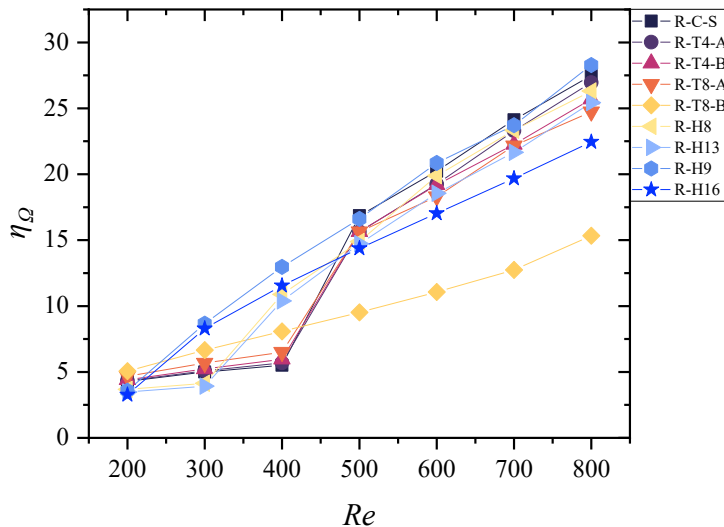


Fig. 44  $\eta_\Omega$  dependence on  $Re$

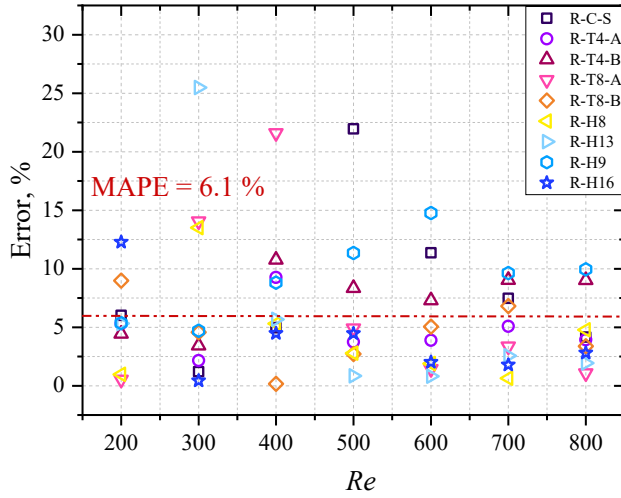


Fig. 45. Errors in numerical values of  $\eta_{\Omega}$  compared to  $TPI$

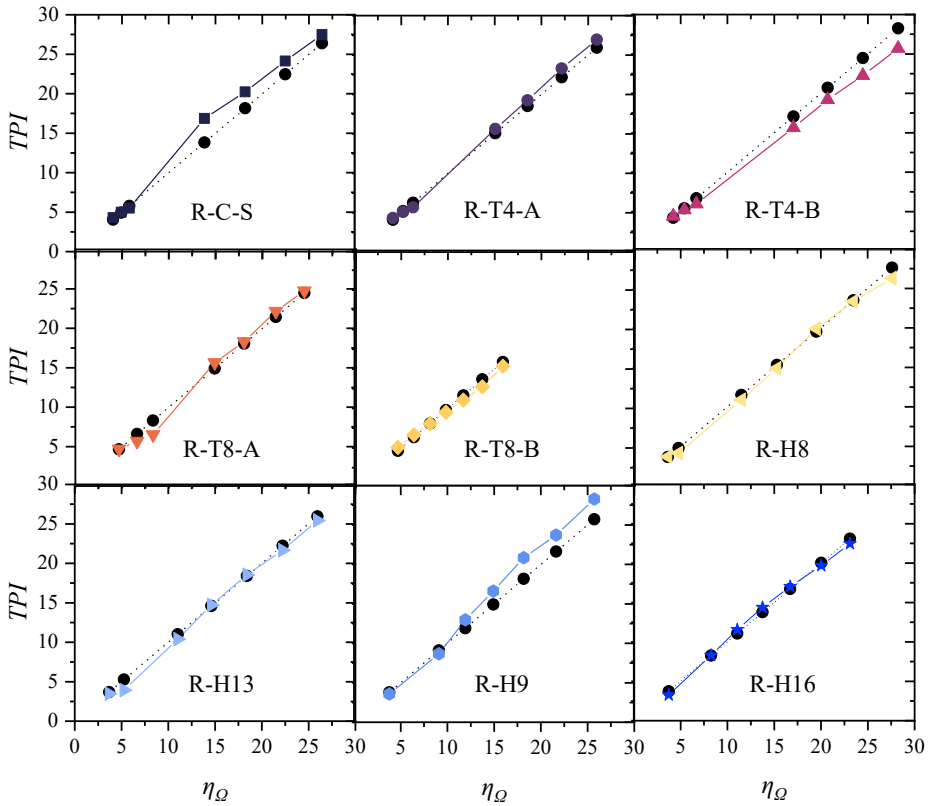


Fig. 46 Comparison of original  $TPI$  (black line) with calculated  $\eta_{\Omega}(TPI)$  values

## 5. CONCLUSIONS

This study employed numerical modelling to investigate the characteristics of coherent flow structures and their impact on the thermohydraulic performance of various microchannel configurations, including Cylindrical (C) as the baseline, Hourglass (H), and Tapered conical (T) pin fins. For T, there is unidirectional (A) and bidirectional (B) conicity orientation. Based on the simulation results obtained for  $Re$  in the range of 200–800, the following conclusions were drawn:

1. Small-angle ( $< 8^\circ$ ) variation in the cross-sectional profile along the axis slightly increases ( $\sim 7\%$ ) or does not change the pressure drop when the flow is steady. When the flow is unsteady, the pressure can be decreased by an average of 6%. While modest angles ( $> 8^\circ$ ) increase pressure drop in the steady regime by  $\sim 13\%$ , and by  $\sim 5\%$  in the unsteady regime, except for the R-T8-B configuration, which reduces pressure drop by 23%. This configuration does not experience unsteady flow and has one of the lower thermal performances. Furthermore, small-angle T pin fins increase both  $Nu$  and  $TPI$  values by 1–11% compared to C. Whereas, H pin fins decrease both  $TPI$  and  $Nu$  when comparing overall steady or unsteady cases to C.
2. When the flow regime changes,  $V_Q/V$  increases from 15% to 32%. Similarly,  $A_Q/A$  rose from 46–55% in a steady flow to 74–81% in unsteady conditions. Regardless of the flow regime, the  $A\Omega$  increases, while  $dV\Omega$  remains steady or decreases in steady flow and decreases in an unsteady regime. This indicates that when the flow regime changes, significantly more vortices are formed due to flow instability (the area and volume of vortices suddenly increase), but later, as the volume decreases while the area increases, vortex breakdown occurs.
3.  $V_Q/V$  increased from 16% to 30% for C pins, from 16% to 26% for H, and from 15.5% to 24% for T as flow transitioned from steady to unsteady conditions. The impact of pin angle was minimal ( $\pm 2\%$ ). On average, the flow around H had the largest  $A_Q/A$  ratio, ranging from 68% to 72%, followed by C (65%) and T (54–66%).  $\Omega$  was greatest in H and lowest in T, with the R-C-S having the maximum overall  $\Omega$  following the flow transition.
4. The created thermohydraulic efficiency assessment method is derived from coherent vortex analysis by integrating vortex interaction area ( $A_Q/A \cdot V_Q/V$ ), vorticity balance ( $(1 - (\Omega_v - \Omega_{ov})) \cdot \Omega_v$ ), and flow transverse motions  $\frac{L \cdot \sqrt{u_z^2 + u_x^2}}{v}$ . The method enables the complete elimination of modelling energy (heat exchange) equations, thereby reducing computational resources and

providing a rapid estimate of thermohydraulic efficiency. The proposed  $\eta_{\Omega}$  formulation shows an MRE of 6.8% compared to TPI. It provides a new analytical perspective that allows for a better understanding of flow-induced mechanisms in cooling systems and complements traditional efficiency indicators.

## 6. SANTRAUKA

### 6.1. Įvadas

Smarkiai mažėjant elektroniniams komponentams, šilumos nuvedimas tampa vis svarbesnė ir sudėtingesnė inžinerinė užduotis. Didėjantis elektroninių sistemų funkcionalumas bei spartėjanti technologinė pažanga lemia tai, kad net kompaktiškuose įrenginiuose susidaro vis daugiau šilumos. Nors pažangūs integriniai grandynai pasižymi geresniu energetiniu efektyvumu, šilumos nuostolių tankis didėja su kiekviena nauja karta. Tai sukuria uždavinį – poreikį efektyviai pašalinti vis daugiau šilumos iš vis mažesnio tūrio sistemų patikimumui, ilgaamžiškumui ir stabiliam veikimui užtikrinti.

Tradiciniai šilumos nuvedimo būdai, tokie kaip natūrali konvekcija ar įprasti šilumokaičiai, nebeatitinka modernių elektroninių sistemų poreikių. Todėl vis dažniau ieškoma pažangių, alternatyvių sprendimų, kurie užtikrintų didesnę šilumos nuvedimo efektyvumą. Vienas iš perspektyviausių metodų laikomas aušinimas mikrokanalais, juos integruojant tiesiai į lustus. Ši technologija leidžia efektyviai pašalinti šilumą iš itin riboto tūrio, pasinaudojant dideliu paviršiaus ploto ir tūrio santykiu bei srauto savybėmis.

Srauto struktūra mikrokanaluose yra vienas esminių veiksnių, lemiančių šilumos mainų intensyvumą ir bendrą šilumokaičių našumą. Tokiuose šilumokaičiuose skystis ar dujos teka per tankiai išdėstytų cilindrinį ar kitokios formos kliūčių masyvą. Dėl šios geometrinės konfigūracijos srautas yra priverstas nuolat keisti kryptį, aptekėdamas kliūtis, o tai lemia sudėtingų sūkurių formavimąsi. Jei srautas yra stabilus, už kiekvienos kliūtis susidaro stovinčių sūkurių zonos – tai šiluminės stagnacijos sritys, kurios gali sukelti vietinį perkaitimą ir sumažinti bendrą aušinimo efektyvumą. Kai srautas tampa nestabilus, už kliūčių ima formuotis atsiskiriantys sūkuriai, kurie tarpusavyje sąveikauja, jungiasi, ir taip sukuria dar sudėtingesnę srauto struktūrą. Nors tai pagerina šilumos mainus, kartu didėja ir slėgio nuostoliai.

Optimaliai suprojektuota kliūčių masyvo konfigūracija turėtų sukurti pakankamą turbulenciją, kad būtų užtikrintas efektyvus šilumos perdavimas, tačiau kartu būtina minimizuoti hidraulinius nuostolius. Turbulencija pagerina skysčio maišymą, taip padidindama konvecinį šilumos mainą ir pagerindama bendrą aušinimo efektyvumą. Termohidraulinio našumo indeksas apjungia tiek  $f$ , tiek  $Nu$ , todėl jis pateikia subalansuotą šiluminio efektyvumo ir srauto pasipriešinimo santykio įvertinimą. Tačiau  $TPI$  formulėje tiesiogiai nėra įtrauktas joks turbulencijos parametras, nors tai yra esminis mechanizmas tiek pasipriešinimo nuostolių, tiek šilumos perdavimo pagerinimo.

Skaičiuojant srauto ir šilumos perdavimo procesus skaitmeniniais metodais (CFD), ypač naudojant didelės raiškos modelius, skaičiavimai gali pareikalauti daug išteklių – tiek laiko, tiek skaičiavimo galios atžvilgiu. Todėl šilumos perdavimo modeliavimo galima atsisakyti, siekiant spartesnio projektavimo ir optimizavimo, ypač atsižvelgiant į platų mikrokanaalų ar kitų aušinimo būdų kiekį.

Turbulencijos parametrai gali būti naudojami kaip alternatyva  $Nu$  našumui įvertinti. Pasitelkiant turbulencijos rodiklius, tokius kaip turbulentinė kinetinė energija, išsisklaidymo greitis ar net  $\Omega$  kriterijus, galima sudaryti alternatyvią formulę, leidžiančią prognozuoti termohidraulinį efektyvumą.

### **Tyrimo objektas**

Srautas mikrokanaaluose su skirtingų formų kliūtimis.

### **Darbo tikslas**

Įvertinus srauto struktūrą mikrokanaaluose sukurti koherentinių struktūrų charakteristikomis pagrįstą termohidraulinio efektyvumo vertinimo metodą

### **Darbo uždaviniai**

Darbo tikslui pasiekti iškelti šie uždaviniai:

1. Ištirti mikrokanaalų kliūčių formos įtaką slėgio nuostoliams ir šiluminiam našumui.
2. Ištirti koherentinių struktūrų charakteristikų kitimą tekmei prarandant stabilumą.
3. Ištirti koherentinių struktūrų formavimosi dėsninumus priklausomai nuo kliūčių formos ir tekėjimo stabilumo.
4. Sukurti koherentinių struktūrų kiekybinę analizę paremtą termohidraulinio efektyvumo prognozavimo metodą.

### **Ginamieji teiginiai**

1. Nedideli kliūčių skerspjūvių pokyčiai išilgai jų ašių padidina mikrokanaalo termohidraulinį efektyvumą. Didesni kliūčių skerspjūvių pokyčiai gali paskatinti nestacionaraus tekėjimo režimo pradžią esant mažesniems Reinoldso skaičiams arba nepakeisti tekėjimo režimo, tai atitinkamai lemia abiejų dydžių padidėjimą arba sumažėjimą.
2. Koherentinių struktūrų plotas nuosekliai didėja, o tūris mažėja, esant stacionariam režimui ir didėjant  $Re$ . Prasidėjus nestacionariam tekėjimui, koherentinių struktūrų tūris ir plotas ženkliai padidėja, po to tūris nuosekliai mažėja, o plotas didėja.

3. Kliūčių skerspjūvių pokyčiai išilgai jų ašių, sumažina koherentinių struktūrų charakteristikų kitimą pasikeičiant tekėjimo režimui.
4. Sukurtas termohidraulinio efektyvumo vertinimo metodas, kuris nesprenžiant energijos lygties, bet kiekybiškai įvertinant koherentinių struktūrų sąveikos paviršių, intensyvumą ir skersinį tekėjimą, prognozuoja tėkmės potencialą nuvesti šilumą.

### **Mokslinis naujumas**

Darbe pirmą kartą mikrokanalų tyrimams pritaikyta koherentinių  $\Omega$  struktūrų analizė, leidusi nustatyti tiesioginį kiekybinį ryšį tarp srauto topologijos ir termohidraulinio efektyvumo. Šis požiūris įgalina prognozuoti šilumos nuvedimo charakteristikas remiantis tik hidrodinaminiais duomenimis (nesprendžiant energijos lygties). Tyrimo pagrindu pasiūlytas tėkmės struktūrine analize grįstas metodas, skirtas projektuoti ir optimizuoti aušinimo sistemas, veikiančias didelio šilumos srauto tankio sąlygomis.

### **Praktinė vertė**

Remiantis analizuotomis srauto charakteristikomis ir kliūčių geometriniais parametrais sukurta metodika leis preliminariai įvertinti, palyginti ir optimizuoti mikrokanalus. Tai palengvins įvairių kliūčių formų ir konfigūracijų projektavimą ir naudojimą, kad būtų galima optimizuoti mikrokanalus naudojant skaičiuojamąją skysčių dinamiką (CFD).

### **Mokslinė sklaida**

Šioje disertacijoje pateikti rezultatai publikuoti 3 moksliniuose straipsniuose žurnaluose ir 1 knygos skyriuje, kurie turi citavimo indeksą ir yra referuojami „Clarivate Analytics“ „Web of Science“ duomenų bazėse. Rezultatai taip pat pristatyti 6 tarptautinėse konferencijose.

## 6.2. Literatūros apžvalga

Šiuolaikinė elektronika sparčiai vystosi, o tuo pačiu didėja jos galia mažėjant fiziniam įrenginių dydžiui. Dėl miniatiūrizacijos žymiai padidėja šilumos tankis, kuris gali siekti  $1000 \text{ W/cm}^2$  (Joshi et al., 2023). Tokios šilumos koncentracijos kelia rimtų problemų komponentų patikimumui – daugiau nei pusė elektronikos gedimų atsiranda dėl perkaitimo (Khattak & Ali, 2019). Nors vibracijos, dulkės ir drėgmė daro įtaką įrenginių veikimui, didėjanti šilumos apkrova tampa dominuojančia rizika.

Elektroninių įrenginių perkaitimas gali sutrikdyti elektroninių grandinių veikimą, sutrumpinti atskirų dalių tarnavimo laiką, sugadinti medžiagas, o kraštutiniais atvejais – visiškai sugadinti įrenginį. Todėl efektyvūs šilumos nuvedimas tampa esminiu veiksmu, užtikrinančiu patikimą mikroprocesorių, atminties lustų ir kitų komponentų veikimą. Tradiciniai aušinimo metodai dažnai neatitinka šiuolaikinių mikroelektronikos sistemų poreikių, todėl diegiami pažangūs aušinimo sprendimai, tokie kaip purškiamos aušinimo sistema, šilumos vamzdžiai, mikrokanalų šilumokaičiai (Sadique et al., 2022).

Mikrokanalų šilumokaičiai išsiskiria savo gebėjimu efektyviai nuvesti šilumą labai ribotose erdvėse (Bhandari et al., 2024; Joshi et al., 2023; Khattak & Ali, 2019; Rahman et al., 2024; Sadique et al., 2022; Yu et al., 2024). Jie leidžia skysčiui judėti itin siaurais kanalais, kurie dėl didelio šilumos mainų paviršiaus plotą pasiekia didelį efektyvumą. Norint pagerinti šių sistemų veikimą, įvedami pasyvūs srauto trikdžiai – kliūtys, kurios skatina turbulenciją, todėl padidėja ne tik šilumos mainų koeficientas, bet ir pasipriešinimas.

Pagrindiniai parametrai, lemiantys mikrokanalų su kliūtimis efektyvumą: forma (cilindrinė, kvadratinė, kūginė, elipsinė ir kt.), tarpas tarp kliūčių centrų, išdėstymas (linijinis arba šachmatinis). Tyrimai rodo, kad kliūčių forma daro didelę įtaką slėgio nuostoliams bei šilumos mainams. Pavyzdžiui, aptakios formos, tokios kaip elipsės, sukuria mažesnę pasipriešinimą nei kvadratinės ar trikampės kliūtys (Frhan Al-Abboodi et al., 2022; İzci et al., 2015; Serkan Şahin et al., 2023; P. Wang & Chen, 2019). Kliūtys, kurių skerspjuvis kinta priklausomai nuo aukščio, buvo mažai tirtos. Vis tik ištirtos kūginės kliūtys pagerina šilumos nuvedimą, suardydamos šiluminį pasienio sluoksnį ir sumažindamos stagnacines zonas, dėl atsirandančių antrinių srautų (Abuşka & Çorumlu, 2023; M. Lv et al., 2022; Mesgarpour et al., 2019; Souida et al., 2022).

Šachmatinis išdėstymas, palyginti su linijiniu, sukelia srauto vingiavimą, todėl žymiai pagerina šilumos mainų efektyvumą, nors tuo pačiu padidina slėgio nuostolius (Jeng & Tzeng, 2007). Be to, toks išdėstymas sukuria antrinius srautus, kurie sumažina recirkuliacines zonas ir taip pagerina šiluminį efektyvumą.

Kitaip nei paprastuose kanaluose, kur  $Re < 2000$  tekėjimas paprastai laminarinis, o  $Re > 4000$  – turbulentinis, kliūčių masyvuose dėl pasikartojančių kliūčių, net ir esant mažam  $Re$ , vyksta vietinė akceleracija, srauto atsiskyrimas ir sūkurių slinkimas. Pasak Žukausko (Žukauskas, 1972),  $Re < 1000$  srautas įprastai yra laminarinis,  $500 < Re < 200000$  – mišrus/subkritisinis, o  $Re > 200000$  – dažniausiai turbulentinis. Tačiau šachmatinis kliūčių išdėstymas su mažais atstumais tarp kliūčių, kai  $Re > 1000$ , greitai tampa turbulentinis. Kiti autoriai nurodo, kad sūkurių slinkimas prasideda ties  $Re = 500-700$  (F. Xu et al., 2018), ar  $Re = 850-1000$ , o von Karmano sūkurių eilutė stebima nuo  $Re > 550$ . Srautas laikomas nestacionariu, kai jo savybės kinta laike ( $\partial\phi/\partial t \neq 0$ ).

Koherentinės struktūros yra erdvėje ir laike koreliuojami srauto dariniai (pvz., sūkurių), atsirandantys dėl skysčio sąveikos su fizinėmis kliūtimis (Fiedler, 1988; Hussain, 1983; Qin et al., 2023). Šios struktūros ne tik padidina turbulencijos intensyvumą, bet ir užtikrina geresnę energijos bei momento pernašą sraute.

Svarbiausia, kad koherentinės struktūros gali atsirasti tiek laminariniuose, tiek turbulentiškuose srautuose, tokios kaip Föppl sūkurių (Cao et al., 2021; Protas, 2004), pasagos formos struktūros (Jiang et al., 2022), sužadinta sritis (angl. *wake region*) (Pereira et al., 2018), segtuko formos sūkurių (Dennis, 2015). Koherentinės struktūros apima įvairius nestabilumus, tokius kaip Kelvin-Helmholtz ar Rayleigh-Taylor nestabilumai (Fiedler, 1988; Mercier et al., 2020). Koherentinės struktūros nebūtinai turi būti visiškai vienodos erdvėje ir laike, tačiau jos turi turėti tam tikrą koreliacijos laipsnį erdvėje ir (arba) laike (Adrian, 2007; Tong et al., 2025). Pagrindinė idėja yra ta, jog jos išlaiko atpažįstamumą, net kai deformuojasi ar sąveikauja su kitomis struktūromis.

Koherentinių struktūrų egzistavimą galima nustatyti naudojant eksperimentinius (PIV) arba skaitmeninius metodus (POD, DMD, Q-kriterijus,  $\Omega$  metodas).  $\Omega$  metodas yra pažangi priemonė koherentinėms struktūroms identifikuoti, leidžianti patikimai atskirti sūkurines srauto sritis nuo deformacinių zonų, vertinant srautą pagal sukimosi ir deformacijos santykį (Belkacem, 2021; Y. Zhang et al., 2019). Skirtingai nuo tradicinių metodų, tokių kaip Q ar  $\lambda_2$  kriterijai,  $\Omega$  metodas yra normalizuotas, mažiau jautrus skaičiavimo tinklelio tankumui, todėl ypač tinka taikyti sudėtinguose skaitmeniniuose srautų modeliuose. Jis sėkmingai aptinka tiek stiprius, tiek silpnus sūkurius, net ir tais atvejais, kai pastarieji daro didelę įtaką šilumos pernašai ar srauto pasipriešinimui. Be to, metodas yra universalus – jį galima taikyti tiek laminariniuose, tiek turbulentiškuose srautuose, įvairiose inžinerinėse sistemose, tokiose kaip mikrokanalų šilumokaičiai, turbinos, siurbliai. Derinant  $\Omega$  kriterijų su kritinių taškų teorija, galima ne tik aptikti, bet ir klasifikuoti srauto struktūras bei suprasti jų formavimosi mechanizmus. Dėl šių savybių  $\Omega$  metodas tampa itin

naudingu įrankiu projektuojant efektyvias aušinimo sistemas, leidžiančiu įvertinti srauto charakteristikas be būtinybės tiesiogiai modeliuoti šilumos mainus.

Dauguma mikrokanalų šilumokaičių analizių remiasi tik  $Nu$  ir  $\Delta p$ , tačiau neatsižvelgia į srauto dinamiką. Šiame darbe siūlomas naujas metodas – analizuoti srauto fiziką tiesiogiai per koherentes struktūras, o tai leidžia įvertinti aušinimo efektyvumą ne tik empiriškai, bet ir fiziškai.

Esami tyrimai aiškiai rodo, jog daug dėmesio skiriama mikrokanalų šilumokaičių šiluminių ir hidraulinių savybių gerinimui, ypač skirtingoms kliūčių formoms ar jų išdėstymui. Daugelyje tyrimų buvo vertinama, kaip skirtingos formos, tokios kaip cilindrinės, kvadratinės, elipsinės, kūginės ir kitos, veikia srauto struktūrą ir šilumos perdavimą. Šie tyrimai daugiausia dėmesio skiria geometrinių parametru optimizavimui siekiant padidinti efektyvumą, dažniausiai naudojant empirines koreliacijas arba išvestus parametrus, tokius kaip PEC ar kliūčių efektyvumas ( $\eta$ ).

Vienas iš pagrindinių literatūroje nustatytų trūkumų yra nepakankamas dėmesys srauto struktūroms, kurios daro įtaką šiluminėms charakteristikoms. Nors koherentinės struktūros yra plačiai tiriamos, jų vaidmuo kliūčių turinčiuose mikrokanaluose dar nebuvo sistemingai ištirtas. Dauguma esamų tyrimų remiasi supaprastinta vizualizacija, kuri suteikia ribotą supratimą apie srauto erdvinį ir laiko organizuotumą. Ryšiai tarp srauto struktūrų, tokių kaip sūkurių slinkimo (angl. *vortex shedding*), šlyties sluoksnių, recirkuliacinių zonų ir dėl to atsirandančių šilumos perdavimo ir slėgio nuostolių charakteristikų išlieka kokybiniai.

Šia disertacija siekiama užpildyti spragą koherentinių struktūrų poveikio mikrokanalų šilumokaičių tyrimuose. Naudojant skaitmeninį modeliavimą ir pažangius sūkurių identifikavimo metodus, tokius kaip  $\Omega$  metodas ir kritinių taškų teorija (Perry & Fairlie, 1975), tyrime nagrinėjama, kaip geometriniai parametrai ir srauto režimai veikia sūkurius. Užuot pasiklojus tik šilumos perdavimo ir slėgio nuostolių vertėmis, tyrime tiesiogiai nagrinėjamas srautas, siekiant suprasti našumą lemiančius mechanizmus. Pagrindinis šio darbo rezultatas – naujo vertinimo metodo, pagrįsto koherentinių struktūrų analize, sukūrimas. Šis metodas leidžia numatyti termohidraulinį efektyvumą nemodeliuojant energijos lygčių, o tai suteikia alternatyvą tradiciniams modeliavimo metodams. Taip pat pagerina preliminarų projektavimo procesą ir padeda geriau suprasti srauto sukeltus mechanizmus aušinimo sistemose. Nauja vertinimo strategija papildė esamus rodiklius ir suteikia galimybę sumažinti naudojamus skaičiavimo resursus.

### **6.3. Modeliavimo metodika**

Srautams ir šilumos mainams mikrokanalų šilumokaičiuose modeliuoti, taikant URANS metodą, tyrime naudojamas skaičiuojamosios skysčių dinamikos (CFD) metodas. Skysčio judėjimas ir šilumos mainai aprašomi masės, impulso ir energijos

tvermės dėsniais, išreikštais Navjė-Stokso lygtimis. Turbulencijai modeliuoti naudojamas k- $\omega$  SST modelis, kuris apjungia k- $\omega$  ir k- $\epsilon$  metodų privalumus.

Tyrimė naudojamos bedimensės charakteristikos, hidraulinis diametras ( $D_h$ ), Reinoldso skaičius ( $Re$ ), pasipriešinimo koeficientas ( $f$ ), Nuselto skaičius ( $Nu$ ) ir šiluminio efektyvumo rodiklis ( $TPI$ ). Čia pasipriešinimo koeficientas apima sienelių šlytį ir kliūčių formos nuostolius.

Kraštinės sąlygos priklauso nuo tyrimo tipo (su / be šilumos perdavimo) ir apima įėjimo / išėjimo, sienelių ir kliūčių sritis. Kraštinės sąlygos pateiktos 18 lentelėje.

**18 lentelė.** Skirtingų skaičiavimo sričių šiluminių ir adiabatinių modelių kraštinių sąlygų parinkimas

	Adiabatinis atvejis		
	Visas kanalas	Periodinė dalis	Ciklinė sritis
Įtekėjimas	$p = p_{in}$ $\nabla \mathbf{u} \cdot \mathbf{n} = 0$ $k = k_{in}$ $\omega = \omega_{in}$	$p = p_{in}$ $\nabla \mathbf{u} \cdot \mathbf{n} = 0$ $k = k_{in}$ $\omega = \omega_{in}$	$\phi_{inlet} = \phi_{outlet}$
Ištekėjimas	$p = p_{atm}(0)$ $\nabla \mathbf{u} \cdot \mathbf{n} = 0$ $\nabla k \cdot \mathbf{n} = 0$ $\nabla \omega \cdot \mathbf{n} = 0$	$p = p_{atm}(0)$ $\nabla \mathbf{u} \cdot \mathbf{n} = 0$ $\nabla k \cdot \mathbf{n} = 0$ $\nabla \omega \cdot \mathbf{n} = 0$	
Kliūtys	$\mathbf{u} = 0$ $\nabla p \cdot \mathbf{n} = 0$ $\nabla k \cdot \mathbf{n} = 0$ $\omega$ wall function	$\mathbf{u} = 0$ $\nabla p \cdot \mathbf{n} = 0$ $\nabla k \cdot \mathbf{n} = 0$ $\omega$ wall function	$\mathbf{u} = 0$ $\nabla p \cdot \mathbf{n} = 0$ $\nabla k \cdot \mathbf{n} = 0$ $\omega$ wall function
Viršutinė / apatinė sienelės	$\mathbf{u} = 0$ $\nabla p \cdot \mathbf{n} = 0$ $\nabla k \cdot \mathbf{n} = 0$ $\omega$ wall function	$\mathbf{u} = 0$ $\nabla p \cdot \mathbf{n} = 0$ $\nabla k \cdot \mathbf{n} = 0$ $\omega$ wall function	$\mathbf{u} = 0$ $\nabla p \cdot \mathbf{n} = 0$ $\nabla k \cdot \mathbf{n} = 0$ $\omega$ wall function
Dešinė sienelė	$\mathbf{u} = 0$ $\nabla p \cdot \mathbf{n} = 0$ $\nabla k \cdot \mathbf{n} = 0$ $\omega$ wall function	$\phi_{right} = \phi_{left}$	$\phi_{right} = \phi_{left}$
Kairė sienelė	$\mathbf{u} = 0$ $\nabla p \cdot \mathbf{n} = 0$ $\nabla k \cdot \mathbf{n} = 0$ $\omega$ wall function		

Su šilumos mainais		
	Ciklinė sritis, šilumai nelaidi	Ciklinė sritis, šilumai laidi
Įtekėjimas	$\mathbf{u}_{in} = \mathbf{u}_{out}$ $p = f(eq)$ $k_{in} = k_{out}$ $\omega_{in} = \omega_{out}$ $T_{in} = T_{fixed}$	<p><i>Skystis</i></p> $\mathbf{u}_{in} = \mathbf{u}_{out}$ $p = f(eq)$ $k_{in} = k_{out}$ $\omega_{in} = \omega_{out}$ $T_{in} = T_{fixed}$ <p><i>Medžiaga</i></p> $\phi_{inlet} = \phi_{outlet}$
Ištekėjimas	$\nabla \mathbf{u} \cdot \mathbf{n} = 0 \text{ (if outflow)}$ $\mathbf{u} = 0 \text{ (if outflow)}$ $p = f(eq)$ $\nabla k \cdot \mathbf{n} = 0 \text{ (if outflow)}$ $k = k_{fixed} \text{ (if outflow)}$ $p = f(eq)$ $\nabla \omega \cdot \mathbf{n} = 0 \text{ (if outflow)}$ $\omega = \omega_{fixed} \text{ (if outflow)}$ $\nabla T \cdot \mathbf{n} = 0 \text{ (if outflow)}$ $T = T_{fixed} \text{ (if outflow)}$	<p><i>Skystis</i></p> $\nabla \mathbf{u} \cdot \mathbf{n} = 0 \text{ (if outflow)}$ $\mathbf{u} = 0 \text{ (if outflow)}$ $p = f(eq)$ $\nabla k \cdot \mathbf{n} = 0$ $\nabla \omega \cdot \mathbf{n} = 0$ <p><i>Medžiaga</i></p> $\phi_{in} = \phi_{out}$
Kliūtys	$\mathbf{u} = 0$ $p = f(eq)$ $\nabla k \cdot \mathbf{n} = 0$ $\omega \text{ wall function}$ $\nabla T \cdot \mathbf{n} = 0$	-
Viršutinė / apatinė sienelės	$\mathbf{u} = 0$ $p = f(eq)$ $\nabla k \cdot \mathbf{n} = 0$ $\omega \text{ wall function}$ $\frac{\partial T}{\partial \mathbf{n}} = \frac{q_{fixed}}{k}$	<p><i>Medžiaga</i></p> $\frac{\partial T}{\partial \mathbf{n}} = \frac{q_{fixed}}{k}$
Dešinė sienelė	$\phi_{right} = \phi_{left}$	<p><i>Skystis</i></p> $\phi_{right} = \phi_{left}$
Kairė sienelė		<p><i>Medžiaga</i></p> $\phi_{right} = \phi_{left}$

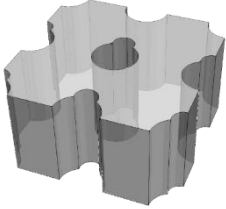
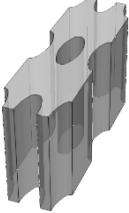
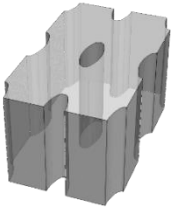
<p style="text-align: center;">Skysčio- medžiagos sąsaja</p>	-	<p style="text-align: center;"><i>Skystis</i> <math>\mathbf{u} = 0</math> <math>p = f(eq)</math> <i>k wall function</i> <i><math>\omega</math> wall function</i> <math>q_{fluid} = q_{solid}</math> <i>Medžiaga</i> <math>q_{solid} = q_{fluid}</math></p>
--	---	--

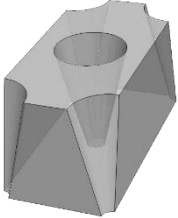
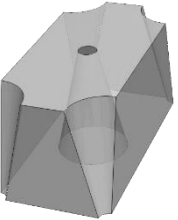
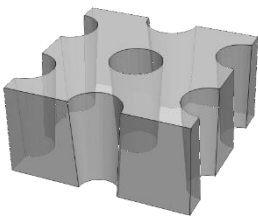
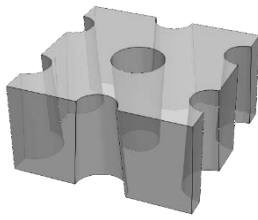
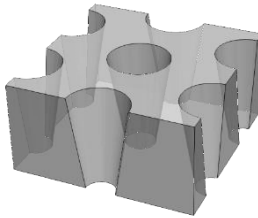
Modelis patikrintas pagal eksperimentinius Renfer et al. (Renfer et al., 2011, 2013) ir Kosar et al. (Koşar et al., 2011) duomenis. Renfer et al. (Renfer et al., 2011, 2013) tyrė šildomus ir nešildomus mikrokanalus su skirtingomis kliūčių konfigūracijomis, naudodamas  $\mu$ PIV metodą. Kai tuo tarpu Kosar et al. (Koşar et al., 2011) nagrinėjo skirtingą kliūčių išdėstymą esant adiabatiniems sąlygoms.

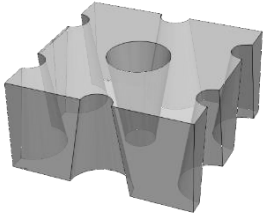
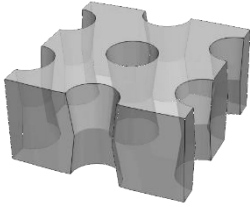
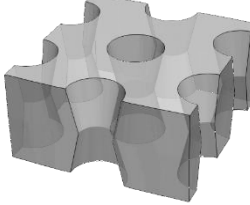
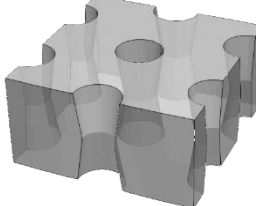
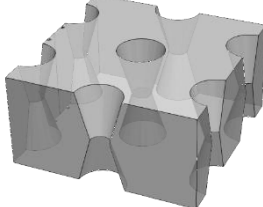
Tyrimė naudojamos Renfer (R) ir Kosar (K) mikrokanalų konfigūracijos su cilindrinėmis kliūtėmis, tačiau skiriasi matmenys ir  $Re$  intervalas, o tai leidžia palyginti skirtingus srauto režimus ir jų įtaką šiluminiam našumui. Siekiant patikimai interpretuoti eksperimentinius duomenis, buvo atlikta komplektinė analizė pagrindiniams skysčių dinamikos ir šilumos parametrų: nustatyti santykiniai neapibrėžtumai –  $\pm 13\%$  tūriniam debitui,  $\pm 11\%$  kinematinei klampai ir  $\pm 1,7\%$  slėgio kritimui. Šios vertės naudotos bendrajam (angl. *propagated*) parametru neapibrėžtumui apskaičiuoti, kuris siekia  $\pm 17\%$  ir reikšmingai veikia tekėjimo režimo klasifikaciją, ypač pereinamajame režime, kur net nedideli  $Re$  pokyčiai gali lemti skirtingą tekėjimo elgseną.

Iš viso buvo ištirta 90 mikrokanalų konfigūracijų. Išsamūs duomenys pateikti 19 lentelėje. Pirma pavadinimo raidė nurodo šaltinį (R/K), antra – kliūtės formą, cilindras (C), dvigubas cilindras (DC), elipsė (E), kūgis (T), smėlio laikrodis (H). Jeigu tai kūgio ar smėlio laikrodžio forma, nurodomas pasvirimo kampas. Kūgiams dar nurodoma jų pasvirimo kryptis – vienkryptė (A) arba dvikryptė (B). Galiausiai nurodomas atstumas tarp kliūčių centrų (P), o šalia pateikiama jo vertė.

**19 lentelė.** Mikrokanalo kliūčių formos, išdėstymų ir modeliavimo sąlygų santrauka

Atvaizdas ir pavadinimas	Konfigūracija		Modeliavimo sąlygos
	Išdėstymas	Forma	
 R-DC	Linijinis $P = 200 \mu\text{m}$ $H = 200 \mu\text{m}$	Dvigubas cilindras $D_1 = 100 \mu\text{m}$ $D_2 = 50 \mu\text{m}$	$u_{in} = 1,25 - 2,25 \text{ m/s}$ Skystis – vanduo (16°C) k- $\omega$ SST adiabatinis
 R-E-P60   R-E-P120  R-E-P(atstumas tarp kliūčių)	Linijinis $P_{ton} = 200 \mu\text{m}$ $P_{tr} = 50 - 140 \mu\text{m}$	Elipsės $D_x = 100 \mu\text{m}$ $D_y = 40 \mu\text{m}$	$u_{in} = 0,165 - 1,584 \text{ m/s}$ Skystis – vanduo (16°C) k- $\omega$ SST adiabatinis
 K-H19	Šachmatinis $P = 250 \mu\text{m}$ $H = 243 \mu\text{m}$	$D_w = 140 \mu\text{m}$ $D_{mid} = 53,6 \mu\text{m}$ $\Theta = 19,573^\circ$	$Re = 85 - 117$ Skystis – vanduo (22°C) k- $\omega$ SST adiabatinis

 <p>K-T14-A-P250</p> <p>K-T(kampas)-A-P(atstumas tarp kliūčių)</p>	<p>Šachmatinis  <math>P = 200\text{--}300\ \mu\text{m}</math>  <math>H = 243\ \mu\text{m}</math></p>	<p><math>D_1 = 41,8 - 91,6\ \mu\text{m}</math></p> <p><math>D_2 = 108,4 - 158,2\ \mu\text{m}</math></p> <p>Priklauso nuo kampo <math>2^\circ - 13,48^\circ</math></p>	<p><math>Re = 40 - 117</math>  Skystis – vanduo (<math>22^\circ\text{C}</math>)  k-<math>\omega</math> SST adiabatinis</p>
 <p>K-T14-B-P250</p> <p>K-T(kampas)-B-P(atstumas tarp kliūčių)</p>			
 <p>R-T4-A</p>	<p>Šachmatinis  <math>P = 200\ \mu\text{m}</math>  <math>H = 200\ \mu\text{m}</math></p>	<p><math>D_1 = 86\ \mu\text{m}</math>  <math>D_2 = 114\ \mu\text{m}</math>  <math>\Theta = 4,004^\circ</math></p>	<p><math>Re = 200 - 800</math>  Skystis – vanduo (<math>T_{in} = 20^\circ\text{C}</math>)  k-<math>\omega</math> SST</p>
 <p>R-T4-B</p>			
 <p>R-T8-A</p>		<p><math>D_1 = 66\ \mu\text{m}</math>  <math>D_2 = 134\ \mu\text{m}</math>  <math>\Theta = 9,648^\circ</math></p>	

 <p>R-T8-B</p>			
 <p>R-H8</p>		$D_1 = 86 \mu\text{m}$ $D_2 = 114 \mu\text{m}$ $\Theta = 7,97^\circ$	
 <p>R-H13</p>		$D_1 = 76 \mu\text{m}$ $D_2 = 122 \mu\text{m}$ $\Theta = 12,953^\circ$	
 <p>R-H9</p>		$D_1 = 70 \mu\text{m}$ $D_2 = 100 \mu\text{m}$ $\Theta = 8,531^\circ$	
 <p>R-H16</p>		$D_1 = 42 \mu\text{m}$ $D_2 = 100 \mu\text{m}$ $\Theta = 16,172^\circ$	

## 6.4. Patikra

Modelio patikra yra suskirstyta į tris dalis: neapibrėžčių analizę dėl tinklelio supaprastinimo, įtekėjimo sąlygų, šilumos laidumo kliūtyje ir tinklelio tankumo analizę bei modelio patikrą.

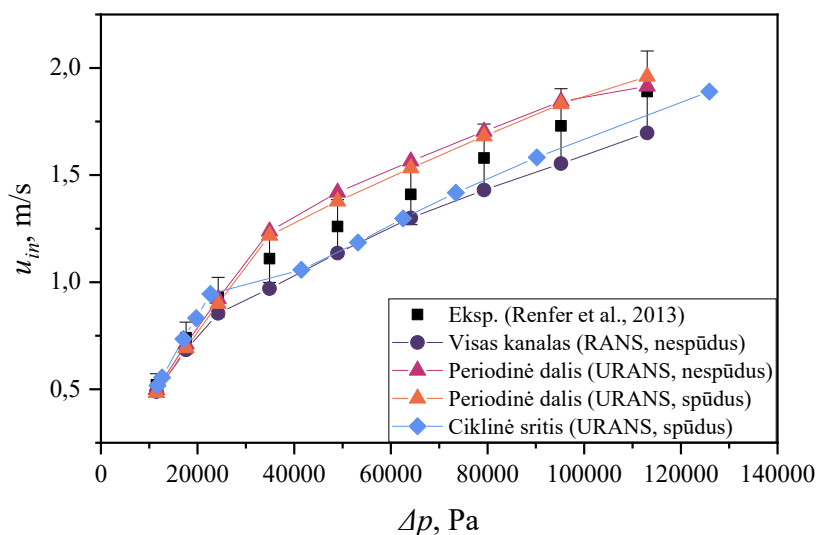
### 6.4.1. Neapibrėžčių analizė

Skaičiavimo sąnaudoms sumažinti viso mikrokanalo modelis buvo supaprastintas iki periodinės dalies, o vėliau – iki ciklinės srities. Tiek viso kanalo, tiek periodinės dalies atvejais slėgio kritimas buvo užduodamas kaip kraštinė sąlyga. Ciklinėje srityje priešingai – taikytos ciklinės (nospūdžiam fluidui) arba „mapped“ (spūdžiam fluidui) kraštinės sąlygos, o greitis  $u$  čia buvo nurodomas kaip pradinė sąlyga (kraštinės sąlygos pateiktos 18 lentelėje).

Įėjimo greičio ir slėgio nuostolių priklausomybė pateikta 8 pav., kuriame taip pat pavaizduota  $\pm 10\%$  paklaida eksperimentiniams duomenims. Be skaičiavimo srities parinkimo, buvo palygintos skirtingos modeliavimo strategijos – RANS ir URANS, taip pat spūdus ir nospūdus skystis. Rezultatai rodo, kad skysčio spūdomas reikšmingos įtakos nedaro. Kadangi čia daugiausia dėmesio skiriama geometrijų palyginimui, pilna modelio patikra pateikta 6.4.2 skyriuje.

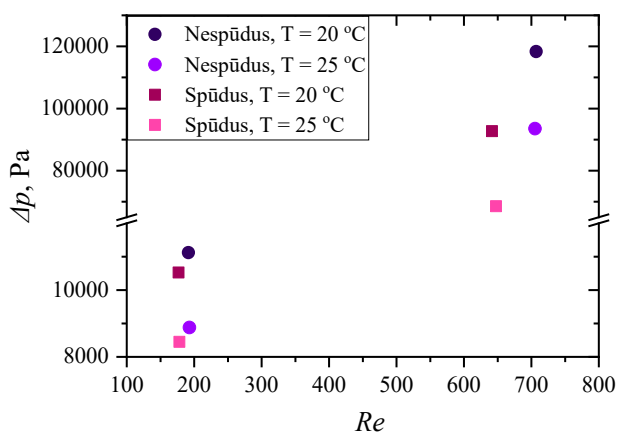
Lyginant  $u_{in}$  visame kanale ir periodinėje dalyje, gauti nuokrypiai siekia 12,8 % nospūdžiam fluidui atvejui ir 11,6 % – spūdžiam (47 pav.). Tuo tarpu  $u_{in}$  skirtumas tarp viso kanalo ir ciklinės srities modelių yra palyginti nedidelis – 4,67 %. Didžiausias nuokrypis atsiranda, kai srautas pereina iš stacionaraus į nestacionarų režimą. Įdomu tai, kad ciklinėje srityje režimo pasikeitimas įvyksta anksčiau, nes srautas greičiau nusistovi. Tai pabrėžia ciklinių kraštinių sąlygų privalumą – jos spartina būdingų srauto savybių nusistovėjimą, palyginti su įprastomis kraštinėmis sąlygomis.

Tyrimas patvirtina, kad ciklinės kraštinės sąlygos tiksliai atkuria mikrokanalo slėgio pasiskirstymą ir srauto charakteristikas, mažindamos skaičiavimo sąnaudas.



47 pav.  $\Delta p$  priklausomybė nuo  $u_m$  visam kanalui, periodinei daliai ir ciklinei sričiai

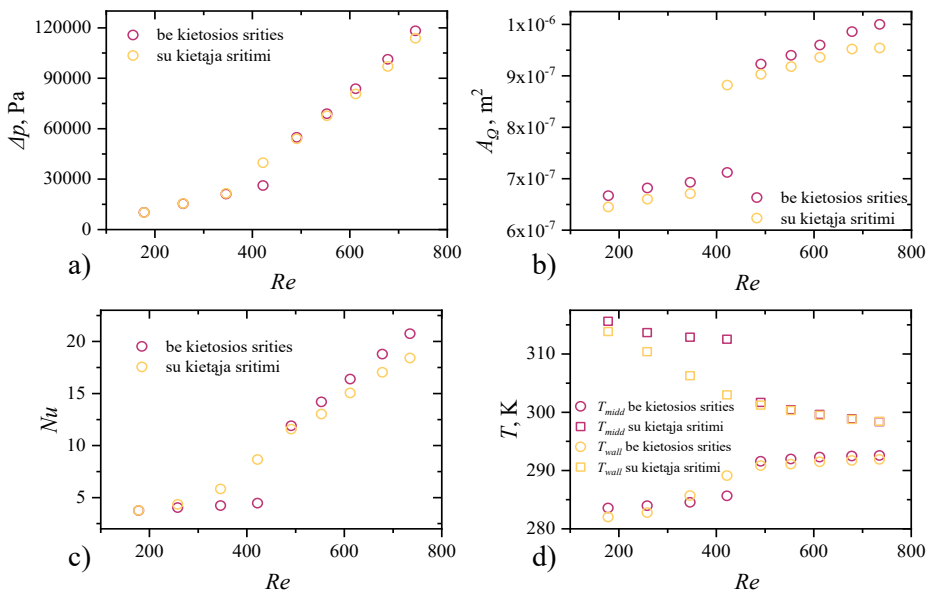
Buvo ištirtas eksploataavimo sąlygų (pradinės temperatūros ir klamos) neapibrėžtumas. Įvertintas pradinės temperatūros ir klamos poveikis slėgio kritimui. Analizė atlikta ciklinėje srityje tiek spūdžiam, tiek nespūdžiam fluidui, esant stacionariam ( $Re \sim 200$ ) ir nestacionariam srautui ( $Re \sim 650-700$ ). Rezultatai pateikti 48 pav. Skirtumas tarp didesnės ir mažesnės pradinės temperatūros (20 °C ir 25 °C) lemia 19,7–26,1 %  $\Delta p$  verčių pokytį.



48 pav. Modelio spūdumo ir pradinės temperatūros įtaka rezultatams

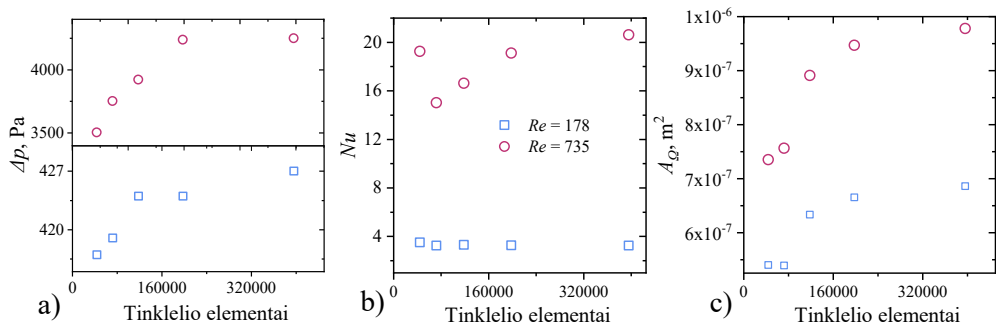
Tolesnis patikrinimas, esant šilumos mainams, rodo, kad ciklinės kraštinės sąlygos yra fiziškai netinkamos, todėl pakeistos į atvaizduotas (angl. *mapped*), kurios perkelia ištekėjimo duomenis į įtekėjimą, taip pat įtraukiant korekcijas, skirtas kompensuoti sklaidos poveikį ir išlaikyti numatytas kraštines sąlygas. Be to, skaičiavimo erdvės ilgis buvo padvigubintas, siekiant išspręsti trumpesnių tinklelių nesugebėjimo išlaikyti cikliškumo naudojant užduotas kraštines sąlygas. Baba-Ahmani ir kt. (Baba-Ahmadi & Tabor, 2009) patvirtina tokių kraštinių sąlygų naudojimą tekėjimui kanaluose ir vamzdžiuose.

Skaitiniuose šilumos mainų tyrimuose, ypač mikrokaneluose, kietosios srities modeliavimas dažnai žymiai didina skaičiavimo kaštus. Nors jungtinė šilumos pernaša leidžia išsamiai aprašyti šilumos laidumą medžiagoje ir konvekciją skystyje, vis tik toks metodas ne visuomet būtinas. Skaičiavimo efektyvumui optimizuoti medžiaga buvo neįtraukta į modeliavimą, o pagrindiniai parametrai, tokie kaip  $\Delta p$ ,  $Nu$ ,  $T_{wl}$ ,  $T_{mid}$ ,  $A_Q$  buvo palyginti su medžiaga ir be jos (49 pav.).  $\Delta p$  MRE yra 5,3 %, 14,1 %  $Nu$ , 3,6 %  $A_Q$  ir mažiau nei 0,5%  $T_w$  ir  $T_{mid}$ . Didžiausias nuokrypis stebimas pereinamojo režimo dalyje, kur medžiagos nebuvimas sukėlė režimo perėjimo vėlavimą ir staigesnius tekėjimo savybių pokyčius. Tai lėmė didesnę MRE, tačiau atsižvelgus į tai ir neįtraukus  $Re = 346$  ir  $422$ , Nuselto skaičiaus MRE sumažėja iki maždaug 7 %. Šie nuokrypiai yra santykinai minimalūs, o tai rodo, jog medžiagos poveikis tampa nereikšmingu. Šis supaprastinimas leidžia sutaupyti skaičiavimo išteklių, išlaikant tikslumą ten, kur tai svarbiausia – skysčio srityje.



49 pav. a) slėgio nuostoliai b) koherentinių struktūrų plotas c) Nuselto skaičius d) temperatūrų priklausomybė nuo  $Re$

Tinklelio patikra tęsiama tinklelio konvergavimo ir tinklelio konvergavimo indekso ( $GCI$ ) analize. Šioms analizėms buvo pasirinkta ciklinė sritis. Palyginti penki skirtingi tinklelių tankumai: 1 su 44032 elementais, 2 – 72160, 3 – 118272, 4 – 198016, 5 – 396032. Lyginimas atliktas mažiausiu ir didžiausiu  $Re$ . Visais atvejais atstumo iki sienelės parametras  $y^+$ , buvo išlaikytas žemesnis nei 1, siekiant užtikrinti pasienio sluoksnio skiriamąją gebą.  $\Delta p$ ,  $Nu$  ir  $A_{\Omega}$  rezultatai pateikti 50 pav. Esant mažam  $Re$ ,  $\Delta p$  skirtumai tarp tinklelių yra  $\sim 1\%$ . Esant dideliame  $Re$ , reikšmingo skirtumo tarp 4 ir 5 tinklelių nepastebėta, tačiau skirtumas tarp 3 ir 4 tinklelių buvo 7 %, tarp 3 ir 2 – 4%, o tarp 2 ir 1 – 7%. Tuo tarpu  $Nu$  skirtumai esant mažam  $Re$  tarp 2–5 tinklelių buvo apie 2 %, o tarp 1 ir 2 – 8 %. Panašiai ir su  $A_{\Omega}$  rezultatais, skirtumai nepriklausė nuo  $Re$ , o mažiausias skirtumas pastebėtas tarp 4 ir 5 tinklelių.



**50 pav.** Tinklelio tankumo įtaka a) slėnio nuostoliams, b) Nuselto skaičiui ir c) koherentinių struktūrų plotui, kai  $Re = 178$  ir 735

$GCI$  metodas buvo pritaikytas 3, 4 ir 5 tinkleliams, kai  $Re = 735$  (žiūrėti 20 lentelę). Apytikslės paklaidos tarp 3 ir 4 tinklelio slėgio nuostoliams buvo 0,26 %, 7,3 % Nuselto skaičiui ir 3,17 % koherentinių struktūrų plotui. Palyginimui, 4 ir 3 tinklelių paklaidos buvo 7,5 % –  $\Delta p$ , 13 % –  $Nu$  ir 6 % –  $A_{\Omega}$ . Išorinės (angl. *external error*) 4 ir 5 tinklelių paklaidos buvo atitinkamai 0,62 %, 3,68 % ir 1,92 %  $\Delta p$ ,  $Nu$  ir  $A_{\Omega}$ , o paklaidos tarp 3 ir 4 tinklelių buvo žymiai didesnės – 20,31 %, 9,68 % ir 5,36 %.

$GCI$  rezultatai rodo, kad konvergavimas tarp 5 ir 4 tinklelių yra patenkinamas, su minimaliomis paklaidomis ( $GCI$  vertės 0,78 %  $\Delta p$ , 4,77 %  $Nu$  ir 2,45 %  $A_{\Omega}$ ). Tačiau perėjimas iš 4 į 3 tinklelį rodo bent tris kartus didesnę paklaidą ( $GCI$  vertės 31,85 %  $\Delta p$ , 13,4 %  $Nu$  ir 7,08 %  $A_{\Omega}$ ), o tai rodo, kad 3 tinklelio detalumas gali būti nepakankamas arba kad rezultatus gali paveikti su tinklelio detalumu susijusios skaitinės paklaidos.

Taigi, tinklelio rezultatai rodo gerą konvergavimą su mažu  $GCI$  ir netikslumo reikšmėmis, o tai rodo, kad tolesnis tinklelio tankinimas greičiausiai nepadidins modeliavimo tikslumo. Todėl daroma išvada, kad vidutinis maždaug 198016

elementų tinklelis yra pakankamas nagrinėjamos problemos analizei. Šis tinklelis bus pagrindas tolesnei analizei, apimančiai kitas konfigūracijas.

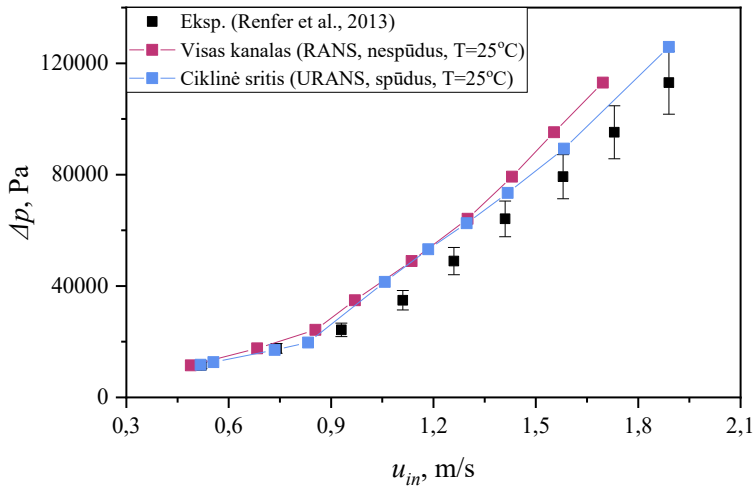
**20 lentelė.** GCI analizė slėgio nuostoliams, Nuselto skaičiui ir koherentinių struktūrų plotui

	$\Delta p$	$Nu$	$A_{\Omega}$
<i>Mesh 5-3</i>	396032, 198016, 118272		
$r_{21}$	2		
$r_{32}$	1,674		
$\varphi_1, \varphi_2, \varphi_3$	4250, 4239, 3922	20,6, 19,11, 16,63	21.,53, 21,32, 19,64
$\zeta$	0,499	1,543	1,387
$\varphi_{ext}^{21}$	4276,60	21,41	$10^{-6}$
$\varepsilon_a^{21}$	0,26 %	7,31 %	3,17 %
$\varepsilon_{ext}^{21}$	0,62 %	3,68 %	1,92 %
$GCI^{21}$	0,78 %	4,77 %	2,45 %
$\varphi_{ext}^{32}$	5319,07	21,16	$10^{-6}$
$\varepsilon_a^{32}$	7,48 %	13,02 %	5,91 %
$\varepsilon_{ext}^{32}$	20,31 %	9,68 %	5,36 %
$GCI^{32}$	31,85 %	13,40 %	7,08 %

#### 6.4.2. Modelio patikra

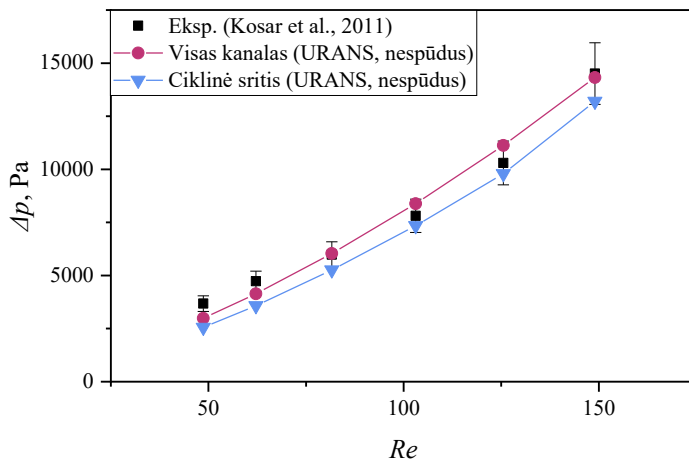
Siekiant išlaikyti atitikimą eksperimentinėms sąlygoms, CFD skaičiavimuose  $\Delta p$  buvo užduotas tarp įėjimo ir išėjimo, o ne tiesiogiai  $u_{in}$ . Tuo tarpu ciklinėje srityje pradinė kraštinė sąlyga buvo  $u_{in}$ . Kadangi ciklinės srities įėjimo plotas skiriasi nuo viso kanalo,  $u_{in}$  buvo perskaičiuotas į pradinio kanalo  $u_{in}$ . Iš viso kanalo skaičiavimų gautas  $u_{in}$  buvo lyginamas su atitinkamomis eksperimentinėmis vertėmis. Tai užtikrino, kad esant tam pačiam slėgio kritimui modeliuotas debitas atitinka eksperimentinį tekėjimą, o tai suteikia tvirtą pagrindą tiek viso kanalo, tiek sumažintų sričių modelių patikrai. Ciklinėje srityje, kadangi  $u_{in}$  buvo užduotas, gautas  $\Delta p$  buvo palygintas su eksperimentine verte.

Modeliavimo ir eksperimento rezultatai pateikti 51 pav. Aplink eksperimentinius duomenis pavaizduota  $\pm 10\%$  paklaidos zona. Viso kanalo rezultatas gerai atitinka eksperimentinę tendenciją ( $MRE_{u_{in}} = 10\%$ ). Ciklinės srities  $MRE_{\Delta p} = 12\%$ . Abiem atvejais skaitiniai duomenys linkę pervertinti atitinkamai  $u_{in}$  arba  $\Delta p$ . Nepaisant to, bendras atitikimas eksperimentui patvirtina rezultatų pagrįstumą.



**51 pav.** Modeliuojamo slėgio kritimo visame kanale ir ciklinėje srityje palyginimas su Renfer ir kt. (Renfer et al., 2013) eksperimentiniais rezultatais

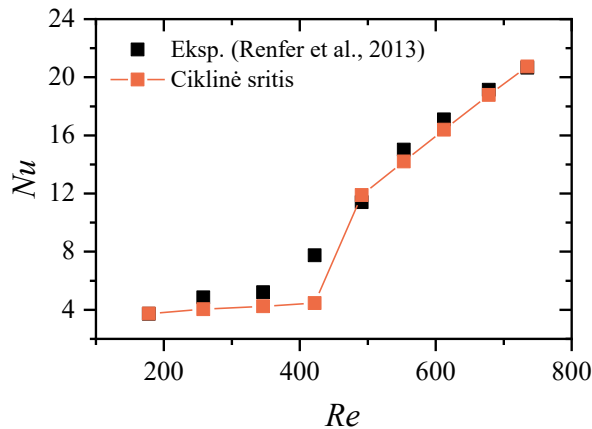
Modeliavimo rezultatai taip pat buvo palyginti ir su Kosar ir kt. (Koşar et al., 2011) atliktais eksperimentais (52 pav.). MRE tarp skaitinių viso kanalo ir eksperimento rezultatų yra 7 %, o tarp ciklinės srities ir eksperimento – 12 %. Ciklinė sritis rodo nepakankamą įvertinimą, tikriausiai dėl taikomos periodiškumo sąlygos, kuri neatsižvelgia į įtekėjimo srities poveikį. Šis nepakankamas įvertinimas greičiausiai susijęs su modeliavime naudojamu periodiškumu, kuris neatsižvelgia į įtekėjimo poveikį. Kadangi įtekėjimo sritis atlieka svarbų vaidmenį bendrame  $\Delta p$ , jos neįtraukimas į ciklinę sritį lemia mažesnes numatomas vertes, palyginti su eksperimentiniais rezultatais. Nepaisant to, bendras atitikimas su eksperimentu patvirtina rezultatų pagrįstumą.



**52 pav.** Viso kanalo ir ciklinės srities slėgio kritimo modeliavimo rezultatų palyginimas su eksperimentiniais duomenimis Kosar ir kt. (Koşar et al., 2011)

Ciklinės srities rezultatai buvo palyginti su Renfer ir kt. eksperimentiniais rezultatais (Renfer et al., 2011, 2013). 53 pav. stacionariame tekėjime matyti, kad  $Nu$  išlieka santykinai pastovus, be reikšmingo padidėjimo. Tačiau staigus  $Nu$  šuolis įvyksta po to, kai  $Re$  pasiekia maždaug 491, o tai rodo tekėjimo režimo pokyčio pradžią.

Bendras  $Nu$  MRE yra 10%, o mažesnis neatitikimas (MRE = 3%) yra po tekėjimo pasikeitimo (po  $Re = 491$ ). Modeliuojant pastebėtas uždelstas režimo perėjimas atitinka anksčiau pateiktas išvadas. Vėlavimą galima priskirti ciklinių kraštinių sąlygų naudojimui modelyje. Nepaisant režimo pasikeitimo uždelimo, rezultatai gerai atitinka eksperimentinius duomenis, ypač po režimo pasikeitimo, patvirtindami modelio pagrįstumą šilumos perdavimo modeliavimui.



**53 pav.** Ciklinės srities  $Nu$  modeliavimo rezultatų palyginimas su eksperimentiniais duomenimis (Renfer et al., 2013)

Siekiant įvertinti, kaip gerai modelis atkuria eksperimentinius rezultatus, apskaičiuotas Pearsono koreliacijos koeficientas  $r$ . Tai statistinis dviejų kintamųjų tiesinės priklausomybės stiprumo ir krypties matas. CFD patikroje jis parodo, kiek tiksliai skaitinės prognozės atitinka eksperimentinių duomenų tendenciją. Nors paklaidų matai, tokie kaip MAE ar RMSE, apibūdina nuokrypių dydį, Pearsono koeficientas tiesiogiai atsako į tai, ar CFD modelis atkuria eksperimentinę tendenciją.  $r_p$  artimas +1 reiškia, kad didėjant eksperimentiniam kintamajam (pvz., įėjimo greičiui ir didėjant slėgio kritimui), modelio išvestis didėja beveik proporcingai – tai svarbu norint patvirtinti teisingus fizikinius skaičiavimus.

Koreliacija tarp eksperimentinio  $u_{in}$  ir CFD rezultatų visam kanalui gauta  $r_p = 0,999$ . Analogiškai, koreliacija tarp eksperimentinės  $\Delta p$  ir ciklinės srities modeliavimo davė tą pačią reikšmę – 0,999. Šios reikšmės yra artimos vienetui, o tai rodo tiesinį CFD rezultatų ir eksperimentinių matavimų atitikimą ir leidžia daryti išvadą, kad modelyje pagrindiniai srauto fizikos dėsniai atkuriami teisingai.

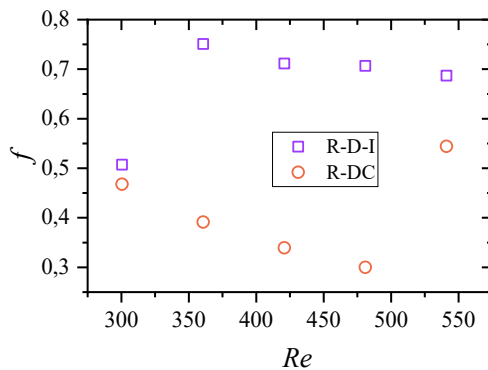
## 6.5. Rezultatai

Rezultatų skyrius padalintas į dvi pagrindines kategorijas: hidraulinės ir šilumos perdavimo charakteristikas. Šie du aspektai yra integruoti į išsamų paskutinį skyrių, kuriame aptariamas naujas efektyvumo kriterijus.

Svarbu pažymėti, jog šilumos perdavimas kiekvienai konfigūracijai nebuvo modeliuojamas. Daugiausiai dėmesio skirta konfigūracijoms su kintančiais kliūčių skerspjuviais išilgai aukščio (kūgio ar smėlio laikrodžio formų). Rezultatai taip pat sugrupuoti pagal K tipo arba R tipo konfigūracijas.

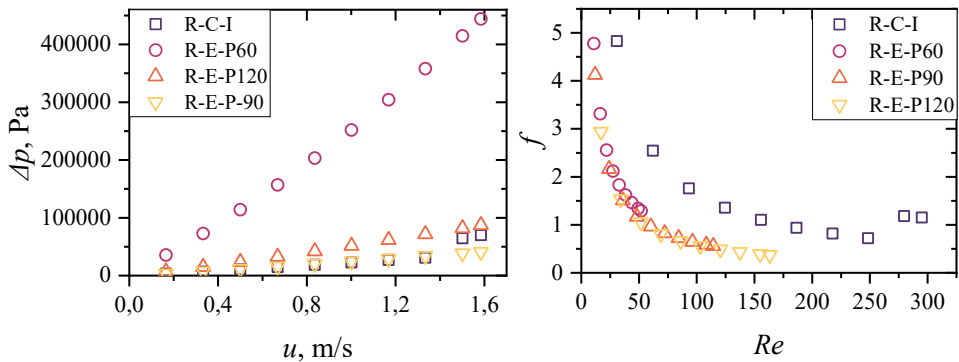
### 6.5.1. Hidraulinės charakteristikos

Palyginamoji cilindrinų kliūčių (R-C-I) ir dvigubo cilindro kliūčių (R-DC-I) analizė parodė, kad esant stacionariam tekėjimui ( $Re = 300$ ),  $f$  R-DC-I mikrokanale buvo 8 % mažesnis nei R-C-I atveju (žr. 54 pav.). Toks sumažėjimas siejamas su stabilesnėmis srauto sąlygomis R-DC-I mikrokanale. Padidėjus  $Re$ ,  $f$  R-C-I dėl išaugusio srauto nestabilumo padidėjo. Tekėjimo režimo pasikeitimas R-C-I mikrokanale įvyksta  $Re = 300$ , kai tuo tarpu R-DC-I tik esant  $Re > 500$ . Net ir pastebėjus sukurių slinkimą abiejose konfigūracijose, R-DC-I pasižymi mažesniu hidraulinio pasipriešinimu,  $f$  sumažėjo iki 21%, kai  $Re = 541$ . Vidutiniškai R-DC-I konfigūracijos  $f$  yra 37 % mažesnis nei R-D-I tirtame  $Re$  intervale ( $300 < Re < 541$ ).



54 pav. R-C-I ir R-DC konfigūracijų  $f$  palyginimas

Elipsinių kliūčių masyvai su kintamu skersiniu žingsniu tarp kliūčių (R-E-P(X)) buvo palyginti tarpusavyje ir su R-C-I (žr. 55 pav.). Pastebėta, kad  $\Delta p$  yra mažiausias R-C-I atveju, kai tekėjimas yra stacionarus, tačiau vertinant  $f$ , elipsinių kliūčių  $f$  yra mažesnis ir tėkmė ilgiau išlaiko stabilumą. Taip pat pastebėta, jog mažėjant skersiniam žingsniui tarp kliūčių, didėja slėgio nuostoliai.

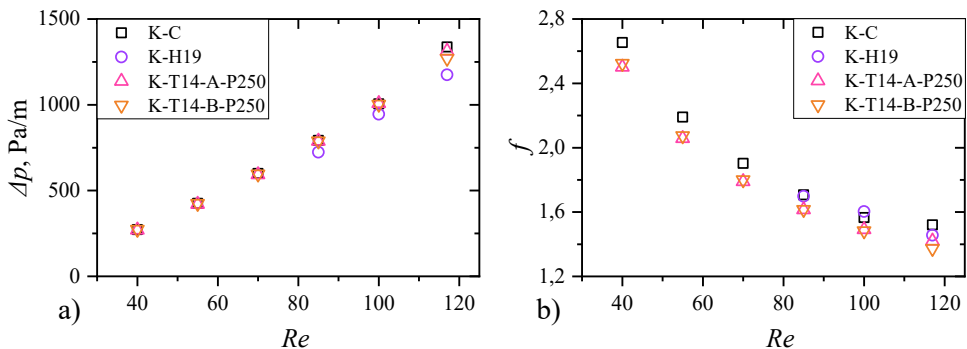


**55 pav.** a)  $\Delta p$  priklausomybė nuo įtekėjimo greičio ir b)  $f$  priklausomybė nuo  $Re$

Dviejų cilindrų ir elipsinės kliūtys išlaiko pastovų skerspjūvį per visą aukštį, todėl aerodinaminės charakteristikos yra nuspėjamos. Priešingai, smėlio laikrodžio ir kūginės kliūtys turi kintamą skerspjūvį. 56 pav. parodyti cilindrinę, kūginių ir smėlio laikrodžio formos kliūčių hidrauliniai nuostoliai. Srautas K-H19 mikrokanale išlieka nestacionarus visame tirtame  $Re$ . Tuo tarpu K-C ir K-T14-A-P250 srauto nestabilumas prasideda  $Re$  viršijus 117, o K-T14-B-P250 yra stacionarus visame tirtame  $Re$  intervale.

56 pav. pateikti duomenys rodo, jog K-H19 pagerina hidraulinį našumą, sumažindamas  $\Delta p$  6-14%, palyginti su K-C. Nepaisant to, kad KC ir K-H19 konfigūracijos turi tą patį tūrį, KC paviršiaus plotas yra 23% didesnis, o tai gali lemti didesnę  $\Delta p$ . Be to, K-H19 srauto struktūra yra sudėtingesnė nei K-C.

Nors kūginėms kliūtims, palyginti su K-C, reikšmingo  $\Delta p$  sumažėjimo nenustatyta, stacionariame režime jos sumažina  $f$  6 % ir iki 11 % nestacionariame režime, o K-H19 sumažina  $f$  4 %.



**56 pav.** a)  $\Delta p$  ir b)  $f$  priklausomybė nuo  $Re$  K tipo konfigūracijoms

57 pav. pavaizduota pasipriešinimo koeficiento  $f$  priklausomybė nuo kūgiškumo kampo, esant skirtingiems atstumams tarp kliūčių ( $P$ ) ir  $Re$ . Mėlynos ir juodos kreivės atitinka vienakryptes (A) ir dvikryptes (B) kūgines kliūtis. Spalvotos sritys žymi srauto režimus: viršutinė – vienakryptėms, apatinė – dvikryptėms kliūtims.

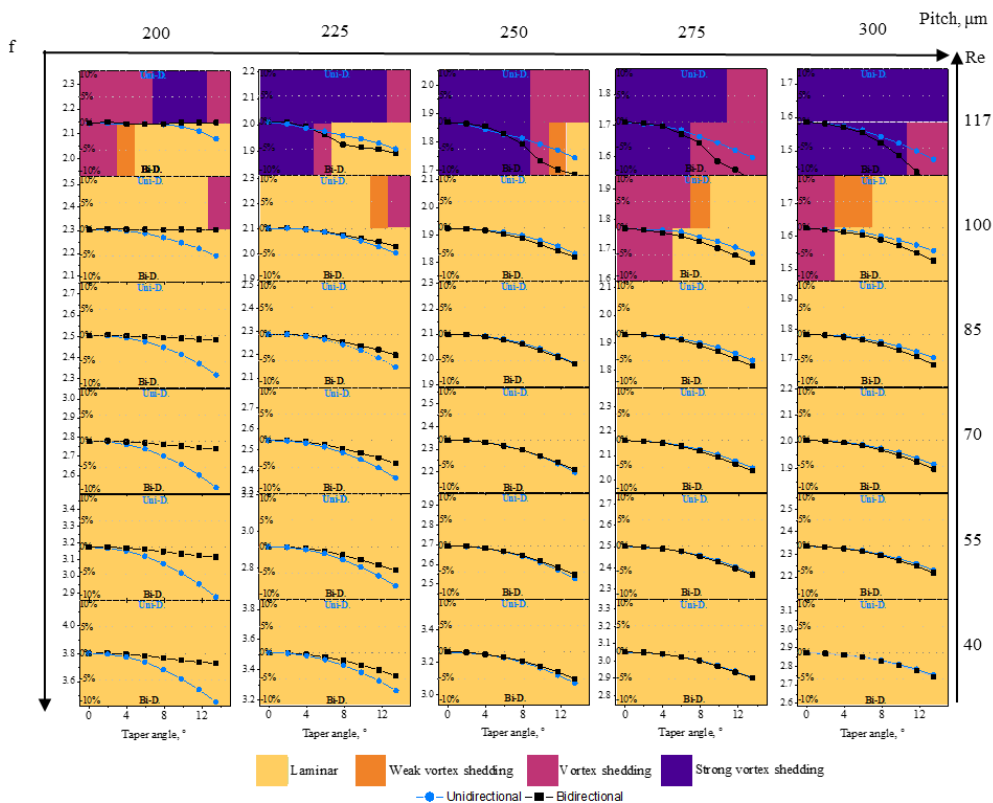
Kūgiškumas apibūdina kliūties skersmens pokytį pagal jo aukštį.  $13,48^\circ$  kampo kliūtis tūris yra 11,3 % didesnis, o paviršiaus plotas 2,83 % didesnis nei cilindrinės kliūtis (K-C).

Didėjant  $P$ , mažesnis  $Re$  sukelia sūkurių formavimąsi. Pavyzdžiui, padidinus  $P$  nuo 200 iki 300  $\mu\text{m}$ , srauto tūris išauga 61 %, o  $f$  sumažėja  $\sim 1,6$  karto ( $Re = 117$ ). Tačiau  $P$  nedaro reikšmingos įtakos  $f$  priklausomybei nuo  $Re$  –  $Re$  padidėjus nuo 40 iki 117,  $f$  padidėja  $\sim 43$  % (A) ir  $\sim 46$  % (B), nepriklausomai nuo  $P$ .

Kai  $P > 250 \mu\text{m}$  ir tekėjimas yra stacionarus, kūginių kliūčių orientacija beveik nepaveikia srauto. Tačiau pereinant į nestacionarų režimą, skirtumai tampa ryškesni: A tipo geometrija užtikrina mažesnę  $f$  esant mažam  $P$  ir stacionariam srautui, o B tipo geometrija stabilizuoja srautą, taip pat mažindama  $f$ .

Esant skirtingiems  $Re$ , nėra aiškios priklausomybės tarp  $f$  ir kūgiškumo kampo. A tipo konfigūracijos rodo nuoseklius rezultatus, o B tipo konfigūracijos pasižymi didesniais svyravimais. Esant mažam  $P$  (pvz., 200  $\mu\text{m}$ ), kampas ir pasvirimo kryptis gali pakeisti  $f$  iki 9 %, o padidinus  $P$  iki 225  $\mu\text{m}$  – iki 7 %. Kai  $P$  vertė viršija kanalo aukštį, orientacijos įtakos tampa nereikšminga. Visais atvejais didinant kūgiškumo kampą  $f$  mažėja.

Taigi, kai  $P > 225 \mu\text{m}$ ,  $f$  mažėja didėjant kampui, nepriklausomai nuo orientacijos. Tuo tarpu, kai  $P = 200 \mu\text{m}$ , tik A konfigūracijose  $f$  reikšmingai sumažėja didėjant kampui; B beveik nepakinta.



57 pav. Pasipriešinimo koeficientas skirtingo kampo kūginėms kliūtims esant skirtingam atstumui tarp jų ir  $Re$

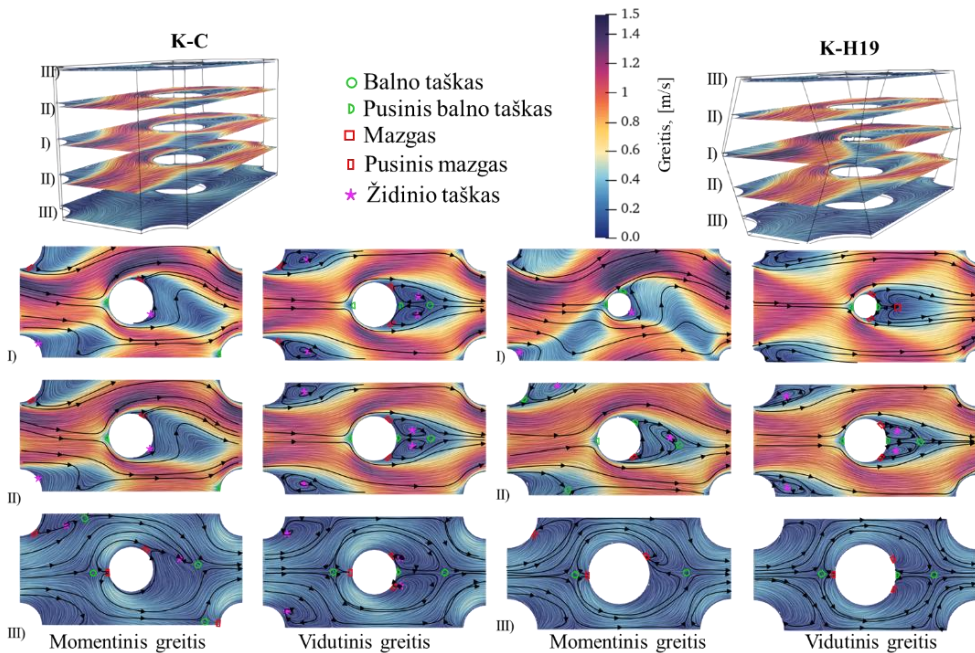
58–60 pav. parodomas srauto linijų pasiskirstymas įvairiose plokštumose, per vidurį, ties galinėmis sienelėmis. Srauto topologijos kritiniai taškai – mazgas (angl. *node*), židinio taškas (angl. *focus*) ir balno taškas (angl. *saddle*).

K-C konfigūracijoje stebimas tipiškas tekėjimas aplink cilindrinę kliūtis – sukuriai išlieka stabilūs visame kanalo aukštyje. Už kliūtis susidaro du priešinga kryptimi besisukantys sukuriai. K-H19 konfigūracijoje, židinio taškų nėra – vietoj to vidurinėje plokštumoje susidaro mazgo taškas (58 pav.). Srautas, pratekėdamas per siauriausią kanalo vietą, pagreitėja, taip pagerindamas šilumos perdavimą ir maišymą. Už kliūčių susiformavę du priešpriešiniai srautai susiduria centre, neleidami susidaryti stovintiems sukuriniams. Smėlio laikrodžio forma pagerina hidraulinės savybes. O kūginė geometrija leidžia valdyti srauto struktūrą priklausomai nuo kūgiškumo krypties. Dvikryptės (K-T14-B-P250) konfigūracijos neturi židinio taškų vidurinėje plokštumoje, bet dėl beveik simetriškų antrinių srautų sukuriai yra išsidėstę per visą kanalo aukštį (59 pav.). Šie srautai dvikrypčiuose kliūčių mikrokanaluose dar labiau pagerina maišymą tarp viršutinės ir apatinės sienelių.

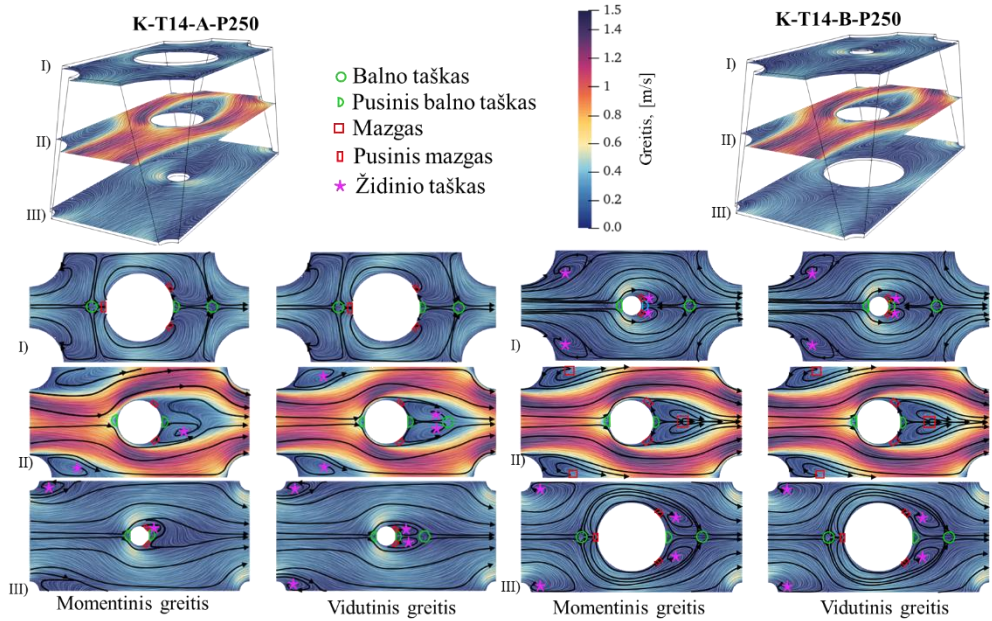
Vertikaloje plokštumoje (60 pav.) K-C ir K-H19 atvejais srauto struktūra yra simetriška. Tačiau kliūčių kūgiškumas ją iškreipia – antriniai srautai siauresnėje kūgio pusėje sukelia papildomų balno taškų atsiradimą. Įdomu tai, kad nors dvikryptės konfigūracijos turi sudėtingesnę srauto topologiją, jos pasižymi didesniu srauto stabilumu nei vienakryptės – dėl geresnio antrinių srautų balanso.

Pagrindinis skirtumas tarp K-C ir K-H19 glūdi jų konfigūracijose: K-H19 turi susiaurėjimą, kuris pagreitina tekėjimą centre ir gali pagerinti šilumos perdavimą. K-C sūkuriai išlieka vientisi visame aukštyje, o K-H19 atveju jie suskyla vidurio plokštumoje, formuodami daugiau mažų ir dinamiškai kintančių sūkurių.

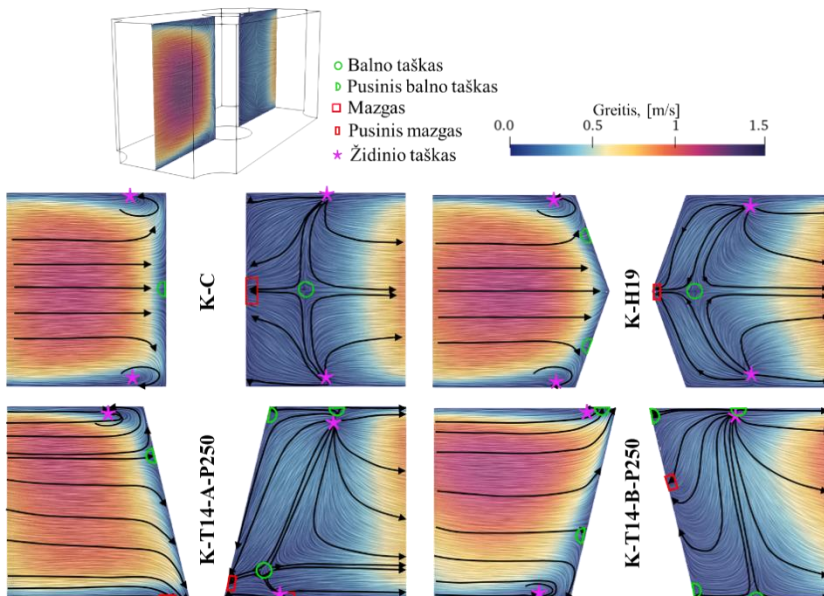
Galiausiai, priešais kūginę kliūtį slėgio gradientas nukreipia tekėjimą žemyn, link siauresnio galo (60 pav.). Už kliūčių susidaro asimetrinis antrinis tekėjimas – stipresnis srautas nuo plačiosios pusės atsitrenkia į silpnesnį nuo siaurosios, o balno taškas pasilenka link siaurojo galo. Ši sąveika žymiai pagerina masės mainus ir maišymą. Dvikryptėse konfigūracijose šie taškai nuolat keičiasi, dar labiau didindami srauto turbulenciją.



**58 pav.** Greičio srauto linijos ir kritiniai taškai įvairiuose K-C ir K-H19 mikrokanalų skerspjūviuose



**59 pav.** Greičio srauto linijos ir kritiniai taškai įvairiuose K-T14-A-P250 ir K-T14-B-P250 mikrokanalų skerspjūviuose



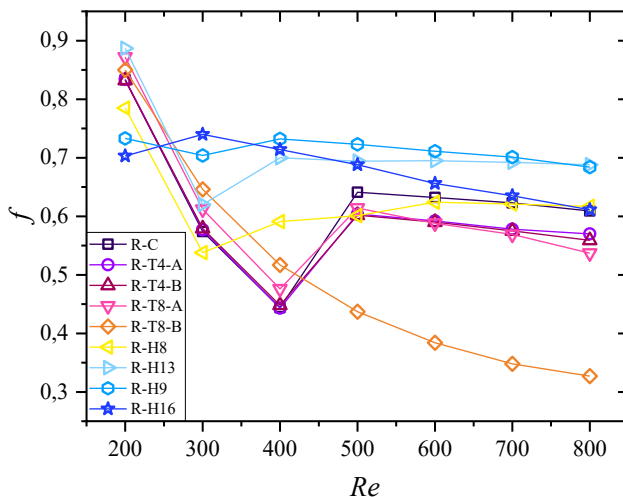
**60 pav.** Greičio srautų linijos ir kritiniai taškai vertikaliuose K-C, K-H19, K-T14-A-P250 ir K-T14-B-P250 mikrokanalų skerspjūviuose

Toliau buvo tiriami 9 skirtingi R tipo mikrokanalai. Tarp jų R-T8-B išsiskiria mažiausiu  $f$ , kai  $Re > 500$ , dėl srauto stabilizavimo efekto. Kitos kūginės konfigūracijos taip pat pasižymi mažesniais  $f$  nei cilindrinės kliūtys. Esant mažam kūgio pasvirimo kampui,  $f$  skirtumas tarp A ir B konfigūracijų yra minimalus, tačiau kampui didėjant, B tipo konfigūracija labiau stabilizuoja srautą, o A tipo – skatina maišymą.

Smėlio laikrodžio formos kliūtys skatina ankstesnį režimo pasikeitimą. Nors jos sukuria didesnę  $f$ , R-H16 rodo mažėjančią  $f$  tendenciją, tai rodo jų potencialą optimizuoti srautą.

Pastebėta, kad tekėjimo režimo pasikeitimo slenksčiai yra skirtingi: R-C, R-T4-A, R-T4-B R-T8-A pasireiškia, kai  $Re > 400$ , R-H8 ir R-H18, kai  $Re > 300$ , R-H9 ir R-H16, kai  $Re > 200$ . Tuo tarpu R-T8-B vienintelė iš tirtų konfigūracijų neparodė jokių režimo pasikeitimo požymių visame tirtame  $Re$  intervale.

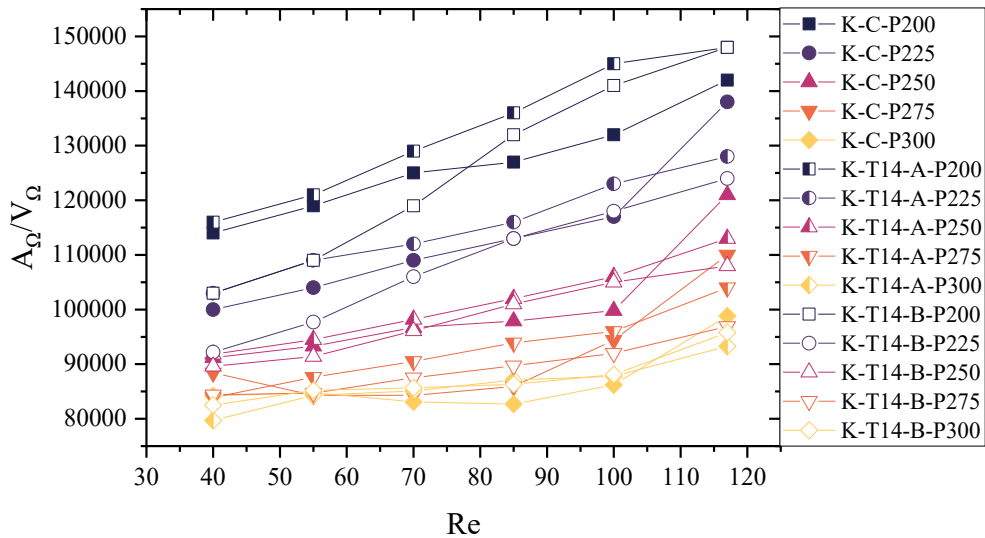
Galima daryti išvadą, kad kintantis smėlio laikrodžio formos kliūčių susiaurėjimas lemia skysčio greitėjimą ir lėtėjimą, o šie greičio svyravimai destabilizuoja srautą, skatindami ankstyvą režimo pasikeitimą. Nors kūginių kliūčių skerspjuvis taip pat kintamas išilgai kliūties ašies, jo poveikis srauto stabilumui yra mažesnis, režimo pasikeitimas vyksta panašiu metu kaip cilindrinė kliūtis masyve. Tačiau išsiskiria vienas atvejis – R-T8-B, kuriame skerspjuvio pokyčiai itin efektyviai stabilizuoja srautą, todėl net ir esant dideliame  $Re$  šioje konfigūracijoje režimo pokyčio nepastebėta.



61 pav.  $f$  priklausomybė nuo  $Re$  R tipo mikrokanalų konfigūracijose

### 6.5.2. $\Omega$ kriterijaus analizė

$\Omega$  kriterijaus analizė neapsiriboja vien vidutinės reikšmės vertinimu – ji taip pat gali būti taikoma sūkurių struktūrų identifikavimui, nustatant jų užimamą plotą ir tūrį. 62 pav. pavaizduota sūkurių struktūrų ploto ir tūrio santykio ( $A_\Omega/V_\Omega$ ) priklausomybė nuo  $Re$  ir atstumo tarp kliūčių centrų ( $P$ ), K tipo mikrokanaluose. Kaip ir tikėtasi, mažiausios  $P$  vertės atitinka didžiausias  $A_\Omega/V_\Omega$  vertes, nes mažesnis modeliuojamos srities tūris riboja sūkurių formavimąsi. Kai nestabilumas ardo sūkurių struktūras, jų  $A_\Omega/V_\Omega$  vertės smarkiai padidėja – ypač cilindrinėse kliūčių atveju. Dvipusio išdėstymo (B) kliūčių masyvai paprastai pasižymi mažiausiu  $A_\Omega/V_\Omega$ , nes jiems būdingas didesnis srauto stabilumas. Tačiau dėl mažesnio užgriozdinimo (angl. *blockage ratio*), esant didžiausiam  $P$ , jų  $A_\Omega/V_\Omega$  vertė yra tarp vienpusio ir cilindrinio išdėstymo konfigūracijų.



62 pav.  $A_\Omega/V_\Omega$  priklausomybė nuo  $Re$

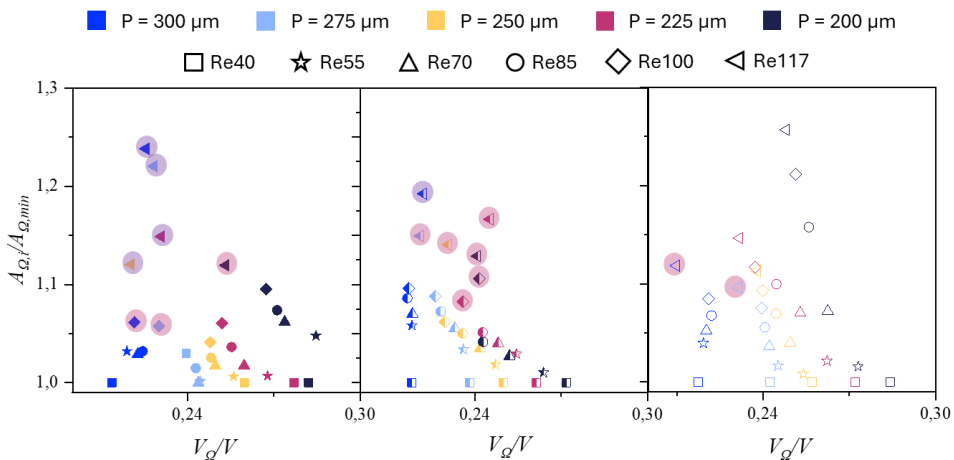
62 pav. atspindi tik sūkurių struktūrų plotą ir tūrį, neįtraukiant vidinių modeliuojamos srities sienelių ploto ar tūrio. Tuo tarpu 63 pav. pateikta normalizuota  $A_\Omega$  ir  $V_\Omega$  priklausomybė. Čia sūkurių plotas normalizuotas pagal atitinkamo žingsnio mažiausią vertę ( $A_{\Omega,min}$ ), o sūkurių tūris pagal bendrą modeliuojamą tūrį ( $V$ ).

Esant didesnėms  $P$  vertėms sūkuriiai užima didesnę tūrio dalį. Pavyzdžiui, kai  $P = 200 \mu\text{m}$ ,  $V_\Omega/V$  yra maždaug 4–5 % didesnis nei  $P = 300 \mu\text{m}$ . Mažesnis  $P$  susiaurina tekėjimo kelią, skatina skysčio sąveiką ir maišymą dėl ribotos erdvės, o tai slopina didelių sūkurių susidarymą ir stiprina lokalią turbulenciją bei energijos sklaidą. Nepaisant to, esant mažam  $P$ , srautas išlieka stacionarus.

Tuo tarpu didesnis  $P$  leidžia formuotis koherentinėms srauto struktūroms, įskaitant didesnius sūkurius. Šis atstumo padidėjimas skatina stipresnę sąveiką tarp tėkmės sluoksnių, todėl net esant mažesniai  $Re$ , perėjimas į nestacionarų režimą pagreitėja. Didesnis  $P$  taip pat leidžia sklandžiau ir stabiliau formuotis pasienio sluoksniui tarp kliūčių, sumažinant srauto atsiskyrimą, prisitvirtinimą ir kinetinės energijos svyravimus. Apskritai, didesnis  $P$  mažina tiek sūkurių paviršiaus plotą, tiek tūrį – nepriklausomai nuo kliūčių formos.

Bendra tendencija rodo, kad  $V_{\Omega}/V$  mažėja didėjant  $Re$ , o  $A_{\Omega}$  didėja. Pažymėtina, kad esant nestacionariam srautui (pažymėtam violetine spalva),  $A_{\Omega}/A_{\Omega,min}$  vertė padidėja net 8–17 % didėjant  $P$  – tai rodo, kad sūkuriai skyla į smulkesnes struktūras. Priešingai, vidutinio nestabilumo atvejais (pažymėti raudonai)  $A_{\Omega}/A_{\Omega,min}$  padidėja tik nežymiai, o  $V_{\Omega}$  dažnai net sumažėja – tai reiškia, kad nors sūkurių slinkimas vyksta, jie visiškai neišsiskaido, o išlieka sujungti.

Įdomu tai, kad dvikrypčio išdėstymo kūginės kliūtys prie mažiausio  $P$  pasižymi itin aukštomis  $V_{\Omega}/V$  ir  $A_{\Omega}/A_{\Omega,min}$  vertėmis esant dideliame  $Re$ , net jei tekėjimas išlieka stacionarus. Mažiams  $Re$ , jų  $A_{\Omega}/A_{\Omega,min}$  yra panaši į kitų konfigūracijų, tačiau ji žymiai didėja didėjant  $Re$  – tai reiškia, kad sūkuriai ne tik išlieka, bet ir plečiasi, o ne silpnėja didėjant  $Re$ .



**63 pav.** Normalizuota sūkurių ploto priklausomybė nuo tūrio

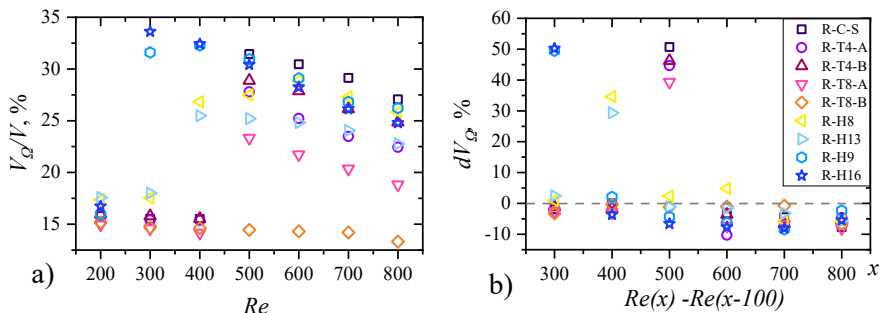
64 pav. a) pateiktas sūkurių struktūrų užimamas plotas, identifikuotas pagal  $\Omega$  kriterijų, o b) dalis rodo šio ploto kitimą nuo  $Re$ , R tipo konfigūracijoms. Rezultatai rodo, kad stacionarioje tekėjime sūkuriai užima apie 15–17 % viso masyvo tūrio. Šis santykinai mažas ir pastovus tūrių santykis atspindi tipiską stacionaraus tekėjimo stabilumą. Skirtingos konfigūracijos rodo tik nežymius skirtumus. Tačiau po perėjimo į nestacionarų tekėjimą šis procentas gali padidėti iki 32 %, t. y. beveik padvigubėti, lyginant su stacionariu režimu. Šis beveik dvigubas padidėjimas atspindi koherentinių

sūkurių sričių išsiplėtimą ir sudėtingesnės srauto dinamikos pradžią. Tokios konfigūracijos kaip R-H16 ir R-T4-B rodo didesnį padidėjimą, tai atskleidžia didesnį jautrumą sūkurių formavimuisi. Tuo tarpu tokios konfigūracijos kaip R-H13 ir R-H8 demonstruoja nuosaikesnę reakciją, dėl struktūrinių savybių, slopinančių sūkurių plitimą ar jų formavimąsi.

64 pav. b) papildo  $\Omega$  analizę, parodydama užimamo tūrio pokyčius ( $dV_\Omega$ ) priklausomai nuo  $Re$ . Stacionariame režime dauguma konfigūracijų rodo neigiamas arba beveik nulines  $dV_\Omega$  reikšmes, rodančias sūkuriams užimto tūrio susitraukimą ar stabilumą, dėl pagerėjusio stabilumo ir srauto nusistovėjimo. Tačiau, kai tekėjimas tampa nestacionarus, dauguma konfigūracijų rodo teigiamus  $dV_\Omega$ , atspindinčius sūkurių sričių išsiplėtimą. Kitais atvejais  $dV_\Omega$  vėl tampa neigiamas, tai rodo struktūrų susiskaidymą į smulkesnius sūkurius ar jų susitraukimą.

Abi tendencijos pereinamojo režimo metu rodo, kad sūkurių elgsena ir jų sąveikos priklausomybė  $Re$  yra nelinijinė. Perėjimas į nestacionarų tekėjimą skatina sūkurių augimą, tačiau tolesnis  $Re$  didėjimas gali sukelti jų struktūrinį suirimą ir chaotiškesnį maišymą.

Apibendrinant, pateikti duomenys pabrėžia R tipo geometrijų jautrumą tekėjimo režimo pokyčiams. Sūkurių tūrio santykio didėjimas tekėjimui tampant nestabiliam išryškina koherentinių struktūrų svarbą nestabilumų raidai, o  $dV_\Omega$  pokyčiai atskleidžia dinaminę sūkurių prigimtį – jų augimą ar susitraukimą priklausomai nuo konfigūracijos ir srauto sąlygų. Šios išvalgos yra esminės norint suprasti energijos sklaidą, srauto pasipriešinimą ir tekėjimo režimo pasikeitimo mechaniką.



**64 pav.** a) Sūkurių užimama bendro tūrio dalis ( $V_\Omega/V$ ) priklausomybė nuo  $Re$ , b) užimto ploto kitimo ( $dV_\Omega$ ) priklausomybė nuo  $dRe$

21 lentelę galima laikyti sisteminė anksčiau gautų ir išanalizuotų rezultatų, susijusių su koherentinių srauto struktūrų charakteristikomis, santrauka ir interpretacija. Ji remiasi trimis pagrindiniais parametrais: koherentinių struktūrų paviršiaus plotu, užimamu tūriu ir intensyvumo rodikliu, atspindinčiu sūkurių ar tekėjimo sūkuringumo stiprumą.

Sujungus šiuos rodiklius, galima gauti išsamesnį vaizdą apie srauto pobūdį ir galimą jo poveikį šilumos perdavimui bei hidrauliniam pasipriešinimui. Pavyzdžiui, kai visos trys vertės yra aukštos, tai reiškia stiprius, plačiai pasiskirsčiusius ir aktyviai sąveikaujančius sukurius, kurie efektyviai skatina skysčio maišymą ir pagerina šilumos mainus. Priešingai, žemos visų parametų vertės rodo silpnus ir mažus sukurius, kurie daro mažą įtaką bendrai srauto dinamikai.

Tarpinės ar mišrios vertės leidžia nustatyti, ar srauto struktūros yra stabilios, išskaidytos, ar būdingos pereinamajam režimui. Tokia klasifikacija ne tik padeda giliau suprasti gautus skaitinės analizės rezultatus, bet ir leidžia tiksliau palyginti skirtingas geometrines konfigūracijas bei jų elgseną esant įvairioms tekėjimo sąlygoms. 21 lentelė yra vertinga interpretavimo priemonė, leidžiantis susieti kiekybinius rodiklius su kokybinėmis srauto charakteristikomis, taip palengvinant rezultatų analizę ir vertinimą.

**21 lentelė.** Sukurių interpretacija pagal  $A_{\Omega}$ ,  $V_{\Omega}$  ir  $\Omega$  dydžius

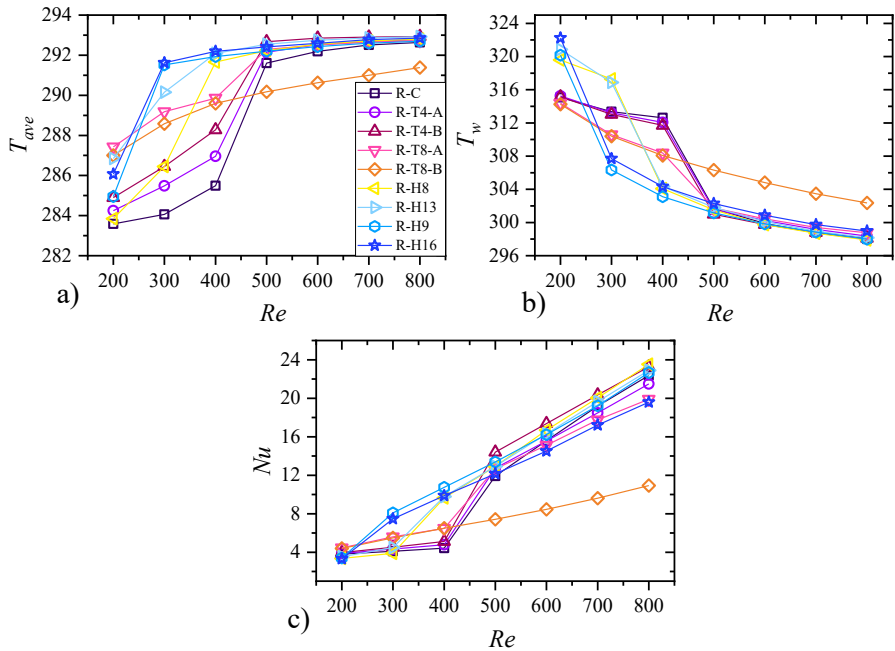
$A_{\Omega}$	$V_{\Omega}$	$\Omega$	Interpretacija
<b>Aukštas</b>	Aukštas	Aukštas	Stiprūs, erdviškai išsiplėtę, aktyviai sąveikaujantys sukuriiai – tikėtina, kad pagerina maišymą ir šilumos perdavimą.
<b>Žemas</b>	Žemas	Žemas	Silpni ir maži sukuriiai, mažai trikdantys srautą.
<b>Aukštas</b>	Žemas	Aukštas	Daug mažų, energingų sukurių su intensyvia paviršiaus sąveika.
<b>Žemas</b>	Aukštas	Žemas	Dideli, bet silpni arba stovintys sukuriiai – galimos recirkuliacinės zonos.
<b>Aukštas</b>	Žemas	Žemas	Daug mažų, bet silpnų sukurių – galimos ankstyvos šlyties sluoksnio nestabilumo apraiškos, dar nesusiformavusios į sukurius. Gali rodyti pereinamąjį režimą.
<b>Žemas</b>	Aukštas	Aukštas	Dideli stiprūs sukuriiai, turintys santykinai mažą paviršiaus sąveiką – galimi stabilūs sukuriiai.
<b>Žemas</b>	Žemas	Aukštas	Maži, labai intensyvūs sukuriiai – galimi izoliuoti sukuriiai arba pereinamojo režimo suintensyvėjimai.
<b>Aukštas</b>	Aukštas	Žemas	Didelės sritys, tačiau neženkliai stipresnės už pagrindinį srautą – gali rodyti netvarkingą srautą arba sukurių disipaciją.

### 6.5.3. Šilumos perdavimo charakteristikos

R-C, R-T ir R-H konfigūracijų šilumos perdavimo analizė buvo atlikta naudojant Nuselto skaičių ( $Nu$ ) ir temperatūros netolygumą ( $\delta_T$ ) kaip pagrindinius našumo vertinimo rodiklius. Papildomai pateikiamos diagramos, kuriose parodyta sienelės temperatūra ( $T_w$ ) ir vidutinė temperatūra ( $T_{ave}$ ) (žr. 65 pav.).

Kaip ir anksčiau analizuoto pasipriešinimo koeficiento atveju, R-T8-B konfigūracija pasižymi išskirtinėmis šilumos perdavimo savybėmis. Nors ji turi

žemiausią  $T_{ave}$ ,  $T_w$  išlieka aukščiausia dėl stacionaraus tekėjimo ir stovinčių sukurių susidarymo. Dėl šių savybių R-T8-B konfigūracija turi mažiausią  $Nu$ , net dvigubai mažesnę nei cilindrinės (R-C-S) konfigūracijos.



**65 pav.** a) Vidutinės temperatūros, b) sienelės temperatūros ir c) Nuselto skaičiaus kitimas skirtingoms konfigūracijoms tiriamame  $Re$

Lyginant  $Nu$  nuokrypį nuo R-C-S kiekvienai konfigūracijai, esant skirtingiems  $Re$ , rezultatai yra nevienareikšmiai (žr. 22 lentelę). Nuokrypis buvo apskaičiuotas pagal šią formulę:

$$Nu \text{ nuokrypis} = \frac{1}{n} \sum_{i=1}^n \frac{Nu_{Re=i}^{atvejis} - Nu_{Re=i}^{R-C}}{Nu_{Re=i}^{atvejis}} \quad (68)$$

**22 lentelė.** Nuselto skaičiaus nuokrypis skirtingiems R-T ir R-H mikrokanalams, lyginant su R-C-S

$Nu$ nuokrypis (%)	R-T4-A	R-T4-B	R-T8-A	R-T8-B	R-H8	R-H13	R-H9	R-H16
$200 \leq Re \leq 800$	1,80%	9,13%	7,92%	-39,67%	8,40%	10,33%	16,09%	7,77%
$500 \leq Re \leq 800$	-2,71%	6,60%	-7,87%	-96,04%	5,23%	3,01%	1,78%	-11,01%

Pavyzdžiui, R-T8-A pasižymi puikiais hidrodinaminėmis savybėmis visame tiriamame  $Re$  intervale. Tačiau jo šiluminis efektyvumas blogėja  $Re$  intervale  $500 \leq$

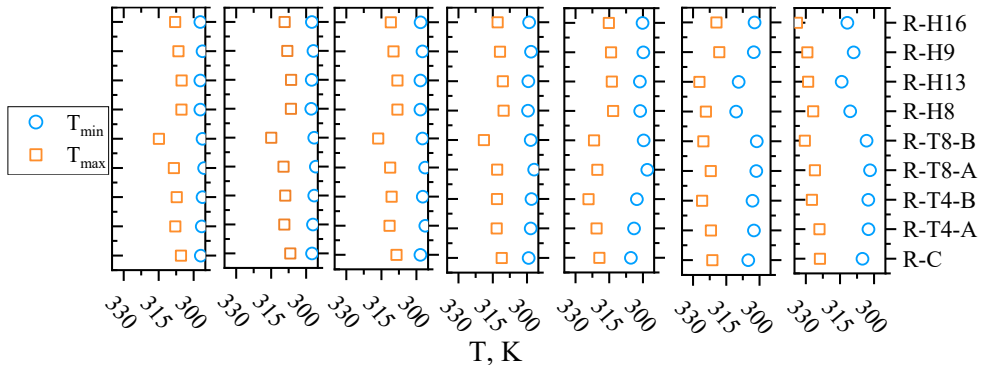
$Re \leq 800$ . Šis intervalas pasirinktas todėl, kad visos konfigūracijos (išskyrus R-T8-B) šiame intervale jau perėjo į nestacionarų tekėjimo režimą. Tas pats reiškinys stebimas ir R-T4-A bei R-H16 atvejais. Daugumoje konfigūracijų, kai  $Re \geq 500$ ,  $Nu$  reikšmės mažėja, palyginti su bendra augimo tendencija (žr. 22 lentelę). Tai nereiškia efektyvumo sumažėjimo – priešingai, tai rodo netolygų perėjimą į nestabilų tekėjimą. Režimui nusistovint, greičiausiai, kad  $Nu$  vėl ims didėti (po  $Re = 500$ , išskyrus R-T8-B atvejį). Iš visų atvejų labiausiai išsiskiria R-T4-B ir R-H8 konfigūracijos, pasižyminčios didžiausiais  $Nu$  nuokrypiais lyginant su bazine cilindrine konfigūracija.

66 pav. pavaizduotos minimali ir maksimali sienelės temperatūra, o 67 pav. – jų skirtumas, žymimas kaip  $\delta_T$ :

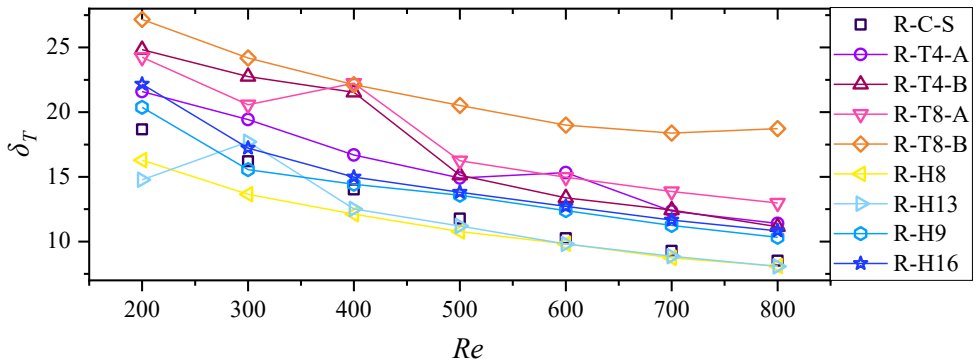
$$\delta_T = T_{max} - T_{min} \quad (69)$$

Šis parametras leidžia įvertinti šilumos pasiskirstymo tolygumą. Mažiausios  $\delta_T$  vertės stebimos R-H13, R-H8 ir R-C-S konfigūracijose, o tai rodo tolygesnį šilumos pasiskirstymą, kuris paprastai yra palankus šilumos valdymo požiūriu. Nepaisant to, smėlio laikrodžio formos kliūtys pasižymi didžiausiu  $T_{min}$  esant mažiems  $Re$  ir viena mažiausių  $T_{max}$  verte esant didesniems  $Re$ . Tai rodo, kad tokia konfigūracija gali padėti stabilizuoti temperatūros svyravimus skirtinguose tekėjimo režimuose.

Kaip jau minėta, R-T4-B konfigūracija pasižymi didesniu  $Nu$  nei R-C-S, tačiau jos  $\delta_T$  buvo viena didžiausių, o tai rodo mažesnę šilumos pasiskirstymo tolygumą. Be to, esant mažam  $Re$ , šios konfigūracijos  $T_{max}$  yra viena didžiausių – tai rodo lokalizuotą karštųjų taškų susidarymą, kai temperatūrų skirtumai yra didesni nei kitose konfigūracijose.



**66 pav.** Minimalios ir maksimalios sienelės temperatūros vertės skirtingoms mikrokanalų konfigūracijoms



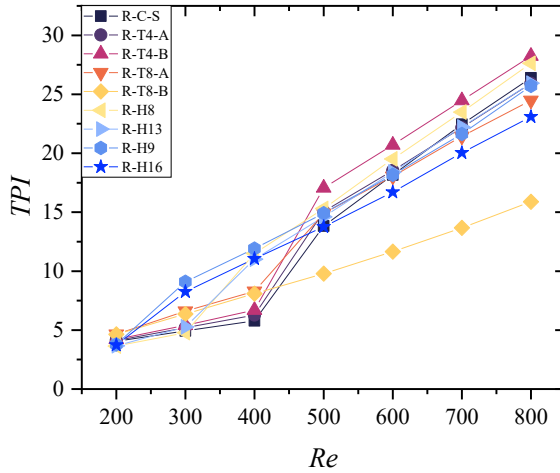
67 pav. Temperatūros netolygumas kintant  $Re$  skirtingoms mikrokanalų konfigūracijoms

#### 6.5.4. Termohidraulinis efektyvumas

Rezultatai rodo, kad net nedideli kliūčių pokyčiai, pavyzdžiui, kūgio kampas, gali reikšmingai paveikti skysčio tekėjimo struktūrą ir šilumos perdavimo efektyvumą. Skerspjūvio formos pokyčiai sukuria antrines tėkmės, kurios sustiprina konvekciją ir pagerina šilumos mainus. Vis dėlto, tokios antrinės tėkmės kliūčių masyvuose turi esminį trūkumą – tekėjimo nestabilumas smarkiai padidina slėgio nuostolius ( $\Delta p$ ).

Šilumos perdavimo ir slėgio nuostolių pusiausvyrai įvertinti naudojamas **šiluminio efektyvumo indeksas** ( $TPI = Nu/f^{1/3}$ ), leidžiantis įvertinti bendrą sistemos efektyvumą skirtingose kliūčių konfigūracijose (žr. 68 pav). Mažų  $Re$  srityje ( $Re = 200\text{--}300$ ) didžiausias  $TPI$  vertes pasiekė R-T8-A ir R-T8-B konfigūracijos – jų indeksas buvo 13–25 % didesnis nei cilindrinės R-C-S konfigūracijos. Tačiau esant didelėms  $Re$  reikšmėms ( $Re = 500\text{--}800$ ), R-T8-B, dėl to tekėjimo režimo nepasikeitimo, pasižymėjo mažiausiu  $TPI$  – jis buvo 41–66 % mažesnis nei R-C-S. Tuo tarpu R-T8-A šioje srityje taip pat šiek tiek nusileido – jos  $TPI$  buvo keliais procentais mažesnis nei R-C-S.

Iš visų tirtų kliūčių konfigūracijų R-T4-B parodė geriausią našumą visame  $Re$  intervale, nuo jos nedaug atsiliko R-H8. R-T4-B padidino  $TPI$  vidutiniškai 10 % visame tirtame  $Re$  diapazone, o R-H8 našumas pagerėjo tik po srauto perėjimo į nestacionarų tekėjimo režimą – vidutiniškai 6 %, tačiau stacionariame tekėjime šio atvejo rodiklis buvo 7 % žemesnis nei bazinė R-C-S konfigūracija.



68 pav. Kliūčių konfigūracijų įtaka šiluminio našumo indeksui

#### 6.4.5. Termohidraulinis efektyvumas taikant $\Omega$

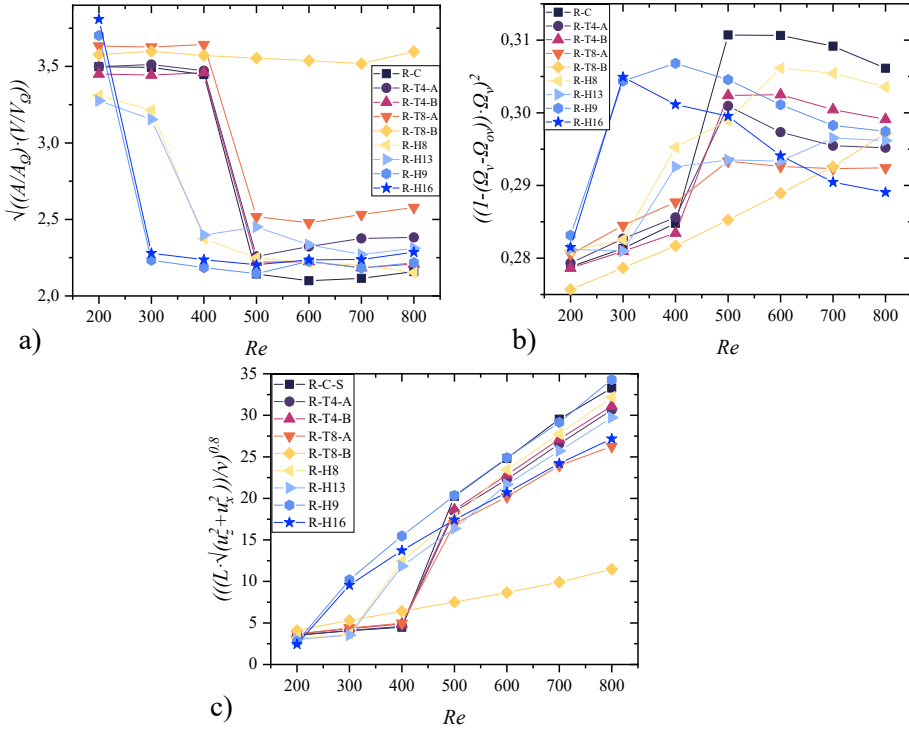
Koherentinių struktūrų pagrindu atliekamas našumo vertinimas gali būti itin naudingas, kai šilumos perdavimas nėra tiesiogiai modeliuojamas, tačiau siekiama prognozuoti termohidraulinį efektyvumą. Visų koherentinių struktūrų paviršiaus plotas ( $A_\Omega$ ) ir tūris ( $V_\Omega$ ) gali padėti įvertinti sūkurių slinkimo potencialą. Didelė  $V_\Omega$  vertė rodo, kad sūkuriai užima didelę dalį tūrio, o  $A_\Omega$  atspindi jų paviršinę sąveiką su aplinkiniu srautu. Didelė  $A_\Omega$  reikšmė reiškia intensyvią sąveiką, kuri skatina konvekcinį šilumos perdavimą. Be to,  $\Omega_v/\Omega_{ov}$  parodo sūkurių stiprumą viso srauto atžvilgiu.

Todėl šiam vertinimui sukurta efektyvumo formulė susideda iš kelių komponentų:

$$\eta_\Omega = 1.25 \cdot \sqrt{\left(\frac{A}{A_\Omega} \cdot \frac{V}{V_\Omega}\right)} \cdot \left(\left(1 - (\Omega_v - \Omega_{ov})\right) \cdot \Omega_v\right)^2 \cdot \left(\frac{L \cdot \sqrt{u_z^2 + u_x^2}}{v}\right)^{0.8} \quad (70)$$

69 pav. pavaizduotas visų (71) lygties narių vertės. Pirmasis komponentas įvertina santykinį sūkurių užimamą plotą ir tūrį – tai atspindi sąveikos paviršių. Mažos reikšmės rodo stiprią sūkurių sąveiką su skysčiu, kas gali padidinti šilumos perdavimo intensyvumą. Antrasis komponentas apibrėžia koherentinių struktūrų santykinį stiprumą. Tai tam tikras savireguliacijos mechanizmas – aukšta  $\Omega_v$  reikšmė yra naudinga tik tol, kol žymiai neviršija viso srauto vidutinio lygio. Jei sūkuriai tampa per stiprūs, jie tampa nuostolingi, todėl formulėje įtrauktas koeficientas, kuris kompensuoja per didelį jų dominavimą ir skatina pusiausvyrą tarp efektyvaus

maišymo ir energijos taupymo. Trečiasis komponentas įvertina naudingą skersinį tekėjimą, kuris perneša šilumą nuo sienelių link pagrindinio srauto.

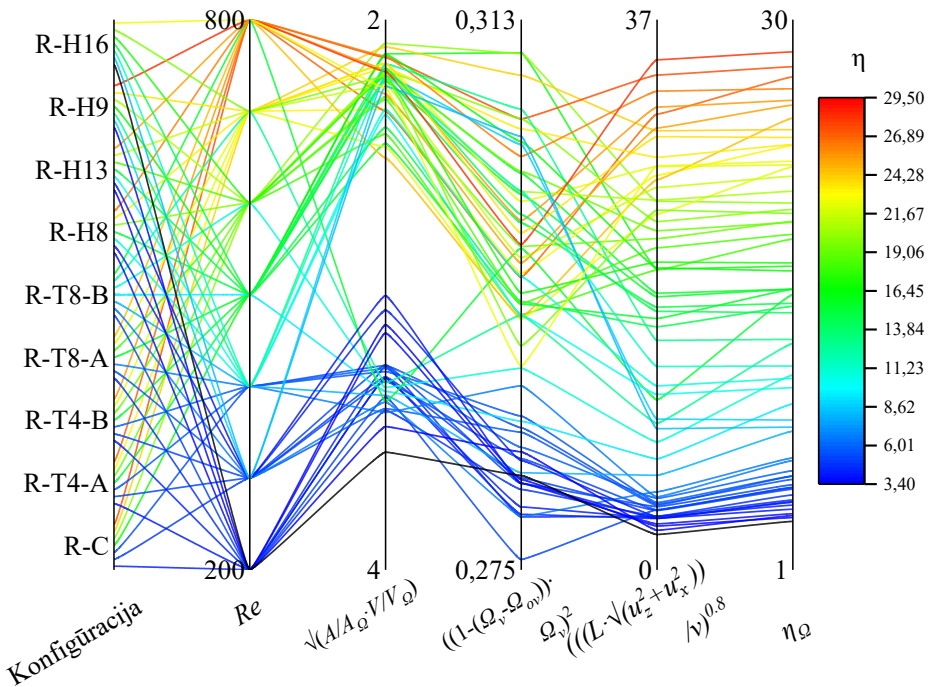


69 pav. a)  $\sqrt{\left(\frac{A}{A_\Omega} \cdot \frac{V}{V_\Omega}\right)}$  b)  $((1 - (\Omega_v - \Omega_{ov})) \cdot \Omega_v)^2$  c)  $\left(\frac{L \cdot \sqrt{u_z^2 + u_x^2}}{v}\right)^{0.8}$  priklausomybės nuo  $Re$

Lygiagrečiųjų koordinatinių diagrama, pateikta 70 pav., leidžia vizualiai palyginti termohidraulinį efektyvumą  $\eta_\Omega$  tarp skirtingų konfigūracijų ir  $Re$  reikšmių. Kiekviena linija atitinka konkretų atvejį (pvz., R-H16, R-T8-B ir kt.), o spalva nurodo pasiektą efektyvumą nuo žemiausio (violetinė) iki aukščiausio (raudona).

Šioje diagramoje matyti, kad aukšto efektyvumo konfigūracijos (raudonos–oranžinės linijos) pasižymi stipria sūkurių sąveika, subalansuotu stiprumu, stipriu skersiniu tekėjimu, kuris palaiko konvecinę pernašą nuo įkaitusių sienelių į pagrindinį srautą. Daugiamatė analizė aiškiai rodo, kad pirmasis komponentas padalina atvejus į dvi grupes, kurių vertės yra mažesnės ir didesnės nei 3. Didesnės vertės rodo mažus, vis dar besiformuojančius sūkurius, kurie nesuteikia didelio  $\eta_\Omega$ , o mažos vertės atspindi intensyvią sūkurių sąveiką. Didelio efektyvumo kategorijai priskiriamos R-H8, R-H9 ir R-H13. Priešingai, mažo efektyvumo konfigūracijos,

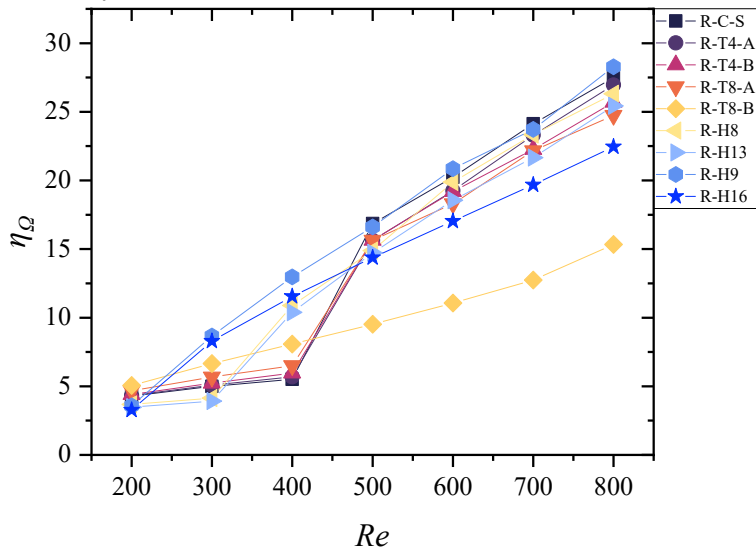
tokios kaip R-T4-A, pasižymi silpna sūkurių sąveika ir menka skersine tėkme. Tačiau didėjant  $Re$  efektyvumas paprastai gerėja, ypač konfiguracijoms, kurios skatina koherentinių sūkurių formavimąsi ir srauto skersinę tėkmę. Tarp tokių konfiguracijų išsiskiria R-H16, R-H9 ir R-H13. Priešingai, žemo efektyvumo atvejai, tokie kaip R-C ir R-T4-A, pasižymi silpnais sūkuriais, menku skersiniu ir dažnai stipriu horizontaliu tekėjimu, kuris blogina jų termohidraulinį našumą. Taip pat pastebėta, kad didėjant  $Re$  gerėja ir sistemos našumas, ypač tose konfiguracijose, kurios skatina koherentinių sūkurių susidarymą bei srauto kryptingumą.



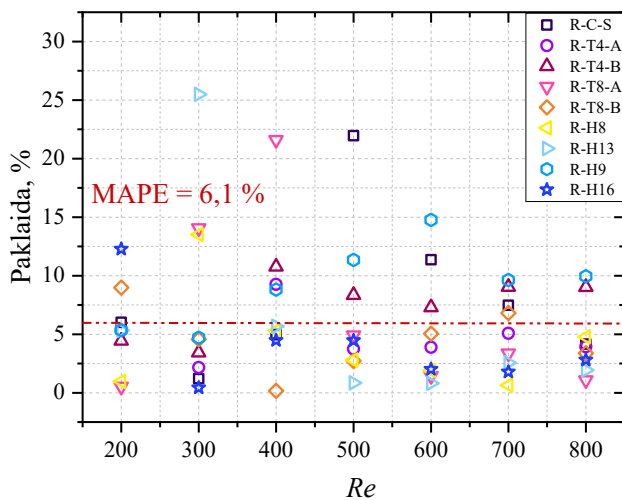
**70 pav.** Daugianarė termohidraulinio efektyvumo analizė, pagrįsta sūkurių charakteristikomis, energijos pasiskirstymu ir srauto kryptingumu

71 pav. pateikti įvairių geometrijų  $\eta_\Omega$  esant skirtingoms srauto sąlygoms. Visų konfiguracijų ir  $Re$  paklaidos pateiktos 72 pav., o TPI verčių palyginimas su  $\eta_\Omega$  (TPI) pateiktas 73 pav.  $\eta_\Omega$  formulės pritaikymas tiksliai atkuria TPI vertes, bendros paklaidos mažos, o tendencijos glaudžiai siejasi su sumodeliuotomis TPI vertėmis. Visų konfiguracijų bendra MAPE  $\approx 6,1\%$ . Pagal konfiguraciją, mažiausi vidutiniai nuokrypiai gauti R-H16 ( $\sim 4,0\%$ ) ir R-H8 ( $\sim 4,3\%$ ), po jų – R-T8-B ( $\sim 4,5\%$ ), o didžiausia vidutinė paklaida – R-H9 ( $\sim 9,1\%$ ). Formulė išlaiko eiliškumą tarp atvejų – R-T4-B tarp aukščiausių, R-T8-B tarp žemiausių, o R-H16 – netoli apačios.

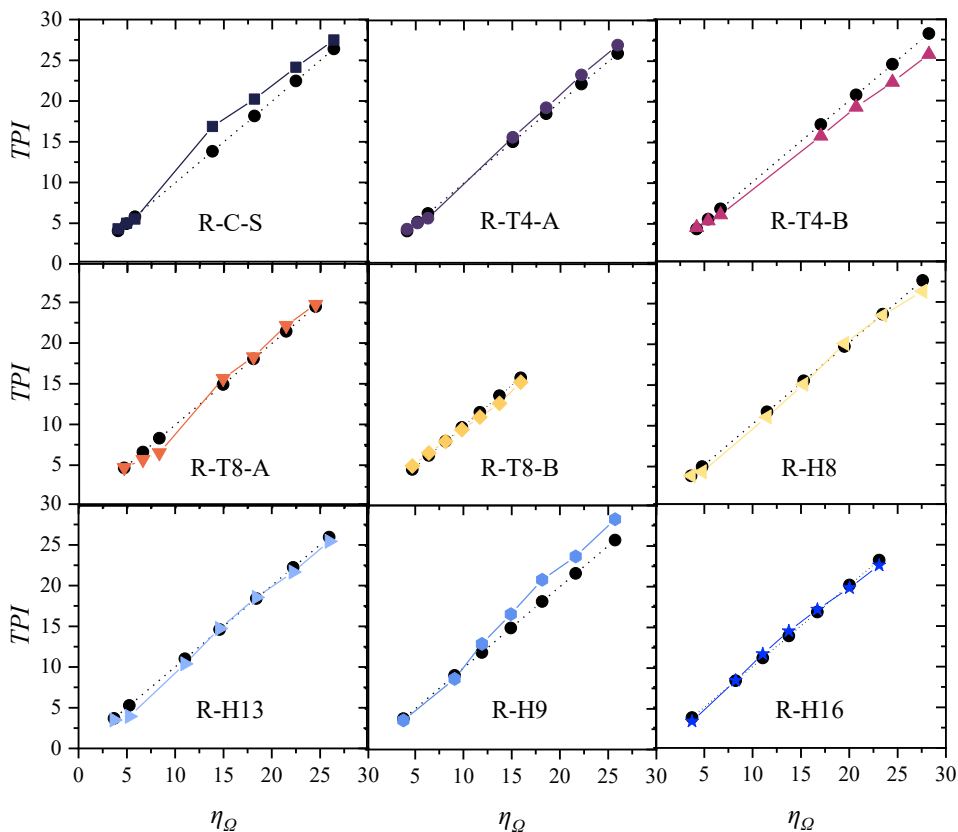
Spearmano koreliacija siekia 0,99, tad ryšys yra monotoniškas. Apibendrinant galima teigti, kad siūloma  $\eta_{\Omega}$  formulė atitinka *TPI* esant įvairioms tekėjimo sąlygoms, daugiau neatitikimų yra mažesniuose *Re*.



71 pav.  $\eta_{\Omega}$  priklausomybė nuo *Re*



72 pav.  $\eta_{\Omega}$  reikšmių paklaidos, lyginant su *TPI*.



73 pav.  $TPI$  (juoda linija) palyginimas su apskaičiuotomis  $\eta_{\Omega}(TPI)$  vertėmis

## 6.6. Išvados

Skaitiniu modeliavimu kiekybiškai ištirtos koherentinių srauto struktūrų savybės ir susietos su įvairių mikrokanalų termohidraulinio efektyvumu, įskaitant cilindrinės (C), kaip bazines, smėlio laikrodžio formos (H) ir kūgines (T) kliūtis. T kliūtys buvo vienkryptės (A) arba dvikryptės (B). Remiantis modeliavimo rezultatais, gautais  $Re$  200-800 diapazone, padarytos išvados:

1. Mažo pasvirimo kampo kliūtys ( $< 8^\circ$ )  $\sim 7\%$  padidina arba nepakeičia slėgio nuostolių, kai tekėjimas stacionarus, o kai nestacionarus – slėgio nuostoliai gali vidutiniškai sumažėti 6%. Didelis kliūčių pasvirimo kampas ( $> 8^\circ$ ) padidina slėgio nuostolius, kai tekėjimas stacionarus vidutiniškai apie 13%, o nestacionariame režime  $\sim 5\%$ , išskyrus R-T8-B atvejį, kuris sumažina slėgio nuostolius 23%, bet srautas visame tirtame  $Re$  intervale išlieka stacionarus, dėl ko pasižymi prasciausiu  $TPI$ . Mažo kampo T formos kliūtys padidina  $Nu$  ir  $TPI$  vertes 1-11%,

- palyginti su **C**. Tuo tarpu **H** kliūtys sumažina  $TPI$  ir  $Nu$ , nepriklausomai nuo tekėjimo režimo.
2. Pasikeitus tėkmės režimui iš stacionaraus į nestacionarų  $V_{\Omega}/V$  padidėja nuo 15–17 % iki 32 %, kai  $A_{\Omega}/A$  išauga nuo 46–55 % iki 74–81 %. Nepriklausomai nuo tėkmės režimo  $A_{\Omega}/A$  auga.  $V_{\Omega}/V$  stacionariame tekėjime išlieka pastovus arba mažėja, o nestacionariame mažėja. Tai rodo, jog, pasikeitus tekėjimo režimui, sūkurių susidaro gerokai daugiau dėl srauto nestabilumo (sūkurių plotas ir tūris staiga išauga), tačiau vėliau tūrio mažėjimas kartu su ploto didėjimu rodo jų disipaciją.
  3. Tekėjimui pereinant iš stabilaus į nestabilų,  $V_{\Omega}/V$  padidėjo nuo 16 % iki 30 % **C** kliūčių masyvuose, nuo 16 % iki 26 % – **H** ir nuo 15,5 % iki 24 % – **T**. Kliūčių pasvirimo kampo įtaka buvo minimali ( $\pm 2$  %). Vidutiniškai **H** tipo kliūtys turėjo didžiausią  $A_{\Omega}/A$  santykį (68–72 %), po jų sekė **C** (65 %) ir **T** (54–66 %). Didžiausias sūkurio intensyvumas ( $\Omega$ ) buvo **H**, o mažiausias – **T**; R-C-S turėjo didžiausią bendrą  $\Omega$  po tekėjimo režimo pasikeitimo.
  4. Sukurtas termohidraulinio efektyvumo vertinimo metodas, sujungiantis sūkurių sąveikos plotą ( $A_{\Omega}/A \cdot V_{\Omega}/V$ ), sūkurio intensyvumą ( $(1 - (\Omega_v - \Omega_{ov})) \cdot \Omega_{vortex}$ ) ir srauto skersinę tėkmę  $\frac{L \cdot \sqrt{u_z^2 + u_x^2}}{\nu}$ . Metodas leidžia visiškai atsisakyti energijos (šilumos mainų) lygties modeliavimo, taip sumažindamas skaičiavimo resursus ir suteikdamas greitą termohidraulinio efektyvumo įvertį. Siūlomas metodas, lyginant su  $TPI$ , rodo 6,8 % vidutinę santykinę paklaidą. Jis suteikia naują analitinę perspektyvą, leidžiančią geriau suprasti srauto sukeltus mechanizmus aušinimo sistemose bei papildančią tradicinius efektyvumo rodiklius.

## LIST OF REFERENCES

1. Abuşka, M., & Çorumlu, V. (2023). A comparative experimental thermal performance analysis of conical pin fin heat sink with staggered and modified staggered layout under forced convection. *Thermal Science and Engineering Progress*, 37, 101560. <https://doi.org/10.1016/j.tsep.2022.101560>
2. Adrian, R. J. (2007). Hairpin vortex organization in wall turbulence. *Physics of Fluids*, 19(4). <https://doi.org/10.1063/1.2717527>
3. Aguirre, I., González, A., & Castillo, E. (2022). Numerical study on the use of shear-thinning nanofluids in a micro pin-fin heat sink including vortex generators and changes in pin shapes. *Journal of the Taiwan Institute of Chemical Engineers*, 136, 104400. <https://doi.org/10.1016/j.jtice.2022.104400>
4. Ahmadian-Elmi, M., Mashayekhi, A., Nourazar, S. S., & Vafai, K. (2021). A comprehensive study on parametric optimization of the pin-fin heat sink to improve its thermal and hydraulic characteristics. *International Journal of Heat and Mass Transfer*, 180, 121797. <https://doi.org/10.1016/j.ijheatmasstransfer.2021.121797>
5. Ahn, J. (2025). Large Eddy Simulation Approaches for Trailing-Edge Heat Transfer in Gas Turbine Blades: A Review. *Energies*, 18(6), 1386. <https://doi.org/10.3390/en18061386>
6. Al-Karooshi, M. A., Chahrour, K. M., Khalil, W. H., & Al-Damook, A. (2024). Numerical investigation of hydrothermal performance over perforated conical pin heat sinks. *Heat Transfer*, 53(2), 666–687. <https://doi.org/10.1002/htj.22969>
7. Amol Dhumal, Nitin Ambhore, Sandeep Kore, Aditya Naik, Vasant Phirke, & Kiran Ghuge. (2024). Investigation of the Effect of Different Fins Configurations on the Thermal Performance of the Radiator. *Journal of Advanced Research in Fluid Mechanics and Thermal Sciences*, 116(1), 27–39. <https://doi.org/10.37934/arfmts.116.1.2739>
8. Amor, C., Corrochano, A., Rota, G. F., Rosti, M. E., & Clainche, S. L. (2024). Coherent structures in elastic turbulent planar jets. *Journal of Physics: Conference Series*, 2753(1), 012020. <https://doi.org/10.1088/1742-6596/2753/1/012020>
9. Application of Omega Identification Method in the Ventilated Cavities Around a Surface-piercing Hydrofoil. (2023). In Y. Zhi, R. Qiu, R. Huang, & Y. Wang, *Springer Proceedings in Physics* (pp. 359–370). Springer Nature Singapore. [https://doi.org/10.1007/978-981-19-8955-1\\_24](https://doi.org/10.1007/978-981-19-8955-1_24)
10. Ateş, A., Parizad Benam, B., Yağcı, V., Çağlar Malyemez, M., Parlak, M., Sadaghiani, A. K., & Koşar, A. (2022). On the effect of elliptical pin Fins, distribution pin Fins, and tip clearance on the performance of heat sinks in flow boiling. *Applied Thermal Engineering*, 212, 118648. <https://doi.org/10.1016/j.applthermaleng.2022.118648>
11. Baba-Ahmadi, M. H., & Tabor, G. (2009). Inlet conditions for LES using mapping and feedback control. *Computers & Fluids*, 38(6), 1299–1311. <https://doi.org/10.1016/j.compfluid.2009.02.001>

12. Bai, X., Zhang, W., Fang, Q., Wang, Y., Zheng, J., & Guo, A. (2019). The visualization of turbulent coherent structure in open channel flow. *Journal of Hydrodynamics*, 31(2), 266–273. <https://doi.org/10.1007/s42241-019-0026-0>
13. Batchelor, G. K. (2010). *An Introduction to fluid dynamics* (14. print). Cambridge Univ. Press.
14. Bauri, K. P. (2022). Coherent structures around submerged circular and square cylinders due to change of orientation angle in steady current over plane bed. *Acta Geophysica*, 70(5), 2223–2250. <https://doi.org/10.1007/s11600-022-00799-3>
15. Belkacem, S. N. (2021). Identification of Vortex Structures in A Coaxial Jet. 3(2).
16. Bhandari, P., Padalia, D., Ranakoti, L., Khargotra, R., András, K., & Singh, T. (2023). Thermo-hydraulic investigation of open micro prism pin fin heat sink having varying prism sides. *Alexandria Engineering Journal*, 69, 457–468. <https://doi.org/10.1016/j.aej.2023.02.016>
17. Bhandari, P., & Prajapati, Y. K. (2021). Thermal performance of open microchannel heat sink with variable pin fin height. *International Journal of Thermal Sciences*, 159, 106609. <https://doi.org/10.1016/j.ijthermalsci.2020.106609>
18. Bhandari, P., & Prajapati, Y. K. (2022). Influences of tip clearance on flow and heat transfer characteristics of open type micro pin fin heat sink. *International Journal of Thermal Sciences*, 179, 107714. <https://doi.org/10.1016/j.ijthermalsci.2022.107714>
19. Bhandari, P., Rawat, K. S., Prajapati, Y. K., Padalia, D., Ranakoti, L., & Singh, T. (2024). A review on design alteration in microchannel heat sink for augmented thermohydraulic performance. *Ain Shams Engineering Journal*, 15(2), 102417. <https://doi.org/10.1016/j.asej.2023.102417>
20. Bovati, O., Yildiz, M. A., Hassan, Y., & Vaghetto, R. (2021). RANS simulations for transition and turbulent flow regimes in wire-wrapped rod bundles. *International Journal of Heat and Fluid Flow*, 90, 108838. <https://doi.org/10.1016/j.ijheatfluidflow.2021.108838>
21. Cao, S.-L., Sun, X., Zhang, J.-Z., & Zhang, Y.-X. (2021). Forced convection heat transfer around a circular cylinder in laminar flow: An insight from Lagrangian coherent structures. *Physics of Fluids*, 33(6). <https://doi.org/10.1063/5.0049219>
22. Chang, S. W., Wu, P.-S., Cai, W. L., & Yu, C. H. (2021). Experimental heat transfer and flow simulations of rectangular channel with twisted-tape pin-fin array. *International Journal of Heat and Mass Transfer*, 166, 120809. <https://doi.org/10.1016/j.ijheatmasstransfer.2020.120809>
23. Chen, S., Zhao, W., & Wan, D. (1993). CFD Study of Free Surface Effect on Flow around a Surface-Piercing Cylinder.
24. Colebrook, C. F. (1939). Turbulent Flow In Pipes, With Particular Reference To The Transition Region Between The Smooth And Rough Pipe Laws. *Journal of the Institution of Civil Engineers*, 11(4), 133–156. <https://doi.org/10.1680/ijoti.1939.13150>
25. Çorumlu, V. (2024). The effects of input power and ambient temperature on the thermal performance of conical pin fin heat sink in natural convection. *International*

- Journal of Thermal Sciences, 197, 108855.  
<https://doi.org/10.1016/j.ijthermalsci.2023.108855>
26. Coşkun, T., & Çetkin, E. (2020). Heat Transfer Enhancement in a Microchannel Heat Sink: Nanofluids and/or Micro Pin Fins. *Heat Transfer Engineering*, 41(21), 1818–1828. <https://doi.org/10.1080/01457632.2019.1670467>
  27. Dennis, D. J. C. (2015). Coherent structures in wall-bounded turbulence. *Anais Da Academia Brasileira de Ciências*, 87(2), 1161–1193. <https://doi.org/10.1590/0001-3765201520140622>
  28. Derakhshandeh, J. F., & Alam, M. M. (2019). A review of bluff body wakes. *Ocean Engineering*, 182, 475–488. <https://doi.org/10.1016/j.oceaneng.2019.04.093>
  29. Deshmukh, P. W., Kasar, S. V., & Prabhu, S. V. (2023). A Comprehensive Compendium on Passive Augmentation Techniques for Enhancement of Single-Phase Heat Transfer Coefficients in Heat Exchanger Tubes under Laminar and Turbulent Flow Conditions. *Heat Transfer Engineering*, 44(6), 530–579. <https://doi.org/10.1080/01457632.2022.2073671>
  30. Fiedler, H. E. (1988). Coherent structures in turbulent flows. *Progress in Aerospace Sciences*, 25(3), 231–269. [https://doi.org/10.1016/0376-0421\(88\)90001-2](https://doi.org/10.1016/0376-0421(88)90001-2)
  31. Forouzi Feshalami, B., He, S., Scarano, F., Gan, L., & Morton, C. (2022). A review of experiments on stationary bluff body wakes. *Physics of Fluids*, 34(1). <https://doi.org/10.1063/5.0077323>
  32. Frhan Al-Abboodi, N. K., Khalaf, K. A., Ridha, H., & Al-Azawy, M. G. (2022). Thermal and Flow Analysis of Different Shaped Pin Fins for Improved Heat Transfer Rate. *International Journal of Heat and Technology*, 40(1), 201–210. <https://doi.org/10.18280/ijht.400124>
  33. Ghasemi, A., & Elham, A. (2021). Multi-objective topology optimization of pin-fin heat exchangers using spectral and finite-element methods. *Structural and Multidisciplinary Optimization*, 64(4), 2075–2095. <https://doi.org/10.1007/s00158-021-02964-6>
  34. Ghorbani, N., Targhi, M. Z., Heyhat, M. M., & Alihosseini, Y. (2022). Investigation of wavy microchannel ability on electronic devices cooling with the case study of choosing the most efficient microchannel pattern. *Scientific Reports*, 12(1). <https://doi.org/10.1038/s41598-022-09859-6>
  35. Gijoy, S., Gayathri, M. A., Rejin, S., & Roy, K. E. R. (2025). Numerical investigation and optimization of an asymmetric elliptical-cylindrical pin fin heat sink. *International Journal of Thermal Sciences*, 209, 109514. <https://doi.org/10.1016/j.ijthermalsci.2024.109514>
  36. He, Z., Yan, Y., & Zhang, Z. (2021). Thermal management and temperature uniformity enhancement of electronic devices by micro heat sinks: A review. *Energy*, 216, 119223. <https://doi.org/10.1016/j.energy.2020.119223>
  37. Hossain, M. I., Chowdhury, M. S. H., Ahmed, S. S. U., Hamja, A., & Siddique, I. J. (2025). Forced convective heat transfer over twisted and perforated forked pin fin heat sink: A numerical study. *International Journal of Thermal Sciences*, 211, 109719. <https://doi.org/10.1016/j.ijthermalsci.2025.109719>

38. Huang, C.-H., & Wu, Y.-T. (2021). An optimum design for a natural convection pin fin array with orientation consideration. *Applied Thermal Engineering*, 188, 116633. <https://doi.org/10.1016/j.applthermaleng.2021.116633>
39. Hussain, A. K. M. F. (1983). Coherent structures—Reality and myth. *The Physics of Fluids*, 26(10), 2816–2850. <https://doi.org/10.1063/1.864048>
40. Ismail, M. (2024). Experimental and numerical analysis of heat sink using various patterns of cylindrical pin-fins. *International Journal of Thermofluids*, 23, 100737. <https://doi.org/10.1016/j.ijft.2024.100737>
41. İzci, T., Koz, M., & Koşar, A. (2015). The Effect of Micro Pin-Fin Shape on Thermal and Hydraulic Performance of Micro Pin-Fin Heat Sinks. *Heat Transfer Engineering*, 36(17), 1447–1457. <https://doi.org/10.1080/01457632.2015.1010921>
42. Jeng, T.-M., & Tzeng, S.-C. (2007). Pressure drop and heat transfer of square pin-fin arrays in in-line and staggered arrangements. *International Journal of Heat and Mass Transfer*, 50(11–12), 2364–2375. <https://doi.org/10.1016/j.ijheatmasstransfer.2006.10.028>
43. Jeong, J., & Hussain, F. (1995). On the identification of a vortex. *Journal of Fluid Mechanics*, 285, 69–94. <https://doi.org/10.1017/s0022112095000462>
44. Jiang, X., Lefauve, A., Dalziel, S. B., & Linden, P. F. (2022). The evolution of coherent vortical structures in increasingly turbulent stratified shear layers. *Journal of Fluid Mechanics*, 947. <https://doi.org/10.1017/jfm.2022.588>
45. Jiao, Y., Hwang, Y., & Chernyshenko, S. I. (2021). Orr mechanism in transition of parallel shear flow. *Physical Review Fluids*, 6(2). <https://doi.org/10.1103/physrevfluids.6.023902>
46. Joshi, S. N., Zhou, F., Liu, Y., Lohan, D. J., Ukegawa, H., Lee, J., & Dede, E. M. (2023). A Review of Select Patented Technologies for Cooling of High Heat Flux Power Semiconductor Devices. *IEEE Transactions on Power Electronics*, 38(6), 6790–6794. <https://doi.org/10.1109/tpel.2023.3243546>
47. Kadiyala, P. K., & Chattopadhyay, H. (2018). Numerical Analysis of Heat Transfer from a Moving Surface Due to Impingement of Slot Jets. *Heat Transfer Engineering*, 39(2), 98–106. <https://doi.org/10.1080/01457632.2017.1288045>
48. Kandlikar, S. G., & Grande, W. J. (2003). Evolution of Microchannel Flow Passages—Thermohydraulic Performance and Fabrication Technology. *Heat Transfer Engineering*, 24(1), 3–17. <https://doi.org/10.1080/01457630304040>
49. Keshari, V., & Maiya, M. P. (2018). Design and investigation of hydriding alloy based hydrogen storage reactor integrated with a pin fin tube heat exchanger. *International Journal of Hydrogen Energy*, 43(14), 7081–7095. <https://doi.org/10.1016/j.ijhydene.2018.02.100>
50. Khattak, Z., & Ali, H. M. (2019). Air cooled heat sink geometries subjected to forced flow: A critical review. *International Journal of Heat and Mass Transfer*, 130, 141–161. <https://doi.org/10.1016/j.ijheatmasstransfer.2018.08.048>
51. Khoshvaght-Aliabadi, M., Deldar, S., & Hassani, S. M. (2018). Effects of pin-fins geometry and nanofluid on the performance of a pin-fin miniature heat sink

- (PFMHS). *International Journal of Mechanical Sciences*, 148, 442–458. <https://doi.org/10.1016/j.ijmecsci.2018.09.019>
52. Kim, B.-C., & Chang, K. (2020). Assessment of Hybrid RANS/LES Models in Heat and Fluid Flows around Staggered Pin-Fin Arrays. *Energies*, 13(14), 3752. <https://doi.org/10.3390/en13143752>
53. Kim, K. S., Kwon, J., Ryu, H., Kim, C., Kim, H., Lee, E.-K., Lee, D., Seo, S., Han, N. M., Suh, J. M., Kim, J., Song, M.-K., Lee, S., Seol, M., & Kim, J. (2024). The future of two-dimensional semiconductors beyond Moore's law. *Nature Nanotechnology*, 19(7), 895–906. <https://doi.org/10.1038/s41565-024-01695-1>
54. Kishore, H., Pal, M., Nirala, C. K., & Agrawal, A. (2024). Thermal Performance Evaluation of Micro Pin-Fin Heat Exchangers: Part II—Numerical Simulation and Fabrication Demonstration. *International Journal of Precision Engineering and Manufacturing*, 25(2), 255–269. <https://doi.org/10.1007/s12541-023-00926-0>
55. Koşar, A., Schneider, B., & Peles, Y. (2011). Hydrodynamic Characteristics of Crossflow over MEMS-Based Pillars. *Journal of Fluids Engineering*, 133(8). <https://doi.org/10.1115/1.4004366>
56. Lee, C.-S., Shih, T. I.-P., Bryden, K. M., Dalton, R. P., & Dennis, R. A. (2023). Strongly Heated Turbulent Flow in a Channel with Pin Fins. *Energies*, 16(3), 1215. <https://doi.org/10.3390/en16031215>
57. Lekkala, M. R., Latheef, M., Jung, J. H., Coraddu, A., Zhu, H., Srinil, N., Lee, B.-H., & Kim, D. K. (2022). Recent advances in understanding the flow over bluff bodies with different geometries at moderate Reynolds numbers. *Ocean Engineering*, 261, 111611. <https://doi.org/10.1016/j.oceaneng.2022.111611>
58. Lewis, D. R., & Radko, T. (2020). On the structure and patterns of von Kármán vortices in two-dimensional high Reynolds number flows. *Physics of Fluids*, 32(11), 116601. <https://doi.org/10.1063/5.0022537>
59. Li, W., Ren, J., Hongde, J., Luan, Y., & Ligrani, P. (2016). Assessment of six turbulence models for modeling and predicting narrow passage flows, part 2: Pin fin arrays. *Numerical Heat Transfer, Part A: Applications*, 69(5), 445–463. <https://doi.org/10.1080/10407782.2015.1081024>
60. Liang, D., Chen, W., Ju, Y., & Chyu, M. K. (2021). Comparing endwall heat transfer among staggered pin fin, Kagome and body centered cubic arrays. *Applied Thermal Engineering*, 185, 116306. <https://doi.org/10.1016/j.applthermaleng.2020.116306>
61. Lin, C.-X., & Kiflemariam, R. (2019). Numerical Simulation and Validation of Thermoelectric Generator Based Self-Cooling System with Airflow. *Energies*, 12(21), 4052. <https://doi.org/10.3390/en12214052>
62. Liu, C., Gao, Y., Dong, X., Wang, Y., Liu, J., Zhang, Y., Cai, X., & Gui, N. (2019). Third generation of vortex identification methods: Omega and Liutex/Rortex based systems. *Journal of Hydrodynamics*, 31(2), 205–223. <https://doi.org/10.1007/s42241-019-0022-4>
63. Liu, C., Wang, Y., Yang, Y., & Duan, Z. (2016). New omega vortex identification method. *Science China Physics, Mechanics & Astronomy*, 59(8). <https://doi.org/10.1007/s11433-016-0022-6>

64. Lotfi, B., & Sundén, B. (2020). Thermo-Hydraulic Performance Enhancement of Finned Elliptical Tube Heat Exchangers by Utilizing Innovative Dimple Turbulators. *Heat Transfer Engineering*, 41(13), 1117–1142. <https://doi.org/10.1080/01457632.2019.1611132>
65. Lv, H., He, K., & Ju, X. (2023). Optimization and Numerical Investigation of Micro-pin-Fin Structure on Heat Sink with Checkerboard Nozzles. In Y. Wang, Y. Liu, J. Zou, & M. Huo (Eds.), *Signal and Information Processing, Networking and Computers* (Vol. 996, pp. 146–154). Springer Nature Singapore. [https://doi.org/10.1007/978-981-19-9968-0\\_18](https://doi.org/10.1007/978-981-19-9968-0_18)
66. Lv, M., Liu, Z., Chi, W., Ma, C., & Duan, L. (2022). Investigation on Flow Through Staggered Micro Pin Fin Arrays with Variable Longitudinal Spacings Using Micro-PIV. *Nanoscale and Microscale Thermophysical Engineering*, 26(4), 198–217. <https://doi.org/10.1080/15567265.2022.2122911>
67. Mei, D., Lou, X., Qian, M., Yao, Z., Liang, L., & Chen, Z. (2014). Effect of tip clearance on the heat transfer and pressure drop performance in the micro-reactor with micro-pin–fin arrays at low Reynolds number. *International Journal of Heat and Mass Transfer*, 70, 709–718. <https://doi.org/10.1016/j.ijheatmasstransfer.2013.11.060>
68. Menter, F. R. (1994). Two-equation eddy-viscosity turbulence models for engineering applications. *AIAA Journal*, 32(8), 1598–1605. <https://doi.org/10.2514/3.12149>
69. Mercier, P., Ikhennicheu, M., Guillou, S., Germain, G., Poizot, E., Grondeau, M., Thiébot, J., & Druault, P. (2020). The merging of Kelvin–Helmholtz vortices into large coherent flow structures in a high Reynolds number flow past a wall-mounted square cylinder. *Ocean Engineering*, 204, 107274. <https://doi.org/10.1016/j.oceaneng.2020.107274>
70. Mesgarpour, M., Heydari, A., & Saedodin, S. (2019). Numerical analysis of heat transfer and fluid flow in the bundle of porous tapered fins. *International Journal of Thermal Sciences*, 135, 398–409. <https://doi.org/10.1016/j.ijthermalsci.2018.09.032>
71. Moores, K. A., Kim, J., & Joshi, Y. K. (2009). Heat transfer and fluid flow in shrouded pin fin arrays with and without tip clearance. *International Journal of Heat and Mass Transfer*, 52(25–26), 5978–5989. <https://doi.org/10.1016/j.ijheatmasstransfer.2009.08.005>
72. Naphon, P., & Sookkasem, A. (2007). Investigation on heat transfer characteristics of tapered cylinder pin fin heat sinks. *Energy Conversion and Management*, 48(10), 2671–2679. <https://doi.org/10.1016/j.enconman.2007.04.020>
73. Pan, Y., & Banerjee, S. (1995). A numerical study of free-surface turbulence in channel flow. *Physics of Fluids*, 7(7), 1649–1664. <https://doi.org/10.1063/1.868483>
74. Parlak, F., & Sertkaya, A. A. (2024). Experimental investigation of forced convection heat transfer of heat exchangers with different pin geometries in in-line and staggered design. *International Journal of Heat and Mass Transfer*, 231, 125892. <https://doi.org/10.1016/j.ijheatmasstransfer.2024.125892>

75. Pati, B., Sharma, B., Palo, A., & Barman, R. (2018). Numerical investigation of pin-fin thermal performance for staggered and inline arrays at low Reynolds number. *International Journal of Heat and Technology*, 36(2), 697–703. <https://doi.org/10.18280/ijht.360235>
76. Pereira, F. S., Eça, L., Vaz, G., & Girimaji, S. S. (2018). Challenges in Scale-Resolving Simulations of turbulent wake flows with coherent structures. *Journal of Computational Physics*, 363, 98–115. <https://doi.org/10.1016/j.jcp.2018.02.038>
77. Perry, A. E., & Fairlie, B. D. (1975). Critical points in flow patterns. In *Advances in geophysics*, 18, 299–315. Elsevier. [https://doi.org/10.1016/S0065-2687\(08\)60588-9](https://doi.org/10.1016/S0065-2687(08)60588-9)
78. Polat, M. E., Ulger, F., & Cadirci, S. (2022). Multi-objective optimization and performance assessment of microchannel heat sinks with micro pin-fins. *International Journal of Thermal Sciences*, 174, 107432. <https://doi.org/10.1016/j.ijthermalsci.2021.107432>
79. Protas, B. (2004). Linear feedback stabilization of laminar vortex shedding based on a point vortex model. *Physics of Fluids*, 16(12), 4473–4488. <https://doi.org/10.1063/1.1808773>
80. Qin, S.-Y., Yu, Z.-Q., Fang, Z.-B., Liu, W., & Shan, F. (2023). Effects of the wall heat flux on the flow characteristics of large-scale coherent structures in a pipe with enhanced heat transfer. *Chemical Engineering Science*, 282, 119284. <https://doi.org/10.1016/j.ces.2023.119284>
81. Qiu, Y., Hu, W., Wu, C., & Chen, W. (2020). An Experimental Study of Microchannel and Micro-Pin-Fin Based On-Chip Cooling Systems with Silicon-to-Silicon Direct Bonding. *Sensors*, 20(19), 5533. <https://doi.org/10.3390/s20195533>
82. Rahman, M. A., Hasnain, S. M. M., Paramasivam, P., & Ayanie, A. G. (2024). Advancing thermal management in electronics: A review of innovative heat sink designs and optimization techniques. *RSC Advances*, 14(43), 31291–31319. <https://doi.org/10.1039/d4ra05845c>
83. Raza, W., Ansari, D., Jeong, J. H., Samad, A., & Duwig, C. (2024). A novel microchannel-twisted pinfin hybrid heat sink for hotspot mitigation. *Applied Thermal Engineering*, 241, 122454. <https://doi.org/10.1016/j.applthermaleng.2024.122454>
84. Renfer, A., Tiwari, M. K., Brunschwiler, T., Michel, B., & Poulikakos, D. (2011). Experimental investigation into vortex structure and pressure drop across microcavities in 3D integrated electronics. *Experiments in Fluids*, 51(3), 731–741. <https://doi.org/10.1007/s00348-011-1091-5>
85. Renfer, A., Tiwari, M. K., Tiwari, R., Alfieri, F., Brunschwiler, T., Michel, B., & Poulikakos, D. (2013). Microvortex-enhanced heat transfer in 3D-integrated liquid cooling of electronic chip stacks. *International Journal of Heat and Mass Transfer*, 65, 33–43. <https://doi.org/10.1016/j.ijheatmasstransfer.2013.05.066>
86. Reynolds, O. (1895). IV. On the dynamical theory of incompressible viscous fluids and the determination of the criterion. *Philosophical Transactions of the Royal Society of London*. (A.), 186, 123–164. <https://doi.org/10.1098/rsta.1895.0004>

87. Roache, P. J. (1997). QUANTIFICATION OF UNCERTAINTY IN COMPUTATIONAL FLUID DYNAMICS. *Annual Review of Fluid Mechanics*, 29(1), 123–160. <https://doi.org/10.1146/annurev.fluid.29.1.123>
88. Rosa, P., Karayiannis, T. G., & Collins, M. W. (2009). Single-phase heat transfer in microchannels: The importance of scaling effects. *Applied Thermal Engineering*, 29(17–18), 3447–3468. <https://doi.org/10.1016/j.applthermaleng.2009.05.015>
89. Sadique, H., Murtaza, Q., & Samsher. (2022). Heat transfer augmentation in microchannel heat sink using secondary flows: A review. *International Journal of Heat and Mass Transfer*, 194, 123063. <https://doi.org/10.1016/j.ijheatmasstransfer.2022.123063>
90. Saito, M. B., & De Lemos, M. J. S. (2006). A Correlation for Interfacial Heat Transfer Coefficient for Turbulent Flow Over an Array of Square Rods. *Journal of Heat Transfer*, 128(5), 444–452. <https://doi.org/10.1115/1.2175150>
91. Sakanova, A., & Tseng, K. J. (2018). Comparison of pin-fin and finned shape heat sink for power electronics in future aircraft. *Applied Thermal Engineering*, 136, 364–374. <https://doi.org/10.1016/j.applthermaleng.2018.03.020>
92. Saravanan, V., & Umesh, C. K. (2018). Numerical comparison for thermo-hydraulic performance of pin fin heat sink with micro channel pin fin heat sink. *Sādhanā*, 43(7). <https://doi.org/10.1007/s12046-018-0875-1>
93. Schlichting, H., & Gersten, K. (2017). *Boundary-Layer Theory*. Springer Berlin Heidelberg. <https://doi.org/10.1007/978-3-662-52919-5>
94. Schumacher, J., Scheel, J. D., Krasnov, D., Donzis, D. A., Yakhot, V., & Sreenivasan, K. R. (2014). Small-scale universality in fluid turbulence. *Proceedings of the National Academy of Sciences*, 111(30), 10961–10965. <https://doi.org/10.1073/pnas.1410791111>
95. Serkan Şahin, Y., İsmet Toprak, B., Solmaz, İ., & Bayer, Ö. (2023). Investigation of flow and heat transfer behavior of integrated pin fin-aluminum foam heat sink. *Applied Thermal Engineering*, 219, 119504. <https://doi.org/10.1016/j.applthermaleng.2022.119504>
96. Shima, K., Funato, Y., Sugiura, H., Sato, N., Fukushima, Y., Momose, T., & Shimogaki, Y. (2016). High-Aspect-Ratio Parallel-Plate Microchannels Applicable to Kinetic Analysis of Chemical Vapor Deposition. *Advanced Materials Interfaces*, 3(16), 1600254. <https://doi.org/10.1002/admi.201600254>
97. Singh, P., Zhang, M., Ahmed, S., Ramakrishnan, K. R., & Ekkad, S. (2019). Effect of micro-roughness shapes on jet impingement heat transfer and fin-effectiveness. *International Journal of Heat and Mass Transfer*, 132, 80–95. <https://doi.org/10.1016/j.ijheatmasstransfer.2018.11.135>
98. Song, P., Wang, H., Wei, M., Zheng, S., Li, J., Zhuge, W., & Zhang, Y. (2023). Flow loss mechanism of a novel co-rotating scroll hydrogen recirculation pump for fuel cell systems. *Case Studies in Thermal Engineering*, 52, 103692. <https://doi.org/10.1016/j.csite.2023.103692>

99. Souida, S., Sahel, D., Ameer, H., & Yousfi, A. (2022). Numerical Simulation of Heat Transfer Behaviors in Conical Pin Fins Heat Sinks. *Acta Mechanica Slovaca*, 26(3), 32–41. <https://doi.org/10.21496/ams.2023.002>
100. Sparrow, E. M., Ramsey, J. W., & Altemani, C. A. C. (1980). Experiments on In-line Pin Fin Arrays and Performance Comparisons with Staggered Arrays. *Journal of Heat Transfer*, 102(1), 44–50. <https://doi.org/10.1115/1.3244247>
101. Spedding, G. R. (2002). The streamwise spacing of adjacent coherent structures in stratified wakes. *Physics of Fluids*, 14(11), 3820–3828. <https://doi.org/10.1063/1.1508442>
102. Sreenivasan, K. R. (2019). Turbulent mixing: A perspective. *Proceedings of the National Academy of Sciences*, 116(37), 18175–18183. <https://doi.org/10.1073/pnas.1800463115>
103. Sundaram, R. D., Madhavan, S., Singh, P., & Ekkad, S. V. (2021). Enhanced fin-effectiveness of micro-scale concentric-shape roughened target surface subjected to array jet impingement. *International Journal of Heat and Mass Transfer*, 173, 121148. <https://doi.org/10.1016/j.ijheatmasstransfer.2021.121148>
104. Tahsin, S. H., Fahad, M. K., Ifraj, N. F., Rimon, Md. S., Rahman, F., & Haque, M. R. (2024). Experimental and Numerical Study of Conical-Shaped Pin Finned Heat Sink with PCM Material. *Malaysian Journal on Composites Science and Manufacturing*, 14(1), 1–15. <https://doi.org/10.37934/mjcs.14.1.0115>
105. Tobak, M., & Peake, D. J. (1982). Topology of Three-Dimensional Separated Flows. *Annual Review of Fluid Mechanics*, 14(1), 61–85. <https://doi.org/10.1146/annurev.fl.14.010182.000425>
106. Tong, F., Cheng, L., An, H., Griffiths, T., & Ren, C. (2025). Coherent flow structures upstream a circular cylinder near a plane wall. *Physics of Fluids*, 37(1). <https://doi.org/10.1063/5.0244473>
107. Tsuruhashi, T., Goto, S., Oka, S., & Yoneda, T. (2022). Self-similar hierarchy of coherent tubular vortices in turbulence. *Philosophical Transactions of the Royal Society A: Mathematical, Physical and Engineering Sciences*, 380(2226). <https://doi.org/10.1098/rsta.2021.0053>
108. Wang, H., Yang, Z., Wu, T., & Wang, S. (2021). Coherent structures associated with interscale energy transfer in turbulent channel flows. *Physical Review Fluids*, 6(10). <https://doi.org/10.1103/physrevfluids.6.104601>
109. Wang, P., & Chen, L. (2019). Thermal and hydraulic performance of micro pin fin heat sinks with different pin fin shapes. *IOP Conference Series: Materials Science and Engineering*, 542(1), 012053. <https://doi.org/10.1088/1757-899x/542/1/012053>
110. Wang, Z., Yin, Y., Yang, L., Wang, Y., & Luan, Y. (2022). Similar Characteristics of Heat Transfer in Different Scale Cooling Channel with Ribs. *Heat Transfer Engineering*, 43(12), 1025–1040. <https://doi.org/10.1080/01457632.2021.1932038>
111. Webb, R. L. (1981). Performance evaluation criteria for use of enhanced heat transfer surfaces in heat exchanger design. *International Journal of Heat and Mass Transfer*, 24(4), 715–726. [https://doi.org/10.1016/0017-9310\(81\)90015-6](https://doi.org/10.1016/0017-9310(81)90015-6)
112. White, F. M. (2011). *Fluid mechanics* (7. ed). McGraw-Hill.

113. Wilcox, D. C. (2010). *Turbulence modeling for CFD* (3. ed., 2. print). DCW Industries.
114. Xu, F., Pan, Z., & Wu, H. (2018). Experimental investigation on the flow transition in different pin-fin arranged microchannels. *Microfluidics and Nanofluidics*, 22(1). <https://doi.org/10.1007/s10404-017-2030-4>
115. Xu, Y., Li, L., & Wang, J. (2023). Experimental and numerical investigations of the thermal-hydraulic characteristics of novel micropin-fin heat sinks. *International Journal of Heat and Mass Transfer*, 209, 124079. <https://doi.org/10.1016/j.ijheatmasstransfer.2023.124079>
116. Yan, H., Luo, L., Zhang, J., Du, W., Wang, S., & Huang, D. (2021). Flow structure and heat transfer characteristics of a pin-finned channel with upright/curved/inclined pin fins under stationary and rotating conditions. *International Communications in Heat and Mass Transfer*, 127, 105483. <https://doi.org/10.1016/j.icheatmasstransfer.2021.105483>
117. Yang, K., Sui, Y., Wang, X., & Feng, Z. (2025). Study on flow and heat transfer characteristics in rectangular channels with lantern-shaped pin fin array: Part I-effect of sphere diameter. *Numerical Heat Transfer, Part A: Applications*, 86(4), 813–843. <https://doi.org/10.1080/10407782.2023.2251085>
118. Younis, M. Y., Zhang, H., Hu, B., Muhammad, Z., & Mehmood, S. (2014). Investigation of different aspects of laminar horseshoe vortex system using PIV. *Journal of Mechanical Science and Technology*, 28(2), 527–537. <https://doi.org/10.1007/s12206-013-1120-9>
119. Yu, Z.-Q., Li, M.-T., & Cao, B.-Y. (2024). A comprehensive review on microchannel heat sinks for electronics cooling. *International Journal of Extreme Manufacturing*, 6(2), 022005. <https://doi.org/10.1088/2631-7990/ad12d4>
120. Zdravkovich, M. M., & Bearman, P. W. (1997). *Flow Around Circular Cylinders Volume 1: Fundamentals*. <https://api.semanticscholar.org/CorpusID:119612383>
121. Zhang, D. (2017). Comparison of Various Turbulence Models for Unsteady Flow around a Finite Circular Cylinder at Re=20000. *Journal of Physics: Conference Series*, 910, 012027. <https://doi.org/10.1088/1742-6596/910/1/012027>
122. Zhang, J., Han, H. Z., Li, Z. R., & Zhong, H. G. (2021). Effect of pin-fin forms on flow and cooling characteristics of three-layer porous laminate. *Applied Thermal Engineering*, 194, 117084. <https://doi.org/10.1016/j.applthermaleng.2021.117084>
123. Zhang, Y., Wang, X., Zhang, Y., & Liu, C. (2019). Comparisons and analyses of vortex identification between Omega method and Q criterion. *Journal of Hydrodynamics*, 31(2), 224–230. <https://doi.org/10.1007/s42241-019-0025-1>
124. Zhao, J., Pei, J., Yuan, J., & Wang, W. (2024). Numerical investigation of vortex structure and unsteady evolution in multi-stage double-suction centrifugal pump. *Journal of Physics: Conference Series*, 2707(1), 012017. <https://doi.org/10.1088/1742-6596/2707/1/012017>
125. Zhou, J., Lu, M., Han, L., Zhao, Q., Li, Q., & Chen, X. (2025). Topological manifold microchannel cooling for thermal management of divertor in fusion reactor. *Energy*, 315, 134145. <https://doi.org/10.1016/j.energy.2024.134145>

126. Zohora, F.-T., Haque, M. R., & Haque, M. M. (2023). Numerical investigation of the hydrothermal performance of novel pin-fin heat sinks with hyperbolic, wavy, and crinkle geometries and various perforations. *International Journal of Thermal Sciences*, 194, 108578. <https://doi.org/10.1016/j.ijthermalsci.2023.108578>
127. Žukauskas, A. (1972). Heat Transfer from Tubes in Crossflow (J. P. Hartnett & T. F. Irvine, Eds; Vol. 8, pp. 93–160). Elsevier. [https://doi.org/10.1016/S0065-2717\(08\)70038-8](https://doi.org/10.1016/S0065-2717(08)70038-8)

## **CURRICULUM VITAE AND DESCRIPTION OF CREATIVE ACTIVITIES (CV)**

Vardas: Justina

Pavardė: Jaseliūnaitė

Gimimo data: 1996 vasario 24 d.

Gimimo vieta: Šiauliai, Lietuva

El. paštas: Justina.jaseliunaite@gmail.com

Išsilavinimas:

2015-2019: Kauno technologijos universitetas, taikomosios fizikos ir pedagogikos bakalauras

2019-2021: Kauno technologijos universitetas, termoinžinerijos magistras

2021-2025: Lietuvos energetikos institutas, doktorantūros studijos technologinių mokslų kryptyje (energetika ir termoinžinerija)

## LIST OF SCIENTIFIC PAPERS AND SCIENTIFIC CONFERENCES

### Articles in journals from “Clarivative Analytics” “Web of Science” database list

1. Jaseliūnaitė, J., Šeporaitis, M.. Performance optimisation of microchannel pin-fins using 2D CFD. // Applied Thermal Engineering, 2022, vol. 206, p. 118040. <https://doi.org/10.1016/j.applthermaleng.2022.118040>
2. Jaseliūnaitė, J., Šeporaitis, M. Extensive computational fluid dynamics analysis of microchannel flow topology and friction factor in arrays of conical pin-fins. // Physics of Fluids, 2024, vol 36, iss. 9. <https://doi.org/10.1063/5.0220609>
3. Jaseliūnaitė, J., Šeporaitis, M. The Potential of Hourglass-Shaped Pin-Fins on Enhancing Thermohydraulic Performance in Microchannel Arrays // Heat Transfer Engineering, 2025, 1-18. <https://doi.org/10.1080/01457632.2025.2480904>

### Book chapters

1. Jaseliūnaitė J., Šeporaitis, M. Comparative Assessment of Flow Patterns and Hydrodynamics in Cylindrical and Hourglass-Shaped Pin-Fin Configurations In: Benim, A.C., Bennacer, R., Mohamad, A.A., Ocoń, P., Suh, SH., Taler, J. (eds) Advances in Computational Heat and Mass Transfer. ICCHMT 2023. Lecture Notes in Mechanical Engineering. Springer, Cham. [https://doi.org/10.1007/978-3-031-67241-5\\_62](https://doi.org/10.1007/978-3-031-67241-5_62)

### Reports in the international conferences

1. J. Jaseliūnaitė, M. Šeporaitis, Numerical Modelling of Flow Behavior in a Micro Cylinder and Double-Cylinder Pin-Fin Arrays, 13th Asian Computational Fluid Dynamics Conference – ACFD 2022. 16-19 October, Jeju, Republic of Korea.
2. Jaseliūnaitė J., Šeporaitis M. Numerical Study of Transverse Pitch Effect On Pressure Loss In An Inline Array Of Elliptical Pins In: Proceedings of the 10th international conference on fluid flow, heat and mass transfer (FFHMT`23). Ottawa: Carleton University, Canada, 2023, 07-09 June, p. 172-1-172-7. ISSN 2369-3029 ISBN 978-1-990800-24-5.
3. Jaseliūnaitė J., Šeporaitis M. Comparative Assessment of Flow Patterns and Hydrodynamics in Cylindrical and Hourglass-Shaped Pin-Fin Configurations In: Proceedings of the 14th International Conference on Computational Heat

and Mass Transfer (ICCHMT 2023). Dusseldorf, Germany, 2023, 4-8 September.

4. Jaseliūnaitė J., Šeporaitis M., Ručys R. Numerical Modelling of Flow Behaviour in a Micro Pin-Fin Arrays. In: Proceedings of the 20<sup>th</sup> International Conference of Young Scientists on Energy and Natural Sciences Issues (CYSENI 2024). Lithuania, Kaunas, 2024, 21-23 May.
5. Jaseliūnaitė J., Šeporaitis M. Analysis of Vortical Structures in Flow Through Pin-fin Arrays Using  $\Omega$  Criterion In: Proceedings of the 19<sup>th</sup> OpenFOAM workshop. Beijing, China, 2024, 25-28 June.
6. Jaseliūnaitė J., Šeporaitis M. Advances in Vortical Structure Analysis for Superior Heat Transfer in Pin-Fin Microchannels. 23rd IACM Computational Fluids Conference – CFC 2025. March 17-20, Santiago, Chile, 2025.

## APPENDICES

**Appendix 1.** Hydraulic diameter, heating area, pin area, pin volume and flow volume of investigated cases

	$D_h$ , $\mu\text{m}$	Heating area, $\mu\text{m}^2$	Pin area, $\mu\text{m}^2$	Pin volume, $\mu\text{m}^3$	Flow volume, $\mu\text{m}^3$
R-C-S (Renfer et al. 2013)	152.79	257195	62792.7	1570796	25731100
R-C-I (Renfer et al. 2011)	133.33				25731100
K-C (Kosar et al.)	206.48	-	76311	1908518	26562900
R-DC	133.33	-	70853.7	1784250	24863700
R-E-P50	19.05	-	46004.25	628318.5	5486726
R-E-P60	36.36	-			7086726
R-E-P70	52.17	-			10286726
R-E-P80	66.67	-			8686726
R-E-P90	80.00	-			11886726
R-E-P100	92.31	-			13486726
R-E-P110	103.70	-			15086726
R-E-P120	114.29	-			16686726
R-E-P130	124.14	-			18286726
R-E-P140	133.33	-			19886726
K-H19	223.44	-			78418.3
K-C-P200	141.69	-	76331	1908518	15628400
K-C-P225	165.08	-			20791600
K-C-P250	185.50	-			26562900
K-C-P275	203.47	-			32940200
K-C-P300	219.41	-			39926200
K-T2-A(B)-P200	163.80	-			76362.6
K-T4-A(B)-P200	163.60	-	76527.3	1926902.9	15591800
K-T6-A(B)-P200	163.27	-	76756.6	1949560.8	15546500
K-T8-A(B)-P200	162.82	-	77075.7	1981196.4	15484100
K-T10-A(B)-P200	162.27	-	77472.6	2020738.4	15405200
K-T12-A(B)-P200	161.60	-	77952.7	2068835.6	15308900
K-T14-A(B)-P200	160.85	-	78499.7	2124004.4	15198700
K-T2-A(B)-P225	186.61	-	76386.3	1913006.4	20782600
K-T4-A(B)-P225	186.40	-	76527.3	1926902.9	20754800
K-T6-A(B)-P225	186.06	-	76756.6	1949560.8	20709700
K-T8-A(B)-P225	185.58	-	77075.7	1981196.4	20647200

K-T10-A(B)-P225	184.99	-	77472.6	2020738.4	20568200
K-T12-A(B)-P225	184.29	-	77952.7	2068835.6	20471900
K-T14-A(B)-P225	183.49	-	78499.7	2124004.4	20361700
K-T2-A(B)-P250	206.41	-	76386.3	1913006.4	26553300
K-T4-A(B)-P250	206.19	-	76527.3	1926902.9	26526100
K-T6-A(B)-P250	205.84	-	76756.6	1949560.8	26480800
K-T8-A(B)-P250	205.35	-	77075.7	1981196.4	26417400
K-T10-A(B)-P250	204.74	-	77472.6	2020738.4	26338500
K-T12-A(B)-P250	204.01	-	77952.7	2068835.6	26242300
K-T14-A(B)-P250	203.18	-	78499.7	2124004.4	26132500
K-T2-A(B)-P275	223.76	-	76386.3	1913006.4	32931300
K-T4-A(B)-P275	223.53	-	76527.3	1926902.9	32903500
K-T6-A(B)-P275	223.17	-	76756.6	1949560.8	32858000
K-T8-A(B)-P275	222.67	-	77075.7	1981196.4	32795500
K-T10-A(B)-P275	222.05	-	77472.6	2020738.4	32716000
K-T12-A(B)-P275	221.31	-	77952.7	2068835.6	32620300
K-T14-A(B)-P275	220.46	-	78499.7	2124004.4	32510200
K-T2-A(B)-P300	239.07	-	76386.3	1913006.4	39917300
K-T4-A(B)-P300	238.85	-	76527.3	1926902.9	39889600
K-T6-A(B)-P300	238.48	-	76756.6	1949560.8	39844000
K-T8-A(B)-P300	237.98	-	77075.7	1981196.4	39781000
K-T10-A(B)-P300	237.36	-	77472.6	2020738.4	39702000
K-T12-A(B)-P300	236.61	-	77952.7	2068835.6	39605900
K-T14-A(B)-P300	235.76	-	78499.7	2124004.4	39495700
R-T4-A(B)	152.55	256379	62885	1581059	25708000
R-T8-A(B)	151.44	250366	63620.8	1631324	25508700
R-H8	160.24	238887	63293.3	1581059	25726000
R-H13	170.69	227079	63713.2	1567236	25764900
R-H9	172.05	257266	53912.3	1146681	27440000
R-H16	191.53	257186	46365.4	835873.1	28674900

UDK 532.5+536](043.3)

SL344. 2025-\*-\*; \* leidyb. apsk. I. Tiražas 14 egz. Užsakymas \*  
Išleido Kauno technologijos universitetas, K. Donelaičio g. 73, 44249 Kaunas  
Spausdino leidyklos „Technologija“ spaustuvė, Studentų g. 54, 51424 Kaunas